

REPORT DOCUMENTATION PAGE		READ INSTRUCTIONS BEFORE COMPLETING FORM
1. REPORT NUMBER Report 7	2. GOVT ACCESSION NO.	3. RECIPIENT'S CATALOG NUMBER
4. TITLE (and Subtitle) Pressure Gradient Effects in the Viscous Wall Region of a Turbulent Flow		5. TYPE OF REPORT & PERIOD COVERED Progress 1983-1986
		6. PERFORMING ORG. REPORT NUMBER
7. AUTHOR(s) Finnicum, Douglas S. and Thomas J. Hanratty, Project Supervisor		8. CONTRACT OR GRANT NUMBER(s)
9. PERFORMING ORGANIZATION NAME AND ADDRESS Department of Chemical Engineering University of Illinois, 1209 W. California St. Urbana, IL 61801		10. PROGRAM ELEMENT, PROJECT, TASK AREA & WORK UNIT NUMBERS NR 657-728
11. CONTROLLING OFFICE NAME AND ADDRESS		12. REPORT DATE 1987, January
		13. NUMBER OF PAGES 271
14. MONITORING AGENCY NAME & ADDRESS (if different from Controlling Office) Office of Naval Research Arlington, Virginia 22217		15. SECURITY CLASS. (of this report)
		15a. DECLASSIFICATION/DOWNGRADING SCHEDULE
16. DISTRIBUTION STATEMENT (of this Report)		
17. DISTRIBUTION STATEMENT (of the abstract entered in Block 20, if different from Report)		
18. SUPPLEMENTARY NOTES		
19. KEY WORDS (Continue on reverse side if necessary and identify by block number) Wall shear stress, turbulence, pulsating flow, unsteady flow		
20. ABSTRACT (Continue on reverse side if necessary and identify by block number) See reverse side		

PRESSURE GRADIENT EFFECTS IN THE VISCOUS
WALL REGION OF A TURBULENT FLOW

The results of a study investigating the effects of an imposed pressure gradient on the viscous wall region of a turbulent flow are presented. Only imposed pressure gradients homogeneous in the streamwise direction are considered.

A computational model that neglects streamwise derivatives is used to study imposed pressure gradients that are constant in time. The shear stress at the edge of the viscous wall region, and not the wall shear stress, is shown to be the proper shear stress to use in scaling the coherent eddy structures responsible for the production of the turbulent kinetic in the viscous wall region. Arguments are presented that show the minimum P_e^+ value at the edge of the viscous wall region, where P_e^+ is defined by $\tau^+ = 1 + P_e^{++} y^+$, corresponds to the point of imminent relaminarization of a turbulent flow. It is suggested that the logarithmic region disappears at this minimum value.

Measurements using electrochemical probes are presented of the variation of the wall shear stress, the turbulent fluctuations of the wall shear stress, and the transverse correlation coefficients of the streamwise velocity gradient at the wall that are caused by the imposition of a sinusoidal pressure gradient on the flow of a turbulent fluid through a two inch pipe. The correlation coefficient measurements are used to provide information about the variation of the streak spacing, λ^+ . Results are presented for pulsations having a constant centerline variation of 10% and dimensionless frequencies, ω^+ , ranging from 0.0012 to 0.0915. At low ω^+ values, the variation of λ^+ is roughly 10%. The scaling relations developed for constant pressure gradients are found to be also applicable for pulsating turbulent flow at low ω^+ values. At higher ω^+ values, the turbulence is no longer able to follow the imposed pressure gradient and the amplitude of the variation of the turbulence is close to zero. However, at ω^+ values larger than the bursting frequency, a highly nonlinear large amplitude variation is observed in the λ^+ measurements. This variation cannot be explained by present theories of turbulence.

LIBRARY
RESEARCH REPORTS-DIVISION
NAVAL POSTGRADUATE SCHOOL
MONTEREY, CALIFORNIA 93940

PRESSURE GRADIENT EFFECTS IN THE VISCOSUS
WALL REGION OF A TURBULENT FLOW.

Prepared by
Douglas Scott Finnicum
Thomas J. Hanratty, Project Supervisor
for
The Office of Naval Research, Arlington, VA 22217
Contract N00014-82-K-0324
Project NR 657-728



Report 7

Department of Chemical Engineering
University of Illinois *University*
Urbana, Illinois
61801

January, 1987

Approved for public release, distribution unlimited

PRESSURE GRADIENT EFFECTS IN THE VISCOUS
WALL REGION OF A TURBULENT FLOW

Prepared by

Douglas Scott Finnicum
Thomas J. Hanratty, Project Supervisor

for

The Office of Naval Research, Arlington, VA 22217
Contract N00014-82-K-0324
Project NR 657-728

Report 7

Department of Chemical Engineering
University of Illinois
Urbana, Illinois
61801

January, 1987

Approved for public release, distribution unlimited

TABLE OF CONTENTS

Chapter		Page
1. INTRODUCTION		1
2. LITERATURE SURVEY		8
I. Zero Pressure Gradient Turbulent Flows		8
A. Description of the Viscous Wall Region		8
B. Coherent Structures in the Viscous Wall Region		9
C. Modelling of Turbulent Flows		12
1. Turbulence Closure Models		12
2. Large-Eddy Simulation		13
3. Simple Eddy Models		14
II. Constant Pressure Gradient Turbulent Flows		19
III. Pulsating Pressure Gradient Turbulent Flows		25
A. Pulsating Laminar Flow		26
B. Measurements of Pulsating Turbulent Flow		28
C. Models of Pulsating Turbulent Flow		30
3. THEORY		34
I. Eddy Model for the Viscous Wall Region		34
A. Model Equations		34
B. Effect of Acceleration on the Viscous Wall Region ..		37
C. Scaling of the Coherent Structures in the Viscous Wall Region		39
D. Boundary Conditions at the Upper Edge of the Viscous Wall Region		46
E. Numerical Scheme		51
1. Numerical Solution of the v,w Equations		51
2. Numerical Solution of the U Equation		54
3. Solution Scheme		55

II.	Eddy Viscosity Model of Turbulent Pulsating Pipe Flow	59
A.	Triple Decomposition and the Phase Average	59
B.	Governing Equations for Turbulent Pipe Flow	61
1.	Quasi-laminar Approximation (Model A)	64
2.	Quasi-steady Approximation (Model C)	67
3.	Relaxation Approximation (Model D)	68
C.	Numerical Scheme	70
4.	DESCRIPTION OF EXPERIMENTS	72
I.	Electrochemical Technique	72
A.	Electrochemical Cell	72
B.	Measuring S_x in Steady and Pulsating Flow	75
II.	Experimental Equipment and Conditions	81
A.	Experimental Flow Loop	81
B.	Test Section Fabrication	83
C.	Differential Pressure Measurement	84
D.	Data Acquisition and Processing	85
E.	Experimental Procedure and Range	91
5.	RESULTS.....	96
I.	Constant Pressure Gradient, Turbulent Flows.....	96
A.	Statistics.....	96
1.	Comparison with Nonaccelerated Experimental Data.....	97
2.	Nonzero Pressure Gradient Statistics.....	97
B.	Energy Balances.....	106
1.	Mean Kinetic Energy Balance.....	110
2.	Fluctuating Kinetic Energy Balance.....	114
II.	Pulsating Pressure Gradient Turbulent Flows.....	116
A.	Experimental Results.....	118

LIST OF FIGURES

Figure		Page
2.1	Idealized coherent eddy structure.....	16
2.2	Variation of the streak spacing and bursting period with pressure gradient. [Kline (1965)].....	22
3.1	Variation of the streak spacing, bursting period, and the edge of the viscous wall region with P_{eo}^+	47
3.2	The effect of acceleration on the Reynolds stress.....	49
3.3	The skin-friction coefficient data of several investigators.....	57
3.4	Eddy viscosity profiles for various models ($r_o = 2"$, $Re = 50,000$).....	63
3.5	Eddy viscosity profiles for the various shear stress formulations ($r_o = 2"$, $Re = 50,000$).....	65
3.6	Sample finite difference grid.....	71
4.1	The electrochemical cell.....	73
4.2	Amplitude correction factor for frequency response.....	78
4.3	Phase lag due to frequency response.....	79
4.4	Experimental apparatus.....	82
4.5	Correction factors for the Viatran transmitter.....	86
4.6	Correction factors for the C.J. Enterprises transmitter	87
4.7	Electrode circuit.....	88
4.8	Block diagram of data acquisition.....	88
4.9	Polarization curves.....	93
5.1	Streamwise mean velocity and intensity for $P_{eo}^+ = 0.0$	98
5.2	Intensities of the normal and spanwise velocity fluctuations for $P_{eo}^+ = 0.0$	99
5.3	Reynolds stress and Reynolds stress correlation for $P_{eo}^+ = 0.0$	100
5.4	Skewness and flatness of the streamwise velocity fluctuations for $P_{eo}^+ = 0.0$	101

1.	Time Averaged Results.....	118
2.	Phase Averaged Results.....	126
B.	Empirical Model Results.....	186
6.	DISCUSSION.....	195
I.	Constant Pressure Gradient Turbulent Flows.....	195
A.	Relaminarization.....	195
1.	Criterion for Relaminarization.....	195
2.	Calculation using $P_{eo}^+ = -0.00962$	200
3.	Scaling Arguments after the Logarithmic Region Disappears.....	203
B.	Uses for the Scaling Arguments.....	204
II.	Pulsating Pressure Gradient Turbulent Flows.....	206
7.	CONCLUSIONS AND RECOMMENDATIONS.....	212
NOMENCLATURE.....		214
REFERENCES.....		218
APPENDIX I. Amplitudes and Phases of the Phase Averaged Data...		224
APPENDIX II. Constant Pressure Gradient Program.....		227
APPENDIX III. Pulsating Pressure Gradient Program.....		260

5.5	Mean velocity profiles for several pressure gradients.....	103
5.6	Comparison of mean velocity profiles with experimental data [Loyd et. al. (1970)].....	104
5.7	Intensity of the streamwise velocity fluctuations for several pressure gradients.....	105
5.8	Intensities of the normal and spanwise velocity fluctuations for several pressure gradients.....	107
5.9	Reynolds stress and Reynolds stress correlation for several pressure gradients.....	108
5.10	Skewness and flatness of the streamwise velocity fluctuations for several pressure gradients.....	109
5.11	Energy supplied by the pressure gradient.....	112
5.12	Mean kinetic energy balance.....	113
5.13	Integrated mean kinetic energy balance.....	115
5.14	Fluctuating kinetic energy balance.....	117
5.15	Time averaged velocity gradient at the wall for pipe flow with and without pulsation.....	119
5.16	Time averaged intensities of turbulent fluctuations of the velocity gradient at the wall with and without pulsation.....	120
5.17	Time averaged transverse correlation coefficients of the streamwise velocity gradient at the wall with and without pulsations at $\omega^+ = 0.0012$	121
5.18	Time averaged transverse correlation coefficients of the streamwise velocity gradient at the wall with and without pulsations at $\omega^+ = 0.00375$	122
5.19	Time averaged transverse correlation coefficients of the streamwise velocity gradient at the wall with and without pulsations at $\omega^+ = 0.0093$	123
5.20	Time averaged transverse correlation coefficients of the streamwise velocity gradient at the wall with and without pulsations at $\omega^+ = 0.021$	124
5.21	Time averaged transverse correlation coefficients of the streamwise velocity gradient at the wall with and without pulsations at $\omega^+ = 0.036$	125
5.22	Phase averaged values at $Re = 44,900$, $f = 0.35$ Hz, $\omega^+ = 0.0012$ and $a = 0.1$	127

5.23	Phase averaged values at $Re = 42,000$, $f = 0.35$ Hz, $\omega^+ = 0.00135$ and $a = 0.101$	128
5.24	Phase averaged values at $Re = 29,400$, $f = 0.25$ Hz, $\omega^+ = 0.00180$ and $a = 0.099$	129
5.25	Phase averaged values at $Re = 23,700$, $f = 0.20$ Hz, $\omega^+ = 0.0021$ and $a = 0.1$	130
5.26	Phase averaged values at $Re = 31,800$, $f = 0.60$ Hz, $\omega^+ = 0.00375$ and $a = 0.098$	131
5.27	Phase averaged values at $Re = 25,200$, $f = 0.40$ Hz, $\omega^+ = 0.00375$ and $a = 0.1$	132
5.28	Phase averaged values at $Re = 20,100$, $f = 0.30$ Hz, $\omega^+ = 0.0042$ and $a = 0.101$	133
5.29	Phase averaged values at $Re = 23,000$, $f = 0.45$ Hz, $\omega^+ = 0.00495$ and $a = 0.098$	134
5.30	Phase averaged values at $Re = 21,400$, $f = 0.60$ Hz, $\omega^+ = 0.0075$ and $a = 0.099$	135
5.31	Phase averaged values at $Re = 17,100$, $f = 0.50$ Hz, $\omega^+ = 0.0093$ and $a = 0.102$	136
5.32	Phase averaged values at $Re = 14,500$, $f = 0.50$ Hz, $\omega^+ = 0.0123$ and $a = 0.1$	137
5.33	Phase averaged values at $Re = 17,900$, $f = 1.00$ Hz, $\omega^+ = 0.0172$ and $a = 0.098$	138
5.34	Phase averaged values at $Re = 10,600$, $f = 0.45$ Hz, $\omega^+ = 0.0195$ and $a = 0.101$	139
5.35	Phase averaged values at $Re = 10,700$, $f = 0.50$ Hz, $\omega^+ = 0.021$ and $a = 0.102$	140
5.36	Phase averaged values at $Re = 15,300$, $f = 1.00$ Hz, $\omega^+ = 0.0225$ and $a = 0.099$	141
5.37	Phase averaged values at $Re = 14,600$, $f = 1.00$ Hz, $\omega^+ = 0.0244$ and $a = 0.098$	142
5.38	Phase averaged values at $Re = 14,200$, $f = 1.00$ Hz, $\omega^+ = 0.0258$ and $a = 0.101$	143
5.39	Phase averaged values at $Re = 10,300$, $f = 0.60$ Hz, $\omega^+ = 0.0270$ and $a = 0.101$	144
5.40	Phase averaged values at $Re = 8,750$, $f = 0.60$ Hz, $\omega^+ = 0.036$ and $a = 0.099$	145

5.41	Phase averaged values at $Re = 11,400$, $f = 1.00$ Hz, $\omega^+ = 0.0375$ and $a = 0.098$	146
5.42	Phase averaged values at $Re = 9,200$, $f = 1.00$ Hz, $\omega^+ = 0.0550$ and $a = 0.100$	147
5.43	Phase averaged values at $Re = 10,300$, $f = 1.50$ Hz, $\omega^+ = 0.0675$ and $a = 0.101$	148
5.44	Phase averaged values at $Re = 8,650$, $f = 1.50$ Hz, $\omega^+ = 0.0915$ and $a = 0.100$	149
5.45	Amplitude of the wall shear stress.....	153
5.46	Phase lag (relative to the pressure gradient) of the wall shear stress.....	155
5.47	Amplitude of the wall shear stress intensity.....	156
5.48	Phase lag (relative to the pressure gradient) of the wall shear stress intensity.....	158
5.49	Determination of the time averaged Taylor microscale.....	162
5.50	Determination of the variation of the streak spacing.....	164
5.51	Phase averaged streak spacing at $Re = 44,900$, $f = 0.35$ Hz, $\omega^+ = 0.0012$ and $a = 0.1$	165
5.52	Phase averaged streak spacing at $Re = 23,700$, $f = 0.20$ Hz, $\omega^+ = 0.0021$ and $a = 0.1$	166
5.53	Phase averaged streak spacing at $Re = 25,200$, $f = 0.40$ Hz, $\omega^+ = 0.00375$ and $a = 0.1$	167
5.54	Phase averaged streak spacing at $Re = 20,100$, $f = 0.30$ Hz, $\omega^+ = 0.0042$ and $a = 0.101$	168
5.55	Phase averaged streak spacing at $Re = 21,400$, $f = 0.60$ Hz, $\omega^+ = 0.0075$ and $a = 0.099$	169
5.56	Phase averaged streak spacing at $Re = 17,100$, $f = 0.50$ Hz, $\omega^+ = 0.0093$ and $a = 0.102$	170
5.57	Phase averaged streak spacing at $Re = 17,900$, $f = 1.00$ Hz, $\omega^+ = 0.0172$ and $a = 0.098$	171
5.58	Phase averaged streak spacing at $Re = 10,700$, $f = 0.50$ Hz, $\omega^+ = 0.021$ and $a = 0.102$	172
5.59	Phase averaged streak spacing at $Re = 15,300$, $f = 1.00$ Hz, $\omega^+ = 0.0225$ and $a = 0.099$	173

5.60	Phase averaged streak spacing at $Re = 14,600$, $f = 1.00 \text{ Hz}$, $\omega^+ = 0.0244$ and $a = 0.098$	174
5.61	Phase averaged streak spacing at $Re = 14,200$, $f = 1.00 \text{ Hz}$, $\omega^+ = 0.0258$ and $a = 0.101$	175
5.62	Phase averaged streak spacing at $Re = 10,300$, $f = 0.60 \text{ Hz}$, $\omega^+ = 0.0270$ and $a = 0.101$	176
5.63	Phase averaged streak spacing at $Re = 8,750$, $f = 0.60 \text{ Hz}$, $\omega^+ = 0.0360$ and $a = 0.099$	177
5.64	Phase averaged streak spacing at $Re = 11,400$, $f = 1.00 \text{ Hz}$, $\omega^+ = 0.0375$ and $a = 0.098$	178
5.65	Phase averaged streak spacing at $Re = 9,200$, $f = 1.00 \text{ Hz}$, $\omega^+ = 0.0550$ and $a = 0.100$	179
5.66	Phase averaged streak spacing at $Re = 10,300$, $f = 1.50 \text{ Hz}$, $\omega^+ = 0.0675$ and $a = 0.101$	180
5.67	Phase averaged streak spacing at $Re = 8,650$, $f = 1.50 \text{ Hz}$, $\omega^+ = 0.0915$ and $a = 0.100$	181
5.68	Estimation of the phase averaged streak spacing using the constant pressure gradient scaling arguments.....	183
5.69	Amplitude of the variation of the streak spacing.....	184
5.70	Phase (relative to the pressure gradient) of the streak spacing.....	185
5.71	Comparison of the phase averaged wall shear stress data with Model C and Model D (amplitude results).....	187
5.72	Comparison of the phase averaged wall shear stress data with Model C and Model D (phase results).....	188
5.73	Normalized amplitude and phase lag (relative to the imposed pressure gradient) of the effective pressure gradient.....	190
5.74	Comparison of the streak spacing experimental data with the results of Model C and Model D.....	191
5.75	Breakdown of the assumption of plug flow in the center of the pipe.....	193
6.1	Variation of P_{eo}^+ and $(d\tau^+/dy^+)_o$ with the edge of the viscous wall region.....	199
6.2	Effect of pressure gradient on the dissipation and production of turbulent kinetic energy.....	202

6.3	Locating the edge of the viscous wall region.....	205
6.4	Streak spacing obtained using the scaling arguments and the mean profiles of several investigators.....	207
6.5	Bursting period obtained using the scaling arguments and the mean profiles of several investigators.....	208

LIST OF TABLES

Table		Page
3.1	Constant Parameter Values.....	51
4.1	Experimental Range.....	80
4.2	Experimental Conditions.....	95
5.1	Summary of Parameter Values.....	96
6.1	Some Proposed Criteria for Relaminarization.....	196

CHAPTER 1. INTRODUCTION

Considerable attention has been focused on the viscous wall region of a bounded turbulent shear flow since the discovery in the late 1950's that this region contains a significant amount of coherent structure. The dye experiments of Beatty, Ferrell, and Richardson (Corrsin 1956) and by Hama (Corrsin 1956) revealed the formation of a streaky structure in the viscous sublayer which repeated in the spanwise direction. These structures are greatly elongated in the streamwise direction. Further experiments using hydrogen bubble techniques as well as dye techniques [Kline et al. (1967), Kim et al. (1971)] showed that the wall dye streaks are regions of low streamwise momentum fluid, and the regions between streaks contain high streamwise momentum. As the streaks move downstream they lift away from the wall and violently interact with the turbulent fluid outside the wall region. This ejection of low momentum fluid has been called "bursting". The two structural parameters, λ , the spanwise spacing of dye streaks, and T_B , the bursting period, are independent of Reynolds number when made dimensionless with wall parameters, kinematic viscosity ν and friction velocity u^* [Kim et al. (1971), Blackwelder and Haritonidis (1983)]. Because these coherent eddy structures are believed to control the generation of turbulence in wall bounded shear flows, it is of considerable importance to understand why these structures form and the interaction between them and the rest of the flow.

This work is part of a research program that has as its main goals the understanding of the processes by which wall turbulence is produced and sustained and an understanding of how these processes can be altered by structural changes in the flow. The practical aspect of this research is that it provides a theoretical basis for determining how wall turbulence

can be controlled and how turbulent drag can be decreased.

Specifically, this thesis presents the results of a study investigating the effects of an imposed pressure gradient on the viscous wall region. Only imposed pressure gradients homogeneous in the streamwise direction are considered. The computational model of the viscous wall region proposed by Nikolaides (1984) was used to investigate imposed pressure gradients that are steady in time. An experimental program was also carried out investigating the changes in the turbulent structure in the viscous wall region due to imposed pressure gradients that are varying sinusoidally in time.

Kline et al.(1967) experimentally observed that the size and period of the coherent eddies could be changed by imposing a pressure gradient on the turbulent flow. Favorable pressure gradients ($dP/dx < 0$) were created by constricting the walls of the flow, while adverse pressure gradients ($dP/dx > 0$) were formed by enlarging the walls. By adjusting the walls correctly constant imposed pressure gradients in the streamwise direction could be created. They found that favorable pressure gradients increased λ^+ and T_B^+ , and that relaminarization of the flow could occur if the imposed pressure gradient was large enough. Adverse pressure gradients were found to decrease λ^+ and T_B^+ . They also found that there was an inverse relationship between these scales and the level of turbulent kinetic energy in the flow. Their results clearly showed that the imposition of a pressure gradient on a turbulent flow can cause dramatic changes in the turbulent structure in the viscous wall region.

Nikolaides (1984) investigated zero pressure gradient flows with a model that solves the unaveraged Navier-Stokes equations in the viscous wall region. The representation of the flow is greatly simplified by neglecting terms representing the variation of hydrodynamic quantities in the flow direction and by representing the turbulent fluctuations at the

edge of the viscous wall region, y_0^+ , by periodic functions having two length scales and two time scales. These calculations gave a fluctuating flow field in excellent agreement with presently available measurements.

The success of the work of Nikolaides in describing nonaccelerated flows suggested using the model to investigate the influence of large favorable pressure gradients on wall turbulence. In nonaccelerated flows there exists enough experimental information on the turbulent quantities in the viscous wall region to be able to specify the boundary conditions at the edge of the viscous wall region. Unfortunately in accelerated flows the experimental information necessary to determine the boundary conditions at y_0^+ are not available; therefore, it became necessary to develop relations that describe the scaling of the coherent structures in the viscous wall region as a function of acceleration.

Imposing a favorable pressure gradient has several effects on the turbulence in the viscous wall region. The fluctuations become less vigorous, the thickness of the viscous wall region, y_0^+ , increases and the shear stress at y_0^+ , normalized with the wall shear stress, decreases below the nonaccelerated value of 1. By using the local shear stress at y_0^+ , τ_0 , instead of the wall shear stress, the mixing length scaling arguments at y_0^+ proposed by Nikolaides were modified to take into account these differences. A relation developed by Julien et al. (1969) using similarity arguments for the prediction of the shear stress profile is used to obtain τ_0^+ . This relationship is different from the frequently used Couette relation in that it is recognized that only a fraction of the imposed pressure gradient contributes to changing the shear stress distribution; the remainder of the imposed pressure gradient is used to change the inertia of the flow.

The imposition of a sinusoidal pulsation of the mean flow through a

circular pipe causes a periodically varying pressure and velocity field.

If the amplitude is small enough, the variation can be described by a single harmonic,

$$\frac{d\tilde{p}}{dx} = - \left| \frac{dp}{dx} \right| \cos(\omega t) \quad (1.1)$$

$$\tilde{u} = |\hat{u}| \cos(\omega t + \theta_u(y)) \quad (1.2)$$

with x being the distance in the streamwise direction and t the time. The angular frequency and the amplitudes of the pulsations are represented by ω , $|\hat{p}/dx|$ and $|\hat{u}|$, respectively. The pulsations in the velocity field give rise to pulsations in the shear stress at the wall,

$$\tilde{\tau}_w = |\hat{\tau}_w| \cos(\omega t + \theta_{\tau_w}) \quad (1.3)$$

where

$$\tau_w = \mu \left. \frac{du}{dy} \right|_{y \rightarrow 0} \quad (1.4)$$

and

$$\theta_{\tau_w} = \lim_{y \rightarrow 0} \theta_u(y). \quad (1.5)$$

Experiments were carried out in a two inch pipe flow loop that was built to measure the wall shear stress variation in turbulent pulsating pipe flow using a technique that does not interfere with the flow. This technique involves carrying out an electrochemical reaction on the surface of a platinum electrode mounted flush with the wall. The current flow in the electrochemical cell is controlled by the rate of mass transfer to the surface. Because the cell is operated at a high Schmidt number, the velocity fluctuations near the wall determine the rate of mass transfer. By measuring the current fluctuations in the electrochemical cell, the velocity fluctuations close to the surface were determined.

A number of previous investigators have studied the influence of controlled flow pulsations on turbulent flows. Previous results have indicated that the influence of the pulsations on the mean properties of the flow is very small and that their effect on the turbulence is felt primarily in the region close to the wall. Unfortunately, in most previous studies accurate velocity measurements could not be made close enough to the wall to determine the time varying velocity gradient at the wall. Thus, there exists a need for accurate measurements of the time varying wall shear stress. Measurements of the wall shear stress at low frequencies of pulsation were reported by Tu and Ramaprian (1983) using flush mounted wall heat transfer probes. They found that the time average wall shear stress was the same for pulsating and steady flow i.e. no change in drag was observed. Binder et al. (1985) also found no change at higher frequencies. They systematically varied the frequency by a factor of 15 and the amplitude from 5 to 70% of the centerline velocity. Neither the mean velocity profile nor the mean turbulent energy distribution was altered despite the large forcing amplitudes which contained an order of magnitude more energy than the random fluctuations. They concluded that in the wall region the appropriate scaling parameter is the dimensionless Stokes length $\delta_s^+ = (2/\omega^+)^{1/2}$. The variation of the turbulent wall shear stress fluctuations was found to depend on both the amplitude and frequency of pulsation.

The study of Mao and Hanratty (1986) in an eight inch pipe focused on measurements of the wall shear stress at high ω^+ . They found that the phase and amplitude of the wall shear stress variation could be correlated by the single parameter ω^+ and that the mean velocity field was unaffected by the imposed flow pulsation. The most striking feature of their results was a relaxation effect, whereby the phase angle characterizing the

temporal variation of the wall shear stress underwent a sharp change over a very narrow range of ω^+ . They suggested that at low frequencies an equilibrium situation exists whereby the flow behaves similarly to that observed in constant pressure gradient flows. Phases of the pulsation with a favorable pressure gradient experience a damping of the turbulence in the viscous wall region; phases with an adverse pressure gradient experience an enhancement of the turbulence. As ω^+ increases the pressure gradient varies so rapidly that the turbulence in the viscous wall region does not respond immediately. This relaxation phenomena has also been observed in flow over wavy surfaces [Abrams and Hanratty (1985)]. Many of the conclusions made by Mao and Hanratty (1986) relied upon the analogy between the two flows because their data did not extend into the equilibrium range. At higher ω^+ than the bursting frequency they observed a highly nonlinear interaction between the imposed pulsation and the turbulent fluctuations. Their data for the variation of the wall shear stress at high ω^+ , which was still linear, was found not to agree with the limiting Stokes solution.

The principal goal of the present experiments was to measure the wall shear stress variation over a wider range of ω^+ than measured by Mao and Hanratty. The use of a two inch pipe provides higher turbulent wall shear stresses, and therefore lower ω^+ , than the eight inch pipe used by Mao. Sinusoidal pulsations with frequencies ranging from 0.2 Hz to 1.5 Hz were introduced into the system with a reciprocating piston pump. The variation of the centerline velocity was held constant at 10% for all the runs.

A test section was fabricated with multiple probes in order to measure transverse spatial correlation coefficients of the streamwise velocity fluctuations near the pipe wall. These measurements were used to estimate the variation of the eddy length scale λ^+ through a period of pulsation. These measurements, believed to be the first of their kind for a pulsating

pipe flow, indicate that a substantial variation of λ^+ occurs in the equilibrium region of the flow. The relaxation phenomena observed by Mao was confirmed by the measurements of λ^+ . However, an unexpected highly nonlinear large variation of λ^+ was observed at ω^+ values higher than the bursting frequency. At present, this behavior at high ω^+ cannot be explained.

CHAPTER 2. LITERATURE SURVEY

Considerable experimental and theoretical work has been done in the past to elucidate why coherent structures form in wall bounded turbulent shear flows. Flow-visualization, multiple probe measurements and direct numerical simulation have provided key information about the structures and their interactions with the rest of the flow. Recently, these tools have been used to look at turbulent shear flows under the influence of an imposed pressure gradient. Important knowledge about the properties of the structures in the viscous wall region has been gained by observing the response of these structures to the imposed pressure gradient. This chapter surveys the work that has been done in the past in this area and is divided into three sections: 1) zero pressure gradient flows, 2) constant pressure gradient flows, and 3) pulsating pressure gradient flows.

I. Zero Pressure Gradient Turbulent Flows

Most of the experimental and theoretical studies in the past have focused on wall bounded shear flows without imposed pressure gradients. Thus, a significant amount of information is known about these flows. Since this study is concerned with changes in a normal flow associated with the imposition of a pressure gradient, a review of the nonaccelerated literature is pertinent.

A. Description of the Viscous Wall Region

Turbulent flow in a pipe or channel is conventionally separated into four regions: the viscous sublayer, the buffer region, the logarithmic region, and the wake or core region. The first two make up the viscous wall region. Wall turbulence is scaled by nondimensionalizing all quantities with wall parameters, the kinematic viscosity ν and the friction

velocity u^* . In terms of these dimensionless quantities, the viscous sublayer extends from $y^+ = 0$ to $y^+ = 6$. In this region the mean velocity profile is linear $\bar{U}^+ = y^+$ and viscous effects dominate. In the buffer region ($6 < y^+ < 40$), both viscous and inertial effects are important. Outside the viscous wall region viscous effects are negligible and the mean velocity profile is logarithmic, $\bar{U}^+ = 1/\kappa \ln(y^+) + A$, hence the name logarithmic region.

Turbulent flows require a statistical description because the velocity and pressure fields vary randomly in space and time. This statistical description begins by assuming a Reynolds decomposition of the velocity and pressure fields, $U_i = \bar{U}_i + u_i$ and $P = \bar{P} + p$. Then various combinations of these quantities and their derivatives are measured and averaged in space and time to give a description of the turbulent flow. These measurements are in the form of mean velocities, intensities, Reynolds stresses, other higher-order moments of the velocity fluctuations, probability distributions, correlations and various spectra. A survey of turbulence measurements in nonaccelerated flows is given in Nikolaides (1984) and will not be reproduced here.

B. Coherent Structures in the Viscous Wall Region

In a bounded shear flow, there exist coherent structures that have characteristic length scales and lifetimes. Spectral and correlation measurements indicate the existence of large-scale structures [Townsend (1976), Grant (1958), Bakewell and Lumley (1967)], but clear evidence wasn't obtained until visual techniques were used [Corrsin (1956), Kline et. al. (1967), Corino and Brodkey (1969), Kim et. al. (1971)].

The dye experiments of Beatty, Ferrell, and Richardson [Corrsin (1956)] and by Hama [Corrsin (1956)] revealed a streaky structure in the viscous

wall region that repeats in the spanwise direction and is greatly elongated in the streamwise direction. Other experimenters also used dye to visualize these wall streaks [Kline and Runstadler (1959), Runstadler et. al. (1963), Offen and Kline (1974)].

Subsequent studies used hydrogen bubble techniques [Kline et. al. (1967), Kim et. al. (1971)] because this method can give quantitative information about the flow field. The Stanford group confirmed the existence of the streaky structure in the viscous wall region and correctly interpreted that the wall dye streaks are regions of low streamwise momentum fluid, and the regions between streaks contain fluid high in streamwise momentum. Kim et. al. (1971) found the dimensionless spanwise spacing of the wall streaks to be 100 ± 20 . The Stanford group also observed the wall streaks undergoing a deterministic sequence of recurring events: the formation of a low-speed streak and the beginning of a vertical oscillation ($8 < y^+ < 12$), the amplification of this oscillation followed by an abrupt breakup ($10 < y^+ < 40$). The entire process was termed a "burst" by Kline and his coworkers. The ejection of low streamwise velocity fluid from the wall into the outer flow is the essential feature of this structure. A return flow is required by continuity and this return flow to the wall, called a sweep or inrush, was observed in almost every case just before the onset of the oscillations of the lifting wall streak. The sweeps were observed to be associated with transverse and streamwise vortical motions [Offen and Kline (1974)].

The Ohio State group [Corino and Brodkey (1969), Nychas et. al. (1973), Praturi and Brodkey (1978)] has also made an extensive study of the wall region using other visualization techniques. Their findings confirmed the bursting process as well as the sweep event described by the Stanford group.

Bakewell and Lumley (1967) suggested that the wall streaks result from counterrotating pairs of eddies homogeneous in the flow direction. Sirkar and Hanratty (1970) also suggested that the flow in the wall region is dominated by a secondary pattern homogeneous in the flow direction that is of the type shown in Figure 2.1a. Their results suggest that the streaks observed when dye is injected from a wall slot result from the sweeping action of the secondary flow in the spanwise direction close to the wall.

Several investigators carried out measurements to determine the spanwise spacing of the wall streaks. The streak spacing can be determined by visual observation, by determining the value that maximizes the Fourier transform of the spanwise correlation of the streamwise velocity close to the wall, or by inference from correlation measurements. Coantic (1967) and Bakewell and Lumley (1967) calculated λ^+ from correlation measurements taken with hot wire probes. Coantic obtained $\lambda^+ \approx 110 - 130$ and Bakewell and Lumley calculated $\lambda^+ \approx 100$. Lee et. al. (1974) measured $\lambda^+ \approx 105$ from correlation measurements obtained using electrochemical wall probes. Gupta et. al. (1971) obtained spanwise correlations of the streamwise velocity below $y^+ = 12$ and found $\lambda^+ \approx 95$. Clark (1968) measured $\lambda^+ \approx 100$ from hydrogen bubble experiments.

The mean bursting period, T_B , has also been measured experimentally. There has been disagreement about the universal scaling of T_B . Originally, it was concluded that T_B scaled with outer flow variables, U_∞ , the free stream velocity, and δ^* , the displacement thickness [Rao et. al. (1971), Kim et. al. (1971)]. Other investigators have found T_B to scale with wall parameters [Meek (1972), Blackwelder and Kaplan (1976), Blackwelder and Eckelmann (1978)]. Recent evidence presented by Blackwelder and Haritonidis (1983) shows the outer scaling observed by Rao et. al. (1971) may be in error due to the large size of the probes used in their measurements.

Blackwelder and Haritonidis report $T_B^+ \approx 250$. The data of Donohue et. al. (1972) give $T_B^+ \approx 99 - 172$. Schraub and Kline (1965) and Runstadler et. al. (1963) report $T_B^+ \approx 110$ and 142 respectively. The data of Kim et. al. (1971) show $T_B^+ \approx 80 - 109$.

The scatter in the results from the different methods and investigators illustrates the level of intricacy involved in making these types of measurements. However, it appears that both the spanwise spacing of the wall streaks and the mean bursting period scale with wall parameters and that they have values of the order of 100 in dimensionless units.

C. Modelling of Turbulent Flows

Numerical simulation of a turbulent flow can provide the turbulent velocity and pressure fields as a function of space and time, which can then be used to compute quantities that are very difficult, if not impossible, to measure. The Navier-Stokes equations apply to turbulent flows as well as laminar flows, but the computation of a turbulent flow field using these equations is extremely difficult due to the wide range of scales that have to be captured. With the advent of supercomputers, direct simulations using the full equations have only recently been performed [Moser and Moin (1984)] and remain limited in application due to the cost involved. In place of the full unsteady solutions, various approaches have been taken to model turbulent flows.

1. Turbulence Closure Models

In this approach a Reynolds decomposition is assumed for all the flow variables in the Navier-Stokes equations. These equations are then time averaged. The resulting Reynolds stresses are modelled [Rodi (1980)]. These models are commonly based on eddy-viscosity and mixing length arguments. The resulting set of equations is termed a zero-equation model.

One-equation models involve an additional partial differential equation, usually the turbulent kinetic energy equation. The eddy viscosity is then related to the turbulent kinetic energy. At this time, the models which appear to have the most promise for engineering calculations are the two-equation models. These models use one more partial differential equation to describe the transport of isotropic dissipation. The Reynolds stresses are modelled as functions of the turbulent kinetic energy, k , and the dissipation of energy, ϵ . This nomenclature has given rise to the name "k- ϵ model". Other models are more complex and some involve solving the complete Reynolds stress tensor. It is not clear that the most complex models are of more value than the k- ϵ models, since all the models are based on empirical constants and assumptions.

The basic problem with the full closure method is that the higher order statistical quantities being modelled respond on time scales that are longer than the time scales of the computed quantities. Any model obtained by truncating at some statistical order has this problem. The next level of complexity in turbulence modelling avoids this difficulty by utilizing the full set of flow equations along with a closure assumption for only the small scale motion. The advantage of this method is that the smaller scales adjust quickly to local flow conditions. Such models are termed subgrid scale approximations in a large-eddy simulation, LES.

2. Large-Eddy Simulation

This approach uses the full three-dimensional time-dependent Navier-Stokes equations to compute the turbulence, but recognizes that it is very costly to compute the details of the smallest scales. Therefore, the method employs a closure model only for the scales smaller than a selected cutoff length ℓ . To do this, a filter is applied to the flow equations which

introduces a Reynolds stress for the flow with length scales less than λ . A variety of filters and subgrid scale approximations have been developed in the past 20 years [Smagorinsky et. al. (1965), Lilly (1967), Schumann (1975), Ferziger (1977), Clark et. al. (1979)].

Deardorff (1970) was the first to demonstrate the feasibility of using LES to do a three-dimensional calculation. Deardorff simulated plane channel flow using 6,720 mesh points. Artificial boundary conditions away from the wall were introduced in order to avoid calculating the flow in the viscous wall region. The wall region was not treated until Moin et. al. (1978) calculated the three-dimensional time-dependent turbulence in a channel using 16,640 grid points. Their numerical results showed reasonable agreement with experimental measurements but their mesh sizes were too large to resolve the scales close to the wall. Since then, Moin and Kim (1982) simulated fully developed turbulent flow in a channel using 516,096 grid points and were able to capture the scales close to the wall. Their turbulent statistics agreed well with experimental data, and in addition, they found turbulence structures in the vicinity of the channel wall similar to those observed experimentally, such as wall streaks, streamwise vortical motions, and horseshoe vortices [Kim and Moin (1984)].

3. Simple Eddy Models

This method has also been termed "coherent-structure" modelling in that an attempt is made to model the organized quasi-periodic eddy structures in the wall layer. In order to do this, the turbulent velocities are modelled at the outer edge of the viscous wall region. The flow field is assumed to be homogeneous in the streamwise direction and the resulting form of the time-dependent Navier-Stokes equations is solved on a plane perpendicular to the flow.

Fortuna and Hanratty [Fortuna (1971), Hanratty et. al. (1977)] assumed that, on average, the streamlines in the secondary flow have the shape shown in Figure 2.1a, and used a pseudosteady state assumption to calculate the streamwise velocity component. They pictured the secondary flow to bring high momentum fluid to the wall at A, to exchange momentum with the wall as it moved fluid in the spanwise direction from A to B and to remove low momentum fluid from the wall at B. According to this picture, the streamwise, s_x , and the spanwise, s_z , components of the velocity gradient at the wall should have the phase relation shown in Figures 2.1b and 2.1c. This has been confirmed in experiments by Lee, Eckelman and Hanratty (1974) and by Hogenes and Hanratty (1982).

Hatzivramidis and Hanratty (1979) undertook a computational study to explore how the viscous wall region would respond to spanwise velocity fluctuations at its outer boundary, $y_0^+ \approx 40$. The basic model is similar to the one used by Fortuna (1971) but it was recognized that his pseudosteady state assumption overlooks important aspects of the flow. The flow field in the viscous wall region was pictured to be coherent and to be associated with flow deviations in a well mixed outer region. The spanwise flow at $y_0^+ \approx 40$ was taken as $w = |\hat{w}| \sin(2\pi z/\lambda) \cos(2\pi t/T_B)$, where λ is the spacing of the dye streaks, T_B , the period between bursts and $|\hat{w}|$, a constant, whose value is consistent with turbulence measurements. Good agreement was obtained between the calculated flow field and experimental results, especially for $y^+ < 15$. The most important results coming from the calculations of Fortuna and of Hatzivramidis are the suggestion of a mechanism by which streamwise velocity fluctuations are created and the good representation of the average velocity profile. These calculations supported the notion that the coherent elongated, $\lambda^+ \approx 100$, structures are the key to understanding how wall turbulence is sustained.

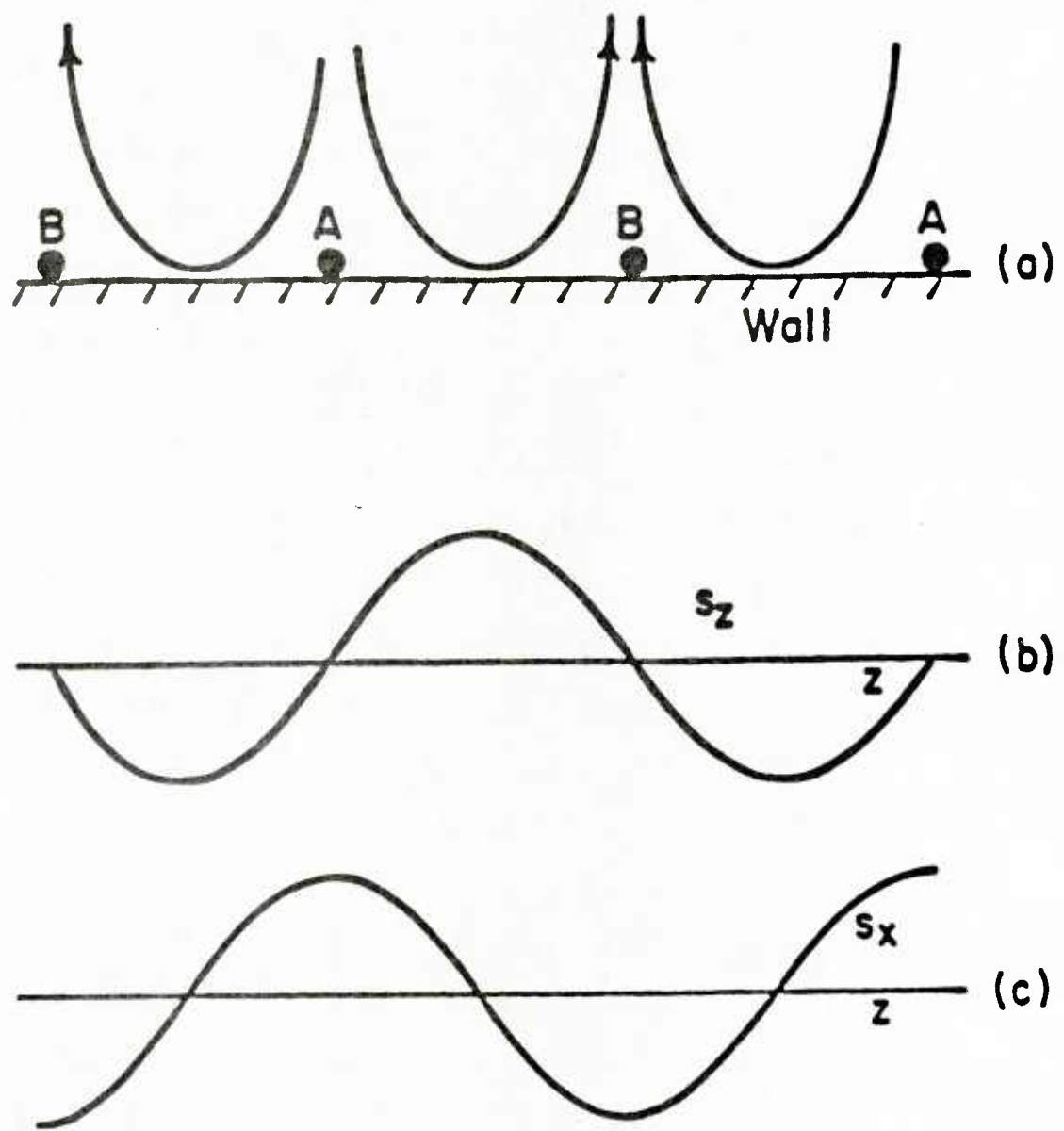


Figure 2.1 Idealized coherent eddy structure.

Chapman and Kuhn (1981) followed up the work of Hatzivramidis by improving the boundary conditions at the edge of the viscous wall region. They visualized the flow in the viscous wall region to result from the interaction of the $\lambda^+ \approx 100$ eddies with eddies that are associated with a "pulsating" type of flow that are on a plane parallel to the wall. Their calculated Reynolds stress and intensity profiles showed better agreement with experiments than the computations of Hatzivramidis, especially in the region $20 \leq y^+ \leq 40$. However, the inclusion of a second wavelength of infinite size produced spanwise wall fluctuations dramatically different from measurements.

Nikolaides and Hanratty [Nikolaides (1984)] developed another computer model similar to Chapman's except that more realistic boundary conditions were used. From examination of the correlation measurements of Grant (1958) and Tritton (1967) and the frequency-wavenumber spectra of Morrison and Kronaur (1969), they realized that the wavelength of the outer flow eddies should be about 400 and not of infinite size. Nikolaides found that the simplest model which gave results conforming to experiments is one where the secondary flow at the outer edge of the viscous wall layer, $y^+ = y_0^+$, is characterized by two harmonics. The use of one harmonic (λ_1^+) gave an adequate description for the region $y^+ < 20$, but a second harmonic (λ_2^+) representing the outer flow eddy interaction is required to obtain good results throughout the viscous wall region.

One of the interesting results of the calculations was the identification of a selection process whereby the flow at $y^+ < 20$ is dominated by the smaller scale, $\lambda_1^+ \approx 100$, eddies. It was found that the same level of Reynolds stress is obtained regardless of whether one or two wavelengths were used. This result indicates that the $\lambda_1^+ \approx 100$ eddies control the transfer of momentum and the production of turbulence in the viscous wall

region. The principal advantages of including the large scale, $\lambda_2^+ \approx 400$, eddies is that the calculations of the spanwise velocity fluctuations and the energy dissipation at $y^+ > 20$ are much improved.

Through various arguments, Nikolaides developed the following conceptual model describing the interaction between the viscous wall region and the outer flow. Streamwise velocity fluctuations are created in the viscous wall region and convected into the outer flow. These streamwise velocity fluctuations are converted to normal and spanwise velocity fluctuations in the outer flow through pressure-velocity correlations. The spanwise and normal velocity fluctuations in the bulk flow in turn "tickle" the wall region to create the flow oriented wall eddies that generate turbulence. Drag is determined by the small eddies at the edge of the viscous wall region whose scale (the microscale of turbulence) is governed by dissipation processes in the outer flow.

Lyons (1985) used the Nikolaides model to develop an understanding of how a particular value of λ_1^+ is established in a turbulent flow. By varying λ_1^+ in the model it was shown that the dominant wall eddy size is the one for which the net production of turbulence in the viscous wall region is just enough to supply the energy dissipated in the core region of a pipe or channel. Using this criteria, the model predicted the dominant wavelength should be about 93. This result is very close to the experimentally observed value of 100.

Recently, Ota and Chapman (1985) used a two-harmonic model to determine the variation of the turbulent Prandtl number across the viscous wall region. It was determined that the dependence of the turbulent Prandtl number on pressure gradient is negligible; but that the dependence on molecular Prandtl number is sizable near the wall ($y^+ < 3$). The turbulent Prandtl number was found to be essentially constant throughout most of the

viscous wall region.

The last two studies illustrate the usefulness of "coherent-structure" modelling. Because of the assumption of homogeneity in the streamwise direction, the streamwise momentum equation is decoupled from the two momentum equations normal to the flow. Associated with this decoupling is a tremendous savings in computer time; therefore, practical engineering calculations can be made. The key to the success of these models is that they describe the structures that are responsible for the transfer of energy from the mean flow to the turbulence and the level of the Reynolds stresses in the flow.

II. Constant Pressure Gradient Turbulent Flows

An equilibrium boundary layer is one that has developed in an imposed pressure gradient so that the parameter

$$\beta = 2KR_2H/C_f \quad (2.1)$$

is a constant, where R_2 , H , and C_f are the conventionally defined momentum-thickness Reynolds number, shape factor and skin-friction coefficient respectively. Term K is the acceleration parameter defined as

$$K = \frac{\nu}{U_{\infty}^2} \frac{dU_{\infty}}{dx}, \quad (2.2)$$

where U_{∞} is the free-stream velocity. A constant β implies that the characteristic viscous and turbulence scales develop at the same rate even though the free-stream velocity is varying. When equilibrium is reached, all of the velocity profile outside the viscous wall region is self-preserving if plotted in velocity-defect coordinates.

A subset of equilibrium flows is the similar sink flow. In this type

of flow, each of the quantities on the right-hand side of (2.1) are constant. Since the skin-friction coefficient is constant, similar sink flows can also be described by P^+ , the imposed pressure gradient made dimensionless with wall parameters,

$$P^+ = \frac{\nu}{\rho u_*^3} \frac{dP}{dx}, \quad (2.3)$$

since

$$P^+ = \frac{-K}{\left(\frac{C_f}{2}\right)^{3/2}}. \quad (2.4)$$

Launder and Stinchcombe (1967) have shown that for $\beta < 0.5$, the Reynolds number will increase indefinitely with x . For $\beta > 0.5$, the boundary layer would approach asymptotically the similar sink flow condition.

Favorable imposed pressure gradients ($dP/dx < 0$) can be created by constricting the walls of a turbulent flow. By conservation of mass, this constriction accelerates the fluid. Thus, flows with favorable imposed pressure gradients are very often called accelerated flows in the literature. Both descriptions are used in this thesis.

The relevant experimental investigations surveyed can be categorized as 1) mild pressure gradients of the asymptotic similar sink flow type, or 2) strong pressure gradient flows where the onset of relaminarization is of major concern. Relaminarization is defined here as the point at which a turbulent flow cannot be sustained and reversion to laminar flow will occur given sufficient distance. The experimental data in both cases are very difficult to obtain because the acceleration of the flow makes the viscous wall region much thinner than in a normal flow. However, the experimental

studies that have been made are complementary and, thus, it is possible to present a fairly complete overview.

Schraub and Kline (1965) examined the viscous sublayer structure of accelerated turbulent boundary layers using dye injection and hydrogen bubble techniques. They found that the organized motions in the viscous sublayer (known as bursting) did not abruptly stop above a certain level of acceleration but, instead, progressively decreased as K was increased. Their data are shown in Figure 2.2. The bursting period was calculated from their measured bursting frequency and streak spacing data using the following relation

$$T_B^+ = \frac{2}{F^+ \lambda^+} . \quad (2.5)$$

As seen from their results, accelerating the boundary layer gives rise to an increase in both the streak spacing and bursting period. However, it should be noted that they do not increase at the same rate; the bursting period rises faster than the streak spacing. Relaminarization of the flow, defined by Kline et. al. as the point at which the production of turbulent kinetic energy is zero, occurred at a value of $K \approx 3.7 \times 10^{-6}$. This result was in agreement with the value of $K \approx 3.5 \times 10^{-6}$ obtained by Moretti and Kays (1965), who studied heat transfer in accelerated turbulent boundary layers.

As the level of the imposed pressure gradient is increased, the mean velocity profile is known to exhibit a smooth shift from a typical turbulent velocity profile towards that corresponding to a laminar boundary layer. This shift is characterized by an "overshoot" of the velocity profile from the log-law, and a decrease in the wake region. Thus, the logarithmic region is observed to decrease in extent as the level of the

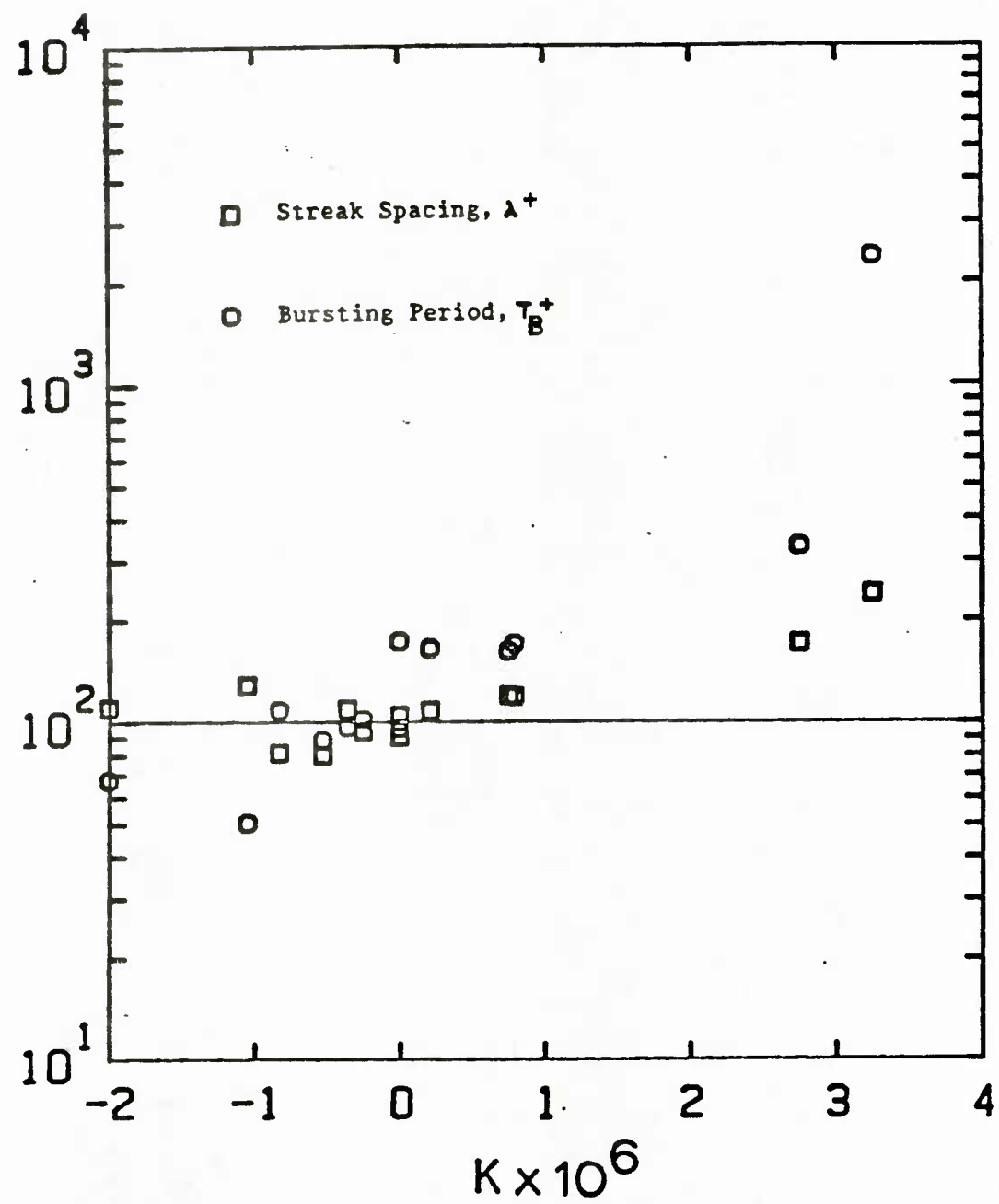


Figure 2.2 Variation of the streak spacing and bursting period with pressure gradient [Kline (1965)]

imposed pressure gradient is increased. This disappearance of the logarithmic region has been suggested [Patel (1965), Launder and Stinchcombe (1967), Badri Narayanan and Ramjee (1969), Blackwelder and Kovasznay (1972), and Okamoto and Misu (1977)] to mark the beginning of the relaminarization of a turbulent flow. Bradshaw (1969) suggests that when the logarithmic region disappears, the energy-containing and dissipating eddies overlap in size and relaminarization will occur.

The study of Patel and Head (1968) was concerned with the initial stages of relaminarization with the objective of defining as closely as possible the conditions leading to the breakdown of the turbulent flow. It was suggested that the favorable pressure gradient and its effect on the wall region of the flow was primarily responsible for the changes in the flow and not some outer layer Reynolds number. Relaminarization was said to occur when the production and dissipation of turbulent kinetic energy in the logarithmic region deviated from equilibrium. They used the theory of Townsend (1961), which is based on a mixing-length model for an equilibrium flow, and the assumption of a linear shear stress distribution to obtain an equation relating \bar{U}^+ to the shear stress gradient, $\Delta\tau^+$, where

$$\Delta\tau^+ = \frac{-\nu}{\rho u_*^3} \frac{d\tau}{dy} . \quad (2.6)$$

This shear stress gradient is only a function of the pressure gradient and local flow accelerations and not the distance from the wall. The value of $\Delta\tau^+$ at which their derived relation failed to predict the measured mean velocity profile was concluded to be the beginning of relaminarization. They suggested that for $\Delta\tau^+ < -0.009$ fully developed turbulent flow could not be maintained.

Jones and Launder (1972) studied accelerated flows corresponding to $K =$

1.5×10^{-6} , 2.5×10^{-6} and 3.0×10^{-6} . Streamwise turbulent fluctuation measurements were made at the three levels of accelerations. At the highest acceleration, an asymptotic flow could not be established as the flow was still changing at the end of the test section. In the viscous wall region, the intensity profiles for the other two accelerations were very similar. A peak intensity of about 2.4 in wall units was observed at $y^+ = 15$. Launder and Stinchcombe (1967) also noted a high streamwise turbulence intensity, although the bulk of the turbulent energy was associated with irrotational fluctuations. Hot-wire measurements of w'' , v'' and the Reynolds stress were also reported by Jones and Launder for the lowest acceleration. The accuracy of these measurements was not very high due to the thinness of the viscous wall region. It was found that the intensity measurements were in roughly the same proportion to each other as those found in the nonaccelerated flow. Badri Narayanan and Ramjee (1968) noted that after relaminarization began to occur the streamwise velocity fluctuations decayed rapidly. Based on their data and a survey of previous data, Jones and Launder suggested that the maximum skin-friction coefficient possible in a asymptotic turbulent flows is about 0.005. This value is equal to the one suggested by Coles (1962) as the maximum attainable in a nonaccelerated turbulent boundary layer. As the level of acceleration increased, C_f was observed to increase to about 0.005 and then stay roughly constant for K values greater than 1×10^{-6} . Only after relaminarization began to occur did C_f decrease below the nonaccelerated value.

Narasimha and Sreenivasan (1973) proposed that relaminarization is primarily the result of the domination of pressure forces over nearly frozen Reynolds stresses. The completion of reversion according to them is when the net effect of the Reynolds stresses is negligible. Random fluctuations inherited from previous history will remain, but they are no

longer relevant to the dynamics of the flow, which under these circumstances may be said to have reached a quasi-laminar state. This limit occurs for sufficiently large values of a pressure gradient parameter

$$\Lambda = -\frac{\delta}{\tau_0} \frac{dP}{dx} \quad (2.7)$$

where δ is the boundary layer thickness and τ_0 the wall stress in the boundary layer just before the imposed pressure gradient is applied. This concept agreed very well with the investigation of Blackwelder and Kovasznay (1972) into rapidly rapidly varying pressure gradient flows that showed the turbulent fluctuations and Reynolds stress were approximately constant along a mean streamline. It should be noted that the pressure gradient parameter, Λ , appears to be better suited for rapidly changing flows than for asymptotic similar sink flows.

Recently, Spalart and Leonard (1985) simulated equilibrium turbulent boundary layers using the full three-dimensional, time-dependent Navier-Stokes equations. Similarity laws were used to approximate the terms associated with the slow spatial growth of the turbulent boundary layer. They obtained good agreement with the experimental data of Jones and Launder (1972) for the flow with an acceleration of $K = 1.5 \times 10^{-6}$. The calculations were preliminary in nature, but it appears that this type of simulation may provide some key information impossible to attain experimentally in the laboratory.

III. Pulsating Pressure Gradient Turbulent Flows

Research in the area of pulsating turbulent flow has grown rapidly in recent years. This recent interest can be associated with the development of instrumentation and the availability of new techniques of data acquisition.

tion and processing. The results from these studies are needed to solve such complex problems as the flow of blood in the arteries of the body and the oscillating flow behind the rotors of helicopters. Mao (1984) presents an excellent review of the pulsating flow literature and only articles of more recent origin are surveyed here. This section begins with a discussion on pulsating laminar flow as this flow is very similar to turbulent flow at high dimensionless frequencies, $\omega^+ = \omega u^* / \nu$. Then a review of the recent experimental studies in pulsating turbulent boundary layers and pipes (or channels) flows are presented. Finally, the literature concerned with the modelling of pulsating turbulent flows is surveyed.

A. Pulsating Laminar Flow

Sexl (1930) and Uchida (1956) studied pulsating laminar flow through a pipe. An unique parameter $\Omega = r_0 \sqrt{\omega/\nu}$ was found to characterize the flow, where ω is the angular frequency and r_0 the radius of the pipe. At very low values of Ω , the velocity profile of the pulsating component is in phase with the imposed variation of the pressure gradient and behaves like that in steady state flow with the same mean flow rate. At very large values of Ω , the pulsating flow field moves like a solid body in the core region of the pipe and varies rapidly close to the wall. For this case the pulsation velocity lags the pressure gradient by 90° in the center of the pipe, but only by 45° in the neighborhood of the wall where viscous effects are important.

The response of turbulent flow to an imposed pulsation is qualitatively similar to that of laminar flow. At very low frequencies, the velocity profile for both flows at each instant is the same as that in a steady flow with the same flow rate. At high frequencies, the periodic velocity component for both flows is flat in the center of the pipe and has rapid

variation near the wall. Mathematically, this similarity is easy to explain. The simplified equation describing the pulsating component of a turbulent flow is

$$\rho \frac{\partial u}{\partial t} = -\frac{\partial p}{\partial x} + \mu \frac{\partial^2 u}{\partial y^2} + \frac{\partial \tau(t)}{\partial y} . \quad (2.8)$$

where $\tau(t)$ is the turbulent stresses. At high frequencies, the last two terms are negligible except very close to the wall and the following relationship results for both laminar and turbulent flows:

$$\rho \frac{\partial u}{\partial t} = -\frac{\partial p}{\partial x} . \quad (2.9)$$

The solution of (2.9) for a periodically varying pressure and velocity field given by (1.1) and (1.2) is

$$\omega \rho |\hat{u}| = \left| \frac{dp}{dx} \right| , \quad (2.10)$$

and

$$\theta_u = -\pi/2 . \quad (2.11)$$

Thus, wherever inertia dominates the characteristics of the two flows will be very similar.

Quantitatively, the presence of the turbulent stresses causes the two flows to be different. For example, the frequency parameter Ω , which characterizes the laminar pulsating flow, is no longer a suitable parameter for the turbulent case. The amplitude of the imposed pulsation and the mean Reynolds number also affect the turbulent pulsating flow. The principal theoretical problem in turbulent flows is the determination of how a pulsating pressure gradient affects the turbulent stresses.

B. Measurements of Pulsating Turbulent Flow

A number of previous investigators have studied the influence of controlled flow pulsations on turbulent flows. An excellent review has recently been presented by Carr (1981). Previous results have indicated that the influence of the pulsations on the mean properties of the flow is very small and that their effect on the turbulence is felt primarily in the region close to the wall. Unfortunately, in most previous studies accurate velocity measurements could not be made close enough to the wall to determine the time varying velocity gradient at the wall. Thus, there exists a need for accurate measurements of the time varying wall shear stress.

Ramaprian and Tu (1982, 1983a, 1983b) reported detailed experimental data on the instantaneous velocity and wall shear stress at a mean Reynolds number 50,000 in a fully developed turbulent pipe flow in which the volumetric flow rate was varied sinusoidally with frequencies 0.5 Hz and 3.6 Hz, and amplitudes 64% and 15% of the mean flow rate respectively. In contrast to most other researchers, they concluded from their data that both the time mean velocity profiles and the time mean turbulent intensities are affected by the imposed pulsation. They considered that these effects are caused by the combination of high pulsation frequency and large amplitude. The phase averaged turbulent intensity data showed that at high frequency the turbulent intensity remains frozen throughout the cycle in the outer region and that at lower frequencies it experiences significant variation. The authors also reported the results of direct measurements of the wall shear stress with flush mounted hot film probes. In their experimental range, the phase shifts of the wall shear stress were found to be of the order of 10 degrees. However, since they didn't consider the frequency response of the probe, serious errors could be present in the

results at high frequency.

Binder et. al. (1985) measured periodic velocity pulsations near the wall in a turbulent pulsating channel water flow. Results were obtained for flows having a centerline velocity variation between 10-70%. They found the mean velocity and the streamwise turbulent intensity to be unchanged by the large amplitude oscillations. At high frequencies, the periodic flow field was best described by the Stokes solution for flow over an oscillating wall. The authors argued that in the region near the wall the Stokes thickness ℓ_s^+ nondimensionalized with the mean viscous sublayer thickness correlated their amplitude and phase data. The wall shear stress was also measured using hot-film wall probes. For $\ell_s^+ < 10$, the shear stress at the wall lead the free-stream by 45°, and the amplitude was slightly less than predicted by Stokes law. For ℓ_s^+ , the amplitude increased above the Stokes value and the phase lead went to zero. The variation of the turbulent wall shear stress fluctuations was found to depend on both the amplitude and frequency of pulsation. The phase of the fluctuations had a time lag which was always approximately 100-200 ν/u^* .

The study of Mao and Hanratty (1986) in an eight in. pipe focused on measurements of the wall shear stress at high dimensionless frequencies, ω^+ . They found that the phase and amplitude of the wall shear stress variation could be correlated by the single parameter ω^+ and that the mean shear stress was unaffected by the imposed flow pulsation. The most striking feature of their results is a relaxation effect, whereby the phase angle characterizing the temporal variation of the wall shear stress undergoes a sharp change over a very narrow range of ω^+ . They suggested that at low frequencies an equilibrium situation exists whereby the flow behaves similarly to that observed in constant pressure gradient flows. As ω^+ increases the pressure gradient varies so rapidly that the turbulence

in the viscous wall region does not respond immediately. This relaxation phenomena has also been observed in flow over wavy surfaces [Abrams and Hanratty (1985)]. At higher ω^+ than the bursting frequency they observed a highly nonlinear interaction between the imposed pulsation and the turbulent fluctuations. Their data for the variation of the wall shear stress at high ω^+ , which was still linear, was found to be lower than the limiting Stokes solution.

Measurements of the wall shear stress in a pulsating turbulent boundary layer were reported by Cousteix and Houdeville (1985). They compared their direct measurements of the wall shear stress with a heat transfer wall probe to values deduced from the logarithmic velocity profile. Agreement was obtained only for low frequencies. The parameter ω^+ was shown to scale their data at high frequencies. The external flow pulsation generated a modulation of the turbulence near the wall. This modulation was found to be more significant at low ω^+ than at high at high ω^+ . Using the VITA technique of Blackwelder and Kaplan (1976), measurements were made of the variation of the bursting period in the pulsating boundary layer. Even though the results were found to be very sensitive to the cut-off threshold, no dramatic effect on the bursting phenomenon was observed.

C. Models of Pulsating Turbulent Flow

The first models of turbulent boundary layers close to a solid wall have used Van Driest's (1957) modification of Prandtl's mixing length hypothesis. This approach, which assumes a universality of the wall region in terms of wall parameters, fails to predict flows subject to mild pressure gradients. Various workers have proposed modifications to the Van Driest formula to better account for these effects.

Patankar and Spalding (1967) proposed that the local value of the shear

stress rather than the wall value be used in the exponent of the Van Driest damping function. This modification has the correct qualitative behavior. In favorable pressure gradients the shear stress decreases from its value at the wall; therefore, this formulation does result in a thickening of the viscous wall region. However, calculations carried out using this formulation show that it does not produce a large enough effect.

Launder and Jones (1969), Cebeci and Smith (1974), Julien et al. (1969), Loyd et. al. (1970), and Reynolds (1976) began experimenting with the idea that the constant A in the Van Driest mixing length model is related to the thickness of the viscous wall region in wall units which, in turn, depends upon the dimensionless pressure gradient, P^+ . These researchers deduced a functional dependency of A^+ on P^+ by examining a large number of equilibrium velocity profiles subject to both positive and negative pressure gradients. A first order lag equation, that was used to predict an effective sublayer thickness, A_{eff} , was proposed by Loyd et. al., Julien et. al., and Launder and Jones to model flows with rapidly changing pressure gradients.

Mao and Hanratty (1986) used models developed for flow over wavy surfaces [Thorsness et. al. (1978), and Abrams and Hanratty (1985)] to model pulsating turbulent pipe flow. Four different eddy viscosity models, labeled Model A, Model B, Model C and Model D, were tried. All of them attempted to relate the oscillation induced Reynolds stress to the induced velocity gradient. Model A is a quasi-laminar model in that the induced oscillation of the turbulent Reynolds stress is set to zero and the turbulent flow is assumed to behave in the same manner as a laminar flow. This formulation is only valid for very high frequency pulsations. Model B, an adaption of the mixing length model of Hussain and Reynolds (1970), assumed that the eddy viscosity is specified only by the mean flow field.

Model C is a quasi-steady approximation in that the eddy viscosity and the Reynolds stress are directly associated with the instantaneous velocity gradient in the same manner as that for a steady flow. Model D defines an effective A^+ , similar to that used by Loyd et. al. (1970), that takes into account the lag between the imposed pressure gradient and the turbulence. All the models predicted correctly the high frequency quasi-laminar behavior. However, only Model D was able to predict the rapid change in phase associated with the relaxation phenomenon described earlier.

Kebede, Launder and Younis (1985) abandoned the mixing length approach by arguing that the prediction of nondimensional flows could not be achieved with a transport hypothesis based so firmly on equilibrium notions. Instead, they developed a second-moment closure that incorporated near wall effects. The model was shown to reproduce fairly well the behavior of equilibrium wall flows. In applying the model to large amplitude, low frequency periodic pipe flow, difficulties were encountered in obtaining time-step-independent results. These troubles were due partly to the time discretization method employed and partly to the dynamic response of the turbulence field in the viscous wall region. The $k-\epsilon$ model of Jones and Launder (1972, 1973) was also modified for pulsating pipe flow. Kebede et. al. found the $k-\epsilon$ model to give better predictions for the velocity and stress fields than the second-moment closure equation. Due to the difficulties involved, no attempt was made by them to model the periodic flow at higher frequencies.

Reddy and McLaughlin (1985) used a nonlinear time dependent three-dimensional model of the viscous wall region to study turbulent pulsating flow. The number of nodes used in their pseudospectral algorithm was only 4096. Only one run at a frequency equal to the bursting frequency of turbulence and an amplitude of 50% of the centerline velocity was reported.

Their calculation predicted negligible enhancement of the momentum transport and the average rate of turbulence production was found to be slightly lower in the pulsed flow than in steady flow. The production of turbulent kinetic energy was shown to be at its maximum level when the pressure gradient was at its minimum.

Chapter 3. THEORY

This chapter describes the models that were used to investigate the effects of an imposed pressure gradient on the viscous wall region. The first section describes the eddy model proposed by Nikolaides (1984) and its modification to include large favorable pressure gradients. The major new contribution to the model was the development of arguments that described the scaling of the coherent structures as a function of the imposed pressure gradient. The second section characterizes the eddy viscosity models used to predict the wall shear stress in turbulent pulsating pipe flow. These models are very similar to those used by Mao and Hanratty (1986) to describe their experimental data at high ω^+ .

I. Eddy Model for the Viscous Wall Region

The dominant wall eddies in the viscous wall region are characterized by a length scale, λ , and a time scale, T_B . The characteristic length in the spanwise direction corresponds to the distance between dye-streaks as observed by Kline et. al. (1967) and the characteristic period corresponds to the frequency of the most energetic velocity fluctuations close to the wall. Kline et. al. (1967) experimentally observed that these scales increase in accelerated flows and decrease in decelerated flows. As the distance from the wall increases, eddies with larger length and time scales become more important. These eddies, associated with the flow far away from the wall, interact with the wall eddies and their interaction completely specifies the dynamics of the viscous wall region. The specification of this interaction, which results in the creation and maintenance of wall turbulence, is the essence of our eddy model.

A. Model Equations

The flow in the viscous wall region is assumed to be homogeneous in the

streamwise direction and coherent on a plane perpendicular to the direction of the mean flow. The equations that describe this flow are the time-dependent Navier-Stokes equations and the continuity equation:

$$\frac{\partial v}{\partial t} + \frac{\partial(v^2)}{\partial y} + \frac{\partial(vw)}{\partial z} = -\frac{1}{\rho} \frac{\partial P}{\partial y} + \nu \left(\frac{\partial^2 v}{\partial y^2} + \frac{\partial^2 v}{\partial z^2} \right) \quad (3.1)$$

$$\frac{\partial w}{\partial t} + \frac{\partial(vw)}{\partial y} + \frac{\partial(w^2)}{\partial z} = -\frac{1}{\rho} \frac{\partial P}{\partial z} + \nu \left(\frac{\partial^2 w}{\partial y^2} + \frac{\partial^2 w}{\partial z^2} \right) \quad (3.2)$$

$$\frac{\partial U}{\partial t} + \frac{\partial(vU)}{\partial y} + \frac{\partial(wU)}{\partial z} = -\frac{d\tau}{dy} + \nu \left(\frac{\partial^2 U}{\partial y^2} + \frac{\partial^2 U}{\partial z^2} \right) \quad (3.3)$$

$$\frac{\partial w}{\partial z} + \frac{\partial v}{\partial y} = 0, \quad (3.4)$$

where $U = \bar{U} + u$ and

$$\frac{d\tau}{dy} = \frac{1}{\rho} \frac{d\bar{P}}{dx} + \bar{U} \frac{\partial \bar{U}}{\partial x} + \bar{V} \frac{\partial \bar{U}}{\partial y}. \quad (3.5)$$

The assumption of homogeneity in the streamwise direction decouples the v and w equations from the U equation which makes the numerical solution of (3.1-3.5) much easier. The $d\tau/dy$ term is only nonzero for accelerated or decelerated boundary layers. It represents the net effect an imposed pressure gradient has on the turbulent boundary layer. Except in the $d\tau/dy$ term, the normal mean velocity is neglected as it is small compared to the fluctuating normal velocity. The effect of acceleration on $d\tau/dy$ is discussed in detail in Section 3.I.B.

The variables in (3.1-3.5) are made dimensionless in all the calculations by a characteristic length ℓ_c and a characteristic velocity U_c . These are selected so that $\ell_c^+ = \lambda^+$ and $U_c^+ = 2(v_0')^+$ where $(v_0')^+$ is the intensity of the normal velocity fluctuations at $y = y_0$. The subscript o

signifies that the quantity is evaluated at the outer edge of the viscous wall region. With these values, the Reynolds number is $Re = U_C \ell / \nu = U_C^+ \ell_C^+ = 182$. Based on scaling arguments presented in Section 3.I.C, the Reynolds number is constant and independent of the level of acceleration.

The above system of equations are solved using the following boundary conditions:

$$U = v = w = 0 @ y = 0$$

$$w = 0, \frac{\partial v}{\partial z} = 0, \frac{\partial U}{\partial z} = 0 @ z = 0 \text{ and } z = z_0,$$

where $z_0 = \lambda_2/2$ and λ_2 is the dimensionless wavelength of the outer flow eddies.

Eliminating the pressure from (3.1) and (3.2) and reformulating the problem using the vorticity and stream functions gives the following equations:

$$\frac{\partial \zeta}{\partial t} + \frac{\partial(w\zeta)}{\partial z} + \frac{\partial(v\zeta)}{\partial y} = \frac{1}{Re} \left(\frac{\partial^2 \zeta}{\partial z^2} + \frac{\partial^2 \zeta}{\partial y^2} \right) \quad (3.6)$$

$$\nabla^2 \Psi = \zeta. \quad (3.7)$$

where $\zeta = \frac{\partial w}{\partial y} - \frac{\partial v}{\partial z}$ and $w = \frac{\partial \Psi}{\partial y}$, $v = -\frac{\partial \Psi}{\partial z}$. There are two reasons for switching to the (Ψ, ζ) formulation: 1) the pressure is eliminated from the problem and, 2) the continuity equation is satisfied by definition. After the Ψ and ζ fields have been determined, v and w can be obtained from the Ψ solution. The boundary conditions in the (Ψ, ζ) formulation are as follows:

$$\Psi = 0, \zeta = \frac{\partial^2 \Psi}{\partial y^2} @ y = 0$$

$$\zeta = 0, \Psi = 0 @ z = 0 \text{ and } z = z_0$$

$$\zeta = - \int_0^Z v(\phi, y_0, t) d\phi, \quad \Psi = \frac{\partial^2 \zeta}{\partial y^2} - \frac{\partial v}{\partial z} \quad @ y = y_0 ,$$

where ϕ is a dummy variable and the temporal and spatial variation of U , v and w is specified at $y = y_0$.

The initial conditions for (3.6) and (3.7) are given by the inviscid-irrotational solution on the y - z plane. The initial field for the U equation was generated using the van Driest profile in the viscous wall region.

The Poisson equation for the pressure is obtained by taking the y -derivative of (3.1) and the z -derivative of (3.2) and adding the resulting equations to give the following relation:

$$\frac{\partial^2 p}{\partial y^2} + \frac{\partial^2 p}{\partial z^2} = 2 \left[\left(\frac{\partial v}{\partial y} \right) \left(\frac{\partial w}{\partial z} \right) - \left(\frac{\partial v}{\partial z} \right) \left(\frac{\partial w}{\partial y} \right) \right] . \quad (3.8)$$

The boundary conditions are obtained directly from the equations of motion applied at a specific boundary and are of the Neumann type. For further information on the pressure solution, see Nikolaides (1984).

B. Effect of Acceleration on the Viscous Wall Region

In order to obtain the U velocity field from (3.3), the variation of $d\tau^+/dy^+$ in the y direction as a function of acceleration is needed. This can be accomplished using the two-dimensional mean streamwise momentum and continuity equations,

$$\frac{\partial \bar{U}}{\partial x} + \frac{\partial \bar{V}}{\partial y} = 0 \quad (3.9)$$

$$\bar{U} \frac{\partial \bar{U}}{\partial x} + \bar{V} \frac{\partial \bar{U}}{\partial y} = \frac{1}{\rho} \left[\frac{d\tau}{dy} - \frac{d\bar{P}}{dx} \right] , \quad (3.10)$$

where $\tau = \mu \partial \bar{U} / \partial y - \rho \bar{u}^T \bar{v}^T$. If the advective terms are neglected, the

familiar Couette flow relations are obtained:

$$P^+ = \frac{d\tau^+}{dy^+} , \quad (3.11)$$

and

$$\tau^+ = 1 + P^+y^+ . \quad (3.12)$$

Experimental evidence [Sandborn and Slogan (1955), Bradshaw (1967)] clearly shows that the shear stress and pressure gradients become unequal as the distance from the wall increases. Using (3.9) and (3.10), Julien et. al. (1969) developed the following relation for the shear stress distribution in asymptotic similar sink flows:

$$\tau^+ = 1 + P^+y^+ \left[1 - \frac{C_f}{2} \frac{1}{y^+} \int_0^{y^+} \bar{U}^{+2} dy^+ \right] . \quad (3.13)$$

This relation differs from (3.12) in that the inertia changes in the fluid as a result of acceleration are taken into account. Julien et. al. (1969) and Loyd et. al. (1970) found that the wall region, $y^+ < 150$, responded very quickly to the imposed pressure gradient and that (3.13) described their data very well. It is convenient at this point to define a quantity P_e^+ such that (3.13) has the same form as the Couette flow relation, (3.12),

$$\tau^+ = 1 + P_e^+y^+ , \quad (3.14)$$

where

$$P_e^+ = P^+ \left[1 - \frac{C_f}{2} \frac{1}{y^+} \int_0^{y^+} \bar{U}^{+2} dy^+ \right] . \quad (3.15)$$

The parameter, P_e^+ , includes the inertial changes of the fluid and represents the net effect of the acceleration on the shear stress profile.

The shear stress gradient profile can be obtained from (3.13) by differentiating with respect to y^+ to obtain:

$$\frac{d\tau^+}{dy^+} = P^+ \left[1 - \frac{C_f}{2} \bar{U}^{+2} \right] . \quad (3.16)$$

The bracketed term in (3.16) is always less than 1 for both favorable and adverse pressure gradients. Thus, the inclusion of the advective terms always results in a damping of the effect of the pressure gradient on the turbulent structure in the viscous wall region.

C. Scaling of the Coherent Structures in the Viscous Wall Region

The upper boundary of the computational domain of the model is located at the outer edge of the viscous wall region where Kline et. al. (1969) observed that the coherent structures (low-speed wall streaks) broke-up into chaotic motion. Thus, the coherent structures are modelled by using the following boundary conditions at $y^+ = y_0^+$:

$$w = \hat{w}_1 \cos\left(\frac{2\pi t}{T_1} + \phi_{w1}\right) \sin\left(\frac{2\pi z}{\lambda_1}\right) + \hat{w}_2 \cos\left(\frac{2\pi t}{T_2} + \phi_{w2}\right) \sin\left(\frac{2\pi z}{\lambda_2}\right) \quad (3.17)$$

$$v = \hat{v}_1 \cos\left(\frac{2\pi t}{T_1} + \phi_{v1}\right) \sin\left(\frac{2\pi z}{\lambda_1}\right) + \hat{v}_2 \cos\left(\frac{2\pi t}{T_2} + \phi_{v2}\right) \sin\left(\frac{2\pi z}{\lambda_2}\right) \quad (3.18)$$

$$U = \bar{U}(y_0) + \hat{u}_1 \cos\left(\frac{2\pi t}{T_1} + \phi_{u1}\right) \sin\left(\frac{2\pi z}{\lambda_1}\right) + \hat{u}_2 \cos\left(\frac{2\pi t}{T_2} + \phi_{u2}\right) \sin\left(\frac{2\pi z}{\lambda_2}\right) \quad (3.19)$$

The components with λ_1 and T_1 scales are associated with the wall eddies, while the components with λ_2 and T_2 scales reflect the contribution of the outer flow eddies to the dynamics of the viscous wall region. For nonaccelerated flows, Nikolaides (1984) used experimental measurements of the turbulent quantities in the viscous wall region to specify the relative

energies of the two components, the temporal phase angles and the relevant length and time scales. In accelerated flows, the experimental information necessary to assign values to these parameters are not available. Thus, it becomes necessary to develop relations that describe the scaling of the coherent structures in the viscous wall region as a function of acceleration. The necessary quantities are the location of the edge of the viscous wall region (y_0^+), the characteristic wavelength (λ_1^+), the bursting period (T_1^+), the turbulent kinetic energy (q_0^+) and the shear stress at the edge of the viscous wall region (τ_0^+). Thus, five scaling relations are needed to describe the coherent structures in the viscous wall region.

Local equilibrium is assumed to exist in the logarithmic region between the production and dissipation of turbulent kinetic energy,

$$-\bar{uv} \frac{d\bar{U}}{dy} = \varepsilon , \quad (3.20)$$

where the rate of dissipation is equal to

$$\varepsilon = a_1 \frac{q^3}{l} , \quad (3.21)$$

and l is the mixing length. Relation (3.21) is a result of dimensional considerations that the energy transfer from large eddies to small eddies proceeds at a rate dictated by the energy of the large eddies (which is of order q^2) and their time scale (which is of order l/q).

In the logarithmic region $l = \kappa y$, where κ is the Von-Karmen constant equal to 0.41. For the case where the shear stress in the logarithmic region is equal to the wall shear stress (nonaccelerated flows), dimensional analysis shows

$$\frac{d\bar{U}}{dy} = \frac{\sqrt{\tau_w/\rho}}{\kappa y} . \quad (3.22)$$

Townsend (1961) was the first to generalize (3.22) to the case where the shear stress is varying in the y direction,

$$\frac{d\bar{U}}{dy} = \frac{\sqrt{\tau/\rho}}{\kappa y} . \quad (3.23)$$

Relation (3.23) has been experimentally shown to be valid for several different types of flows. Combining (3.23), (3.20) and (3.21) and using the assumption $-\bar{u}\bar{v}|_0 \approx \tau_0/\rho$ at the edge of the logarithmic region, the following is obtained:

$$q_0^0 \equiv \frac{q_0}{\sqrt{\tau_0/\rho}} , \quad (3.24)$$

where the superscript 0 is used to represent a quantity scaled with the shear stress at the outer edge of the viscous wall region. These are assumed constant for all levels of accelerations. By changing (3.24) to wall variables, the following is obtained:

$$q_0^+ = q_0^0 \sqrt{\tau_0 F} , \quad (3.25)$$

where q_0^0 is constant and equal to 2.72, the nonaccelerated value. This relation is a direct statement of the fact that the eddies containing most of the turbulent kinetic energy are those that are associated with the creation of Reynolds stress. This is the first of the five desired relations needed to describe the coherent structures in the viscous wall region.

It has been observed experimentally that the region of direct viscous

effects increases (in wall units) with acceleration. Thus, the location of the edge of the viscous wall region is known to be a function of acceleration. We need to define a quantity that adequately determines the location of y_0^+ for all levels of acceleration. A natural choice is the ratio of the viscous shear stress to the total shear stress

$$\frac{\text{viscous shear stress}}{\text{total shear stress}} = \frac{\mu d\bar{U}/dy}{\tau} \Big|_{y=y_0} = a_2 . \quad (3.26)$$

Thus, the location of the edge of the viscous wall region is marked by the distance away from the wall at which the ratio of the two shear stresses is equal to some arbitrary determined constant.

Substituting (3.23) into (3.26) and taking the reciprocal gives

$$y_0^0 \equiv \frac{\sqrt{\tau_0/\rho}}{\nu} y_0 , \quad (3.27)$$

where $y_0^0 = 1/(\kappa a_2) = 40$, the nonaccelerated value (values ranging from 30 to 50 can be found in the literature). Thus, the location of the outer edge of the viscous wall region is found to be constant if scaled with the shear stress at the edge of the viscous wall region. By scaling (3.27) in wall units, the following is obtained:

$$y_0^+ = \frac{y_0^0}{\sqrt{\tau_0^+}} . \quad (3.28)$$

This relation has the correct qualitative behavior in that the viscous wall region thickens during acceleration and thins during deceleration. This is the second of the five necessary relations.

An alternative form to (3.21) for the rate of dissipation of turbulent kinetic energy, valid for isotropic turbulence [Hinze (1975)], is

$$\varepsilon = 30 \nu \frac{q^2}{\lambda_T^2} , \quad (3.29)$$

where λ_T is the Taylor microscale. It should be noted that λ_T is not a dissipative length scale (the Kolmogorov microscale, η , is the only truly dissipative length scale), but a dissipative time scale when used in conjunction with q . Thus, q/λ_T is representative of the time it takes for a large eddy to transfer its energy to a smaller one. Equating the two dissipation relations, (3.21) and (3.29), and using (3.24), the following is obtained:

$$\frac{\lambda_T^2}{y_0} = \frac{30\kappa\nu}{2.72a_1\sqrt{\tau_0/\rho}} . \quad (3.30)$$

For a Gaussian signal the zero-crossing scale, defined as $\Lambda \equiv 1/(2\pi N_0)$ (where N_0 is the frequency with which the signal crosses zero), is equal to λ_T [Rice (1954)]. Measurements of the ratio Λ/λ_T by Antonia et. al. (1976), Sreenivasan et. al. (1977) and Sreenivasan et. al. (1983) indicate that it is also equal to 1 for several different types of flows including asymptotic similar boundary layers. The dominant eddies in the viscous region used in our model have two zero crossings over the wavelength λ_1 , therefore, $N_0 = 1$ and

$$\lambda_T = \frac{\lambda_1}{2\pi} . \quad (3.31)$$

By substituting (3.31) into (3.30) and rearranging, the following is obtained:

$$\frac{\lambda_1^2 \sqrt{\tau_0/\rho}}{y_0 \nu} = \frac{120\kappa\pi^2}{2.72a_1} . \quad (3.32)$$

By substituting (3.27) into (3.32), the following is obtained:

$$\lambda_1^0 \equiv \frac{\lambda_1 \sqrt{\tau_0/\rho}}{\nu} , \quad (3.33)$$

where $\lambda_1^0 = (120 \kappa \pi^2 y_0^0 / 2.72 a_1)^{1/2} = 100$, the nonaccelerated value.

Expressing (3.33) in wall units,

$$\lambda_1^+ = \frac{\lambda_1^0}{\sqrt{\tau_0^+}} . \quad (3.34)$$

Comparing (3.34) to (3.28), it is seen that y_0^+ and λ_1^+ have the same dependence on τ_0^+ . This should be expected since the relations derived so far suggest that the dominant wall eddies are scaling with τ_0^+ and, therefore, the height and width of these eddies should be proportional for all accelerations. Equation (3.34) is the third necessary equation.

The next to last relation is obtained by assuming that away from the wall, where viscosity is not very important, the transient terms of the Navier-Stokes equations are of the same order of magnitude as the convective terms, i.e.,

$$\frac{\partial u_i}{\partial t} \sim u_i \frac{\partial u_i}{\partial x_j} . \quad (3.35)$$

The two terms can only be of the same order of magnitude if the following is true

$$\frac{\sqrt{\tau_0/\rho}}{T_1} \sim \frac{\tau_0/\rho}{\lambda_1} , \quad (3.36)$$

or equivalently

$$\frac{T_1}{\lambda_1} = \frac{1}{\sqrt{\tau_0/\rho}} . \quad (3.37)$$

Substituting (3.33) into (3.37),

$$T_1^0 \equiv \frac{T_1 \nu}{\tau_0 / \rho} , \quad (3.38)$$

where $T_1^0 = \lambda_0^0 = 100$, the nonaccelerated flow value. Changing to wall units,

$$T_1^+ = \frac{T_1^0}{\tau_0^+} . \quad (3.39)$$

Comparing (3.39) to (3.34), it is seen that T_1^+ has a higher dependence on the local shear stress than λ_0^+ . This qualitatively agrees with the measurements of Kline et. al. (1967).

By using various arguments, it has been shown that the parameters characterizing the flow in the viscous wall region scale with the shear stress at the outer edge of the viscous wall region. However, before these relationships can be used, a fifth equation relating τ_0^+ to the scaling parameters is needed. This equation, (3.14), has been derived in the previous section. Substituting (3.14) into (3.28) gives the following relation:

$$y_0^+ = \frac{y_0^0}{(1 + P_{eo}^+ y_0^+)^{\frac{1}{2}}} , \quad (3.40)$$

where, as previously noted, y_0^0 is set at 40. Equation (3.40) can be solved for y_0^+ for a given value of P_{eo}^+ . Once y_0^+ is known, τ_0^+ can be obtained from (3.14) and all the other scaling parameters can be determined. The variation of y_0^+ , λ_1^+ , and T_1^+ with P_{eo}^+ is shown in Figure 3.1. Negative P_{eo}^+ values correspond to favorable pressure gradients and positive values to adverse pressure gradients. The pressure gradient

associated with each P_{eo}^+ value cannot be determined apriori because a knowledge of the mean velocity profile, which has to be obtained in the laboratory, as done in this study, from a computer model, is needed.

The curves in Figure 3.1 exhibit a minimum point at $P_{eo}^+ = -0.00962$. Physically it is believed that this point corresponds closely to the disappearance of the logarithmic region and the point of relaminarization of the flow. The dotted branch of the curves in Figure 3.1 have no quantitative meaning since the relationships that they are based on depend on the existence of the logarithmic region. At the inflection point, the scaling parameters have the following values: $y_0^+ = 69.28$, $\lambda_1^+ = 173$, $T_1^+ = 300$, $\tau_0^+ = 0.333$, and $q_0^+ = 1.57$. At higher favorable pressure gradients than that at the inflection point, relaminarization occurs and a turbulent asymptotic similar boundary layer is not possible. These points are discussed in detail in Chapter 6.

D. Boundary Conditions at the Upper Edge of the Viscous Wall Region

Because of the limited experimental data on the viscous wall region for accelerated flows, complete specification of the boundary conditions at the upper edge of the viscous wall region is not possible. Instead, the scaling arguments presented in the last section are used to supplement the available data.

Because the following discussion involves the quantities in (3.17-3.19), they are rewritten here for convenience,

$$w = \hat{w}_1 \cos\left(\frac{2\pi t}{T_1} + \phi_{w1}\right) \sin\left(\frac{2\pi z}{\lambda_1}\right) + \hat{w}_2 \cos\left(\frac{2\pi t}{T_2} + \phi_{w2}\right) \sin\left(\frac{2\pi z}{\lambda_2}\right) \quad (3.17)$$

$$v = \hat{v}_1 \cos\left(\frac{2\pi t}{T_1} + \phi_{v1}\right) \sin\left(\frac{2\pi z}{\lambda_1}\right) + \hat{v}_2 \cos\left(\frac{2\pi t}{T_2} + \phi_{v2}\right) \sin\left(\frac{2\pi z}{\lambda_2}\right) \quad (3.18)$$

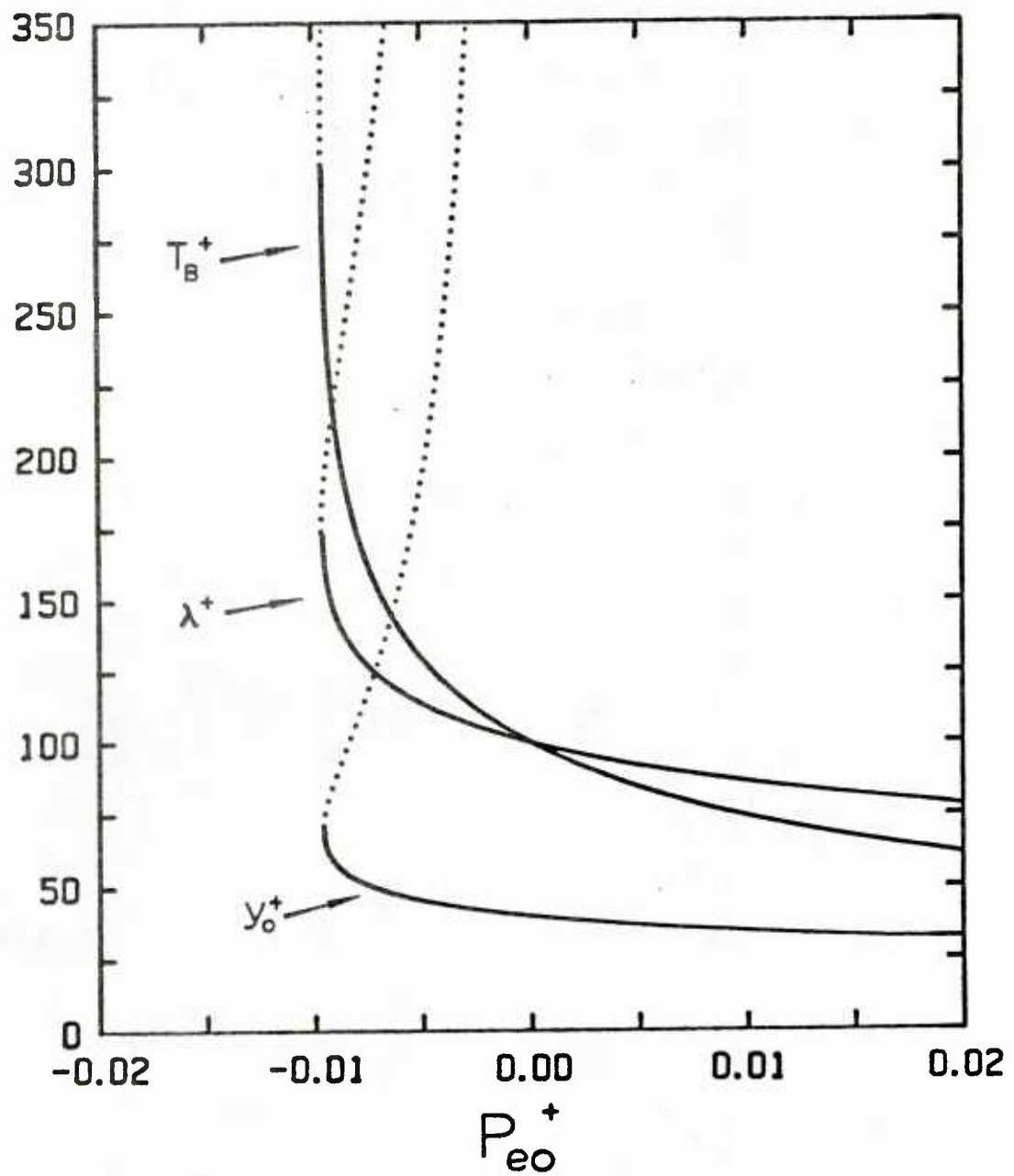


Figure 3.1 Variation of the streak spacing, bursting period, and the edge of the viscous wall region with Peo^+ .

$$U = \bar{U}(y_0) + \hat{u}_1 \cos\left(\frac{2\pi t}{T_1} + \phi_{u1}\right) \sin\left(\frac{2\pi z}{\lambda_1}\right) + \hat{u}_2 \cos\left(\frac{2\pi t}{T_2} + \phi_{u2}\right) \sin\left(\frac{2\pi z}{\lambda_2}\right) \quad (3.19)$$

Equation (3.25) suggests that any decrease in the Reynolds stress at y_0^+ comes about as a reduction in the amplitude of the fluctuations of the turbulent eddies and not as a result of decorrelation between the u and v fluctuations. The data of Badri Narayanan et. al. (1974), presented in Figure 3.2, shows that the Reynolds stress correlation stays roughly constant at about 0.5 in nonaccelerated as well as accelerated flows. Using this information, the phase angles and relative energies of the two components, $Eu_1 = \hat{u}_1/(\hat{u}_1 + \hat{u}_2)$, are assumed independent of the acceleration and equal to their nonaccelerated values. It is further assumed that the amplitudes of each fluctuating component at the upper boundary are reduced by the same amount i.e. $u_0^{+'} = (q_0^+/q_0^0)u_0^0$, $v_0^{+'} = (q_0^+/q_0^0)v_0^0$ and $w_0^{+'} = (q_0^+/q_0^0)w_0^0$. These assumptions are also consistent with the work of Jones and Launder (1972) who found that the intensity measurements of a flow with $K = 1.5 \times 10^{-6}$ are in roughly the same proportion to each other as those found in the nonaccelerated case. Their data, which starts just outside the viscous wall region, suggest that the intensity levels are set by the local shear stress. Moreover, their measured intensities in wall units fall off more rapidly with distance from the wall than in the nonaccelerated case which they attributed to the relative difference in the shear stress distribution of the two flows. Thus, it appears that (3.25) is valid everywhere in the logarithmic region. This result also agrees with the measurements of Bradshaw (1967) in decelerated flows.

The wall eddy scales, λ_1^+ and T_1^+ , are given by (3.34) and (3.39) respectively. It is assumed that the scales of the outer flow eddies, λ_2^+ and T_2^+ , respond to the imposed shear stress distribution the same way as

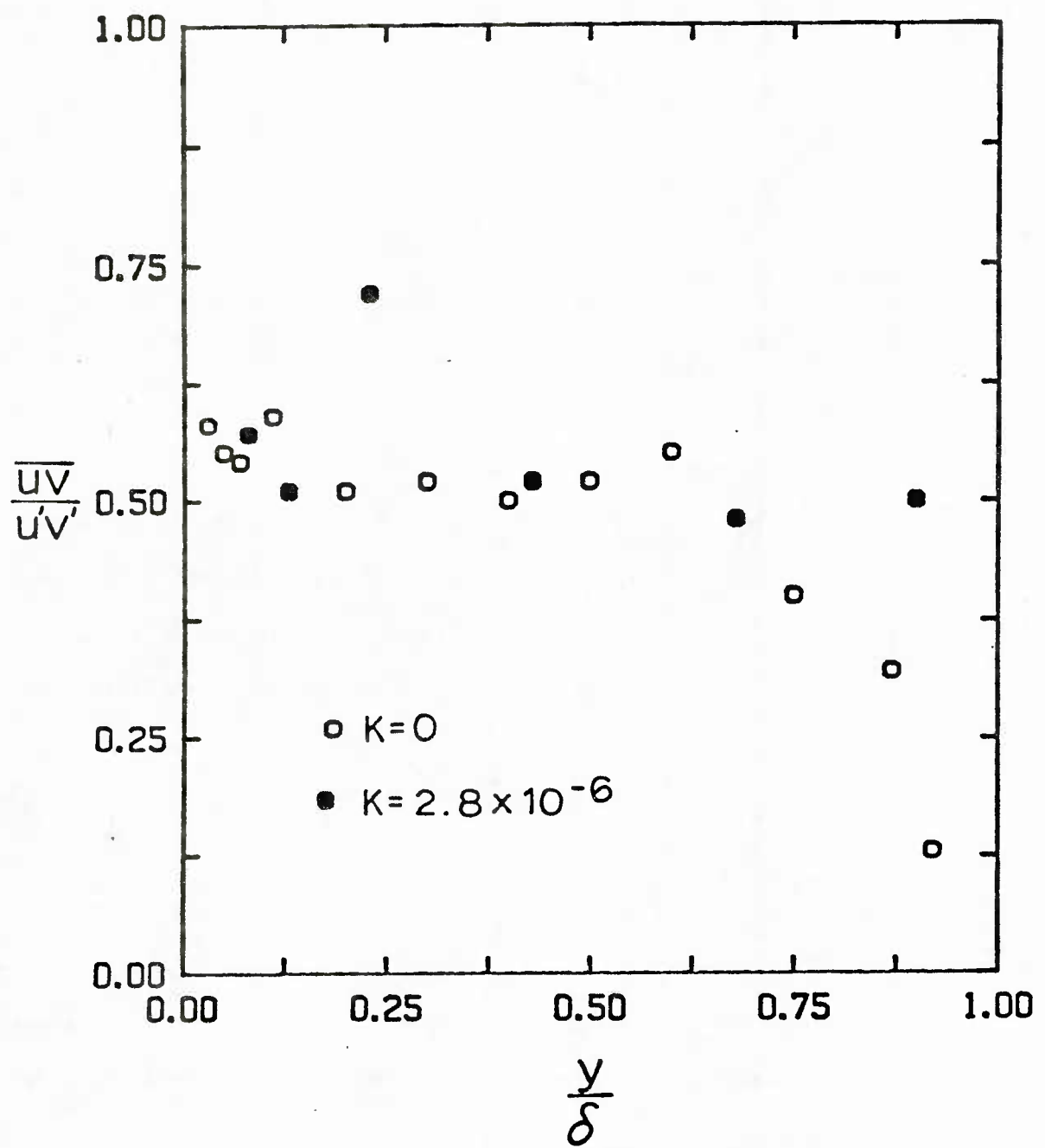


Figure 3.2 The effect of acceleration on the Reynolds stress.

the wall eddies do. Nikolaides (1984) found from spectral and correlation measurements that λ_2^+ and T_2^+ are roughly equal to 400 for the nonaccelerated boundary layer. He found that the flow structures were not very sensitive to λ_2^+ and T_2^+ and that values ranging from 300 to 700 gave essentially the same results. Therefore, the outer flow eddy scales were set by the following relations for all the runs:

$$\lambda_2^+ = 4\lambda_1^+ \quad (3.41)$$

$$T_2^+ = 4T_1^+ . \quad (3.41)$$

Most of the parameters used by Nikolaides (1984) for the nonaccelerated boundary layer are also used in this study. Some small adjustments were necessary in order to satisfy the logarithmic equation for the mean velocity and the slope at the outer edge of the viscous wall region, i.e.,

$$\bar{U}^+ = 2.44 \ln(y^+) + 5.0 \quad (3.43)$$

$$\frac{d\bar{U}^+}{dy^+} = \frac{2.44}{y^+} , \quad (3.44)$$

where the constants are those of Coles (1962). Evaluating (3.43) and (3.44) at $y^+ = 40$ gives $\bar{U}^+ = 14$ and $d\bar{U}^+/dy^+ = 0.061$. The Reynolds stress at y_0^+ (scaled with the stress at $y = y_0$) is also set at 0.939, since $\overline{u^+v^+} = 1 - d\bar{U}^+/dy^+$ in a nonaccelerated boundary layer. To satisfy these relations, the model parameters were changed in the following manner:

E_{V1} from 0.75 to 0.70

E_{W1} from 0.40 to 0.37

ϕ_{U2} from 194.4° to 196° .

Table 3.1 lists all the parameter values used in this study that are assumed independent of acceleration.

Table 3.1
Constant Parameter Values

Component	E_1	ϕ_1	ϕ_2
u	0.15	216	196
v	0.70	36	90
w	0.37	0	270

The other model parameters depend on the shear stress at y_0^+ or, equivalently, the level of acceleration in the turbulent boundary layer.

E. Numerical Scheme

All the computations performed in this work were done on a Floating Point Systems 164 Attached Array Processor using a Vax-11/780 computer as a host. The FPS-164 uses a 64-bit data word which provides 15 decimal digit accuracy. A listing of the computer program is given in Appendix II.

1. Numerical Solution of the v,w Equations

Acceleration of the flow does not directly affect the numerical solution of the v,w momentum equations, (3.17) and (3.18), because all derivatives in the streamwise direction are assumed negligible. The mean normal velocity that results from acceleration is also assumed negligible since it is at least an order of magnitude less than the intensity of the normal velocity fluctuations. Thus, the alternating direction implicit (ADI) scheme used by Nikolaides (1984) to solve the (ζ, ψ) field of a nonaccelerated flow is used for all the flows studied in this work. The main advantage in using the ADI-scheme is its unconditional stability with respect to the selection of the time step [Roache (1982)].

The discretization of (3.6) and (3.7) results in the following finite difference approximation for the vorticity-stream function formulation:

$$\frac{\zeta_{i,j}^{n+\frac{1}{2}} - \zeta_{i,j}^n}{(\Delta t/2)} = - \left(\frac{(w\zeta)_{i+1,j}^{n+\frac{1}{2}} - (w\zeta)_{i-1,j}^{n+\frac{1}{2}}}{2\Delta z} \right) - \left(\frac{(v\zeta)_{i,j+1}^n - (v\zeta)_{i,j-1}^n}{2\Delta y} \right)$$

$$+ \frac{1}{Re} \left[\frac{\zeta_{i+1,j}^{n+\frac{1}{2}} - 2\zeta_{i,j}^{n+\frac{1}{2}} + \zeta_{i-1,j}^{n+\frac{1}{2}}}{\Delta z^2} + \frac{\zeta_{i,j+1}^n - 2\zeta_{i,j}^n + \zeta_{i,j-1}^n}{\Delta y^2} \right] \quad (3.45)$$

$$\begin{aligned} \frac{\zeta_{i,j}^{n+1} - \zeta_{i,j}^{n+\frac{1}{2}}}{(\Delta t/2)} &= - \left(\frac{(w\zeta)_{i+1,j}^{n+\frac{1}{2}} - (w\zeta)_{i-1,j}^{n+\frac{1}{2}}}{2\Delta z} \right) - \left(\frac{(v\zeta)_{i,j+1}^{n+1} - (v\zeta)_{i,j-1}^{n+1}}{2\Delta y} \right) \\ &+ \frac{1}{Re} \left[\frac{\zeta_{i+1,j}^{n+\frac{1}{2}} - 2\zeta_{i,j}^{n+\frac{1}{2}} + \zeta_{i-1,j}^{n+\frac{1}{2}}}{\Delta z^2} + \frac{\zeta_{i,j+1}^{n+1} - 2\zeta_{i,j}^{n+1} + \zeta_{i,j-1}^{n+1}}{\Delta y^2} \right] \end{aligned} \quad (3.46)$$

and

$$\frac{\Psi_{i+1,j}^{n+1} - 2\Psi_{i,j}^{n+1} + \Psi_{i-1,j}^{n+1}}{\Delta z^2} + \frac{\Psi_{i,j+1}^{n+1} - 2\Psi_{i,j}^{n+1} + \Psi_{i,j-1}^{n+1}}{\Delta y^2} = \zeta_{i,j}^{n+1}. \quad (3.47)$$

Equation (3.45) is solved for $\zeta_{i,j}^{n+\frac{1}{2}}$ and subsequently $\zeta_{i,j}^{n+1}$ is obtained from (3.46). Then, (3.47) is inverted to give $\Psi_{i,j}^{n+1}$. The values for the velocities $w_{i,j}^{n+\frac{1}{2}}, v_{i,j}^{n+1}$ and the values for the boundary vorticities $\zeta_{1,j}^{n+\frac{1}{2}}, \zeta_{M+1,j}^{n+\frac{1}{2}}, \zeta_{i,1}^{n+1}, \zeta_{i,N+1}^{n+1}$ are needed to solve (3.45-3.47) for a given time step. The number of panels in which the computational domain is divided in the z and y directions are given by M and N respectively. Thus, an iterative procedure is used where guessed values for v,w and the boundary vorticity are used in (3.45) and (3.46) to solve for $\zeta_{i,j}^{n+1}$ which are then used in (3.47) to obtain $\Psi_{i,j}^{n+1}$. The guessed values of v,w and the boundary vorticity are recalculated using the new values of $\Psi_{i,j}^{n+1}$ and the process repeated till the criteria $\max \left| (\Psi_{i,j}^{n+1})_{\text{new}} - (\Psi_{i,j}^{n+1})_{\text{old}} \right| \leq 10^{-12}$ is satisfied. The details of the iteration process and numerical scheme used to solve (3.45-3.47) can be found in Nikolaides (1984). Further details

about the general numerical solution of the stream function and vorticity equations in planar flows can be found in Roache (1982).

Acceleration affects the solution of the (Ψ, ζ) field thru the boundary conditions at y_0^+ , (3.17) and (3.18). Recalculating the (Ψ, ζ) field for each acceleration was highly undesirable because it takes up 90% of the CPU time for the whole program. Therefore, a method was devised to use the nonaccelerated (Ψ, ζ) field as input for the solution of the accelerated U field.

The values for v and w at the upper boundary are not affected by changes in λ^+ and T^+ that are caused by an imposed pressure gradient. This is because these parameters are used in ratios with z^+ and t^+ in (3.17) and (3.18). These ratios do not change as long as the number of grid points in all the calculations (accelerated and nonaccelerated) is held constant. However, the parameters that do have an effect on the calculations are the amplitudes of the fluctuations ($\hat{v}_1, \hat{v}_2, \hat{w}_1, \hat{w}_2$). From (3.25), it is seen that these amplitudes scale with $(\tau_0^+)^{\frac{1}{2}}$. Thus, scaling the nonaccelerated (Ψ, ζ) field with $(\tau_0^+)^{\frac{1}{2}}$ should give the same results as a full recalculation. Subsequent tests showed this to be the case. Therefore, the accelerated (Ψ, ζ) field was calculated for all the runs by scaling the nonaccelerated (Ψ, ζ) field by $(\tau_0^+)^{\frac{1}{2}}$.

The main program was rewritten to be able to input or output the Ψ field and the upper boundary and wall vorticity at every time step (It is not necessary to I/O the full ζ field since it can be generated from the Ψ field and boundary ζ .). One run was made to calculate the Ψ field and boundary vorticity. This was then used as input in all the rest of the runs. This resulted in significant savings of CPU time.

2. Numerical Solution of the U Equation

Unlike the v, w field, the U velocity field has to be recalculated for each acceleration because of the additional source term, $d\tau/dy$, and the presence of a significant mean velocity. As discussed earlier in Section 3.I.B, $d\tau/dy$ is used in (3.3) instead of the pressure gradient as a way of accounting for the effects of acceleration on the inertia of the fluid. Directly including the advective terms in (3.3) is not possible since the model neglects streamwise derivatives. Because $\left|\frac{d\tau}{dy}\right| \leq \left|\frac{1}{\rho} \frac{dP}{dx}\right|$, the inclusion of these terms will always result in a dampening of the effect of the imposed pressure gradient on the boundary layer. From (3.16), $d\tau/dy$ is seen to be only a function of the distance from the wall, $d\tau/dy = f(t, z)$, and, thus, is relatively easy to incorporate into the solution scheme of Nikolaides (1984).

Equation (3.3) is discretized in time and space using two half-steps as is standard in the ADI-scheme:

$$\frac{U_{i,j}^{n+\frac{1}{2}} - U_{i,j}^n}{(\Delta t/2)} + \left(\frac{(wU)_{i+1,j}^{n+\frac{1}{2}} - (wU)_{i-1,j}^{n+\frac{1}{2}}}{2\Delta z} \right) + \left(\frac{(vU)_{i,j+1}^n - (vU)_{i,j-1}^n}{2\Delta y} \right) = - \left(\frac{d\tau}{dy} \right)_j + \frac{1}{Re} \left[\frac{U_{i+1,j}^{n+\frac{1}{2}} - 2U_{i,j}^{n+\frac{1}{2}} + U_{i-1,j}^{n+\frac{1}{2}}}{\Delta z^2} + \frac{U_{i,j+1}^n - 2U_{i,j}^n + U_{i,j-1}^n}{\Delta y^2} \right] \quad (3.48)$$

$$\frac{U_{i,j}^{n+1} - U_{i,j}^{n+\frac{1}{2}}}{(\Delta t/2)} + \left(\frac{(wU)_{i+1,j}^{n+\frac{1}{2}} - (wU)_{i-1,j}^{n+\frac{1}{2}}}{2\Delta z} \right) + \left(\frac{(vU)_{i,j+1}^{n+1} - (vU)_{i,j-1}^{n+1}}{2\Delta y} \right) = - \left(\frac{d\tau}{dy} \right)_j + \frac{1}{Re} \left[\frac{U_{i+1,j}^{n+\frac{1}{2}} - 2U_{i,j}^{n+\frac{1}{2}} + U_{i-1,j}^{n+\frac{1}{2}}}{\Delta z^2} + \frac{U_{i,j+1}^{n+1} - 2U_{i,j}^{n+1} + U_{i,j-1}^{n+1}}{\Delta y^2} \right] \quad (3.49)$$

where i, j are the indices in the z and y directions respectively. Equation (3.48) is solved for $U_{i,j}^{n+\frac{1}{2}}$ and then $U_{i,j}^{n+1}$ is obtained from (3.49). Each

equation is solved by inverting tridiagonal matrices. The IMSL subroutine LEQT1B was used to perform the inversion. It can be shown that the computational effort at a given time step involves the solution of $(M-1) + (N-1)$ tridiagonal matrices where $M-1$ and $N-1$ are the number of interior points in the z and y directions respectively. For more details on the numerical solution of the U equation, see Nikolaides (1984).

3. Solution Scheme

The solution scheme of the program can be organized in either of two ways, depending upon whether information at a specific P_{eo}^+ or P^+ is desired. These two parameters are related thru (3.15), which requires a knowledge of the mean velocity profile. The solution is iterative because $U^+(y^+)$ depends on the value of P^+ or P_{eo}^+ . Specification of P_{eo}^+ sets τ_0^+ and all the other scaling parameters so that the only quantities that change from cycle to cycle are P^+ and $\bar{U}(y^+)$. Fixing P^+ does not specify any other parameter because τ_0^+ will vary from cycle to cycle. Because of this variation the number of cycles needed to reach steady state (invariant statistics when averaged over a cycle equal in time to T_2^+) is higher than when P_{eo}^+ is specified. However, specifying P^+ enables easy comparison with the literature which is always reported at a fixed P^+ or K and not P_{eo}^+ . Due to the savings in CPU time, it was decided to organize the program on the basis of knowing P_{eo}^+ .

There are two real values of y_0^+ for every negative value of P_{eo}^+ , as shown in Figure 3.1. This could present a problem near the inflection point where the location of the two solutions are very close to each other. Therefore, it was decided to specify y_0^+ and to obtain P_{eo}^+ from

$$P_{eo}^+ = \frac{(y_0^0)^2}{(y_0^+)^3} - \frac{1}{y_0^+}, \quad (3.50)$$

which is a rearrangement of (3.40). For a given y_0^+ there is only one Pe_0^+ value and the ambiguity is no longer a problem. From (3.14) τ_0^+ can be obtained which in turn specifies all the other scaling parameters since they are only functions of τ_0^+ .

The iterative process that is used in the program is as follows: P^+ is guessed and the initial $\bar{U}(y^+)$ is generated using the modified van Driest mixing length of Loyd et. al. (1970) where the constant A^+ is adjusted such that (3.15) is satisfied at y_0^+ . Once $\bar{U}^+(y^+)$ is known, $d\tau^+/dy^+$ is calculated at each y^+ location using (3.16). The program is then run for one time cycle equal to T_2^+ . The calculated U field is the solution of (3.3). However, this solution multiplied by a constant is also a solution since (3.3) is a linear equation. The correct solution must also satisfy the Couette flow relation,

$$\bar{U}_c^+ = y^+ + P^+ y^{+2}/2 , \quad (3.51)$$

near the wall. Therefore, the calculated U field is scaled so that the \bar{U} velocity at the grid point closest to the wall satisfies the Couette flow relation. A new P^+ is then calculated from (3.15) and the process is repeated till P^+ is constant from one cycle to the next. After this criterion is met, the flow is assumed to have reached steady state and the statistics are calculated and stored over the next cycle.

A parameter in all the calculations that has to come from experimental data is the skin-friction coefficient, $C_f/2$. The value chosen for $C_f/2$ directly affects the calculations since the new P^+ value is calculated from (3.15) which contains $C_f/2$. Fortunately, the experimental data for asymptotic boundary layers under the influence of a strong favorable pressure gradient indicate that $C_f/2$ is a constant independent of the imposed pressure gradient. The data of several researchers are shown in Figure 3.3. It is seen that for K values greater than 1.5×10^{-6} (pressure

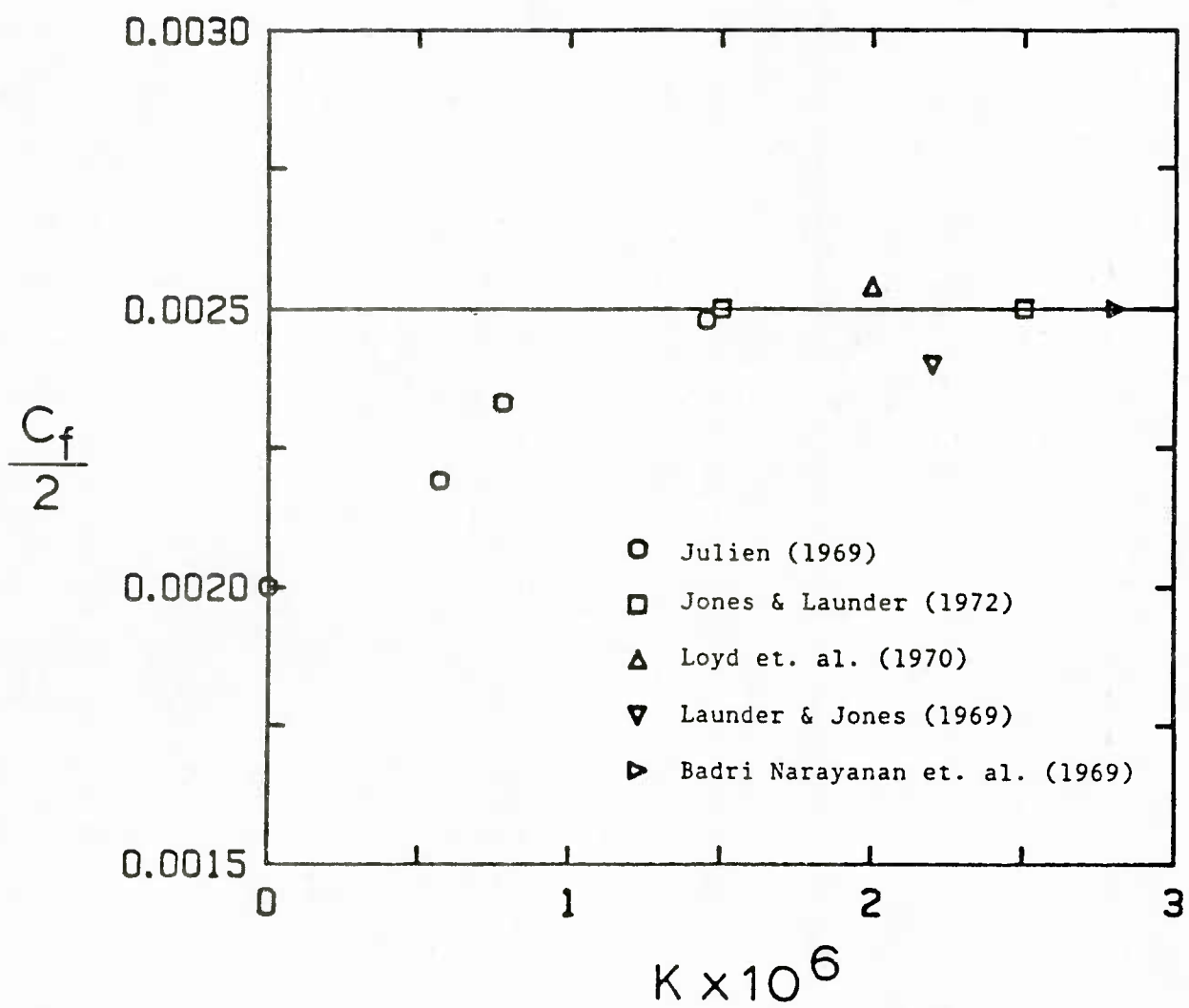


Figure 3.3 The skin-friction coefficient data of several investigators.

gradients less than -0.012) $C_f/2$ is constant and equal to 0.0025. Jones and Launder (1972) arrived at the same conclusion and noted that this value is practically the same as that suggested by Coles (1962) as the maximum attainable in nonaccelerated boundary layers. Stronger accelerations than about $K = 2.8 \times 10^{-6}$ causes relaminarization of the boundary layer which results in a drop of $C_f/2$ to the accelerated laminar value which can be determined analytically as [Launder and Stinchcombe (1967)]

$$C_f/2 = 1.155 (K)^{1/2} . \quad (3.52)$$

For example an accelerated boundary layer with $K = 2.8 \times 10^{-6}$ that is undergoing relaminarization will have its skin-friction coefficient decrease from 0.0025 to 0.00193. Therefore, as seen in Figure 3.3, a turbulent boundary layer will have an increase in drag till relaminarization causes a decrease in drag. Only strongly accelerated boundary layers that have not relaminarized are studied in this work. In this range of P^+ , $C_f/2$ is known without question to be equal to 0.0025.

The time step used for the calculation and storage of the v, w field was $\Delta t^+ = 0.333$. The time step for the calculation of the U field varied from 4 to 10 depending on how close the solution was to steady state with the higher value being used for the first few cycles and the lower value during the last few cycles. The statistics were generally calculated at $\Delta t^+ = 4$ since test runs comparing the fourth-order moments using Δt^+ equal to 0.333 and 4 were identical to five significant figures. These relatively large time steps are possible because the v, w field used in the U field calculation was generated with the more accurate time step of 0.333.

To test the spatial resolution of the program, the number of grid points in the y -direction was increased from 51 to 101 and from 101 to 201 in the z -direction. The nonaccelerated flow was then calculated for both

meshes and the fourth order moments were found to be equivalent to six significant figures. This result indicates that a mesh size of 51,101 is adequate for resolving the flow field and, therefore, all the rest of the runs were done at this mesh size.

II. Eddy Viscosity Model of Turbulent Pulsating Pipe Flow

This section describes the turbulent pulsating pipe flow eddy viscosity models that were developed to explain the experimental wall shear stress data. These models are similar to those used by Mao and Hanratty (1986) to describe their data at high ω^+ . However, there are some major differences: 1) The assumption of plug flow in the center of the pipe was relaxed in order to expand the range of validity of the models. 2) A relation developed by Cess (1958) for the eddy viscosity profile was used to provide a continuous and analytic transition between the inner and outer regions of the flow. 3) The numerical code was rewritten to handle a nonlinear behavior.

A. Triple Decomposition and the Phase Average

In steady turbulent flow, variables can be decomposed into time mean values and turbulent fluctuations. When an organized unsteadiness is imposed on the system, this additional component, which is a deterministic function of time, has to be included. Following Hussain and Reynolds (1970), variables are decomposed into three components:

$$E(\underline{x}, t) = \bar{E}(\underline{x}) + \tilde{e}(\underline{x}, t) + e(\underline{x}, t) \quad (3.53)$$

where $\bar{E}(\underline{x})$ is the time mean value of $E(\underline{x}, t)$ at a given location \underline{x} , $\tilde{e}(\underline{x}, t)$, the organized response component due to the imposed excitation and $e(\underline{x}, t)$, the turbulent fluctuation.

In order to separate the three components of a flow variable, two different averaging procedures are employed, a time average and a phase average. The time average is conventionally used in steady turbulent studies, and is defined as

$$\bar{E}(\underline{x}) = \lim_{T \rightarrow \infty} \frac{1}{T} \int_0^T E(\underline{x}, t) dt . \quad (3.54)$$

In discrete form, the time average is the average of a large number of samples in a record of sufficiently long duration. That is

$$\bar{E}(\underline{x}) = \lim_{N \rightarrow \infty} \frac{1}{N} \sum_{i=1}^N E(\underline{x}, t_i) , \quad (3.55)$$

where i identifies a particular sample and N is the total number of samples. In practice, the total time duration in which all the samples are taken is large compared to the imposed pulsation period and the longest turbulent fluctuation period.

The phase average is defined as the average of samples from a large number of cycles at a fixed cycle angle,

$$\langle E(\underline{x}, \theta) \rangle = \lim_{N \rightarrow \infty} \frac{1}{N} \sum_{n=0}^{N-1} E(\underline{x}, \theta + 2\pi n) , \quad 0 \leq \theta \leq 2\pi . \quad (3.56)$$

where θ is the cycle phase angle. In practice, N is a large finite number.

By definition, phase averaging eliminates the term involving random turbulent fluctuations, namely,

$$\langle E(\underline{x}, \theta) \rangle = \bar{E}(\underline{x}) + \tilde{e}(\underline{x}, \theta) , \quad (3.57)$$

and the time average of $\langle E(\underline{x}, \theta) \rangle$ eliminates the pulsating component,

$$\overline{\langle E(\underline{x}, \theta) \rangle} = \bar{E}(\underline{x}) . \quad (3.58)$$

From the above expressions, the pulsating component and the turbulent fluctuations can be extracted from the flow variable as

$$\tilde{e}(\underline{x}, t) = \langle E(\underline{x}, t) \rangle - \bar{E}(\underline{x}) , \quad (3.59)$$

and

$$e(\underline{x}, t) = E(\underline{x}, t) - \langle E(\underline{x}, t) \rangle . \quad (3.60)$$

B. Governing Equations for Turbulent Pipe Flow

If the flow in a circular pipe is fully developed and symmetric in the angular direction, the phase averaged Navier-Stokes equations for an incompressible flow of a Newtonian fluid simplify to

$$\rho \frac{\partial \langle u \rangle}{\partial t} = - \frac{\partial \langle p \rangle}{\partial x} - \frac{1}{r} \frac{\partial}{\partial r} (r \langle \tau(t) \rangle) + \frac{\mu}{r} \frac{\partial}{\partial r} \left(\frac{r \partial \langle u \rangle}{\partial r} \right) , \quad (3.61)$$

where $\langle \tau(t) \rangle = -\rho \langle uv \rangle$ is the phase averaged Reynolds stress and r is the distance from the center of the pipe.

To solve this equation, the Reynolds stress has to be specified in terms of the mean velocity and r . Following Boussinesq (1877), a turbulent eddy viscosity, which relates the Reynolds stress to the velocity gradient by an analogy with Newton's law of viscosity, is defined in order to close (3.61). Thus, the phase averaged Reynolds stress is written as

$$\langle \tau(t) \rangle = \rho \langle v_t \frac{\partial u}{\partial y} \rangle . \quad (3.62)$$

An empirical equation proposed by Cess (1958) is used to describe the radial variation of the eddy viscosity,

$$\frac{\langle \nu_T \rangle}{\nu} = \frac{1}{2} \left\{ -1 + \left[1 + \left(\frac{2\kappa y (\tau_w/\rho)^{1/2}}{3\nu} \right)^2 \left(1 - \frac{y^+}{2r_0^+} \right)^2 \left(3 - 4\frac{y^+}{r_0^+} + 2\frac{y^{+2}}{r_0^{+2}} \right)^2 \right. \right. \\ \left. \left. \left(1 - \exp \left[- \frac{y(\tau_w/\rho)^{1/2}}{A^+ \nu} \right] \right)^2 \right]^{1/2} \right\}. \quad (3.63)$$

where r_0 is the radius of the pipe. The van Driest parameter, A^+ , is a measure of the thickness of the viscous wall region. The Cess expression is a combination of van Driest's (1957) mixing length wall region law,

$$\frac{\langle \nu_T \rangle}{\nu} = \frac{1}{2} \left\{ -1 + \left[1 + \left(\frac{2\kappa y (\tau/\rho)^{1/2}}{\nu} \right)^2 \left(1 - \exp \left[- \frac{y(\tau_w/\rho)^{1/2}}{A^+ \nu} \right] \right)^2 \right]^{1/2} \right\}, \quad (3.64)$$

and Reichardt's (1951) middle law,

$$\frac{\langle \nu_T \rangle}{\nu} = \left(\frac{\kappa y (\tau_w/\rho)^{1/2}}{3\nu} \right) \left(1 - \frac{y^+}{2r_0^+} \right) \left(3 - 4\frac{y^+}{r_0^+} + 2\frac{y^{+2}}{r_0^{+2}} \right). \quad (3.65)$$

where $\kappa = 0.41$ and $A^+ = 26$. Figure 3.4 shows the eddy viscosity profiles generated by (3.63) for the case of steady flow in a two in. pipe at a $Re = 50,000$. As seen in Figure 3.4, the main advantage of the Cess profile is that it provides a continuous and analytic transition between the inner and outer regions of the flow.

Patanker and Spalding (1967), Abrams and Hanratty (1985), and Mao and Hanratty (1986) suggest using the local value of the shear stress in the exponent of the van Driest damping function. This change induces a thickening and thinning of the viscous wall region that agrees with experimental data of flows with imposed pressure gradients. Thus, (3.63) was modified to give:

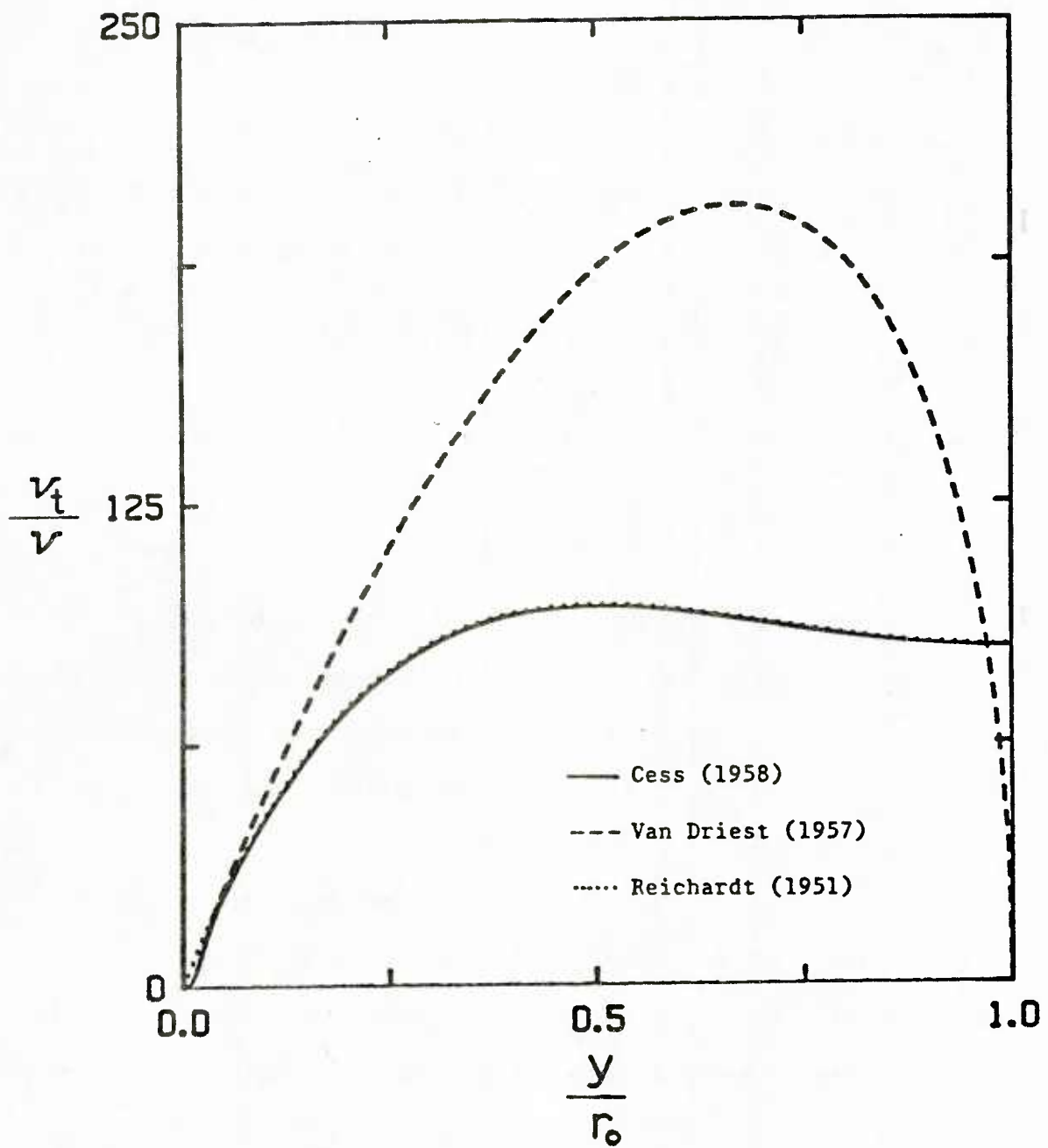


Figure 3.4 Eddy viscosity profiles for various models
($r_o = 2"$, $Re = 50,000$)

$$\frac{\langle \nu_T \rangle}{\nu} = \frac{1}{2} \left\{ -1 + \left[1 + \left(\frac{2\kappa y(\tau/\rho)^{1/2}}{3\nu} \right)^2 \left(1 - \frac{y^+}{2r_0^+} \right)^2 \left(3 - 4\frac{y^+}{r_0^+} + 2\frac{y^{+2}}{r_0^{+2}} \right)^2 \right]^{1/2} \left(1 - \exp \left(- \frac{y(\tau/\rho)^{1/2}}{A^+ \nu} \right) \right)^2 \right\}. \quad (3.66)$$

where τ is used from the wall to y_0^+ and τ_0 is used from y_0^+ to the center of the pipe. To be consistent with the van Driest law in the wall region, the leading shear stress (term containing κ in the Cess relation) was also changed to the local shear stress. Equation (3.66) with the local shear stress for all y is represented by the dotted line in Figure 3.5 for a steady flow in a two inch pipe at a $Re = 50,000$. As seen in Figure 3.5, a problem occurs near the center of the pipe where the local value of the shear stress goes to zero (a typical behavior of mixing length theories). This result is inconsistent with measurements that have shown that the eddy viscosity is large and nearly constant in the core region. Therefore, it was decided to use the local shear stress from the wall to y_0^+ and to use τ_0 from y_0^+ to the center of the pipe in this term as well as in the van Driest damping function. This formulation is plotted as the solid line in Figure 3.5. For comparison purposes the dashed line was generated from (3.63). It is seen that using τ_0 from y_0^+ to the center of the pipe has very little effect on the eddy viscosity values, but does eliminate the problem at the center of the pipe.

1. Quasi-laminar Approximation (Model A)

The simplest model for pulsating turbulent pipe flow involves the assumption that the pulsating pressure gradient has no effect on the turbulent Reynolds stresses and that the induced pulsations in the turbulent flow will behave in the same manner as for laminar pulsating flow. This assumption is assumed to be valid for high frequencies where the

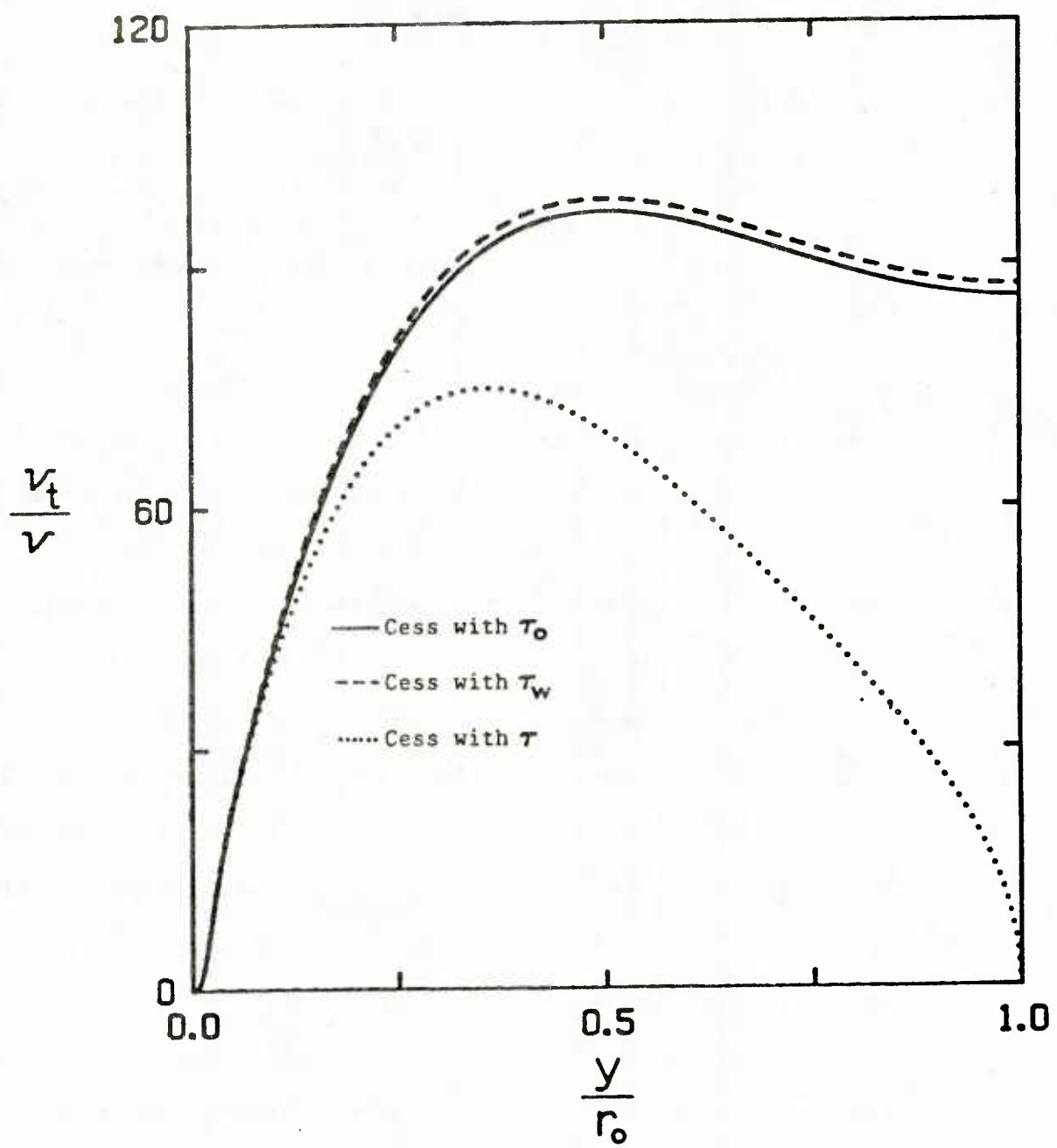


Figure 3.5 Eddy viscosity profiles for the various shear stress formulations ($r_o = 2"$, $Re = 50,000$)

spatial variation of the imposed flow pulsation is confined to a very thin layer near the wall where turbulence has negligible effect. This case has been solved by Sexl (1930) and Uchida (1956) for a sinusoidal pressure gradient,

$$\frac{1}{\rho} \frac{dp}{dx} = \hat{a} \cos(\omega t) , \quad (3.67)$$

where \hat{a} is the amplitude of the imposed pressure gradient and ω is the angular frequency of the pulsation. At high frequencies, $(\omega/\nu)^{1/2}r_0 \gg 1$, the solution is given as

$$\begin{aligned} \tilde{u}(r, t) \approx \frac{\hat{a}}{\omega} & \left[\sin(\omega t - \left(\frac{r_0}{r}\right)^{1/2} \exp\left(-\left(\frac{\omega}{2\nu}\right)^{1/2} (r_0 - r)\right) \right. \\ & \left. \sin\left(\omega t - \left(\frac{\omega}{2\nu}\right)^{1/2} (r_0 - r)\right) \right] . \end{aligned} \quad (3.68)$$

The second term in (3.68) quickly damps out as the distance from the wall, $r_0 - r$, increases and (3.68) simplifies to

$$\tilde{u}(r, t) = \frac{\hat{a}}{\omega} \cos(\omega t - \pi/2) . \quad (3.69)$$

Thus, the pulsating component in the central portion of the pipe behaves as a solid body with an amplitude given by:

$$|\hat{u}_c| = \frac{\hat{a}}{\omega} , \quad (3.70)$$

and the phase of the pulsating velocity lags behind the imposed pressure gradient by 90° .

Only in the Stokes layer close to the wall, of thickness

$$\delta_s = \left(\frac{2\nu}{\omega} \right)^{\frac{1}{2}} , \quad (3.71)$$

does the pulsating velocity vary rapidly with distance from the wall. The velocity gradient at the wall is obtained from (3.68) as

$$\frac{\partial \tilde{u}}{\partial y} \Big|_{y \rightarrow 0} \approx |\hat{u}_c| \left(\frac{\omega}{\nu} \right)^{\frac{1}{2}} \cos(\omega t - \pi/4) . \quad (3.72)$$

Converting to wall units, the following is obtained

$$\tilde{\tau}_w^+ = |\hat{u}_c^+| (\omega^+)^{\frac{1}{2}} \cos(\omega^+ t^+ - \pi/4) . \quad (3.73)$$

From (3.69) and (3.73), it is seen that the oscillating shear stress at the wall leads the center velocity by 45° and lags the pulsating pressure gradient by 45° . If the amplitude of the variation of the wall shear stress scale in the following manner (as suggested by (3.73)):

$$\frac{|\hat{\tau}_w^+|}{|\hat{u}_c^+|} = (\omega^+)^{\frac{1}{2}} . \quad (3.74)$$

It is noted that $|\hat{\tau}_w^+|/|\hat{u}_c^+|$ is independent of the amplitude of the imposed pressure gradient and depends upon ω^+ to the one-half power.

2. Quasi-steady Approximation (Model C)

For the case of very low frequencies a pseudo-steady approximation can be made whereby the relation between the instantaneous wall shear stress and the instantaneous center line velocity is the same as for a steady flow. Mao and Hanratty (1986) have shown that making this assumption gives the following relation:

$$\frac{|\hat{\tau}_w^+|}{|\hat{u}_c^+|} = (2 - n) \left(\frac{f}{2} \right)^{\frac{1}{2}} , \quad (3.75)$$

where

$$f = A \left(\frac{2r_0 U_c}{\nu} \right)^{-n}. \quad (3.76)$$

If the Blasius friction law is used, then (3.75) becomes

$$\frac{|\hat{\tau}_w^+|}{|\hat{u}_c^+|} = 0.339 Re^{-0.125}. \quad (3.77)$$

For Reynolds numbers between 10,000 and 50,000, this ratio is approximately equal to 0.095. Equation (3.75) is useful in that it provides a rough estimate of the amplitude variation at very low frequencies which can be used to check numerical models of turbulent pulsating pipe flow.

One such model is the quasi-steady model (called Model C) used by Thorsness et. al. (1978) and Abrams and Hanratty (1985) to describe flow over wavy surfaces and modified by Mao and Hanratty (1986) to describe pulsating pipe flow. This model assumes that the turbulent shear stress responds instantaneously to the velocity gradient and eddy viscosity as dictated by (3.61), (3.62) and (3.66). Therefore, the solution of these equations constitutes Model C.

3. Relaxation Approximation (Model D)

As previously noted strong steady favorable and unfavorable pressure gradients have been found, respectively, to dampen and to enhance turbulence in the viscous wall region. A number of investigators [Launder and Jones (1969), Cebeci and Smith (1974), Julien et. al. (1969), Loyd et. al. (1970)] have argued that this behavior causes the thickness of the viscous wall region to increase in favorable pressure gradients and to decrease in unfavorable pressure gradients. They represented this effect by allowing A^+ to be a function of P^+ . For small P^+ , it was found that

$$A^+ = \bar{A}^+(1 + k_1 P^+ + k_2 P^{+2} + \dots) \quad (3.78)$$

with $k_1 \approx -30$ and $k_2 \approx 1,540$. This predicts that A^+ increases for increasing negative values of P^+ and decreases with increasing positive values.

For situations in which the pressure gradient is varying rapidly in the flow direction, Launder and Jones (1969), Julien et. al. (1969), and Loyd et. al. (1970), have proposed a first order lag equation whereby the flow close to the wall sees an effective pressure gradient given by the equation

$$\frac{dP_{eff}^+}{dx^+} = \frac{P^+ - P_{eff}^+}{k_r}, \quad (3.79)$$

where k_r is a relaxation constant approximately equal to 3000. Alternative approaches have been tried where the entire Reynolds stress was relaxed [Shemer and Wygnaski (1981), Abrams (1984)] and where the entire van Driest damping function was relaxed [Abrams and Hanratty (1985)]. No significant difference was noted in results obtained from these approaches.

Mao and Hanratty (1986) applied this concept to pulsating flow where the pressure gradient is varying with time rather than space. A direct application of (3.79) to this case requires the definition of a convection velocity which characterizes the streamwise propagation of disturbances in the viscous wall region to relate spatial variations to time variations. Therefore, a convection velocity equal to 15 was chosen to take this effect into account. Equation (3.79) is then rewritten as

$$\frac{dP_{eff}^+}{dt^+} = \frac{P^+ - P_{eff}^+}{(k_r/15)}. \quad (3.80)$$

Thus, Model D introduces a lag between the imposed pressure gradient and the change of scale in the viscous wall region.

C. Numerical Scheme

Equations (3.61), (3.62), (3.66) were numerically solved by a forward-in-time, central-difference explicit scheme with variable grid size. Since the pulsating velocity changes rapidly in the wall region and the final goal of the calculations is to find the velocity gradient at the wall, it is necessary to use a very small grid size close to the wall. Grid sizes which are increasing in a geometric series of y^+ were chosen:

$$y_j^+ = \frac{\Delta y_1^+ (H^{j-1} - 1)}{(H - 1)}, \quad 1 < j \leq J, \quad (3.81)$$

where Δy_1^+ is the first grid size near the wall, and H is the ratio of two consecutive grid sizes.

The first grid size Δy_1^+ was selected small enough so that the velocity gradient at the wall can be calculated by assuming a linear variation of the velocity. After several tries, Δy_1^+ was taken to be equal to 1/25 of the Stokes thickness. The last grid size in the center of the pipe was always set to 10 wall units. Thus, the ratio H was determined from

$$H = \left(\frac{\Delta y_C^+}{\Delta y_1^+} \right)^{(1/J)}. \quad (3.82)$$

Figure 3.6 displays the grid spacing for a run with $\Delta y_1^+ = 0.1$, $\Delta y_C^+ = 10.0$, $H = 1.05$ and $J = 95$.

The quasi-laminar solution was used to start the program. By trial and error, it was determined that Δt^+ had to be at least 2π less than Δy_1^+ in order for the program to converge. The program was run until the wall shear stress at the beginning of the pulsation cycle was constant from one cycle to the next. After convergence, the program ran for one more cycle to determine the phase averages. A listing of the program can be found in Appendix III.

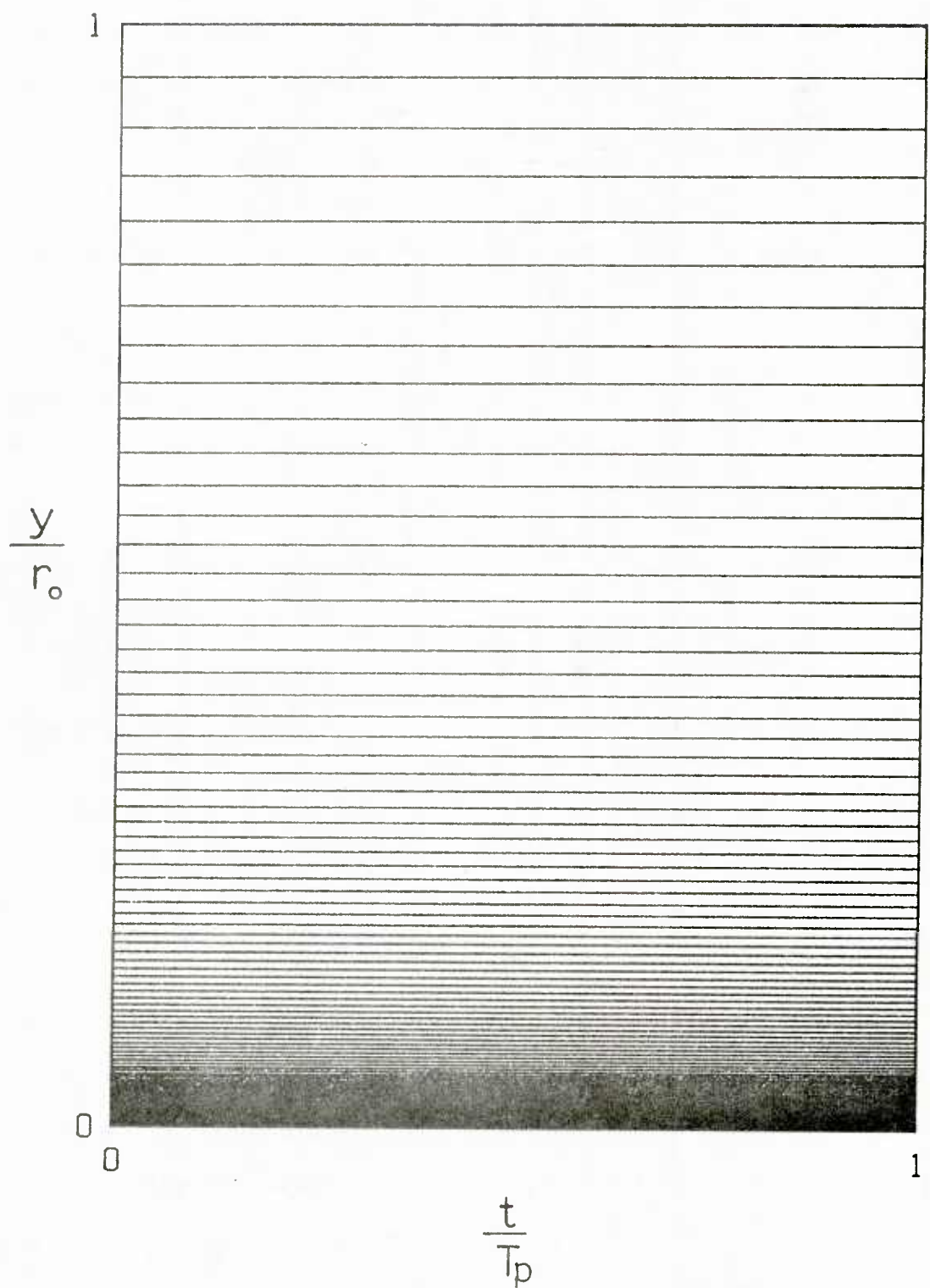


Figure 3.6 Sample finite difference grid

CHAPTER 4. DESCRIPTION OF EXPERIMENTS

This chapter describes the electrochemical technique and experimental equipment that were used to make measurements of the velocity gradient at the wall in turbulent pulsating pipe flow.

I. Electrochemical Technique

The theory behind the use of the electrochemical technique to measure the velocity gradient at the wall in steady flow is discussed in detail in Hanratty and Campbell (1983). The proper use of the wall probes in turbulent pulsating flow is described in Mao and Hanratty (1985). The contents of these two references are summarized in this section.

A. Electrochemical Cell

The following electrochemical reactions are carried out on the surface of the electrodes:



An aqueous solution of potassium iodide and iodine is used as the electrolyte which supplies the tri-iodide ion, I_3^- , due to the reaction



An excess of potassium iodide is needed to minimize the effect of ionic migration of the reacting ion on the mass flux. The bulk concentration of I_3^- remains constant because the electrode reactions destroy and produce equimolar quantities of I_3^- ions.

The electrochemical cell is shown in Figure 4.1. The area of the cathode, the test electrode, is many times smaller than the area of the

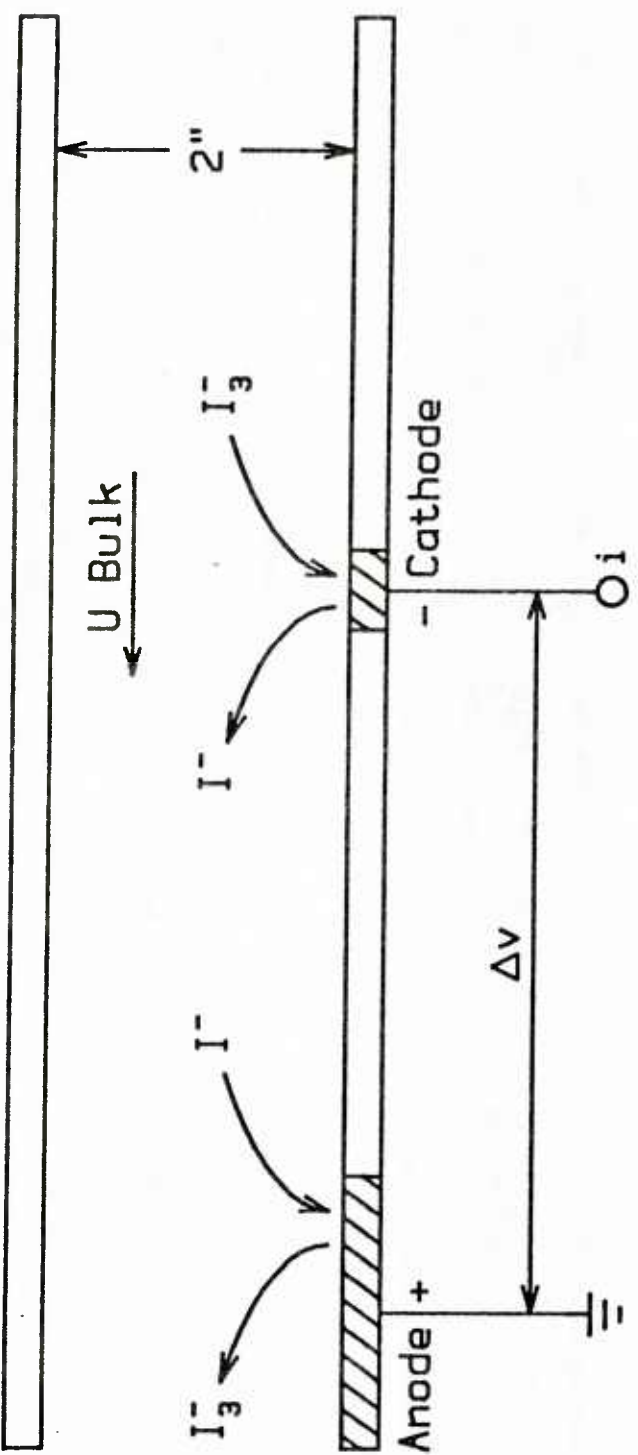


Figure 4.1 The electrochemical cell

anode, which is a large section of piping downstream of the test section. Thus the reaction at the cathode is the step controlling the current flow.

If the voltage applied to the cell is sufficiently high, the electrochemical reaction on the surface of the electrode will proceed at a high enough rate so that the concentration of I_3^- at the surface can be considered as zero. The rate of reaction is then controlled by the rate which I_3^- is transferred to the surface by diffusion or convection.

The flux of mass, N , to the electrode surface can be related to the current flow in the electrochemical cell by

$$N = \frac{I}{2A_e F} , \quad (4.4)$$

where A_e is the surface area of the electrode and F is Faradays constant. A mass transfer coefficient, K , can be defined by

$$K = \frac{N}{C_b - C_w} \quad (4.5)$$

where C_b is the bulk concentration of the reacting species and C_w is the concentration at the surface of the electrode. If the reaction is diffusion controlled, C_w can be considered to be zero. Substituting for N in (4.5) with (4.4), the following is obtained:

$$K = \frac{I}{2C_b A_e F} . \quad (4.6)$$

If the electrode is polarized (diffusion limited) the current flowing through the electrochemical cell is determined by

$$I = \frac{V - V_{app}}{R_f} , \quad (4.7)$$

where V is the output voltage of the electronic circuit, V_{app} is the applied voltage and R_f the feedback resistor. Substituting (4.7) into (4.6), the following is obtained:

$$K = \frac{V - V_{app}}{2C_b A_e F R_f} . \quad (4.8)$$

Therefore, the mass transfer coefficient can be determined from the output voltage of the electronic circuit.

B. Measuring S_x in Steady and Pulsating Flow

In order to use this technique to study turbulence close to the wall, it is necessary to relate the mass transfer coefficient to the flow field. The mass balance equation in the concentration boundary layer can be described as

$$\frac{\partial C}{\partial t} + S_x y \frac{\partial C}{\partial x} = \alpha \frac{\partial^2 C}{\partial y^2} , \quad (4.9)$$

where α is the diffusivity and diffusion in the axial direction has been neglected. In deriving (4.9), Reiss and Hanratty (1963) assumed the concentration boundary layer thickness to be small enough that the effect of velocities normal to the surface could be neglected and that the streamwise velocity was given by

$$U = S_x y . \quad (4.10)$$

The boundary conditions used with (4.9) were the following:

$$C(x, 0, t) = C_w \approx 0 \quad 0 \leq x \leq L \quad (4.11)$$

$$C(x, \infty, t) = C(0, y, t) = C_b \quad (4.12)$$

where L is the effective length of the electrode.

For steady flow or if the flow is changing slowly with time, the first term in (4.9) can be neglected. Mitchell and Hanratty (1966) used this pseudosteady state approximation to obtain the following expression for the mass transfer coefficient:

$$\frac{K L}{D} = 0.807 \left[\frac{S_x L^2}{D} \right]^{1/3}, \quad (4.13)$$

where D is the diameter of the pipe. This relation is used to obtain the velocity gradient at the wall from measured values of K . A more detailed discussion of measurements using electrochemical wall probes can be found in a review article by Hanratty and Campbell (1983).

The pseudosteady state approximation is not expected to be valid for all oscillation frequencies studied in this work. Therefore, the results of Mao and Hanratty (1985), who numerically solved (4.9) using a linearized form of the conservation equation, are used to correct for the frequency response of the concentration boundary layer to the imposed streamwise flow oscillation. The discussion that follows is based on their work.

The mass transfer coefficient can be represented as the sum of an average and time dependent term,

$$K = \bar{K} + k, \quad (4.14)$$

where

$$k = \hat{k} e^{i\omega t} \quad (4.15)$$

and \hat{k} is a complex amplitude equal to

$$\hat{k} = \hat{k}_r + i\hat{k}_i \quad (4.16)$$

The periodic variation of k is characterized by an amplitude,

$$|\hat{k}| = \left[(\hat{k}_r)^2 + (\hat{k}_i)^2 \right]^{\frac{1}{2}} \quad (4.17)$$

and by a phase angle

$$\theta = -\tan^{-1} \left[\frac{\hat{k}_i}{\hat{k}_r} \right], \quad (4.18)$$

where a positive θ means k lags the velocity gradient. Therefore, (4.18) represents the phase correction and

$$A = \frac{\hat{k}_s}{|\hat{k}|} \quad (4.19)$$

represents the amplitude correction that must be applied to the signal coming from a probe, if the pseudosteady state relation (4.13) is used to calculate S_x from the time varying signal.

The numerically calculated results of Mao and Hanratty (1985) are shown in Figures 4.2 and 4.3. It is readily seen from the figures that correction for phase is necessary at lower $\omega^+ Sc^{1/3} L^{+2/3}$ values than it is for the correction of amplitude. Table 4.1 lists the high and low extremes for the amplitude and phase corrections used in this study. As shown in Table 4.1, the maximum phase correction was 17.5 degrees and the maximum amplitude correction was less than 5%.

The following restrictions on L^+ must be met if wall transfer probes are to be properly used in pulsating turbulent flow:

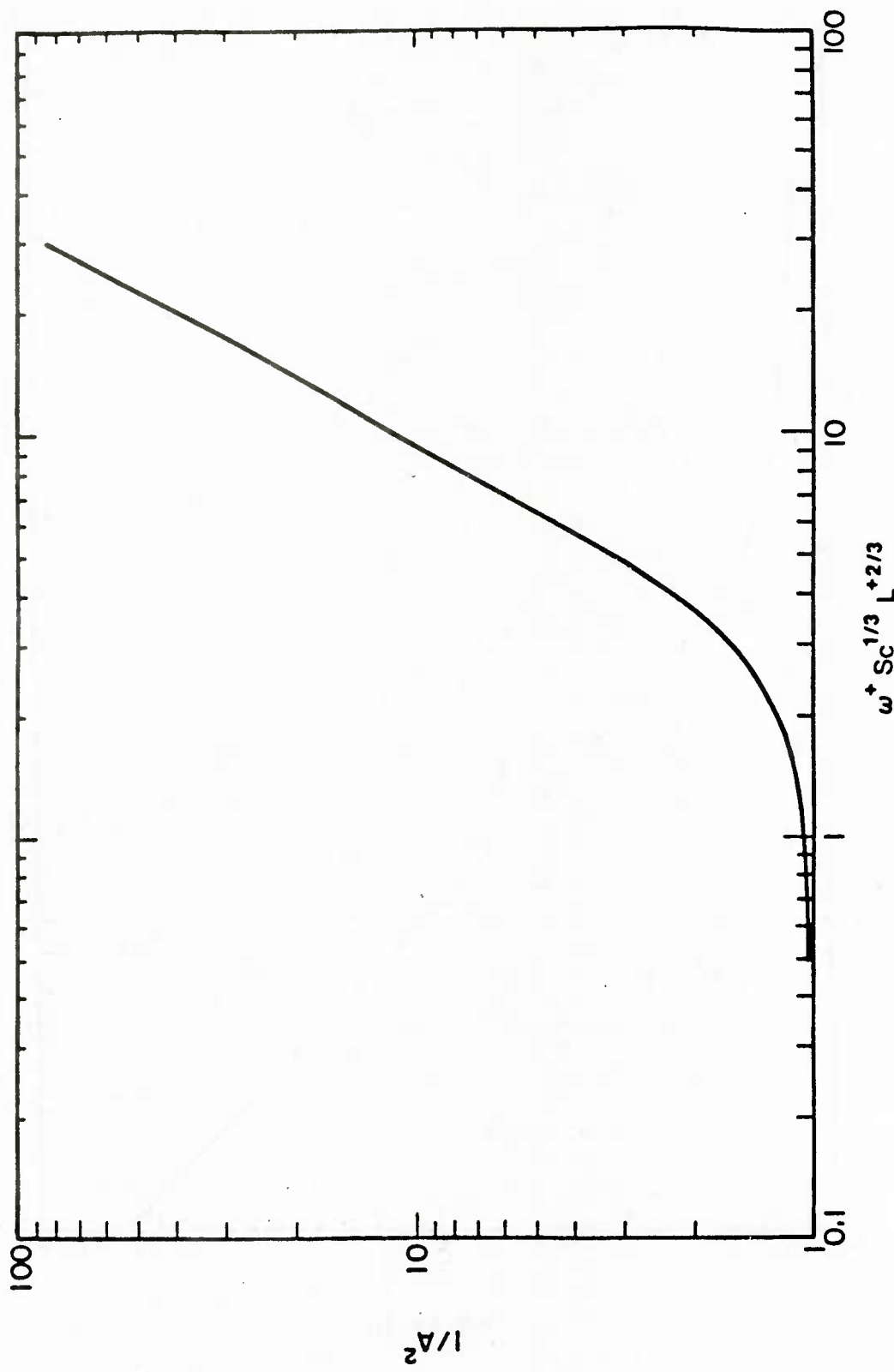


Figure 4.2 Amplitude correction factor for frequency response

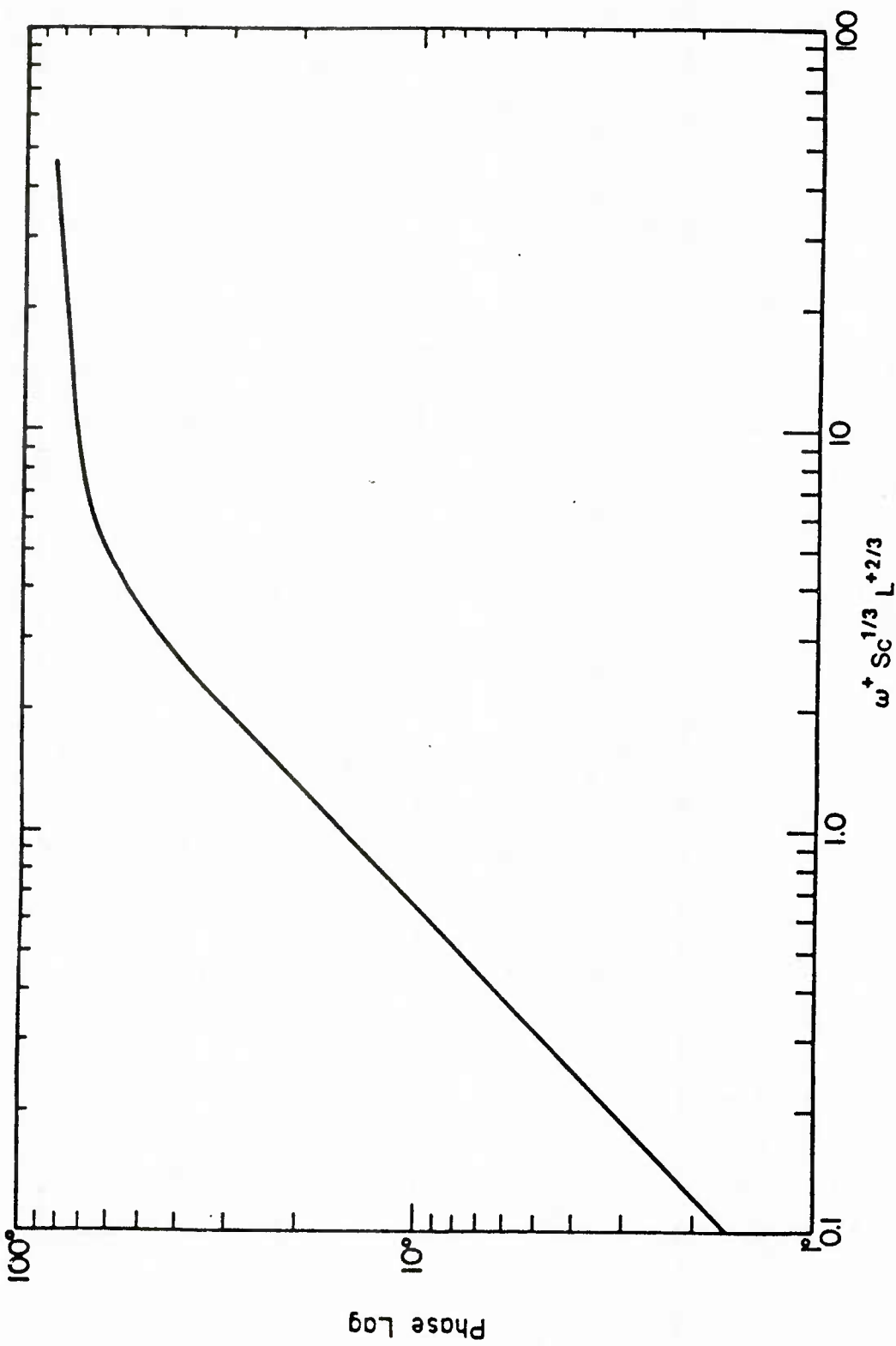


Figure 4.3 Phase lag due to frequency response

$$1) L^+ < 5 Sc \quad (4.20)$$

$$2) L^+ < 0.11 (\omega^+)^{-3/2} Sc \quad (4.21)$$

$$3) L^+ > \frac{14}{Sc^{\frac{1}{2}} \left[1 - \left| \frac{\tau_w}{\tilde{\tau}_w} \right|^{\frac{1}{2}} \right]^{\frac{1}{2}}} \quad (4.22)$$

The requirement that the concentration boundary layer be thinner than the viscous sublayer and the Stokes layer imposes restrictions 1 and 2 on the experimental conditions. Restriction 3 needs to be satisfied if the effects of diffusion in the streamwise direction are to be neglected. Table 4.1 lists the experimental conditions for the lowest and highest values. The limiting restriction is number 3. It requires that an effective electrode length greater than 0.007 cm. be used in the experiments. The numerical calculations of Mao and Hanratty (1985) suggest a maximum value of $L = 0.014$ cm. if the amplitude correction is to be less than 5%. A large electrode (higher current) is desirable in order to minimize the noise content of the signal from the electrode. Therefore, electrodes with $L=0.013$ cm. were used in all the experiments.

Table 4.1
Experimental Range

ω^+	0.0012	0.0912
Re	44900	8650
Sc	850	850
L (cm) = $0.813 D_e$	0.013	0.013
L^+	6.0	1.42
$\omega^+ Sc^{1/3} L^{+2/3}$	0.037	1.09
A	1.00	0.95
θ	0.6	17.5
5 Sc	4250	4250
$0.11 (\omega^+)^{-3/2} Sc$	2,250,000	3400
$\frac{14}{Sc^{\frac{1}{2}} \left[1 - \left \frac{\tau_w}{\tilde{\tau}_w} \right ^{\frac{1}{2}} \right]^{\frac{1}{2}}}$	0.54	0.76

II. Experimental Equipment and Conditions

Experiments were carried out in a two inch pipe flow loop built by the author to measure turbulent pulsating pipe flow. A test section was designed and built to study transverse spatial correlation coefficients of the streamwise velocity fluctuations near a wall using electrochemical wall probes. The flow loop was interfaced with a Digital LSI-11/21 computer to enable digital analysis of the velocity fluctuations.

A. Experimental Flow Loop

The flow loop is shown schematically in Figure 4.4. An electrolyte solution is pumped continuously from the holding tank through the system and returned. The reservoir has a capacity of 225 liters and is constructed of type 316 stainless steel. It is covered with a 1/2 inch thick piece of plexiglass which is painted black to exclude light. Operation of the loop requires a minimum of 170 liters of solution. The temperature of the solution was maintained at 25 ± 0.1 C° by a temperature controller which activates the cooling water solenoid valve to allow laboratory cold water to flow through stainless steel cooling coils in the tank. Two Pall polypropylene filters of either 5 micron or 0.5 micron size were used to remove debris from the solution.

The majority of the flow loop is constructed of one inch 316 stainless steel pipe. A 7 degree diffuser provides a smooth transition from the one inch pipe to the two inch plexiglass tubing. The entrance section to the test section is 340 inches, which is 170 pipe diameters. The length of the entry section is such that fully developed flow is insured in the test section. During the steady state runs (no pulsations) the mean flow was measured by a rotameter (Fisher and Porter, Model FP-2-27-G-10). When pulsations were present in the flow, a volumetric measuring tank was used.

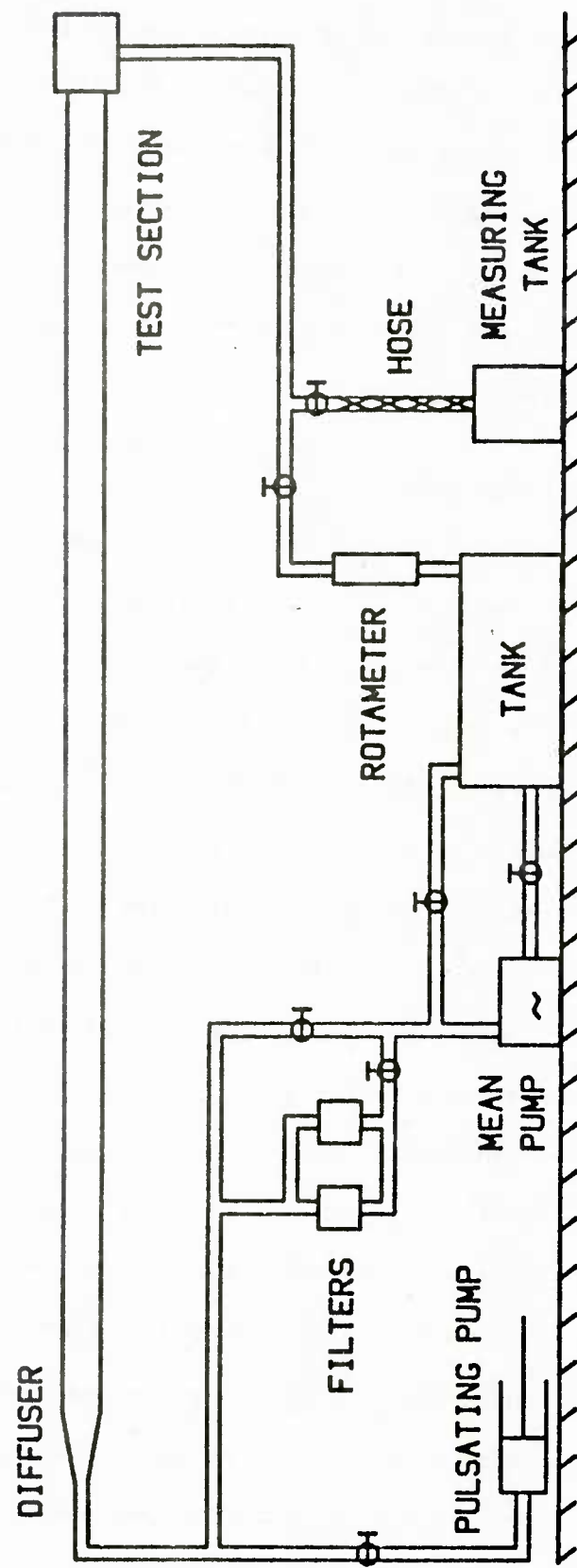


Figure 4.4 Experimental apparatus

The fluid was circulated by a one-stage positive displacement Moyno pump and the pulsation was introduced by a piston with a diameter of 5.08 cm. and a stroke length adjustable from 0 to 10.16 cm.. The frequency of pulsation was changed by adjusting the voltage applied to the D.C. motor responsible for driving the piston. This particular motor was chosen for its superior response time since a study investigating nonsinusoidal pulsations is planned in the future.

B. Test Section Fabrication

A test section was built to measure the transverse correlation coefficients of the streamwise velocity. An array of 15 circular platinum electrodes 0.016 cm. in diameter (34 gauge) were mounted flush with the wall in the transverse direction. The center-to-center distance between each electrodes was 0.0254 cm. and the total distance between electrodes 1 and 15 was 0.3556 cm.. Male-female type joints were used to provide a smooth and continuous connection between the test section and the flow loop.

Preparation of the electrodes for use in the flow loop required several steps. A 0.5 cm. wide, 0.7 cm. long groove was milled into the test section in the transverse direction. The groove was cut about two-thirds through the plexiglass wall, leaving only a 2/5 cm. distance to be drilled with a 0.02 cm. drill. The drilled holes were only 0.004 cm. larger in diameter than the 34 gauge platinum wires. The leads of the platinum wires were soldered to copper wires and sprayed with electrical insulation.

After the spray dried, the platinum wire was inserted through the drilled hole and a small drop of Techkits A-12 epoxy was placed on the wire on both sides of the pipe wall. The wire was then drawn back and forth through the hole to fill the cavity with epoxy. Excess epoxy was added to the groove to fill it and provide support for the electrode wires. The

epoxy was then cured overnight at room temperature.

A small-toothed file was used to remove excess epoxy and exposed wire from the inside of the pipe. Care was taken to avoid defacing the plexiglass pipe wall. Sanding of the electrode surface was done with progressively finer grades of wetted emery paper. Polishing paper of grade 4.0 was used to finish the sanding process. Final polishing was done using Mirror Glaze Plastic Cleaner and Polish on a soft rag. This sanding and polishing procedure produced circular electrodes without deformation of the pipe wall.

C. Differential Pressure Measurement

Determination of the amplitude and phase of the pulsating pressure gradient served as a standard for characterizing the imposed flow pulsation. Careful measurements of the time varying pressure gradient were necessary since only part of the flow pulsation from the pulsating pump travelled downstream to the test section. The variation of the centerline velocity was determined by using (2.10) and the pressure gradient measurements. The phase of the pressure gradient was also used as a reference to determine the phase lag of the wall shear stress.

Two differential pressure transducers were used in this study. For low frequencies of pulsation, a Viatran differential pressure transmitter (Model 704-115, 5 inches water column) was used. Because of its superior frequency response, a C.J. Enterprises differential pressure transmitter (Model CJVR, 2.5 inches water column) was used for frequencies above 0.6 Hz. To eliminate any high frequency noise or vibration that the C.J. Enterprises transmitter may sense, a Wavetek Rockland filter (Model 432) was used to low-pass filter the differential pressure signal.

Calibration of the frequency response of the transmitters was necessary

since both exhibited response delays at high frequencies. The calibration procedure was as follows: The flow loop was filled with solution and the valves upstream of the pump were closed in order to force all of the flow pulsation downstream to the test section. Because of the incompressibility of the fluid, the motion in the test section was in phase with the piston and the amplitude of the pressure gradient variation could be calculated from the piston stroke length and frequency. Several frequencies and amplitudes of pulsation were tested. Figures 4.5(a) and 4.5(b) are for the Viatran transmitter and Figures 4.6(a) and 4.6(b) are for the C.J. Enterprises transmitter. As shown in Figures 4.5(a) and 4.6(a), the calculated amplitudes when compared to the measured amplitudes gave a straight line passing through zero. This result indicates that the amplitude response of the transmitters is flat for all the frequencies used in this study. It was found that the phase lag of the transmitters was frequency dependent as shown in Figures 4.5(b) and 4.6(b). The response of the C.J. Enterprises transmitter was found to depend on the cut-off frequency of the filter. This variation was eliminated by scaling the pulsation frequency with the filter cut-off frequency. Using these calibration curves, the differential pressure measurements were used as the standard for characterizing the imposed flow pulsations.

D. Data Acquisition and Processing

The basic electrode circuit is shown in Figure 4.7. An 118A amplifier was used to apply a negative potential (-0.4 volts) to the electrode and to act as a current-to-voltage converter. The applied potential was set to the desired level by adjusting the 1K helipot. The magnitude of the current flow is a function of the size of the electrode, the concentration of the KI-I₂ solution and the Reynolds number. In this study, the feedback

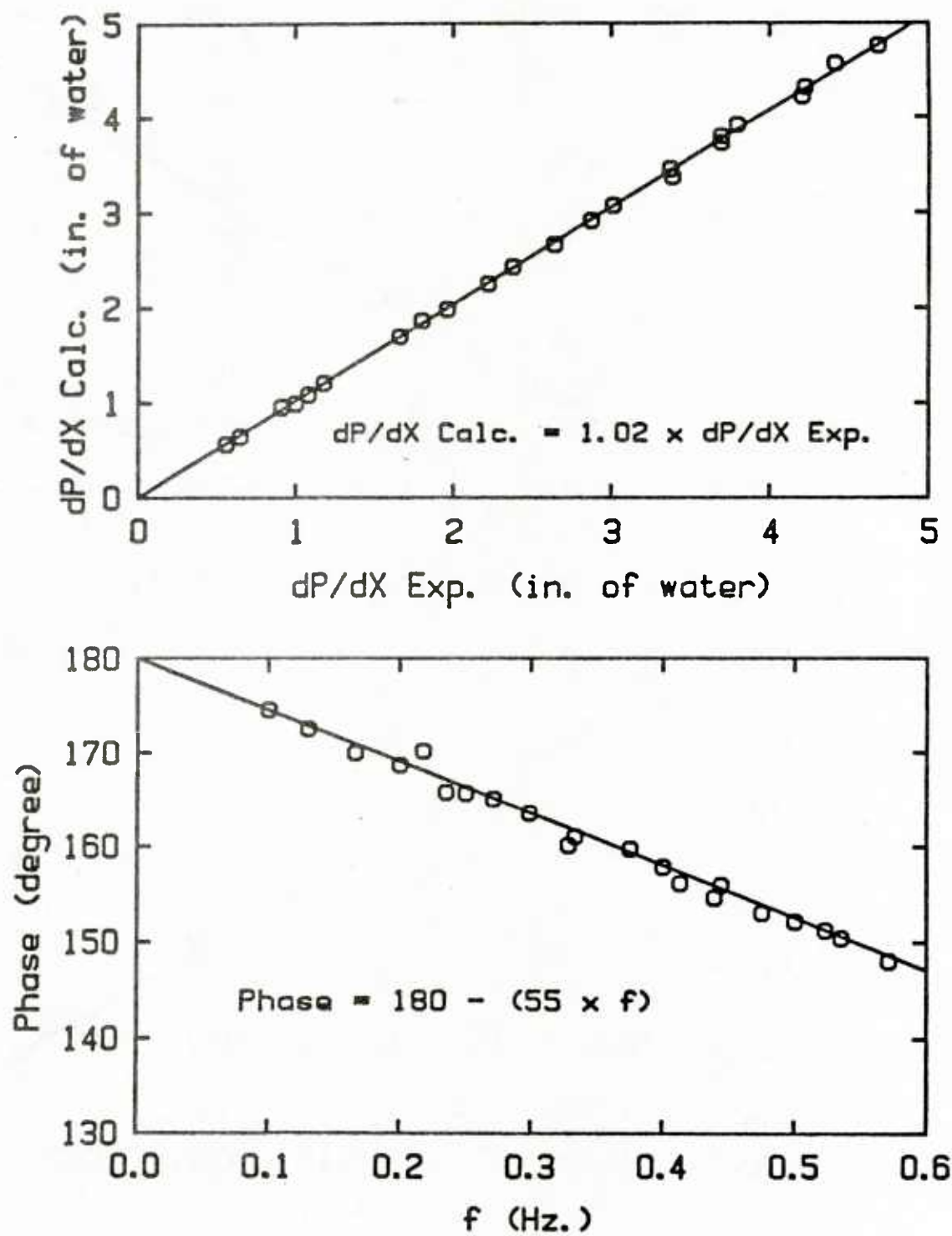


Figure 4.5 Correction factors for the Viatran transmitter

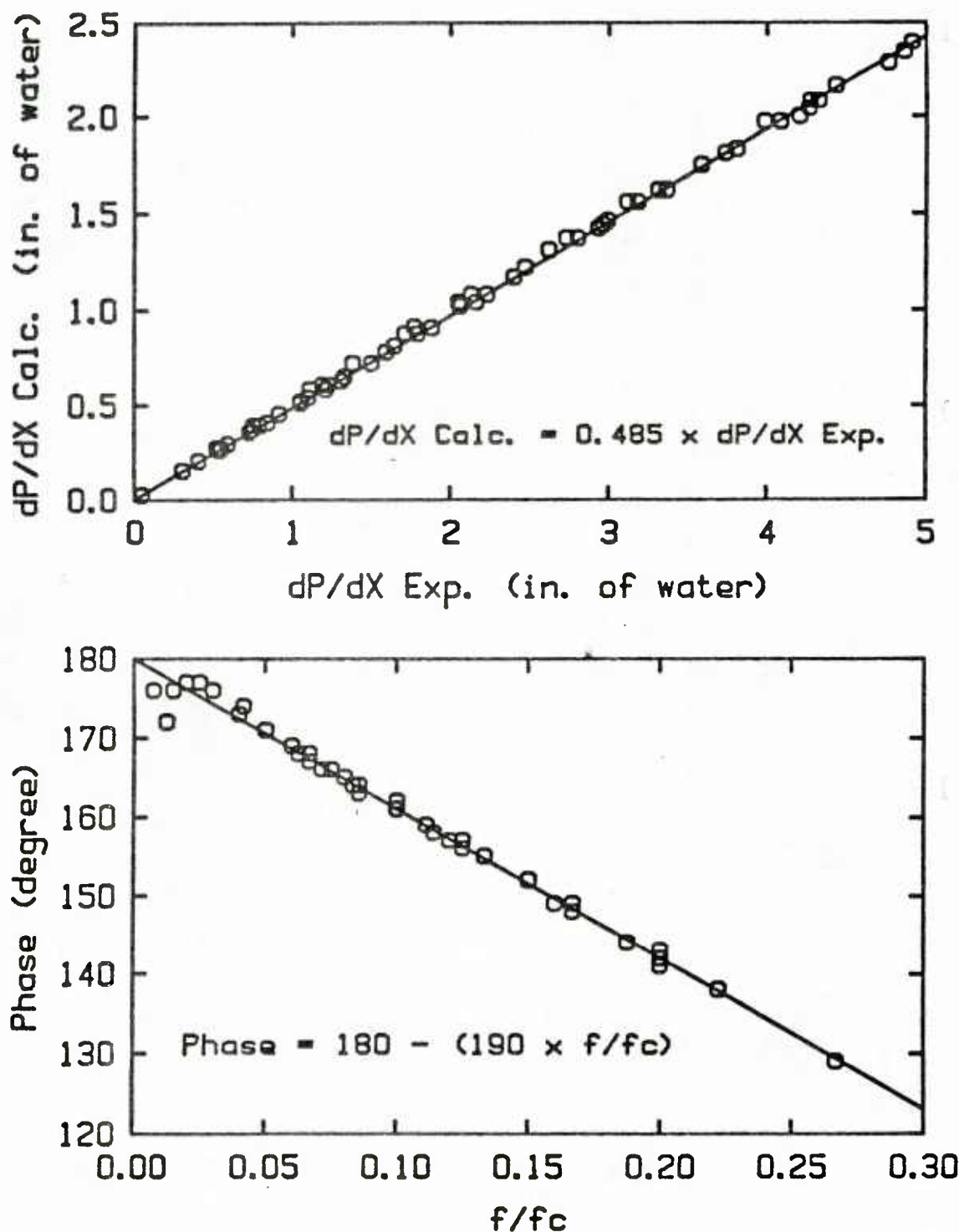


Figure 4.6 Correction factors for the C.J. Enterprises transmitter

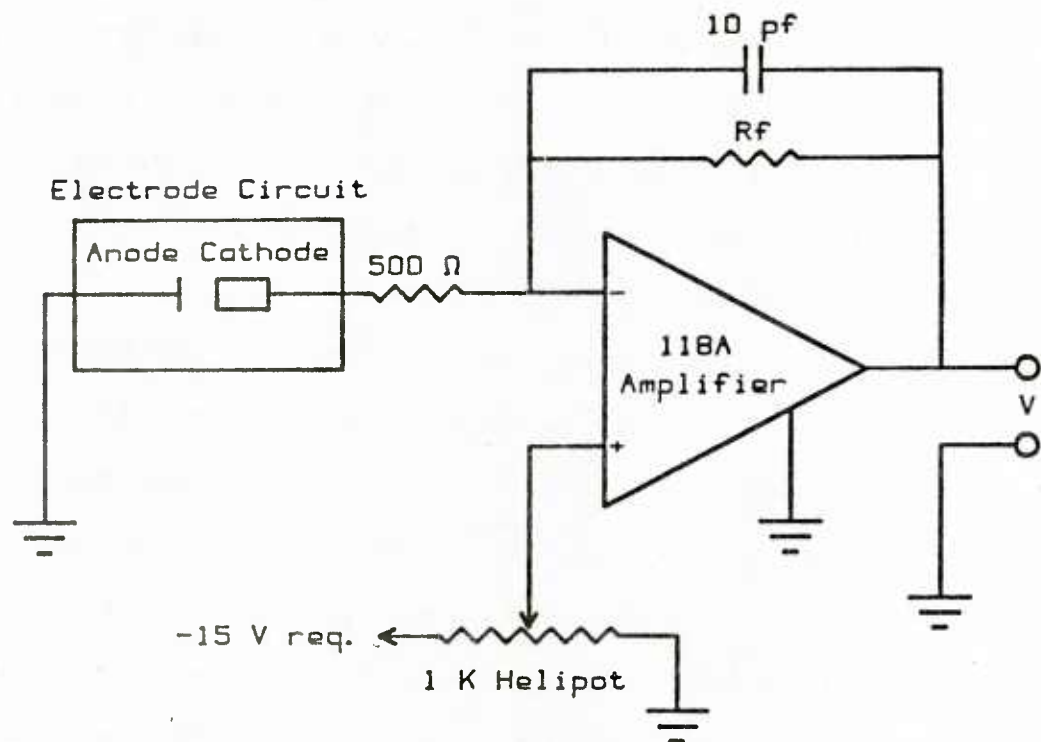


Figure 4.7 Electrode circuit

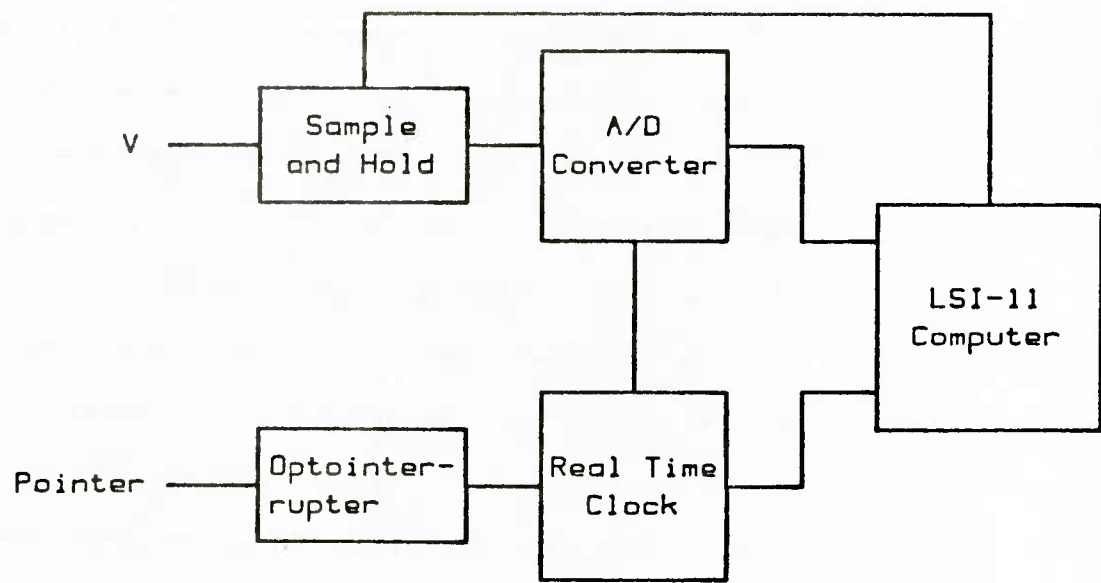


Figure 4.8 Block diagram of data acquisition

resistor was chosen so that the output voltage of the amplifier was in the range of five to seven volts in order to obtain good resolution in the analog-to-digital conversion. Very small capacitors were used in the feedback loop of these circuits to avoid line capacitance problems in the total circuit.

The analog signals from the wall electrodes and the differential pressure transmitter were digitized by a 12 bit A/D converter with a resolution of 0.00488 volts and sampled by a minicomputer (DEC, LSI-11/21). A block diagram of the data acquisition system is shown in Figure 4.8.

In the measurement of pulsating flow, an optointerrupter on the pulse generator was used to provide a pulse of 4 volts when the piston reached a certain position in each cycle. This pulse served as a phase reference. The time between two consecutive pulses determined the period of pulsation. It was measured with a programmable timer (Itron, 680) and sampled through a real time clock board in the computer. For each cycle of pulsation, the optointerrupter pulse initiated data sampling. Thirty-two samples per cycle were taken in equal time intervals and a total of 1000 periods of data were collected on the disc of the computer during each experiment. At each sampling point the electrodes and differential pressure transmitter were simultaneously sampled using a sample and hold circuit located on the A/D board. After the thirty-second sample the A/D was reset to wait for the next optointerrupter pulse at which point the data taking cycle would start again. Since the time required to reset the A/D was substantial, data taking occurred during every other pulsation cycle. Thus, the 1000 periods of data were collected over 2000 periods of pulsation.

The digitized data were recorded in binary format in order to save storage space. During data processing, the binary data were converted to voltages in decimal format. These voltages corresponded to the output

voltages of the electrode circuit and the differential pressure transmitter at each sampling instant. The output voltage of the current-to-voltage converter is related to the velocity gradient at the wall through (4.8) and (4.13),

$$S_x = \beta(V_{out} - V_{app})^3 \quad (4.23)$$

where V_{out} is the output voltage and V_{app} is the voltage applied to the electrode circuit. Parameter β is a constant for each run. Therefore, the periodic variation of the wall shear stress normalized by the time-averaged value was obtained as

$$\frac{\langle S_x \rangle}{\bar{S}_x} = \frac{\langle (V_{out} - V_{app})^3 \rangle}{(V_{out} - V_{app})^3} . \quad (4.24)$$

The intensity of the turbulent velocity gradient fluctuations at the wall was given as

$$\frac{(\overline{S_x^2})^{1/2}}{\bar{S}_x} = \frac{[(S_x - \langle S_x \rangle)^2]^{1/2}}{\bar{S}_x} , \quad (4.25)$$

and the intensity of the phase-averaged turbulent fluctuations, as

$$\frac{(\langle S_x^2 \rangle)^{1/2}}{\bar{S}_x} = \frac{[\langle (S_x - \langle S_x \rangle)^2 \rangle]^{1/2}}{\bar{S}_x} . \quad (4.26)$$

The time averaged correlation coefficient of the streamwise velocity gradient at the wall in the transverse direction was given as,

$$\bar{R}_{11} = \frac{(S_x(0) - \langle S_x(0) \rangle)(S_x(z) - \langle S_x(z) \rangle)}{[(S_x(0) - \langle S_x(0) \rangle)^2(S_x(z) - \langle S_x(z) \rangle)^2]^{1/2}} , \quad (4.27)$$

where z represents the differential distance in the transverse direction

between two electrodes. The phase-averaged correlation coefficient was obtained as

$$\langle \bar{R}_{11} \rangle = \frac{\langle (S_x(0) - \langle S_x(0) \rangle)(S_x(z) - \langle S_x(z) \rangle) \rangle}{[(S_x(0) - \langle S_x(0) \rangle)^2 (S_x(z) - \langle S_x(z) \rangle)^2]^{1/2}}, \quad (4.28)$$

Phase-averages were calculated on the computer in the following manner:

$$\langle E \rangle = E_i = \frac{1}{n} \sum_{j=1}^n E_{ij}, \quad (4.29)$$

where $\langle E \rangle$ are the phase-averaged data in one period and n , the number of periods to be averaged. Time-averaging was done by averaging the phase-averaged data over one period,

$$\bar{E} = \bar{E}_i = \frac{1}{m} \sum_{i=1}^m E_i = \frac{1}{mn} \sum_{i=1}^m \sum_{j=1}^n E_{ij}, \quad (4.30)$$

where m is the number of samples in one period. The pulsating component was then obtained from

$$\tilde{e} = \langle E \rangle - \bar{E}. \quad (4.31)$$

The phase-averaged data was fit with a three-harmonic cosine function using a least-square analysis. Since the amplitude of pulsation in this study was relatively small (10% of the center velocity), only the phase and amplitude of the first harmonic was considered.

E. Experimental Procedure and Range

Before starting an experiment the differential pressure transducer was zeroed and the span adjusted. Then the mean and pulsating pumps were turned on. It generally required about one hour for all the electrical equipment (including the pumps) to warm up and reach steady state. The mean flowrate was adjusted by opening or closing the mean flow by-pass

valve and the solution temperature was maintained at $25 \pm 0.1^\circ\text{C}$ by a temperature controller.

The working fluid was an aqueous solution of 0.1 M potassium iodide and 0.004 M iodine. The kinematic viscosity of the solution was 0.00866 cm^2/sec . The results of polarization tests using this solution are shown in Figure 4.9. The plateau region in each curve represents the currents at which the mass transfer to the electrode is diffusion limited. The results show that an applied voltage of -0.4 volts polarized the electrodes over the range of Reynolds numbers used in this investigation. Therefore, all measurements were taken at this applied voltage.

To prevent distortion of the sine wave generated by the pulsating pump it was important to design the flow loop with large amounts of pressure drop between the pulsating and mean pumps. Therefore, the mean flow was forced to go through the cleansing filters which have relatively high pressure drop. This forced about 95% of the flow pulsation to travel downstream to the test section and minimized the distortions caused by the time response of the whole flow loop.

For all the experiments, the amplitude of pulsation (centerline velocity variation) was set at $10\% \pm 0.2$. The reason for using a small amplitude was to eliminate nonlinear effects and, therefore, to make the analysis of the results easier. The centerline variation was not measured directly. Instead, the following method was used. Assuming the Blasius friction law to be valid, $\bar{U}_C/\bar{U}_B = 0.8$. From the measured pressure gradient and the plug flow relation, (3.70), the amplitude of the centerline variation can be calculated from the following:

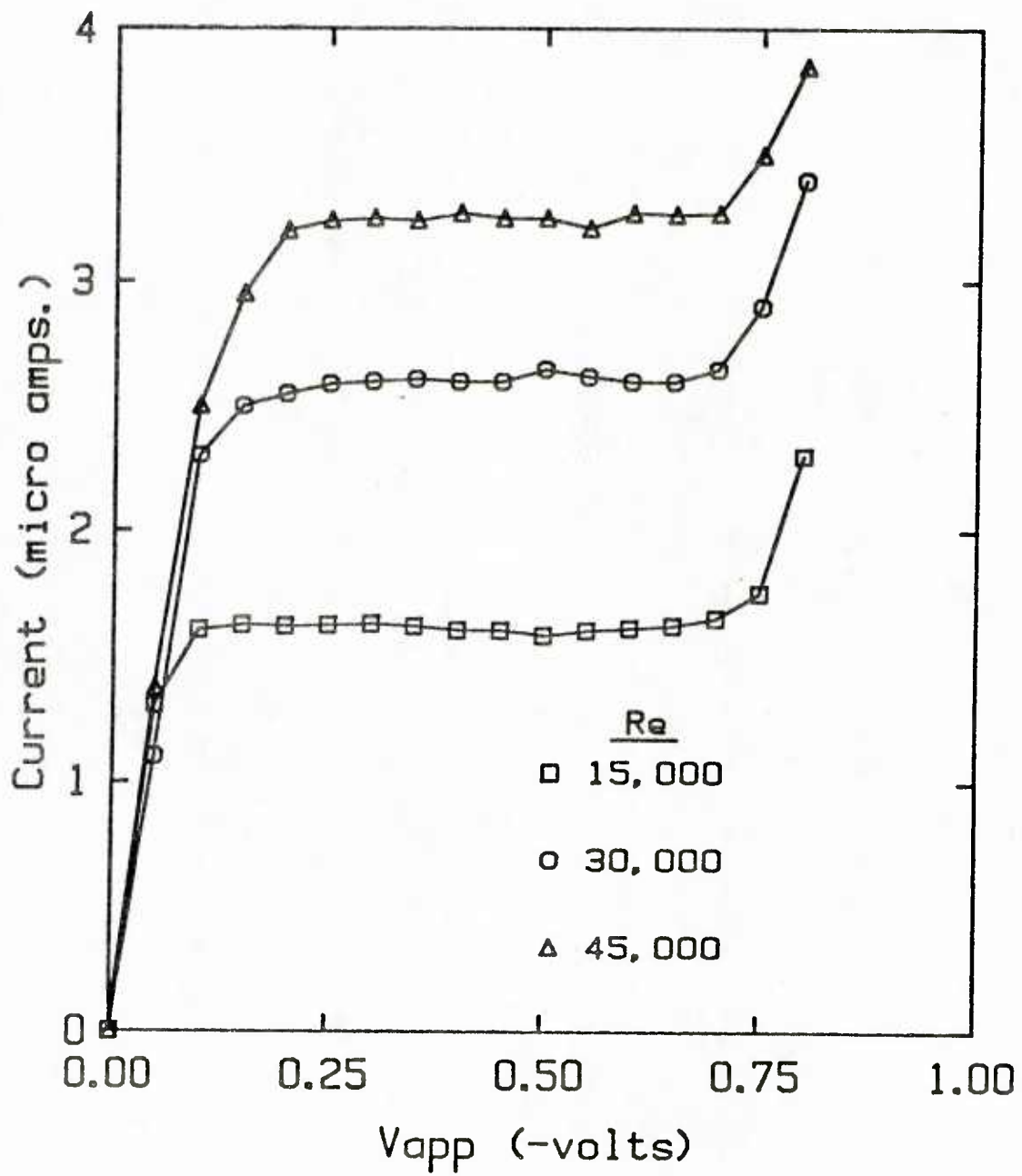


Figure 4.9 Polarization curves

$$\frac{\hat{U}_C}{U_C} = \frac{(dP/dx)/\omega}{\left[Re \nu \left(\frac{\hat{U}_C}{U_B} \right) \right] D} \quad (4.31)$$

For some of the lower ω^+ runs, a plug flow condition may not have existed in the center of the pipe and, therefore, the use of (3.70) is not valid. However, the empirical eddy viscosity model results, which are discussed in Section 5.II.B, indicate that the error in assuming plug flow for these runs is less than 5%. Therefore, (4.31) was used to determine the amplitude of the centerline variation for all the runs.

The experimental flow loop was designed to cover as wide a range of pulsation frequencies and amplitudes as possible. For comparison purposes, it was desired to overlap the high frequency data of Mao and Hanratty (1986) taken in an eight inch pipe. Measurements of turbulent structure at lower frequencies, where inertia is not expected to dominate the flow field, were also desirable. These goals were realized by using frequencies between 0.2 and 1.5 Hz. and Reynolds numbers between 8650 and 44900. The experimental conditions for each run is listed in Table 4.2 along with some important dimensionless groups used to characterize the flow field.

Table 4.2
Experimental Conditions

ω^+	$\sqrt{2/\omega^+}$	Re	f (Hz.)	u_c/u_b
0.00120	40.8	44,900	0.35	0.100
0.00135	38.5	42,000	0.35	0.101
0.00180	33.3	29,400	0.25	0.099
0.00210	30.9	23,700	0.20	0.100
0.00375	23.1	31,800	0.60	0.098
0.00375	23.1	25,200	0.40	0.100
0.00420	21.8	20,100	0.30	0.101
0.00495	20.1	23,000	0.45	0.098
0.00750	16.3	21,400	0.60	0.099
0.00930	14.6	17,100	0.50	0.102
0.0123	12.8	14,500	0.50	0.100
0.0172	10.8	17,900	1.00	0.098
0.0195	10.1	10,600	0.45	0.101
0.0210	9.76	10,700	0.50	0.102
0.0225	9.43	15,300	1.00	0.099
0.0244	9.05	14,600	1.00	0.098
0.0258	8.80	14,200	1.00	0.101
0.0270	8.61	10,300	0.60	0.101
0.0360	7.45	8,750	0.60	0.099
0.0375	7.30	11,400	1.00	0.098
0.0550	6.03	9,200	1.00	0.100
0.0675	5.44	10,300	1.50	0.101
0.0915	4.67	8,650	1.50	0.100

Chapter 5. RESULTS

The first section of this chapter presents the numerical results of the constant pressure gradient study for three values of the pressure gradient. In the second section, the pulsating pressure gradient experimental and numerical results are discussed.

I. Constant Pressure Gradient Turbulent Flows

Solutions of the vorticity and stream-function equations subject to the boundary conditions (3.17), (3.18) and (3.19) are presented for three P^+ . All the relative parameters that are needed to specify completely (3.17), (3.18) and (3.19) were selected according to the arguments presented in Section 3.I.C, and are summarized in Table 5.1.

TABLE 5.1
Summary of Parameter Values

P_{eo}^+	P^+	$K \times 10^6$	y_0^+	T_1^+	λ_1^+	T_2^+	λ_2^+			
0.0	0.0	0.0	40.0	100	100	400	400			
-0.0087	-0.0162	2.03	56.0	196	140	784	560			
-0.0096	-0.0225	2.81	69.3	300	173	1200	692			
<hr/>										
P_{eo}^+	P^+	E_{u1}	E_{v1}	E_{w1}	ϕ_{u1}	ϕ_{u2}	ϕ_{v1}	ϕ_{v2}	ϕ_{w1}	ϕ_{w2}
0.0	0.0	0.15	0.70	0.37	216	196	36	90	0	270
-0.0087	-0.0162	0.15	0.70	0.37	216	196	36	90	0	270
-0.0096	-0.0225	0.15	0.70	0.37	216	196	36	90	0	270

A. Statistics

Average properties of the fluctuating quantities are calculated at a fixed distance from the wall by averaging both in time and in the spanwise direction. These are compared with laboratory measurements of the statistical properties of wall turbulence.

1. Comparison with Nonaccelerated Experimental Data

This section presents the results of the calculations of flows without imposed pressure gradients. Comparison with zero pressure gradient experimental data provides a basis for judging the validity of the model. Also, the zero pressure gradient calculations provide the standard by which the changes in the viscous wall region that are due to an imposed pressure gradient can be determined.

After the mean velocity profile reached steady state (invariant from cycle to cycle), space and time averages of the flow variables were calculated over an additional cycle equal to T_2 in time. Figures 5.1 through 5.4 present the average mean velocity profile, the intensities of the fluctuating components of the velocity, the Reynolds stress and uv correlation coefficient, and the skewness and flatness of the streamwise velocity component. It can be seen that, overall, the agreement with the experimental data is satisfactory. In particular the calculated Reynolds stress shows very good agreement with experiments. The calculated v -intensity profile attains somewhat lower values than what the experiments indicate close to the wall, but agrees with the experimental data quite well in the region $y^+ > 25$. Recent measurements of the turbulent velocity fluctuations normal to the wall obtained by Finnicum and Hanratty (1985) with flush mounted wall electrodes suggest that the experimental data close to the wall are in error due to probe-wall interactions and that the true values are closer to those obtained from the calculations.

2. Nonzero Pressure Gradient Statistics

This section presents the statistical results of the calculations of flows with imposed constant pressure gradients. Two pressure gradients are considered: an intermediate pressure gradient of $P^+ = -0.0162$ and the

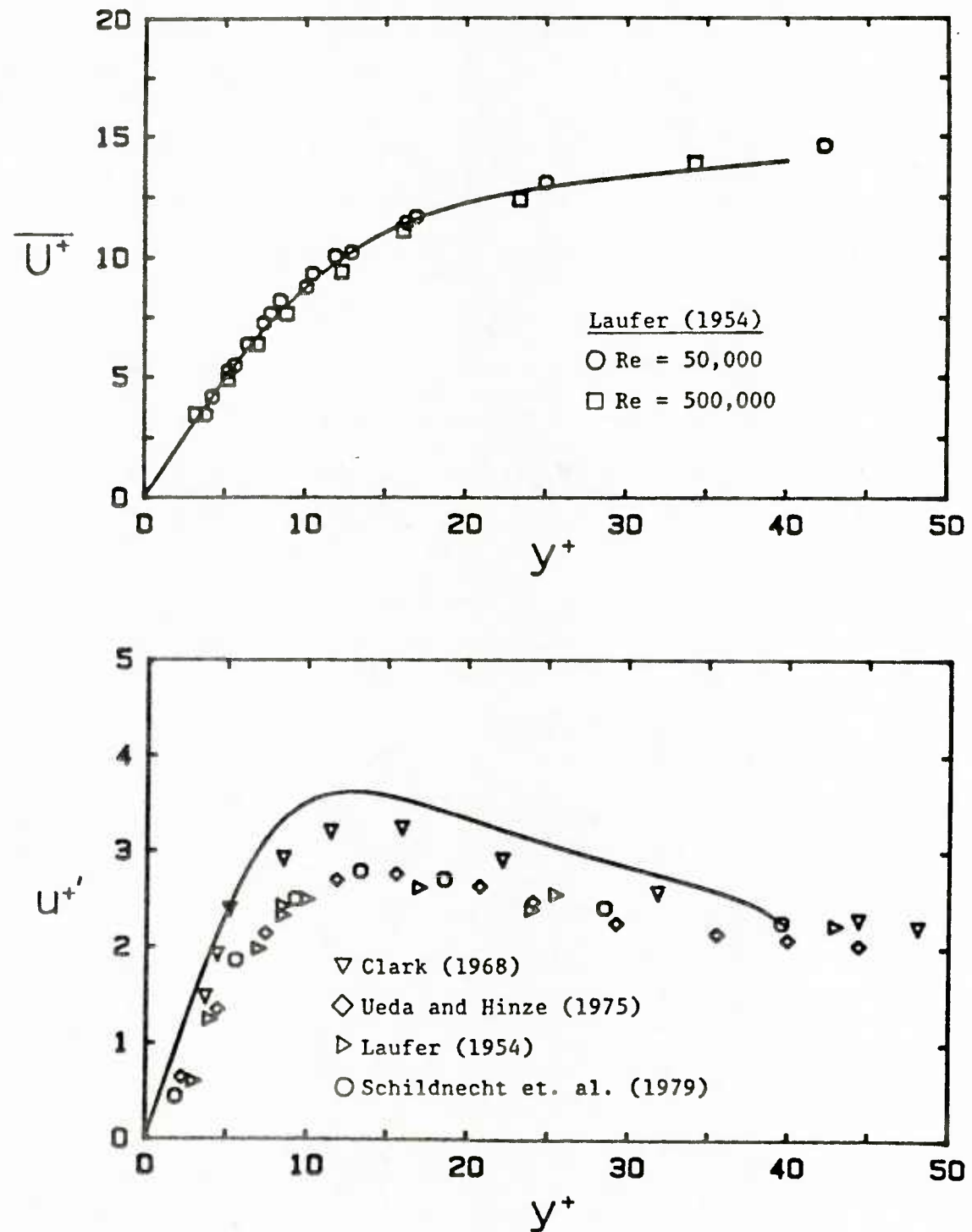


Figure 5.1 Streamwise mean velocity and intensity for $P_{eo}^+ = 0.0$

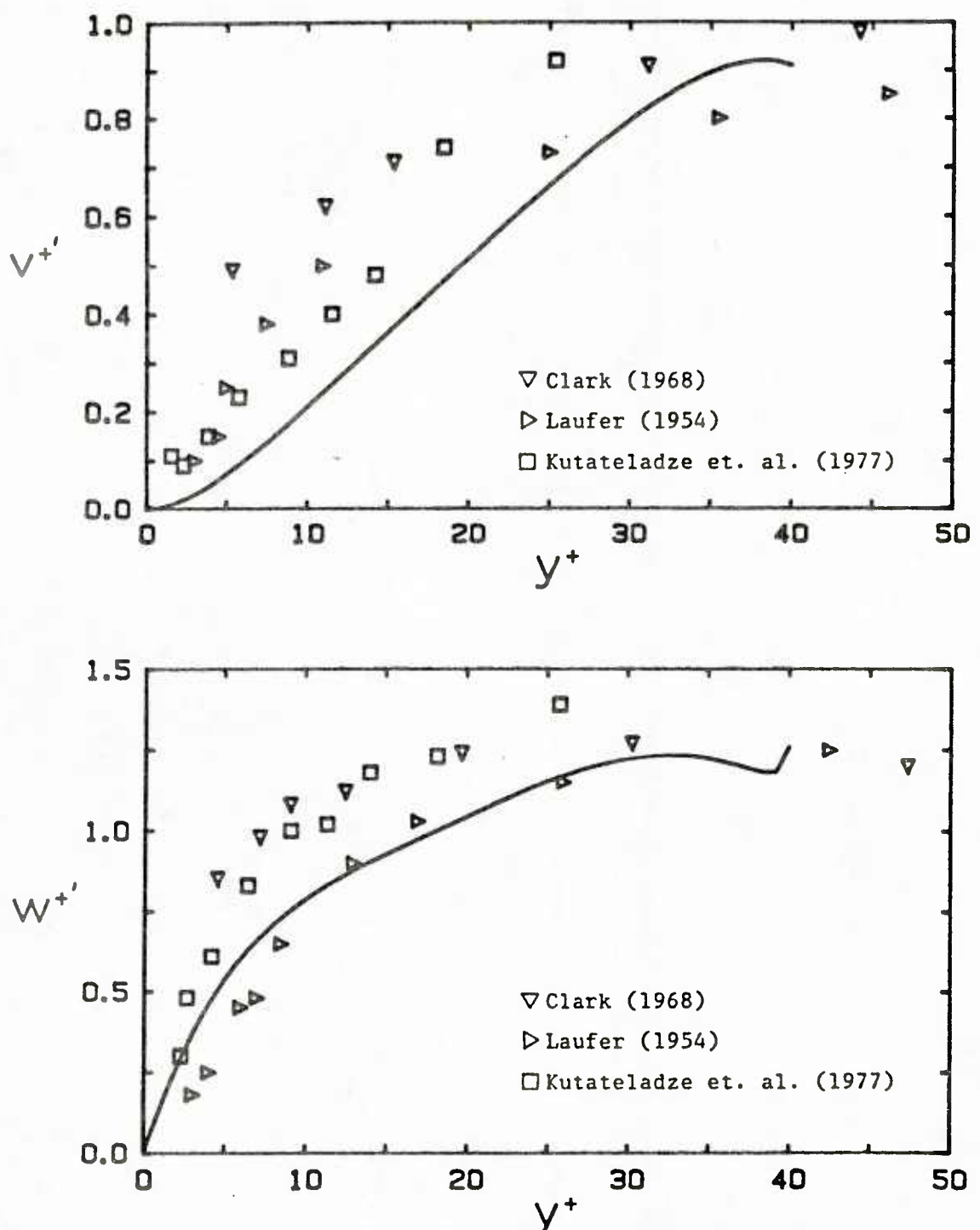


Figure 5.2 Intensities of the normal and spanwise velocity fluctuations for $Pe_{eo}^+ = 0.0$

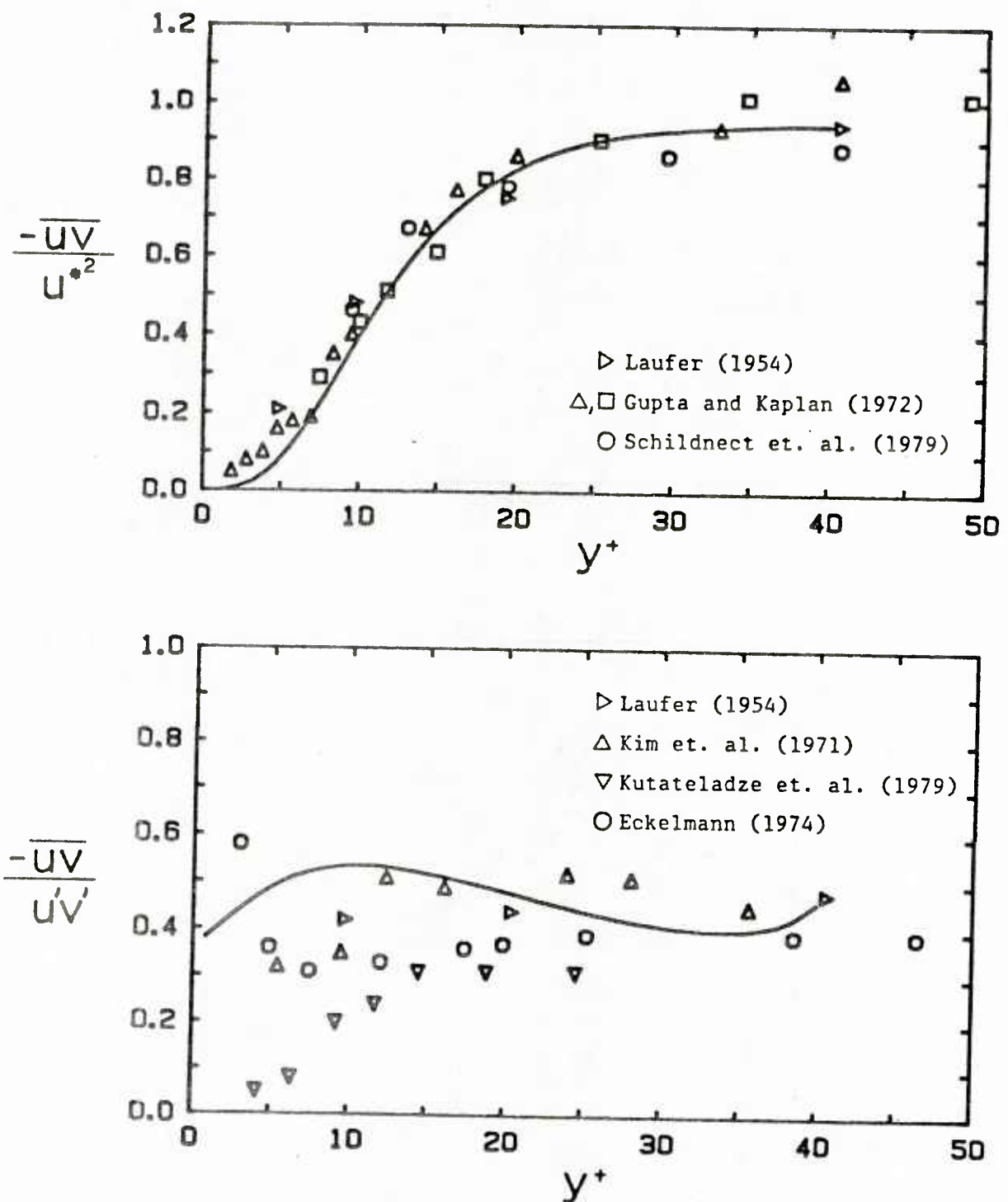


Figure 5.3 Reynolds stress and Reynolds stress correlation for $P_{eo}^+ = 0.0$

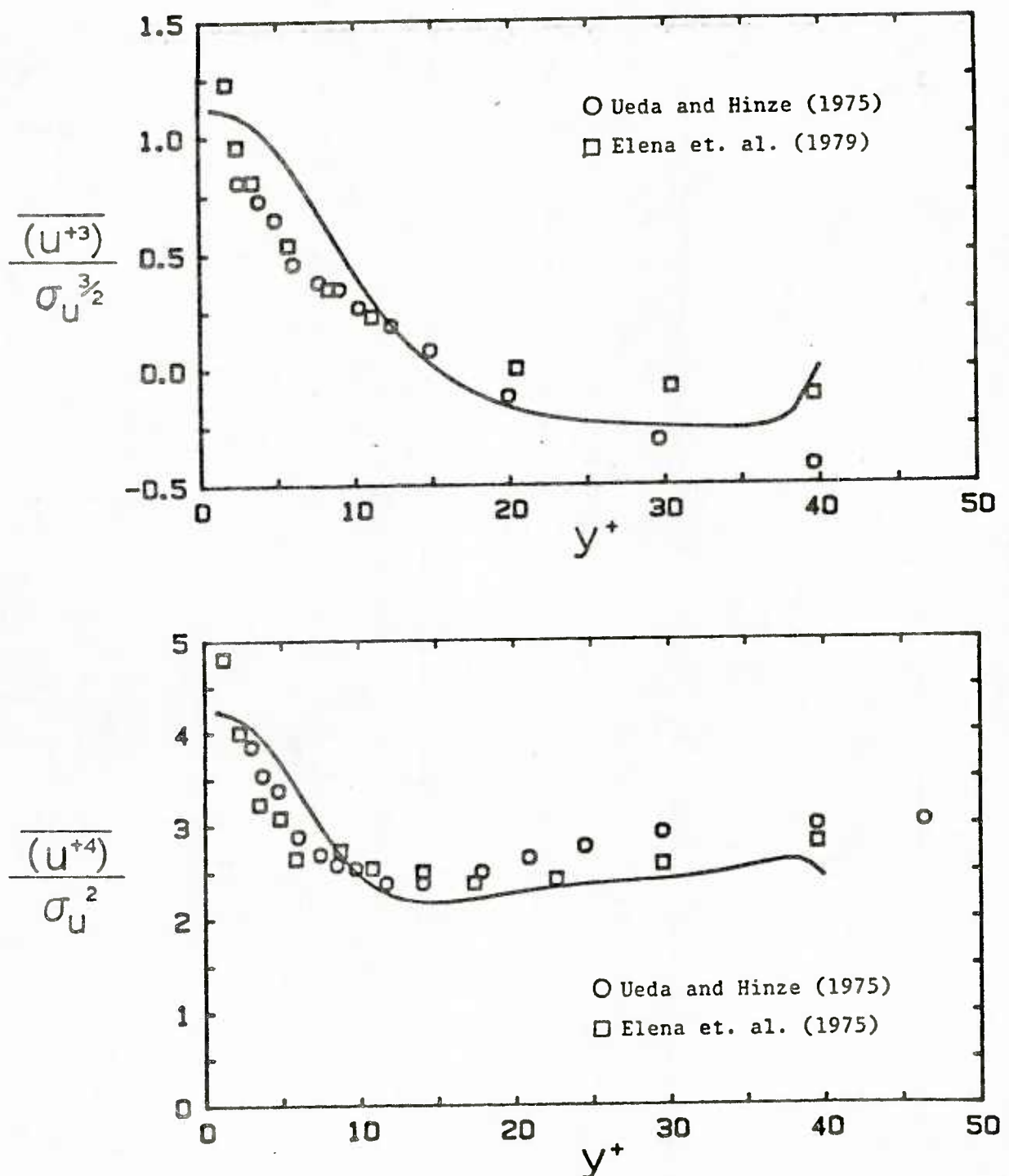


Figure 5.4 Skewness and flatness of the streamwise velocity fluctuations for $Pe_o^+ = 0.0$

incipient relaminarization run of $P^+ = -0.0225$. As discussed in Section 3.E.3, these values are obtained by specifying P_{eo}^+ , performing the calculation, and then determining P^+ from (3.15). In all the figures in this section, the solid lines correspond to the nonaccelerated flow, the dashed lines correspond to the intermediate pressure gradient flow, and the dotted lines correspond to the relaminarization run.

Figure 5.5 shows the results for the mean velocity profiles. The analytical relation of Launder and Stinchcombe (1967) for accelerated laminar boundary layers is also included in the figure. The dash-dot-dash line corresponds to the laminar mean velocity profile that would be obtained after the relaminarization of a flow with a pressure gradient just greater than -0.0225 . Three effects on the mean velocity profile are noted. In the viscous wall layer ($y^+ \lesssim 6$), the accelerated flows are slightly less than the nonaccelerated flow. This is due to the velocity profile having to satisfy the Couette flow relation, (3.51), as $y^+ \rightarrow 0$. As the imposed pressure gradient increases, the velocity profile outside the viscous wall layer increases toward the laminar value indicating that the flow is becoming less turbulent. Relation (3.23) predicts that the slope of the mean profile at y_0^+ would be lower, since τ_0^+ is lower and y_0^+ is higher, in favorable pressure gradients. The results of the calculation agree with (3.23) in that the slopes at y_0^+ are decreasing as P^+ is increased. These trends are in agreement with experimental results found in the literature [Jones and Launder (1972), Badri Narayanan and Ramjee (1969), and Blackwelder and Kovasznay (1969)]. The mean velocity data of Loyd et. al. (1970) for $K = 0, 2 \times 10^{-6}$ are compared with the calculated profiles in Figure 5.6. Good agreement is observed.

The u intensity profiles for the three runs are shown in Figure 5.7. Increasing the pressure gradient has the effect of moving the peak in the

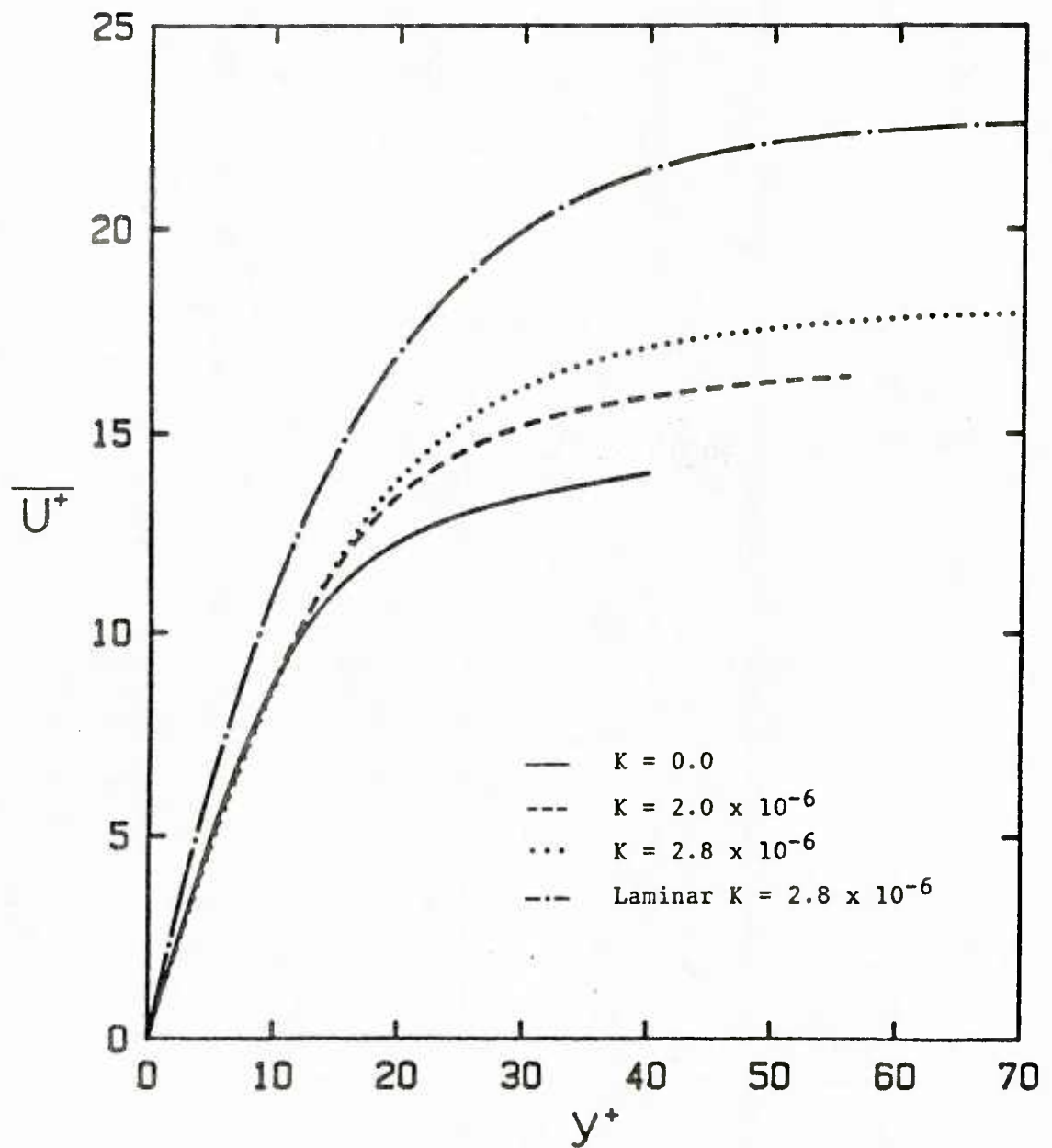


Figure 5.5 Mean velocity profiles for several pressure gradients

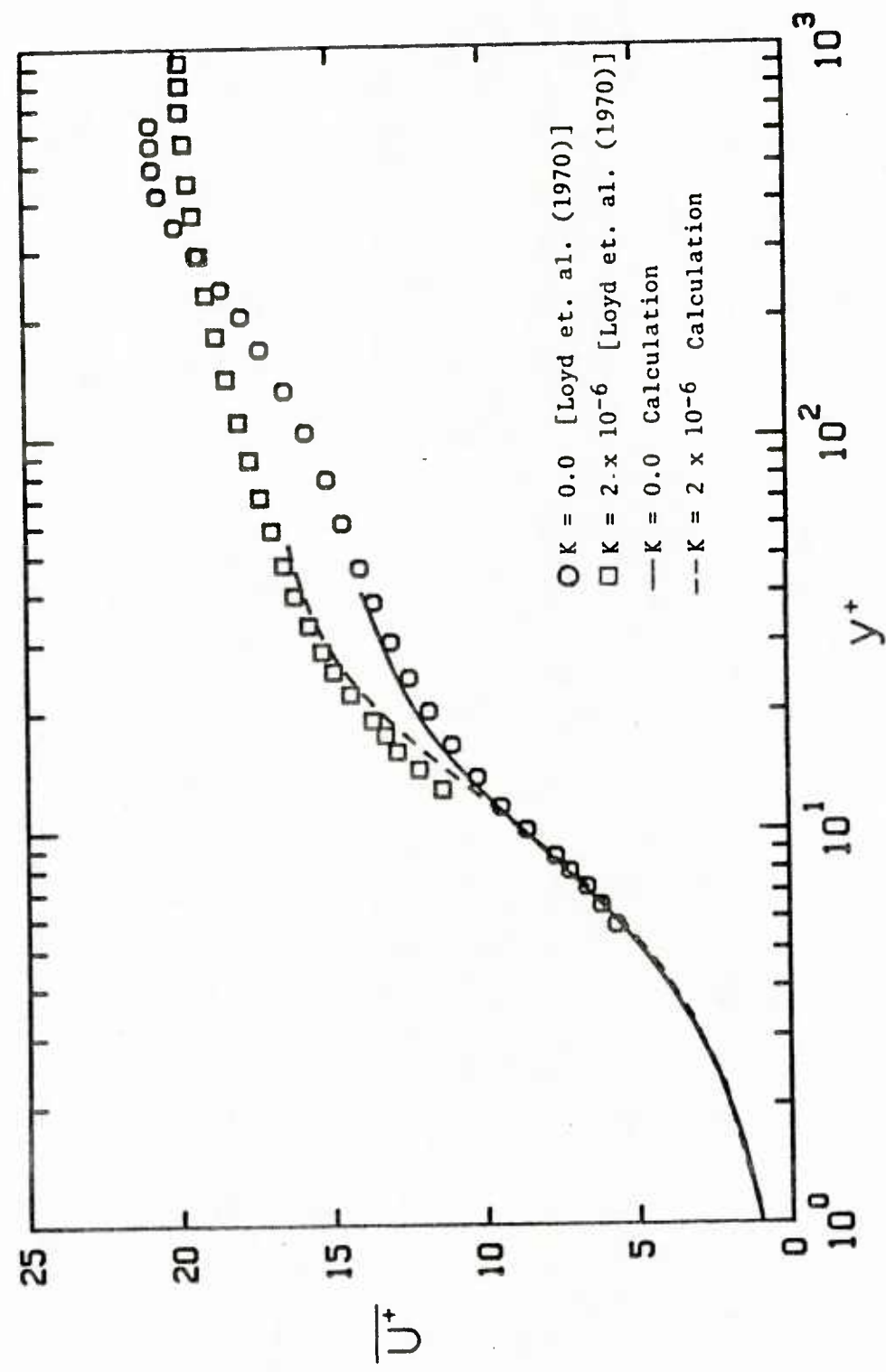


Figure 5.6 Comparison of mean velocity profiles with experimental data

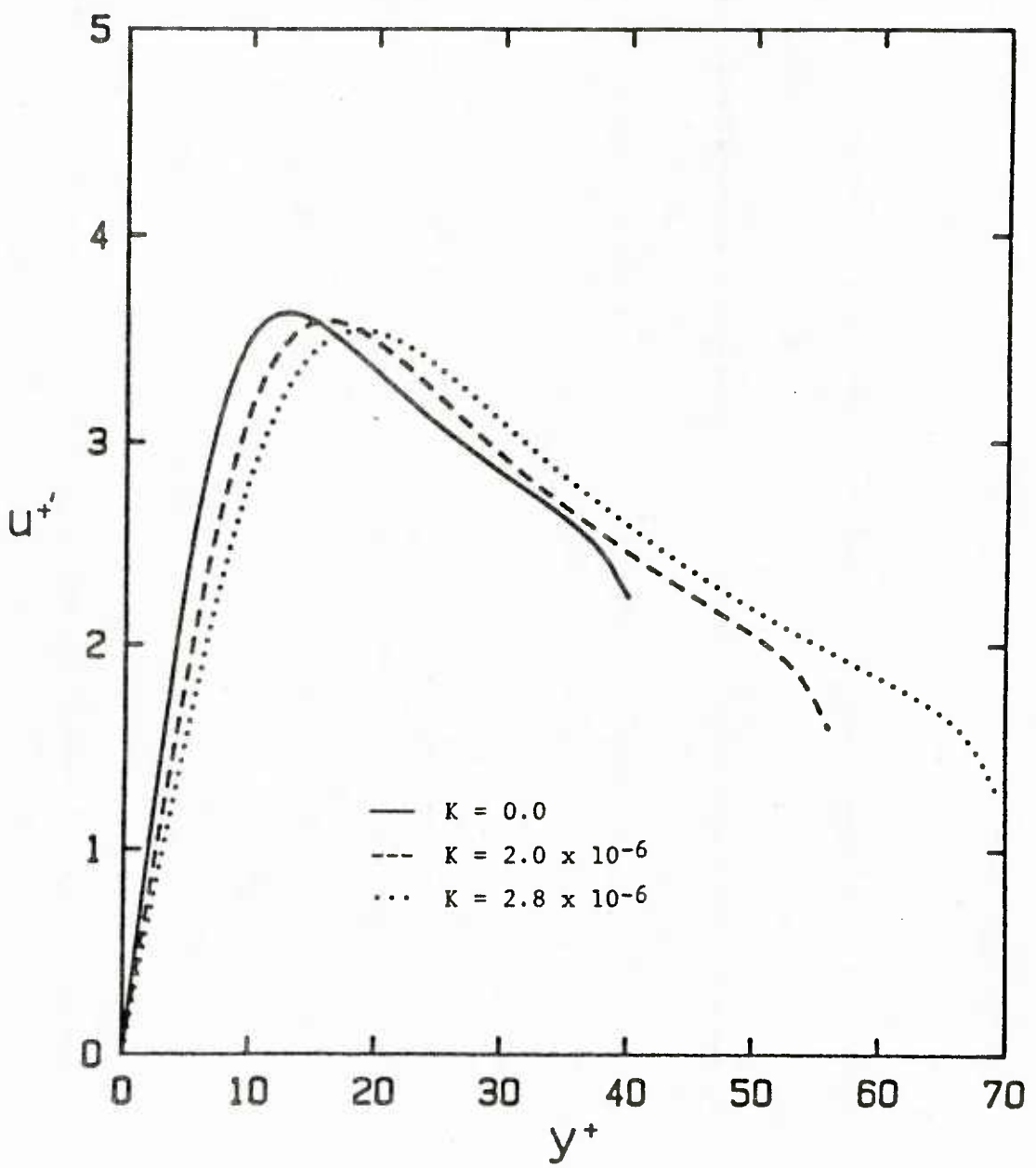


Figure 5.7 Intensity of the streamwise velocity fluctuations for several pressure gradients

profile away from the wall and of slightly lowering the maximum value. Figure 5.8 shows the v and w intensity profiles. In contrast to the u intensity profile, there is a dramatic decrease in the fluctuations throughout the viscous wall region as the imposed pressure gradient is increased. The Reynolds stress, shown in Figure 5.9, also shows a dramatic decrease in amplitude.

These results agree with experimental data [Jones and Launder (1972), Launder and Stinchcombe (1967), and Badri Narayanan and Ramjee (1968)] showing a high streamwise intensity at pressure gradients up to the relaminarization point. The data of Badri Narayanan and Ramjee (1968) indicate that after relaminarization there is a rapid decay of streamwise fluctuations till an essentially laminar flow remains. The Reynolds stress correlation results are also shown in Figure 5.9. No effect of pressure gradient is observed on the correlation of the Reynolds stress. This indicates that the decrease in the Reynolds stress is associated more with a reduction in the amplitude of the secondary motion than with a change in the basic processes involved.

Figure 5.10 shows the streamwise skewness and flatness profiles for the three cases. The large positive skewness near the wall is the result of inflows of high streamwise momentum close to the wall and the negative skewness is the result of ejections of low momentum fluid. As seen in Figure 5.10, both quantities are roughly independent of pressure gradient.

B. Energy Balances

According to the classical theory of turbulence [Tennekes and Lumley (1981)] the internal dynamics of turbulence transfers energy from large scales to small scales. For a fully developed turbulent flow the energy supplied to the flow comes from the imposed pressure gradient. This energy

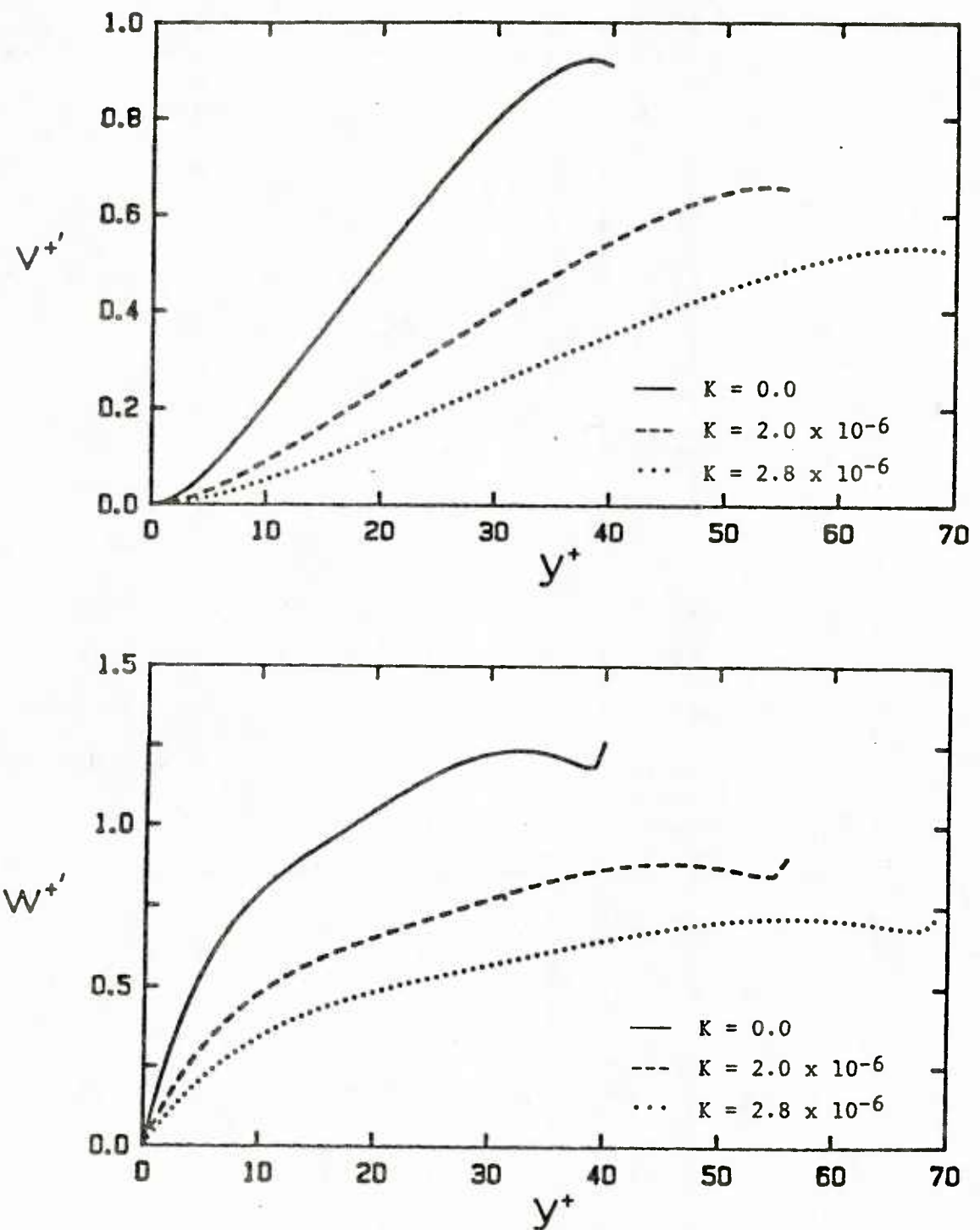


Figure 5.8 Intensities of the normal and spanwise velocity fluctuations for several pressure gradients

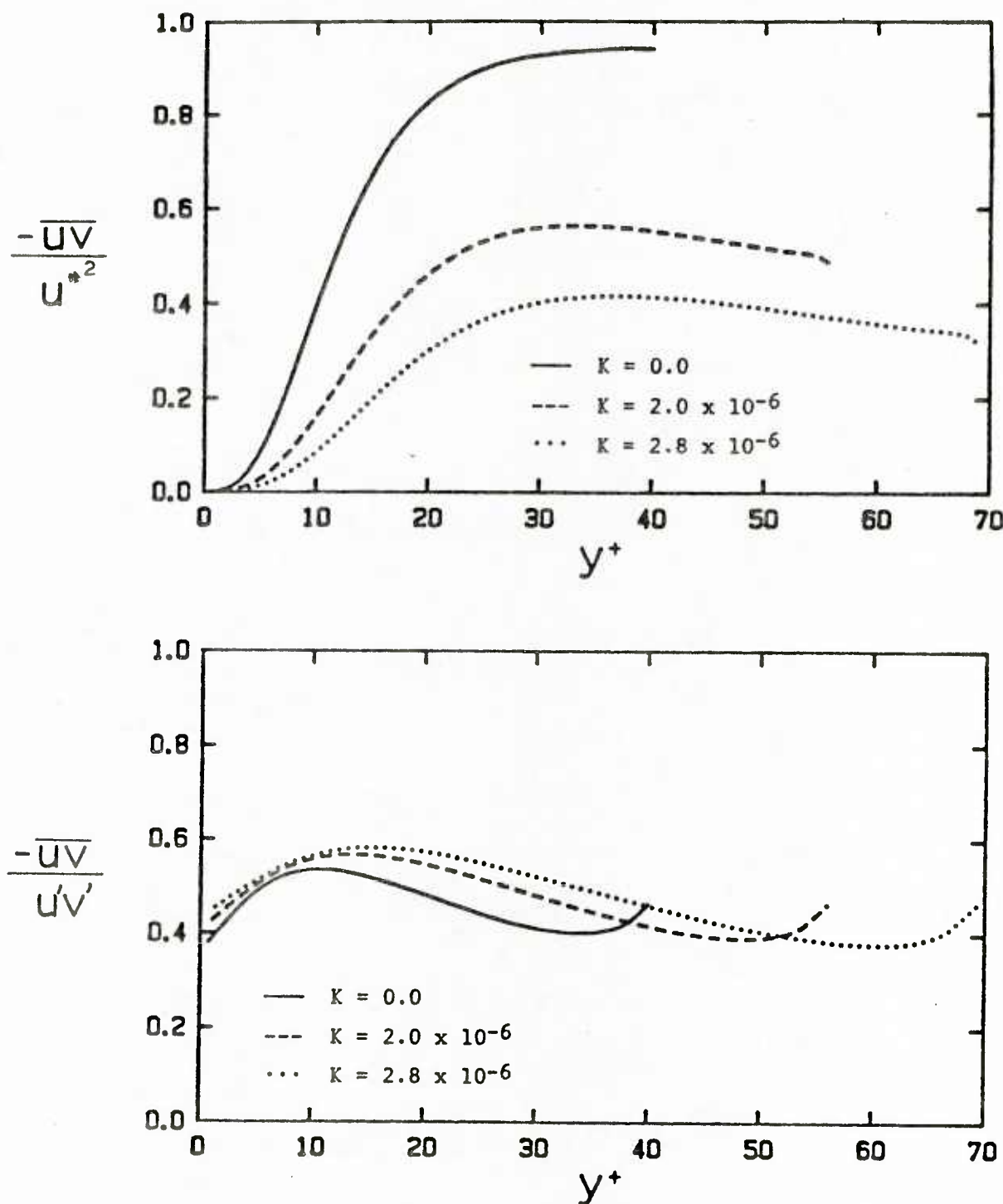


Figure 5.9 Reynolds stress and Reynolds stress correlation for several pressure gradients

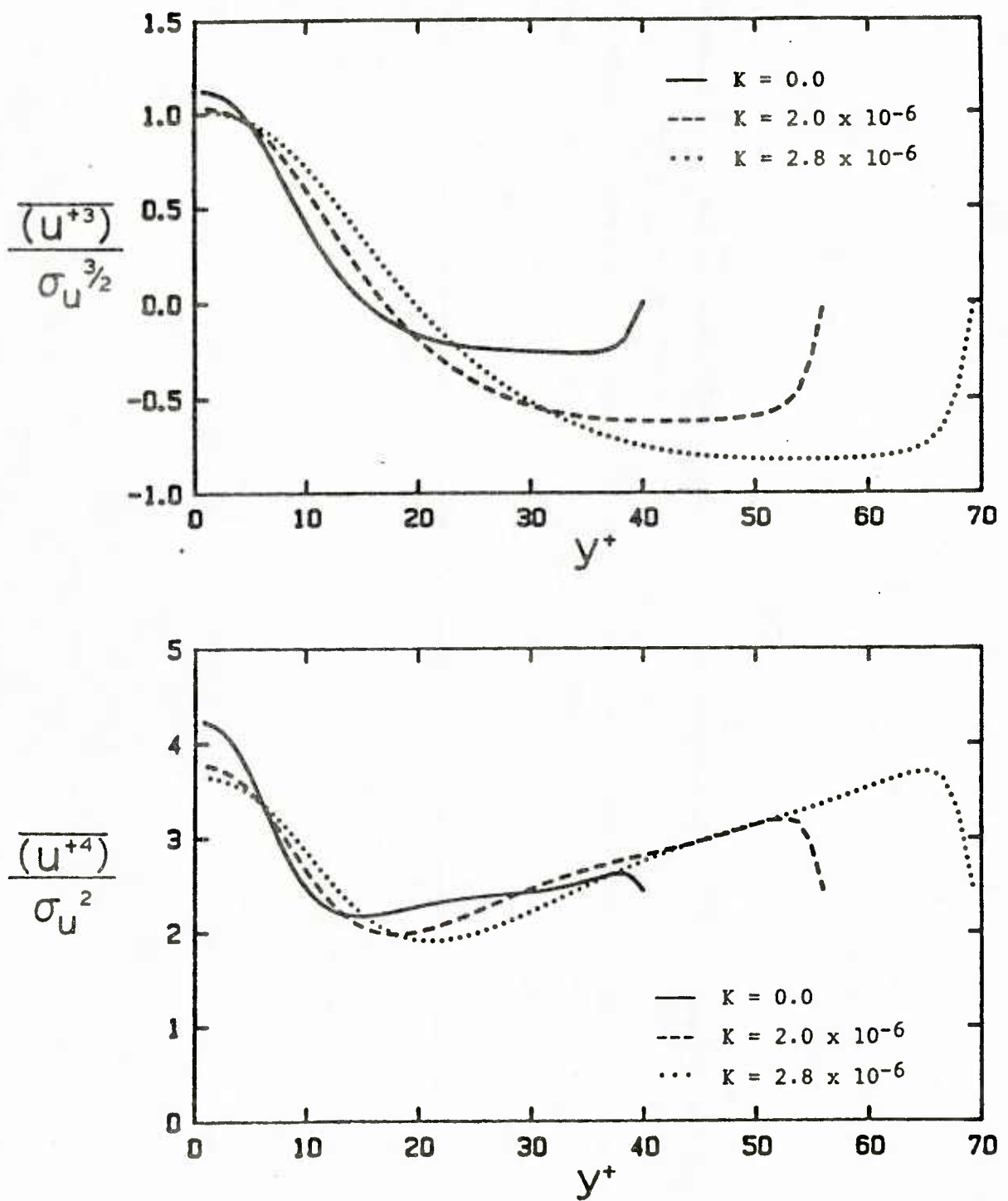


Figure 5.10 Skewness and flatness of the streamwise velocity fluctuations for several pressure gradients

is supplied to the mean flow eddies whose size is comparable to the thickness of the boundary layer. Turbulence, then, extracts energy from the mean flow eddies and by nonlinear interaction cascades it from large small eddies, down to the Kolmogorov microscale eddies where the energy is dissipated into heat.

1. Mean Kinetic Energy Balance

From Townsend (1976), the equation for the mean flow kinetic energy in a boundary layer is as follows (all quantities are dimensionless):

$$-\bar{U} \left(\bar{U} \frac{d\bar{U}}{dx} + \bar{V} \frac{d\bar{U}}{dy} \right) - \bar{U} \frac{dP}{dx} - \frac{d(\bar{U}\bar{U})}{dy} + \bar{U}\bar{V} \frac{d\bar{U}}{dy} + \frac{1}{Re} \frac{d}{dy} \left(\bar{U} \frac{\partial \bar{U}}{\partial y} \right) - \frac{1}{Re} \left(\frac{d\bar{U}}{dy} \right)^2 = 0 . \quad (5.1a)$$

I II III IV V VI

Term I is the advection term and Term II represents the rate of energy supply to the mean flow by the imposed pressure gradient. Term III represents the energy flux in toward the wall by Reynolds stresses working on the mean velocity. Term IV is the amount of energy extracted from the mean flow by the working of the Reynolds stress against the mean shear. Term V is the transport of mean flow energy by viscous stresses and Term VI is the direct viscous dissipation of mean flow energy.

Terms I and II can be combined to give the following:

$$-\bar{U} \frac{d\tau}{dy} = -\bar{U} \left(\bar{U} \frac{d\bar{U}}{dx} + \bar{V} \frac{d\bar{U}}{dy} \right) - \bar{U} \frac{dP}{dx} . \quad (5.1b)$$

VII I II

Term VII represents the net amount of energy supplied to the mean flow by the pressure gradient. The shear stress gradient is calculated from (3.16) and Term I is obtained by subtracting II from VII. For a flow without acceleration Terms I, II and VII are negligible. The balance for the three

terms is shown in Figure 5.11(a) for the $P_{eo}^+ = -0.00962$ run. Terms I and II are shown to have high values throughout the viscous wall region that are opposite in sign. The difference between the two terms, which represents the net amount of energy supplied by the pressure gradient, increases from zero at the wall to a maximum of 0.15 at $y^+ = 14$ and, then, steadily decreases as the distance from the wall increases. Near the edge of the viscous wall region the amount of energy supplied by the pressure gradient to the turbulence is less than 20%; the rest is used to change the inertia of the fluid. Because the effect of the pressure gradient outside the viscous wall region is small, the viscous wall region reacts faster to an imposed pressure gradient than the outer regions of the flow.

Integration of each term as a function of y^+ produces the curves shown in Figure 5.11(b). The integrated value of Term VII at the edge of the viscous wall region represents the total amount of energy supplied by the shear stress gradient to the turbulence in the viscous wall region. Even though it is only one-third the contribution of the pressure gradient, it is still a relatively large amount of mean flow energy.

The full mean kinetic energy balance for the nonaccelerated flow ($P^+ = 0.0$) is shown in Figure 5.12(a). The loss of mean flow energy to the turbulent fluctuations is replenished by an energy flux to the wall. A large amount of mean flow energy is transported into the viscous wall region by Term III. This input of energy is roughly balanced by the loss of energy to the turbulent fluctuations and to direct viscous dissipation. The balance for the $P_{eo}^+ = -0.00962$ run is shown in Figure 5.12(b). Term VII, the net amount of energy supplied by the pressure gradient, is observed to be a relatively large source of mean flow energy in the viscous wall region. This extra source of energy in the viscous wall region relieves the demand for mean flow energy from outside the viscous wall

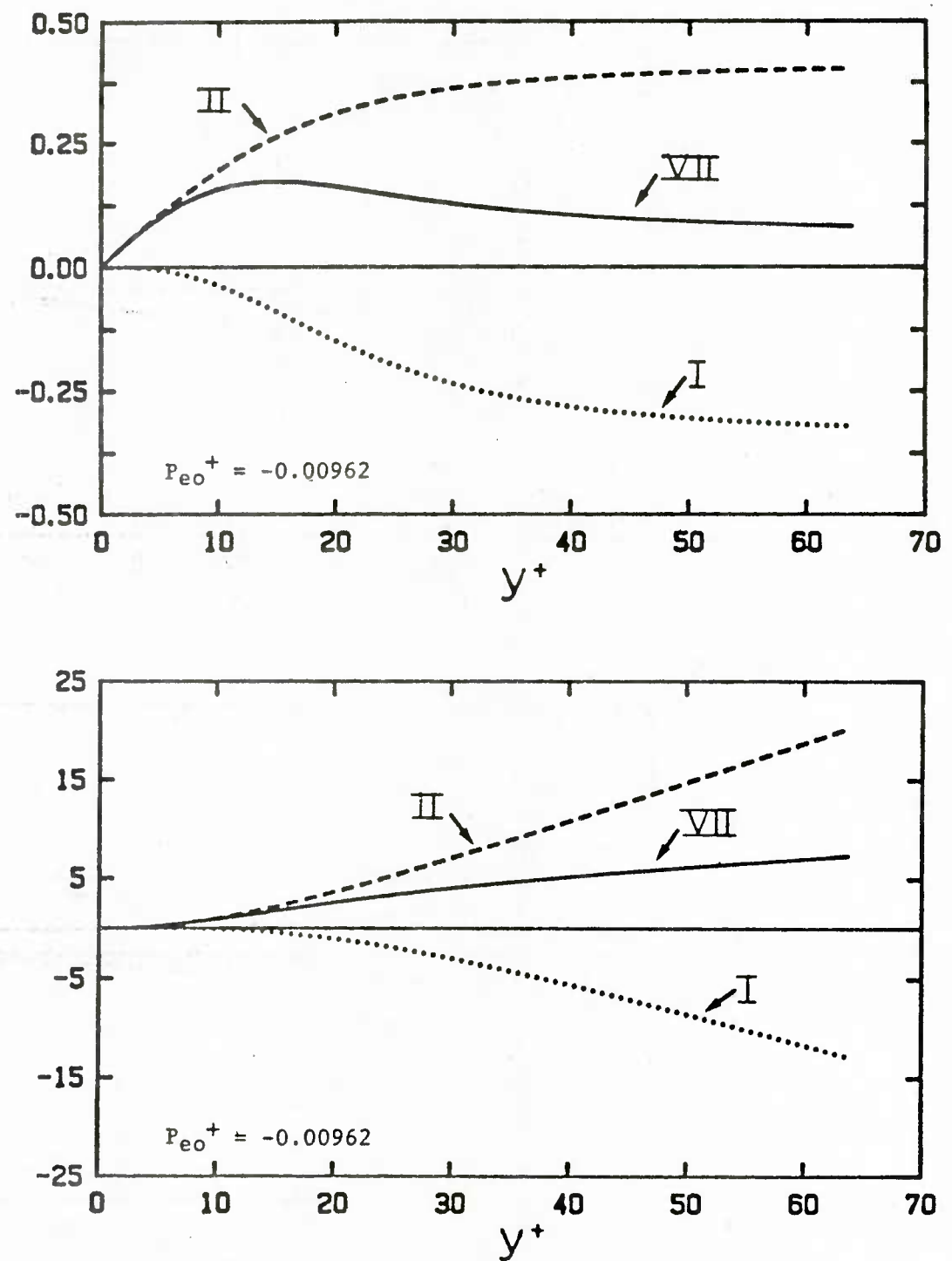


Figure 5.11 Energy supplied by the pressure gradient

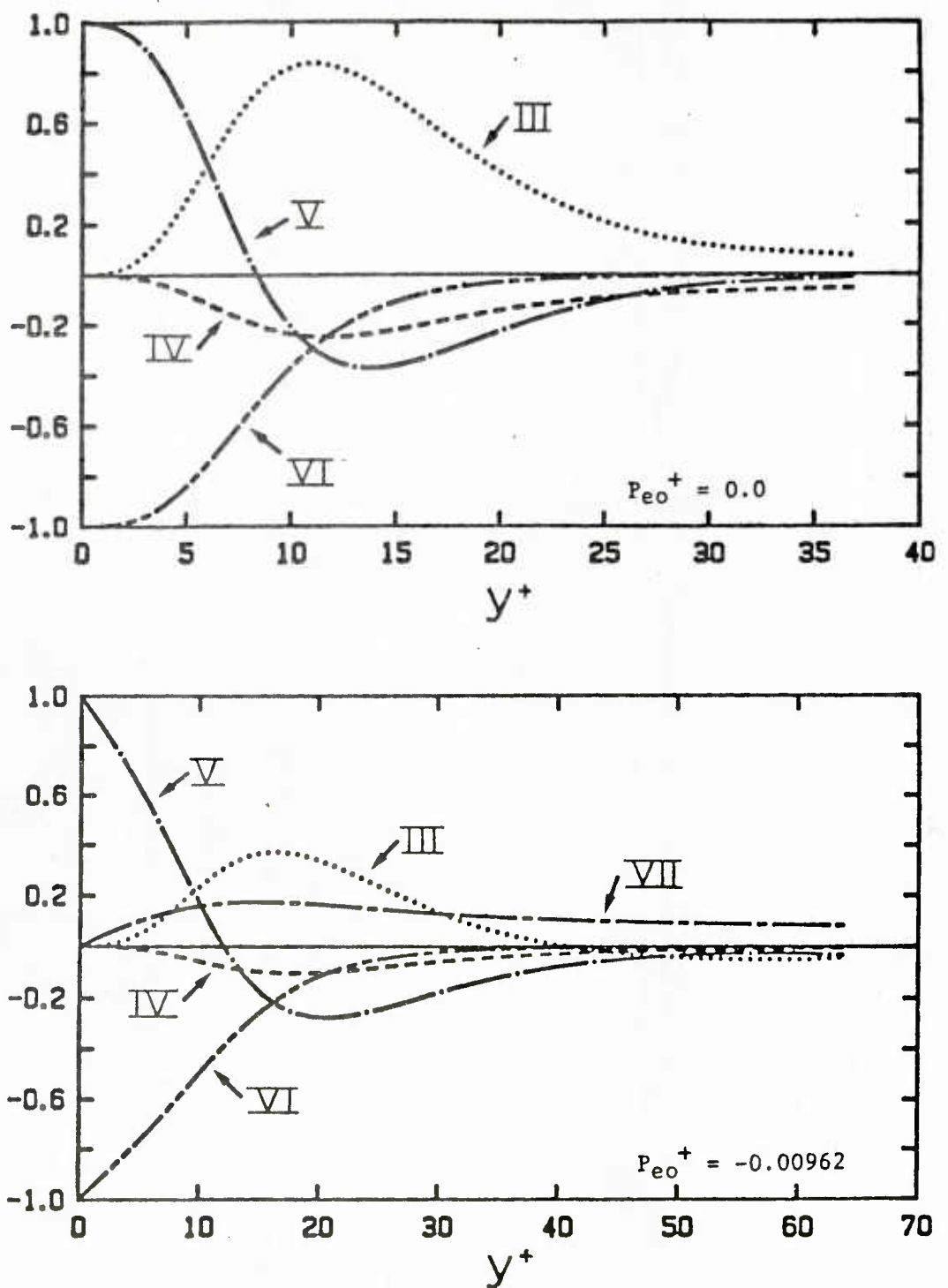


Figure 5.12 Mean kinetic energy balance

region and, therefore, a drop is observed in Term III. The flow is less turbulent since the amount of energy lost to the fluctuations, Term IV, also decreases. Integration of each term with respect to y^+ for the two runs is shown in Figure 5.13. Focusing on the values near the edge of the viscous wall region, it is observed that the presence of the large favorable pressure gradient reduces by over 50% the amount of energy transported into the viscous wall region from the rest of the flow. This loss of energy is compensated by the presence of the large amount of energy supplied by the shear stress gradient.

Thus, the pressure gradient, through the shear stress gradient, is seen to be a large source of energy in the viscous wall region. This is a major change from the nonaccelerated flow where all of the energy is transported into the viscous wall region by Reynolds stresses working on the mean velocity.

2. Fluctuating Kinetic Energy Balance

From Hinze (1975), the equation for the total turbulent fluctuating kinetic energy in a boundary layer is as follows (all quantities are dimensionless):

$$0 = -\frac{\partial}{\partial y} \left[\overline{v \left(p + \frac{q^2}{2} \right)} \right] - \overline{uv} \frac{d\bar{U}}{dy} + \frac{1}{Re} \frac{\partial^2}{\partial x_j \partial x_j} \left[\overline{\frac{q^2}{2}} \right] - \frac{1}{Re} \frac{\partial \overline{u_i u_j}}{\partial x_j \partial x_j} . \quad (5.2)$$

Terms I and III are transfer terms that redistribute the turbulent kinetic energy between different regions of the flow. Term I represents the convective diffusion by turbulence of the turbulent kinetic energy. Term III represents the viscous diffusion of turbulent kinetic energy. Term II represents the production of turbulent kinetic energy from the mean kinetic energy. This term is exactly the same as Term IV in (5.1) except of

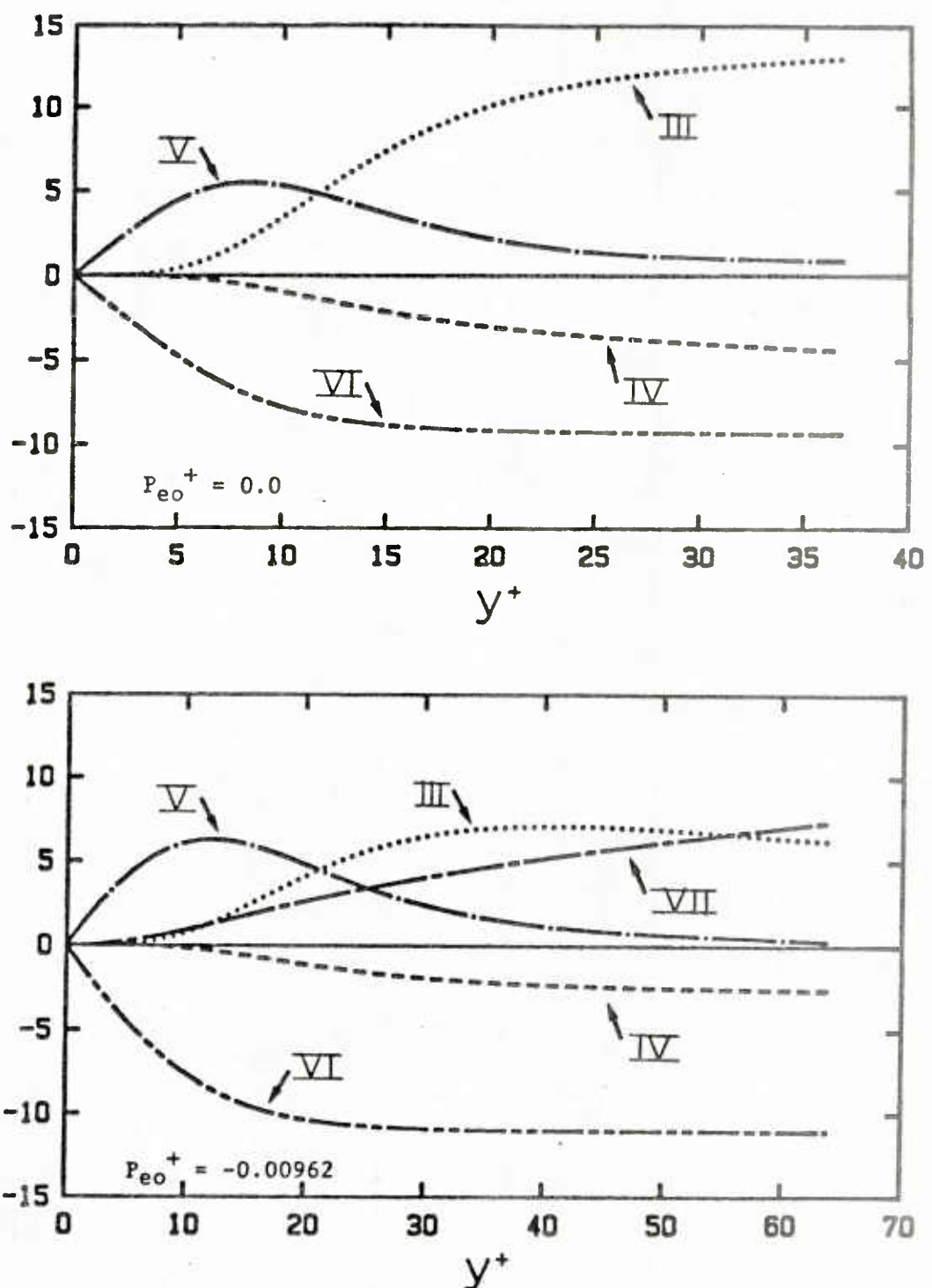


Figure 5.13 Integrated mean kinetic energy balance

opposite sign. And Term IV is the dissipation that would occur in an isotropic field. It is used here instead of the true dissipation because this formulation allows for straightforward physical interpretation of the viscous terms.

The turbulent kinetic energy balance is shown in Figure 5.14. The production of turbulent kinetic energy is large throughout the viscous wall region. The production curve reaches a maximum of 0.25 at $y^+ = 12$. This is expected since the production is the product of the turbulent and viscous stresses, whose sum is equal to 1 in wall variables. This means that the product is maximized when the two stresses are equal to each other and attain the value of 0.5 in wall units. At the wall the dissipation is equal to the viscous diffusion of the turbulent kinetic energy. The dissipation is fairly large throughout the viscous wall region. The balance for the $P_{eo}^+ = -0.00962$ run is shown in Figure 5.14. The effect of the favorable pressure gradient is to dramatically reduce the magnitudes of all the terms. However, no dramatic changes are observed in the turbulent kinetic energy balance. If the bursting process itself was changed by a favorable pressure gradient, then a radically different fluctuating kinetic energy balance would be observed. The absence of this change supports the idea presented in Section 5.1.2 that the major effect of the large favorable pressure gradient is the reduction in magnitude of the secondary flow. The amount of reduction is determined by the decreased value of the shear stress at the edge of the viscous wall region.

II. Pulsating Pressure Gradient Turbulent Flows

In this section, measurements of the wall shear stress in turbulent pulsating pipe flow are presented. Comparison is made with the numerical results, using eddy viscosity models developed in Chapter 3.

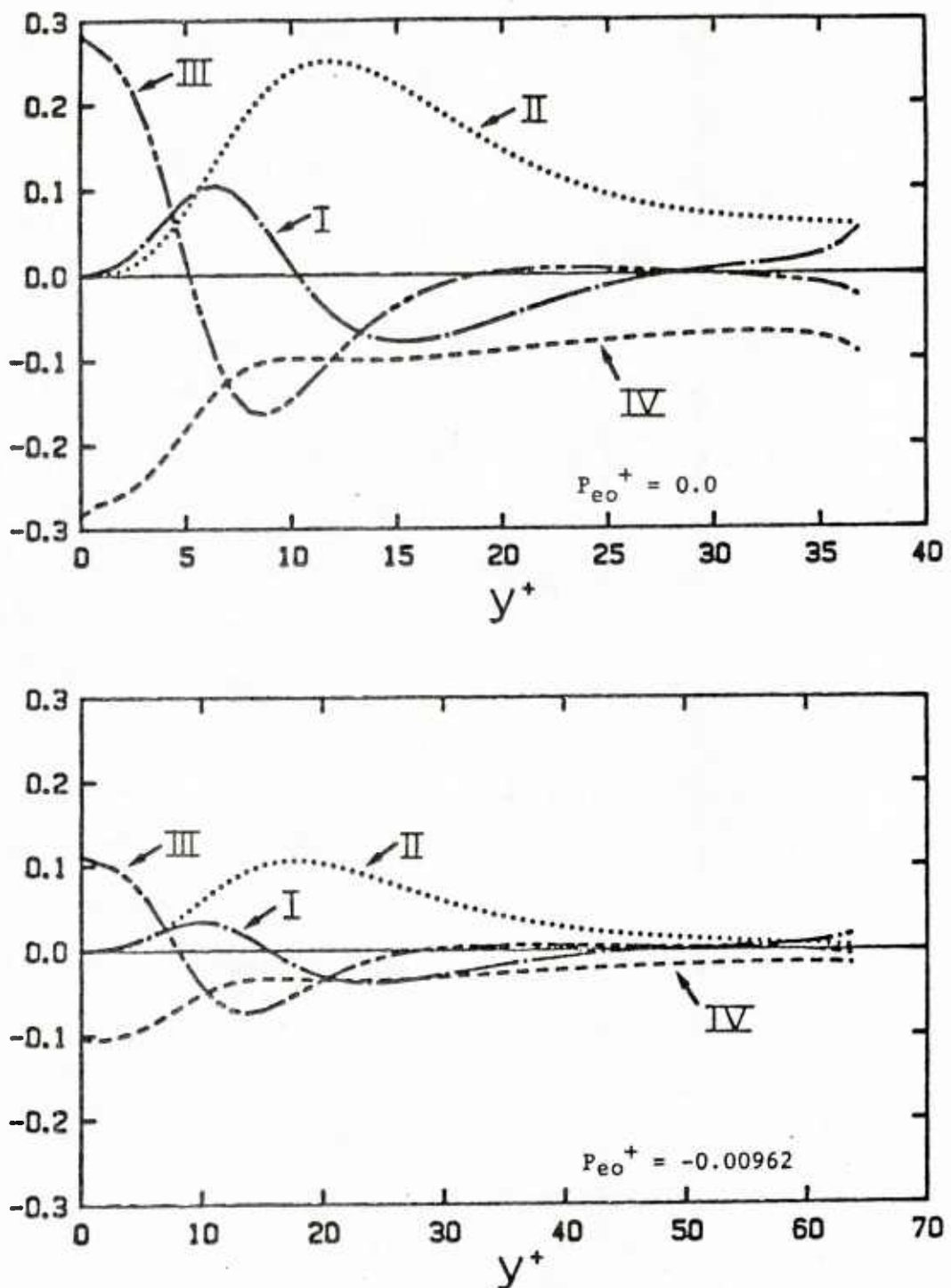


Figure 5.14 Fluctuating kinetic energy balance

A. Experimental Results

The time averaged and phase averaged results are presented for the wall shear stress, the turbulent fluctuations of the wall shear stress, and the transverse correlation coefficients of the streamwise velocity gradient at the wall. The correlation coefficient measurements are analyzed to determine the effect of the time varying pressure gradient on the streak spacing at the wall, λ_0^+ .

1. Time Averaged Results

The measured time averaged values of the velocity gradient at the wall are shown in Figure 5.15. The results agree with the Blasius friction law for turbulent pipe flow. No differences are observed between the results with and without pulsation. This clearly shows that the imposed pulsations do not reduce drag in the flow. This was expected since the amplitude of the pulsations was small (10% centerline velocity variation), and the pulsations were sinusoidal in nature.

Intensities of the turbulent fluctuations of the velocity gradient at the wall are shown in Figure 5.16. The intensities are independent of Reynolds number and of the imposed flow pulsation. The value, 0.31, agrees with previous measurements by other researchers [Sirkar (1969), Fortuna and Hanratty (1971), Eckelman (1971)].

Figures 5.17 to 5.21 show the time averaged results of the measurements of the transverse correlation coefficient of the streamwise velocity gradient at the wall for a wide range of w^+ values. Physical distances when normalized with wall variables are smaller at lower Reynolds numbers. Thus, the correlation curves for the low Reynolds number runs do not extend as far in the z^+ direction as the runs at higher Reynolds numbers. It is seen from the figures that the imposed pulsations have no effect on the

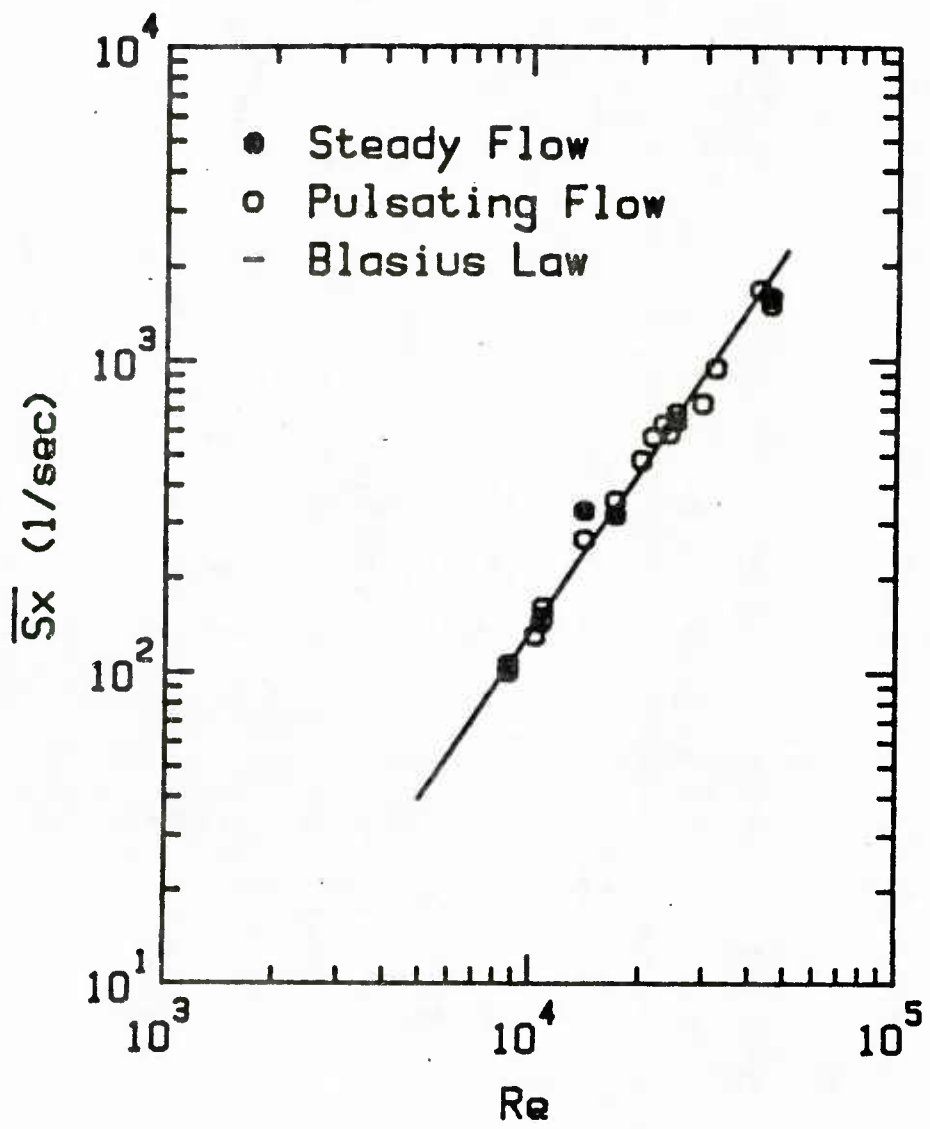


Figure 5.15 Time averaged velocity gradient at the wall
for pipe flow with and without pulsation

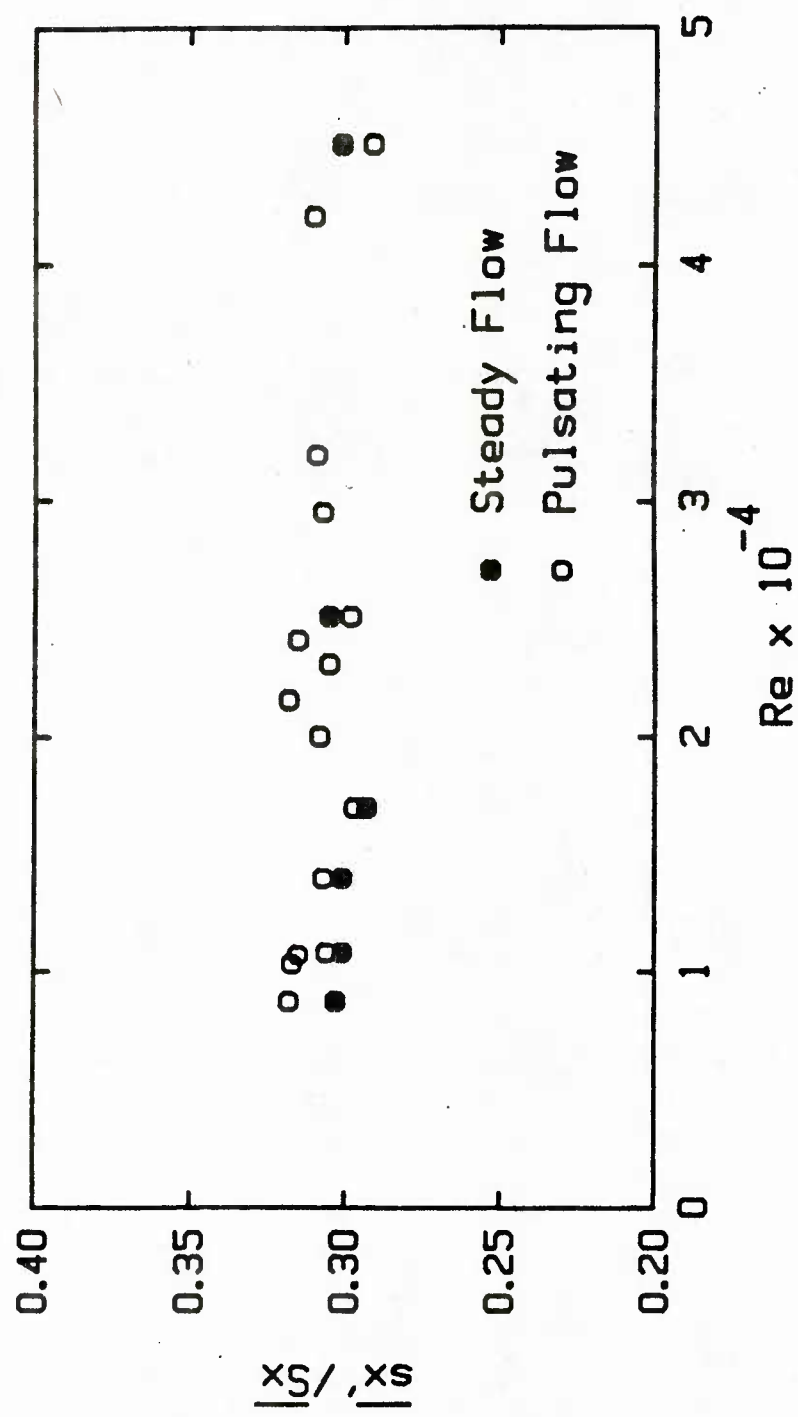


Figure 5.16 Time averaged intensities of turbulent fluctuations of the velocity gradient at the wall with and without pulsation

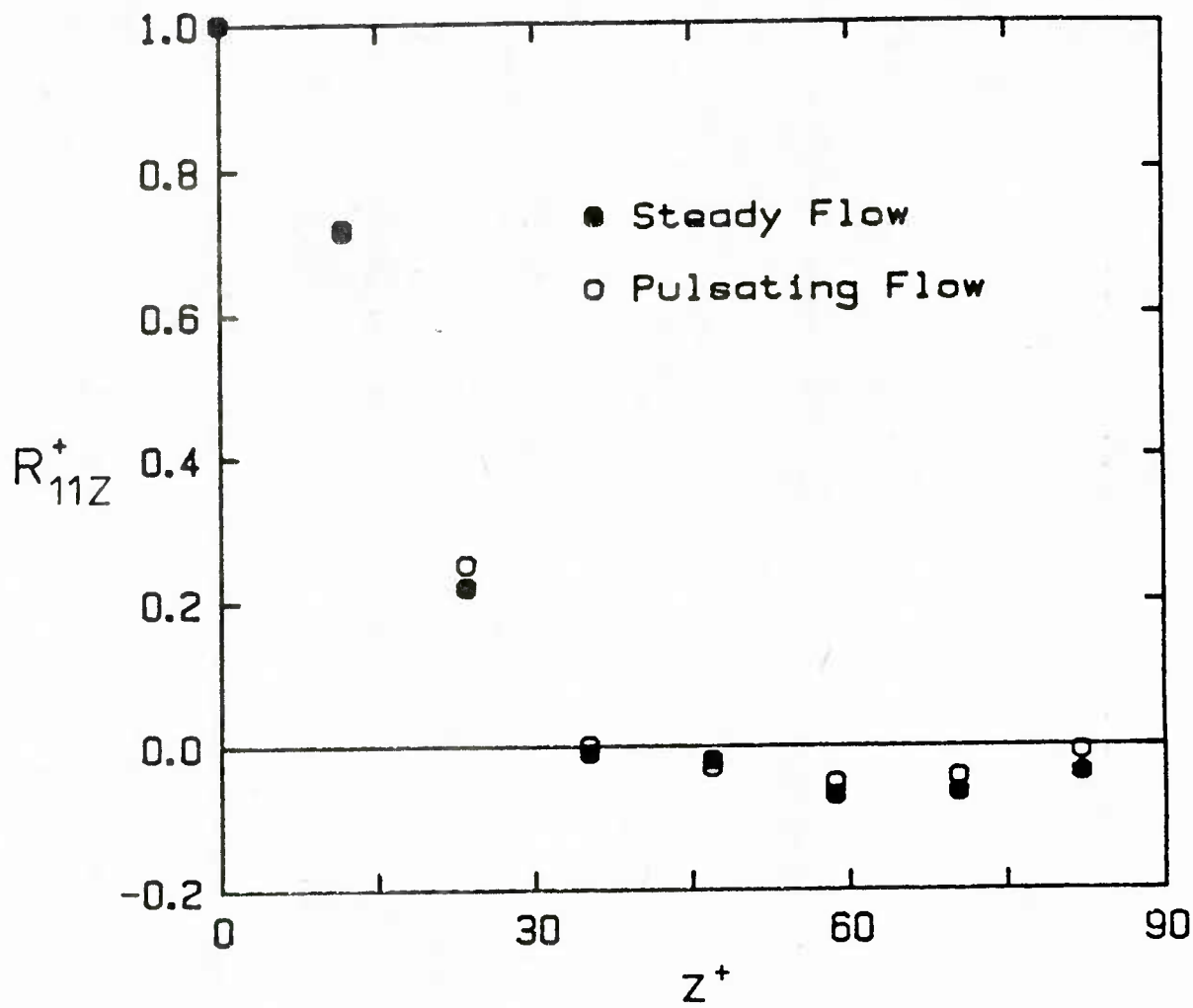


Figure 5.17 Time averaged transverse correlation coefficients of the streamwise velocity gradient at the wall with and without pulsation at $\omega^+ = 0.0012$

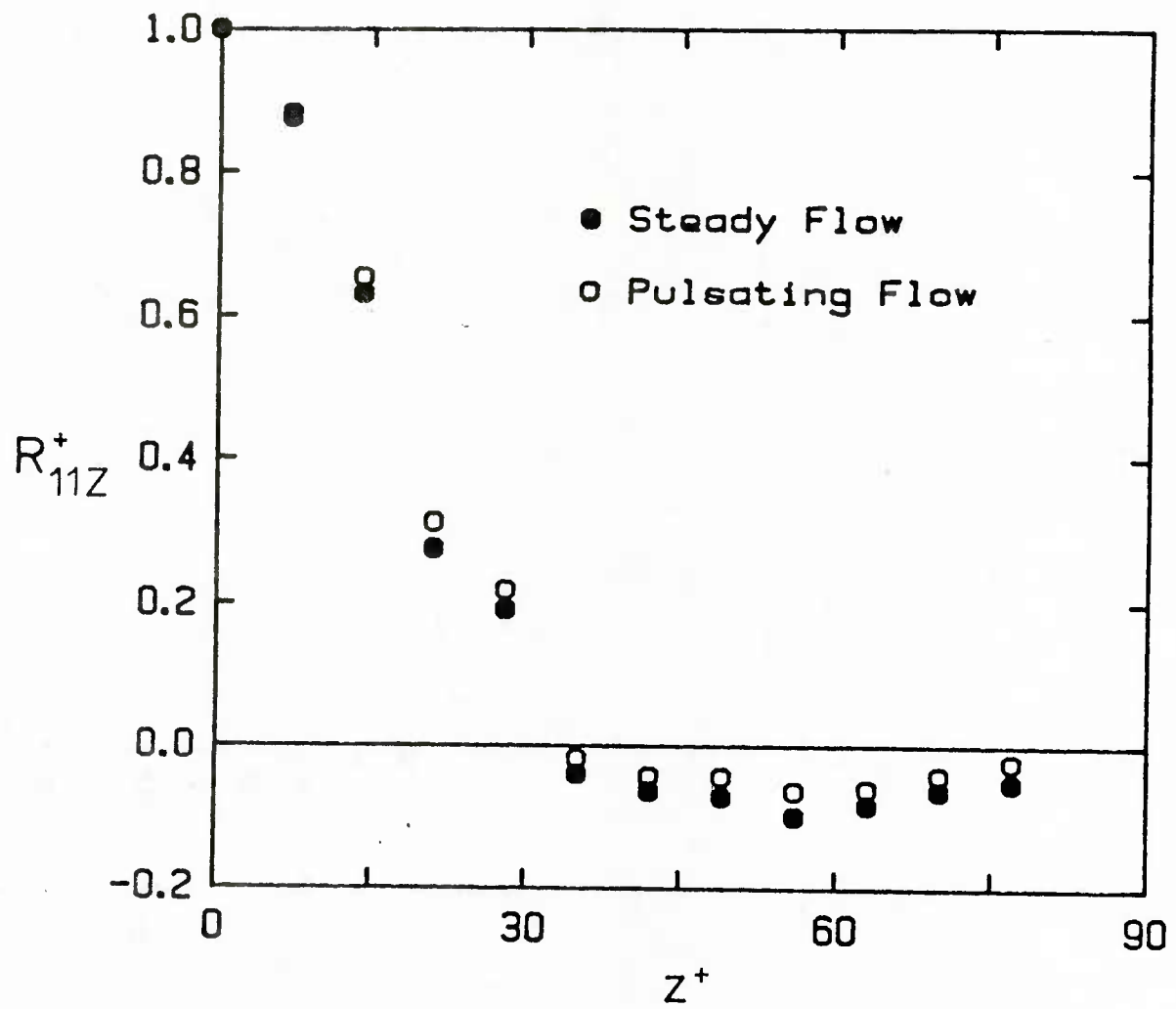


Figure 5.18 Time averaged transverse correlation coefficients of the streamwise velocity gradient at the wall with and without pulsation at $\omega^+ = 0.00375$

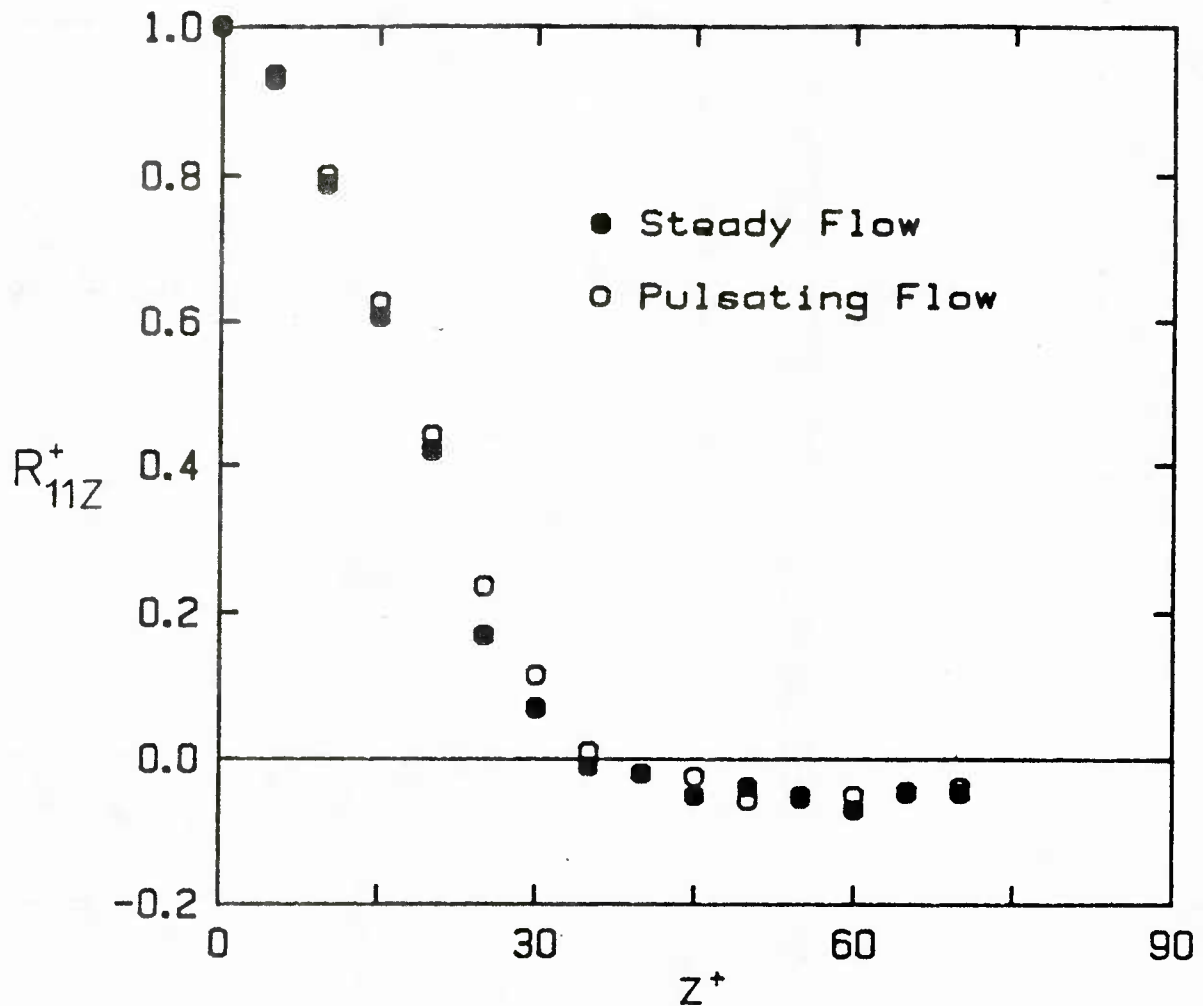


Figure 5.19 Time averaged transverse correlation coefficients of the streamwise velocity gradient at the wall with and without pulsation at $\omega^+ = 0.0093$

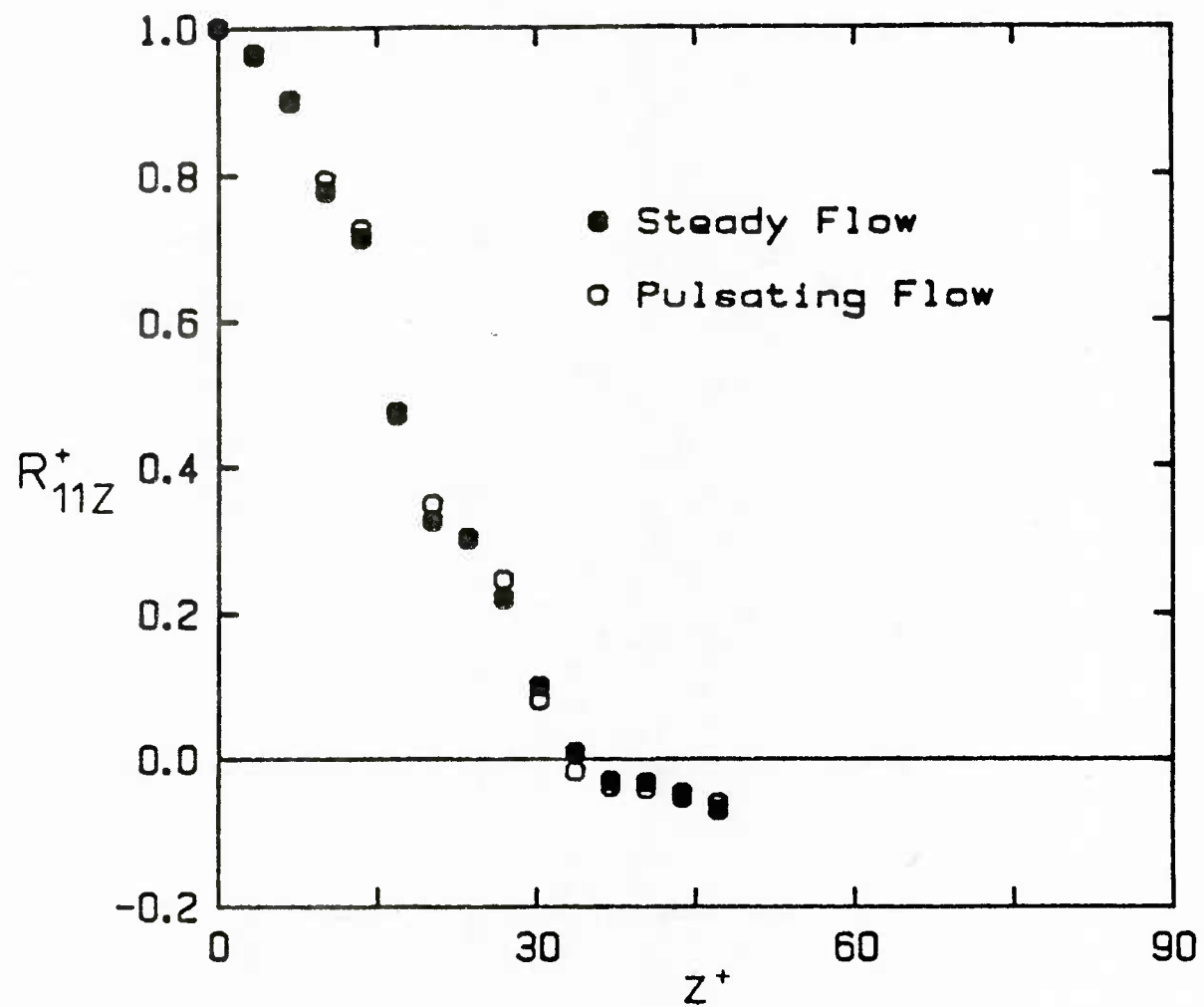


Figure 5.20 Time averaged transverse correlation coefficients of the streamwise velocity gradient at the wall with and without pulsation at $\omega^+ = 0.021$

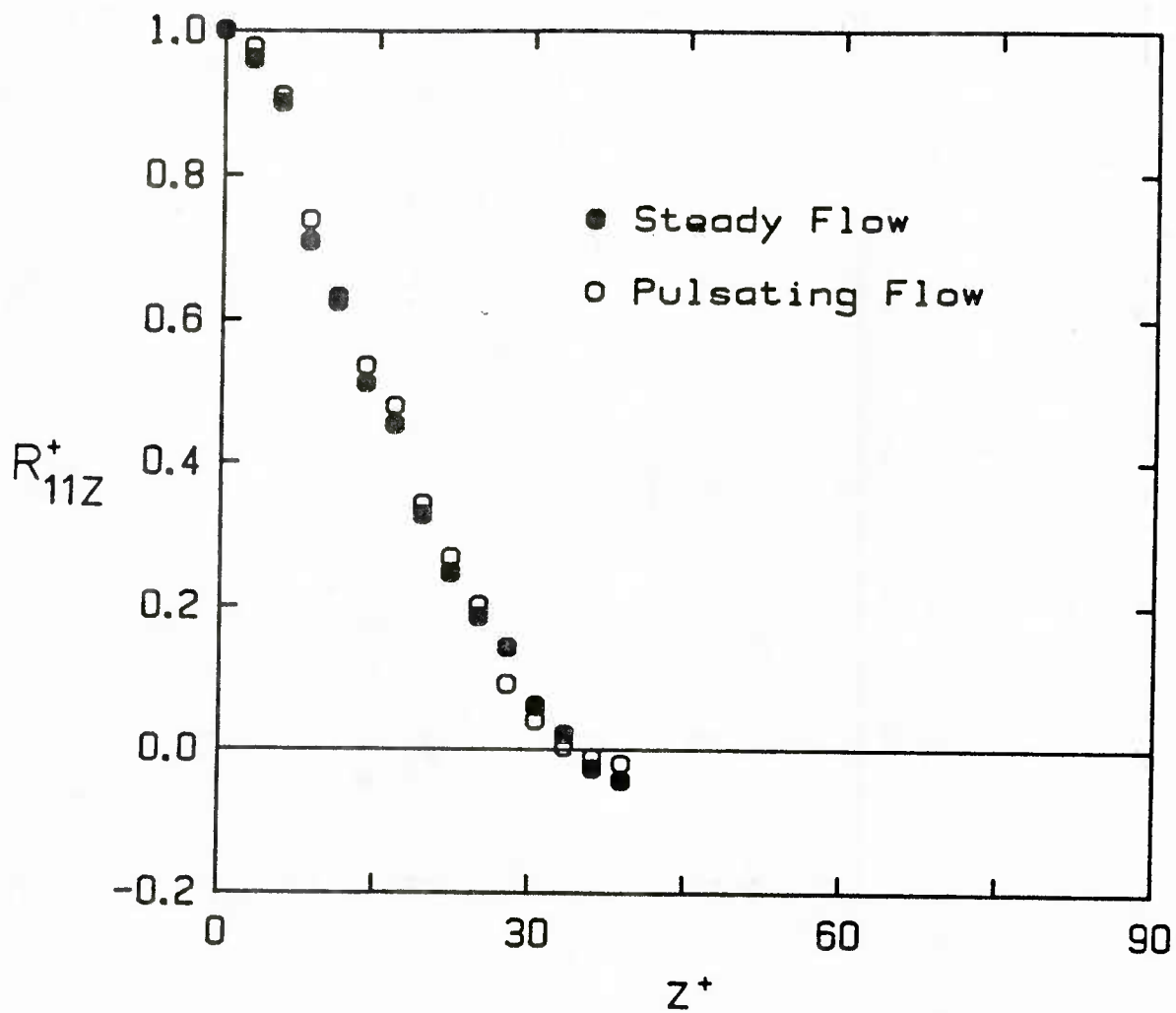


Figure 5.21 Time averaged transverse correlation coefficients of the streamwise velocity gradient at the wall with and without pulsation at $\omega^+ = 0.036$

time averaged correlation curves.

2. Phase Averaged Results

Figures 5.22 to 5.44 give a set of phase averaged data for ω^+ values ranging from 0.0012 to 0.0915. In each figure, the phase averaged favorable pressure gradient normalized with wall variables is given in (a), the phase averaged velocity gradient at the wall normalized with its time mean value is shown in (b), and the phase averaged intensity of turbulent fluctuations of velocity gradient at the wall is plotted in (c). The abscissa is the phase in a cycle. The data have been phase averaged over 1000 periods and corrected for frequency response.

There are two extremes in the data. One extreme has the characteristics of a high Re and a low frequency of pulsation. This corresponds to low ω^+ values. The high ω^+ extreme corresponds to a low Re and a high frequency of pulsation. The amplitude characteristics of the pulsating pressure gradient at these two extremes can be quantitatively explained using well known empirical relationships. Fixing the centerline variation at 10% gives the following:

$$\hat{U}_C = \frac{0.1 \text{ Re } \nu}{D (\bar{U}_B/\bar{U}_C)} \quad (5.3)$$

Using (3.70), (5.3), and the Blasius friction law ($n = \frac{1}{4}$),

$$u^* = 0.19875 (\nu/D) \text{ Re}^{7/8}, \quad (5.4)$$

the amplitude of the pulsating pressure gradient for a 10% variation of the centerline velocity can be calculated from the following:

$$\frac{d\hat{P}^+}{dx^+} = 1000 \left[\frac{D^2}{\nu} \right] \left[\frac{f}{\text{Re}^{13/8}} \right]. \quad (5.5)$$

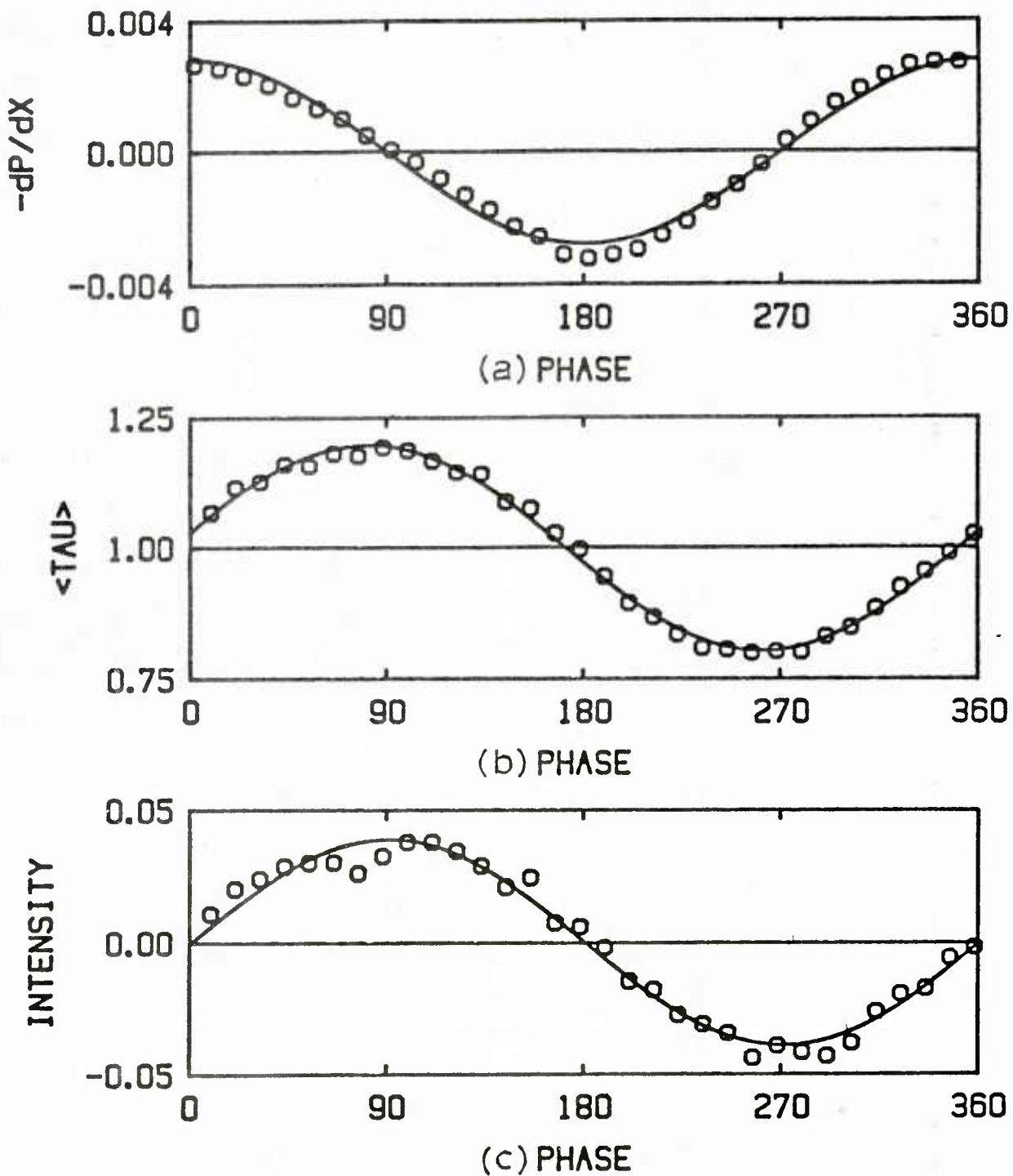


Figure 5.22 Phase averaged values at $Re = 44,900$, $f = 0.35$ Hz,
 $\omega^+ = 0.0012$ and $a = 0.1$

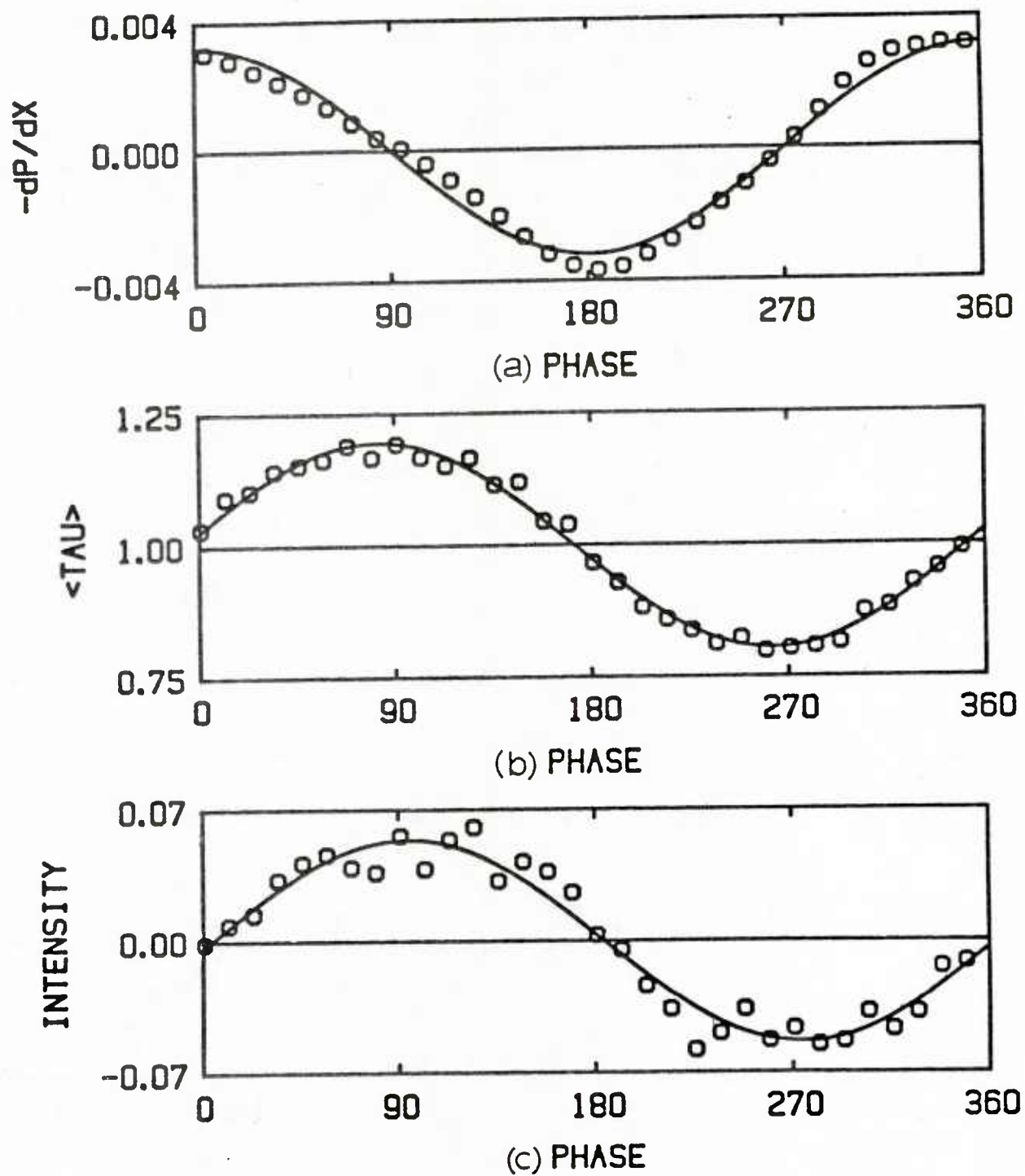


Figure 5.23 Phase averaged values at $Re = 42,000$, $f = 0.35$ Hz,
 $\omega^+ = 0.00135$ and $a = 0.101$

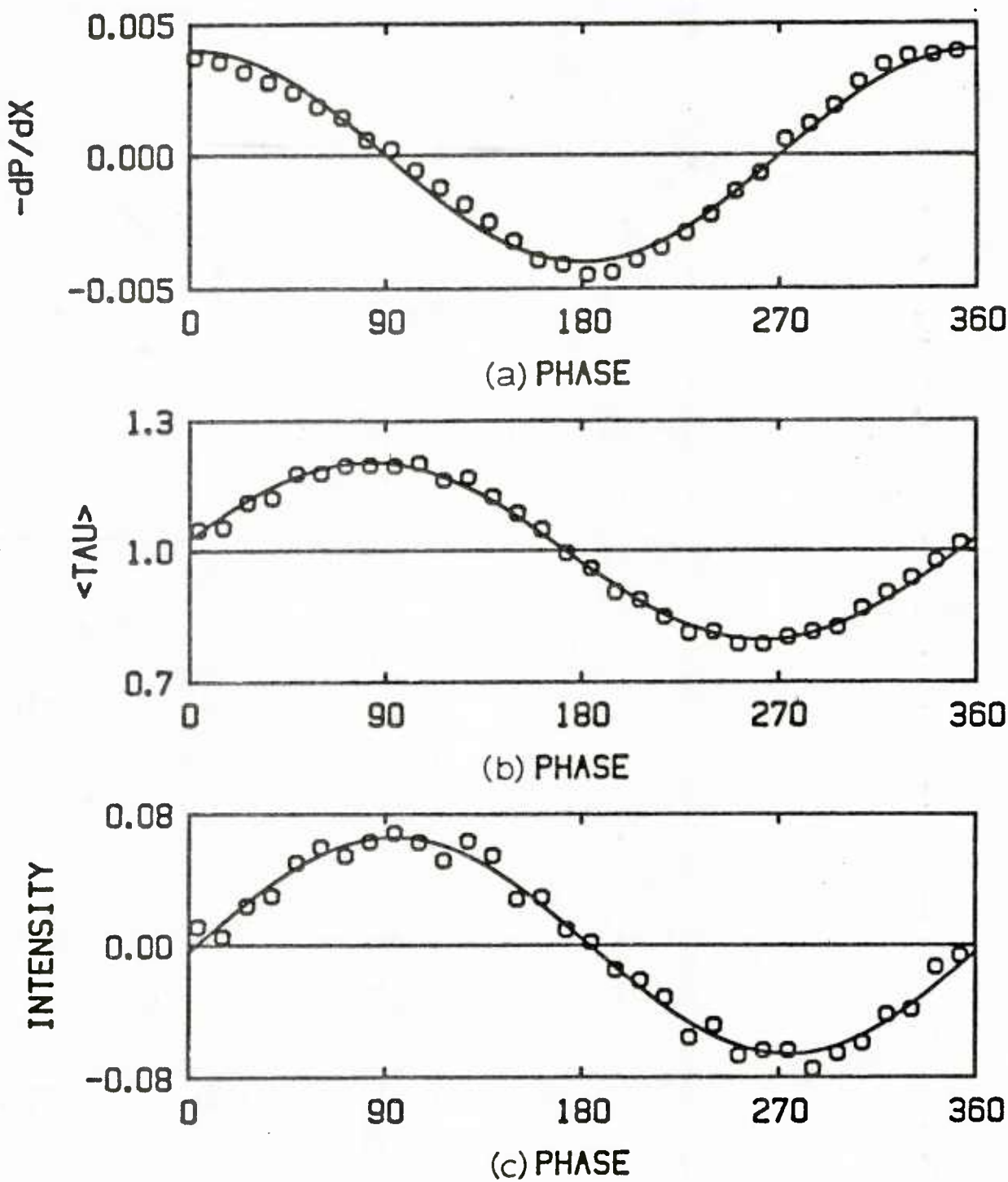


Figure 5.24 Phase averaged values at $Re = 29,400$, $f = 0.25$ Hz,
 $\omega^+ = 0.0018$ and $a = 0.099$

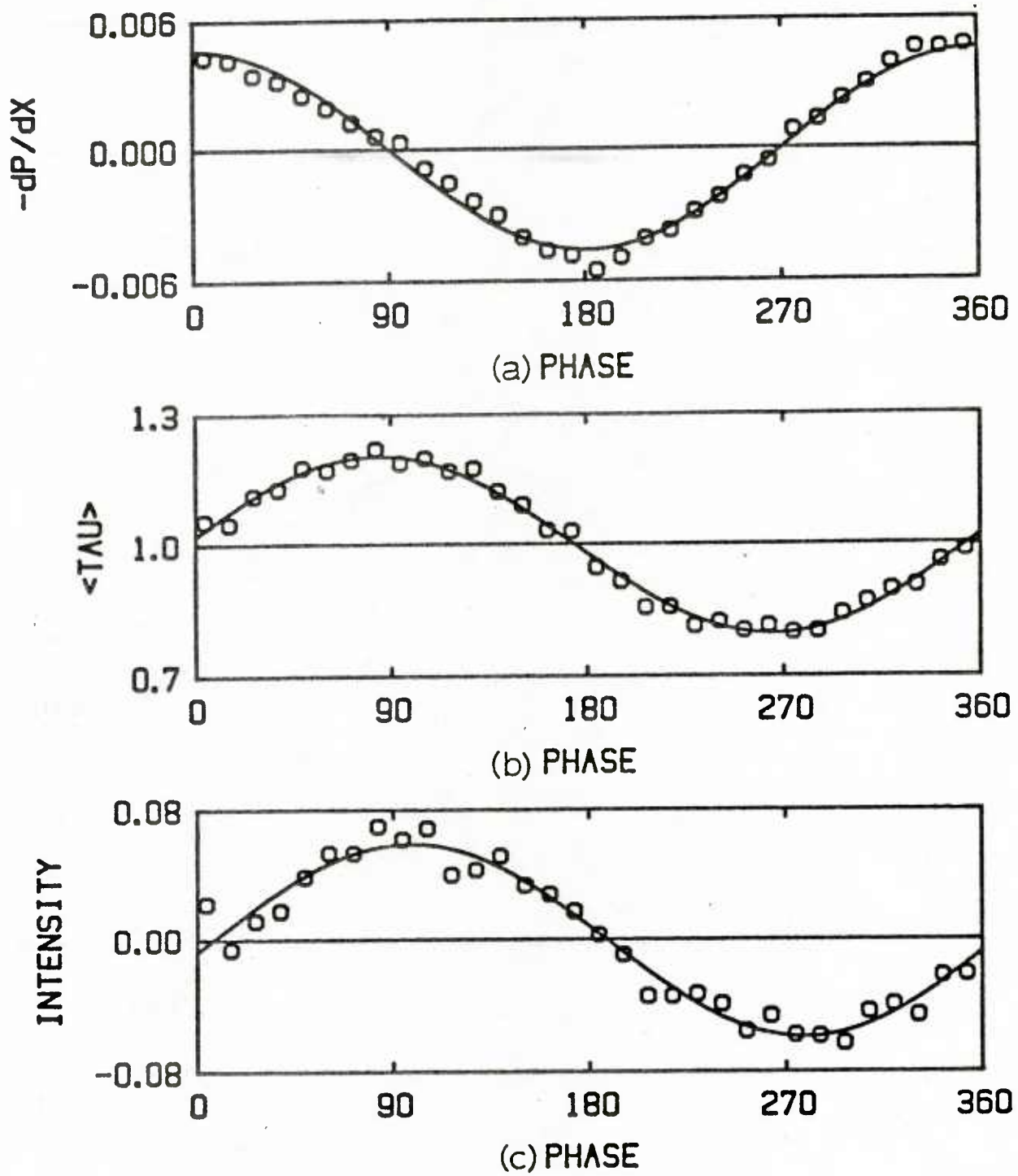


Figure 5.25 Phase averaged values at $Re = 23,700$, $f = 0.20$ Hz,
 $\omega^+ = 0.0021$ and $a = 0.1$

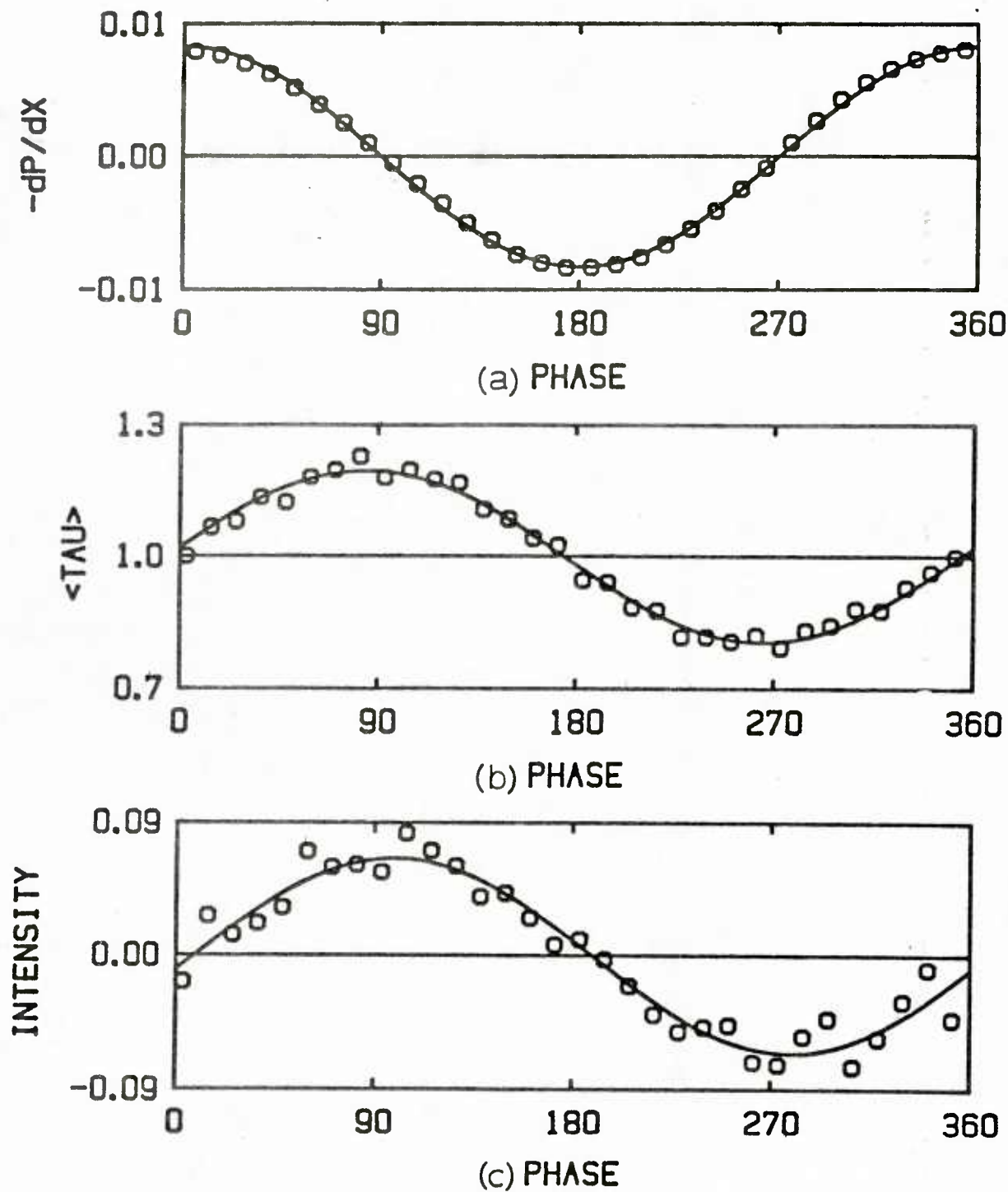


Figure 5.26 Phase averaged values at $Re = 31,800$, $f = 0.60$ Hz,
 $\omega^+ = 0.00375$ and $a = 0.098$

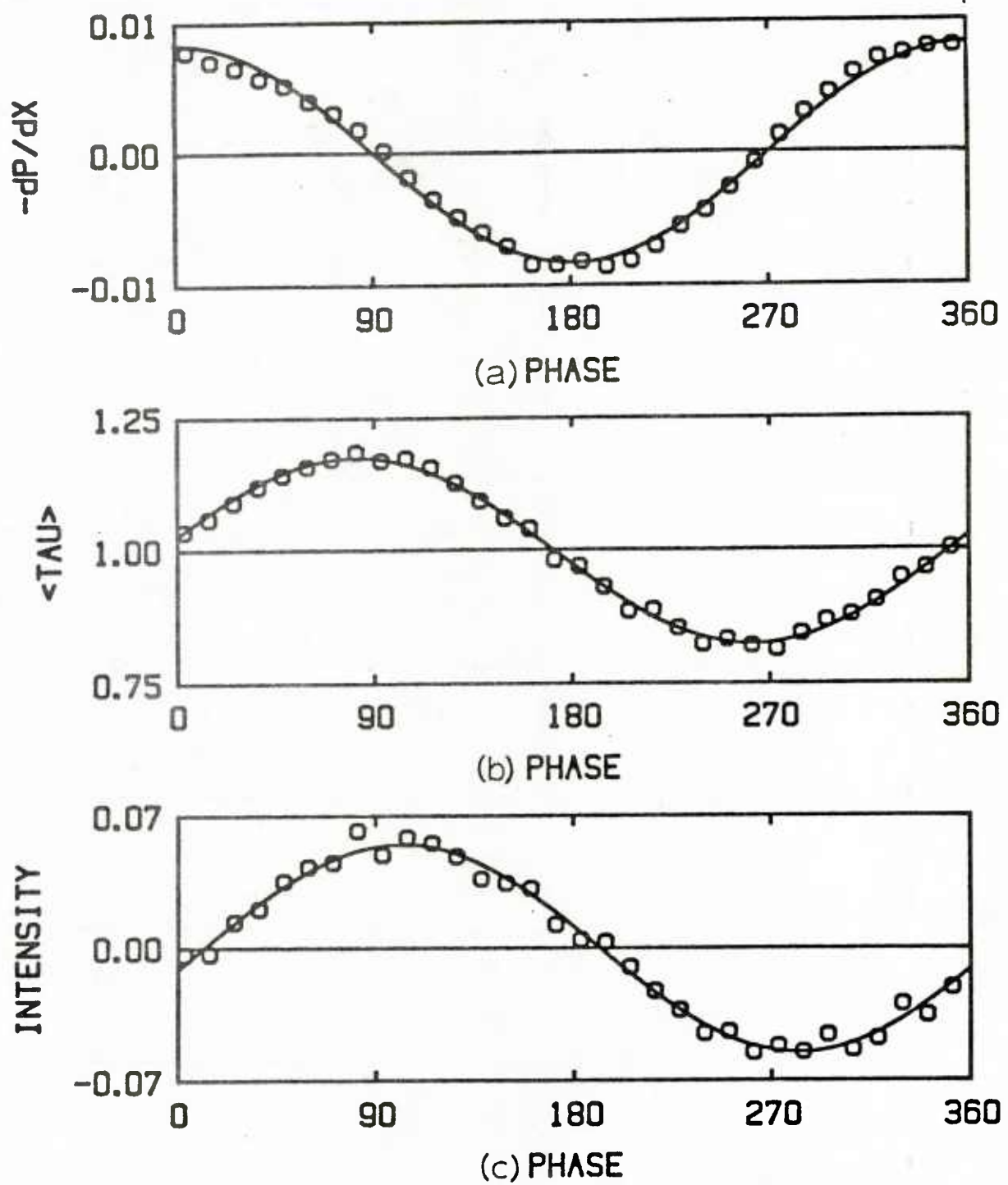


Figure 5.27 Phase averaged values at $Re = 25,200$, $f = 0.40$ Hz,
 $\omega^+ = 0.00375$ and $a = 0.1$

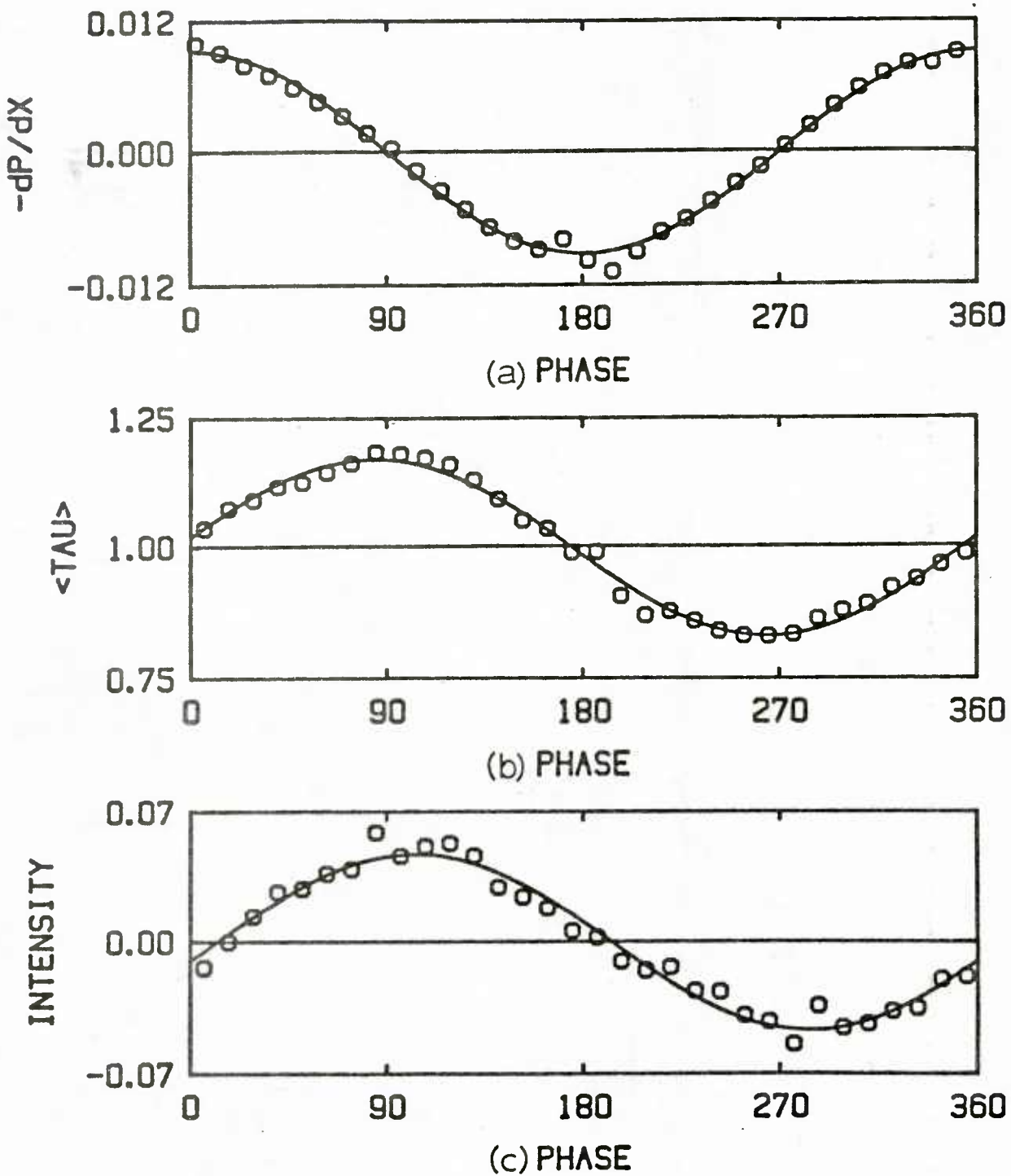


Figure 5.28 Phase averaged values at $Re = 20,100$, $f = 0.30$ Hz,
 $\omega^+ = 0.0042$ and $a = 0.101$

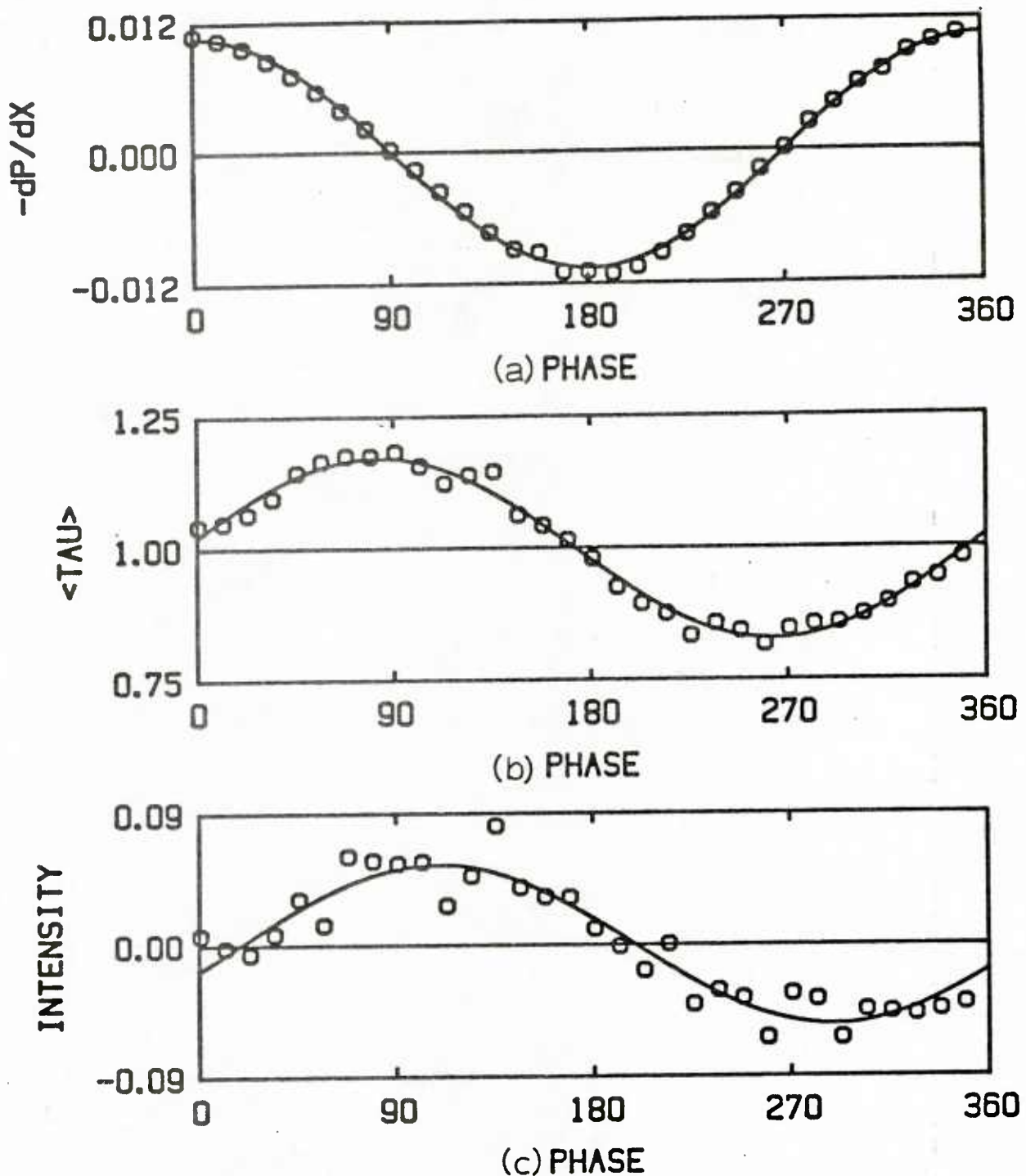


Figure 5.29 Phase averaged values at $Re = 23,000$, $f = 0.45$ Hz,
 $\omega^+ = 0.00495$ and $a = 0.098$

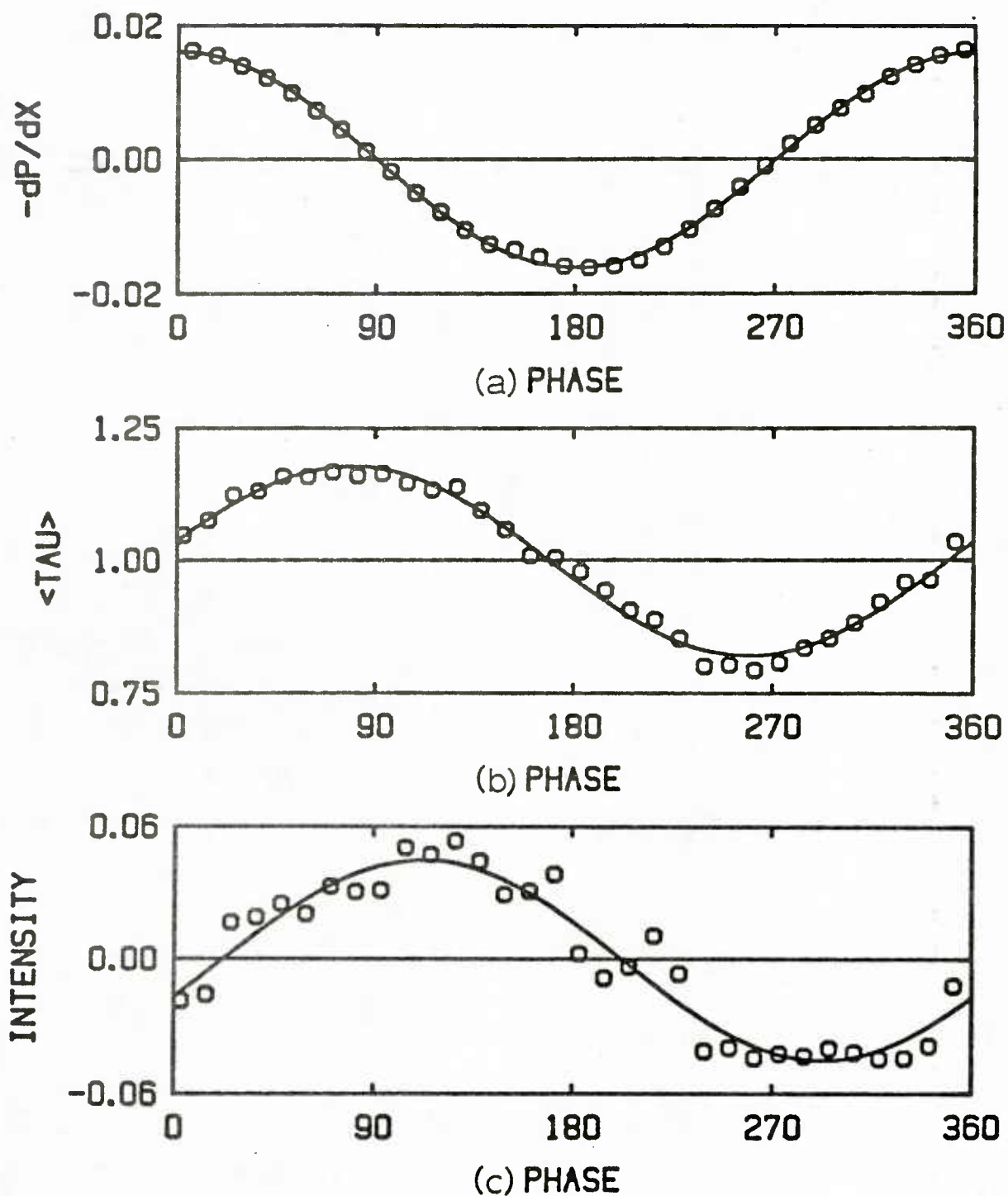


Figure 5.30 Phase averaged values at $Re = 21,400$, $f = 0.60$ Hz,
 $\omega^+ = 0.0075$ and $a = 0.099$

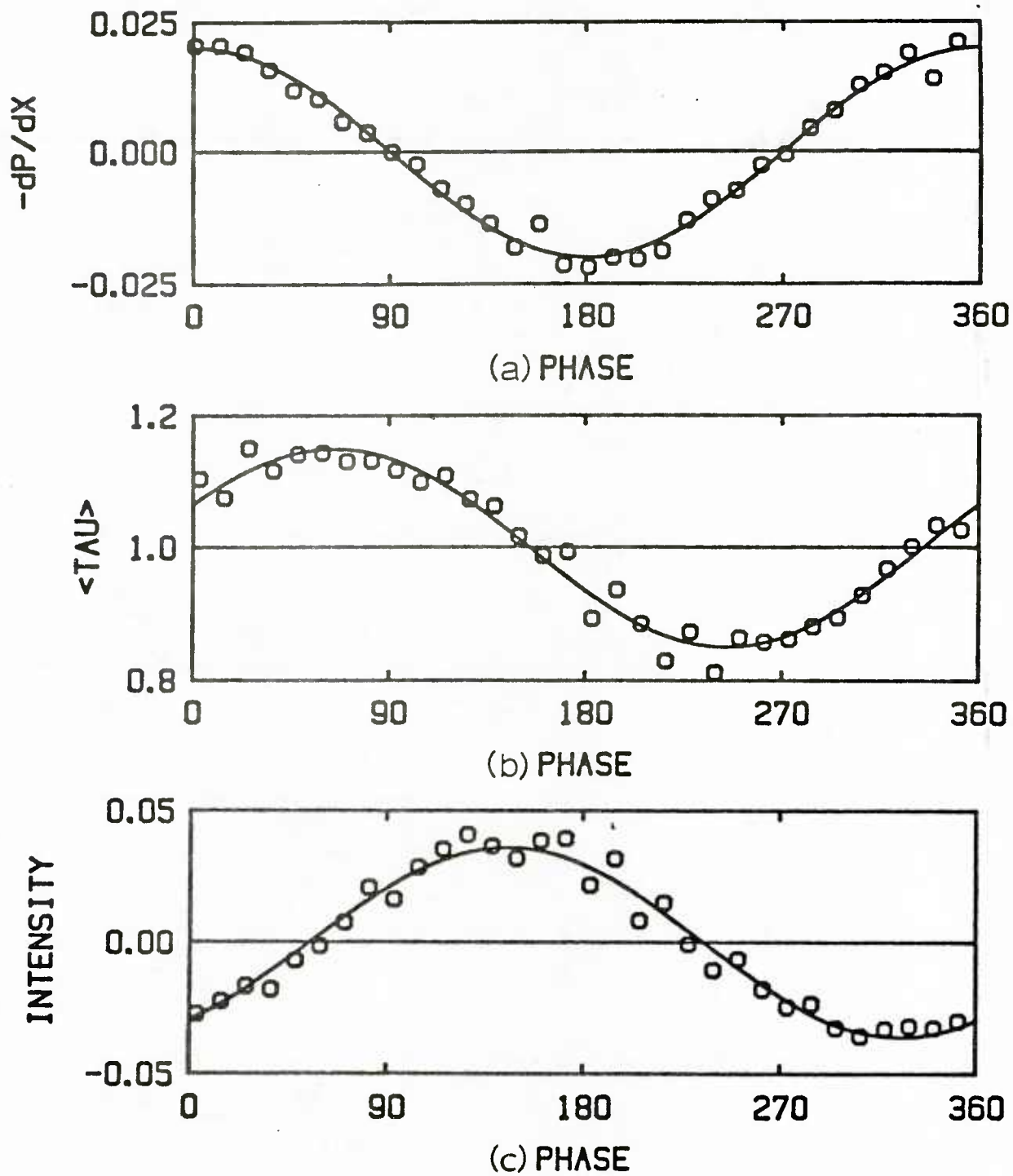


Figure 5.31 Phase averaged values at $Re = 17,100$, $f = 0.50$ Hz,
 $\omega^+ = 0.0093$ and $a = 0.102$

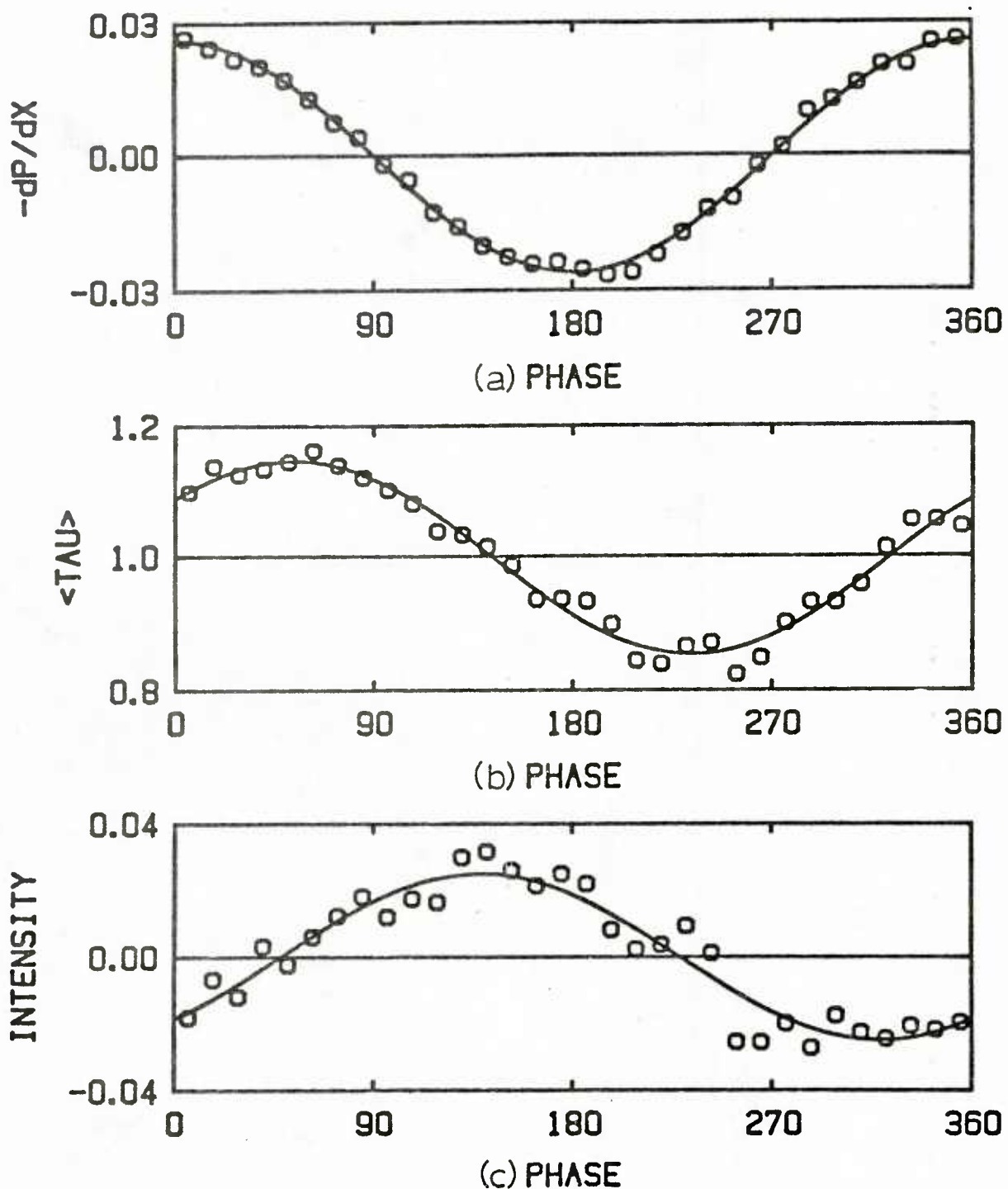


Figure 5.32 Phase averaged $Re = 14,500$, $f = 0.50$ Hz,
 $\omega^+ = 0.0123$ and $a = 0.1$

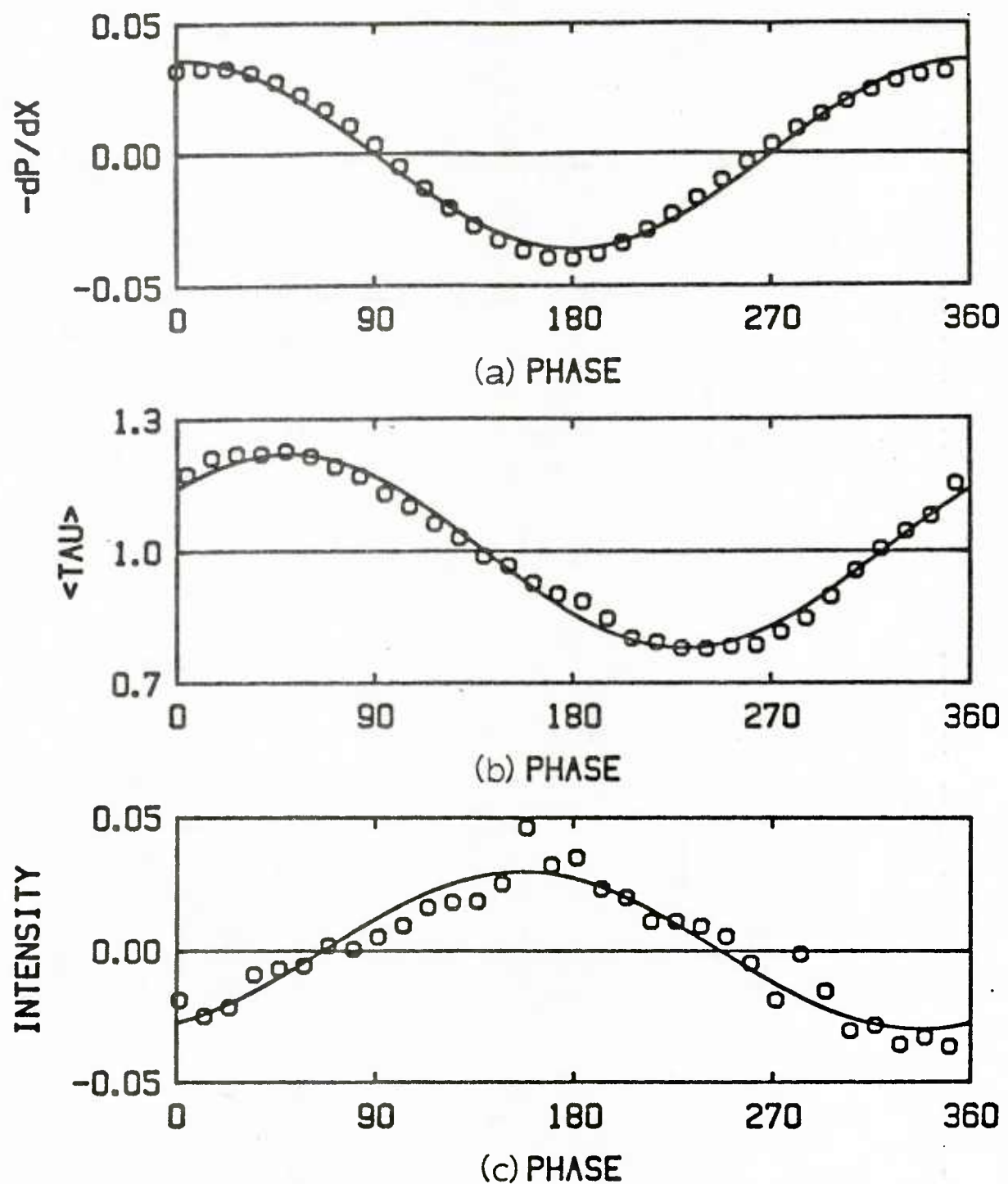


Figure 5.33 Phase averaged values at $Re = 17,900$, $f = 1.00$ Hz,
 $\omega^+ = 0.0172$ and $a = 0.098$

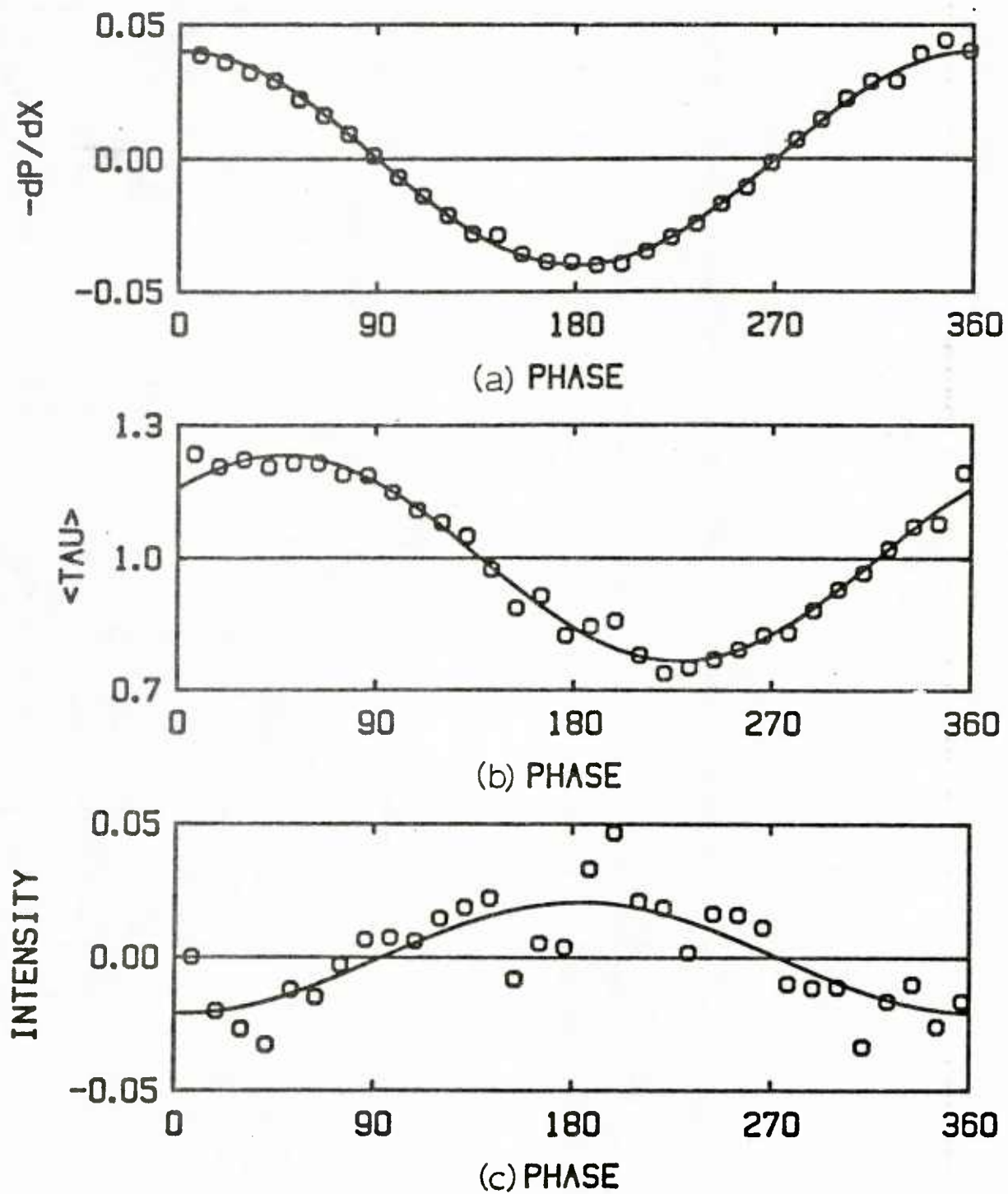


Figure 5.34 Phase averaged values at $Re = 10,600$, $f = 0.45$ Hz,
 $\omega^+ = 0.0195$ and $a = 0.101$

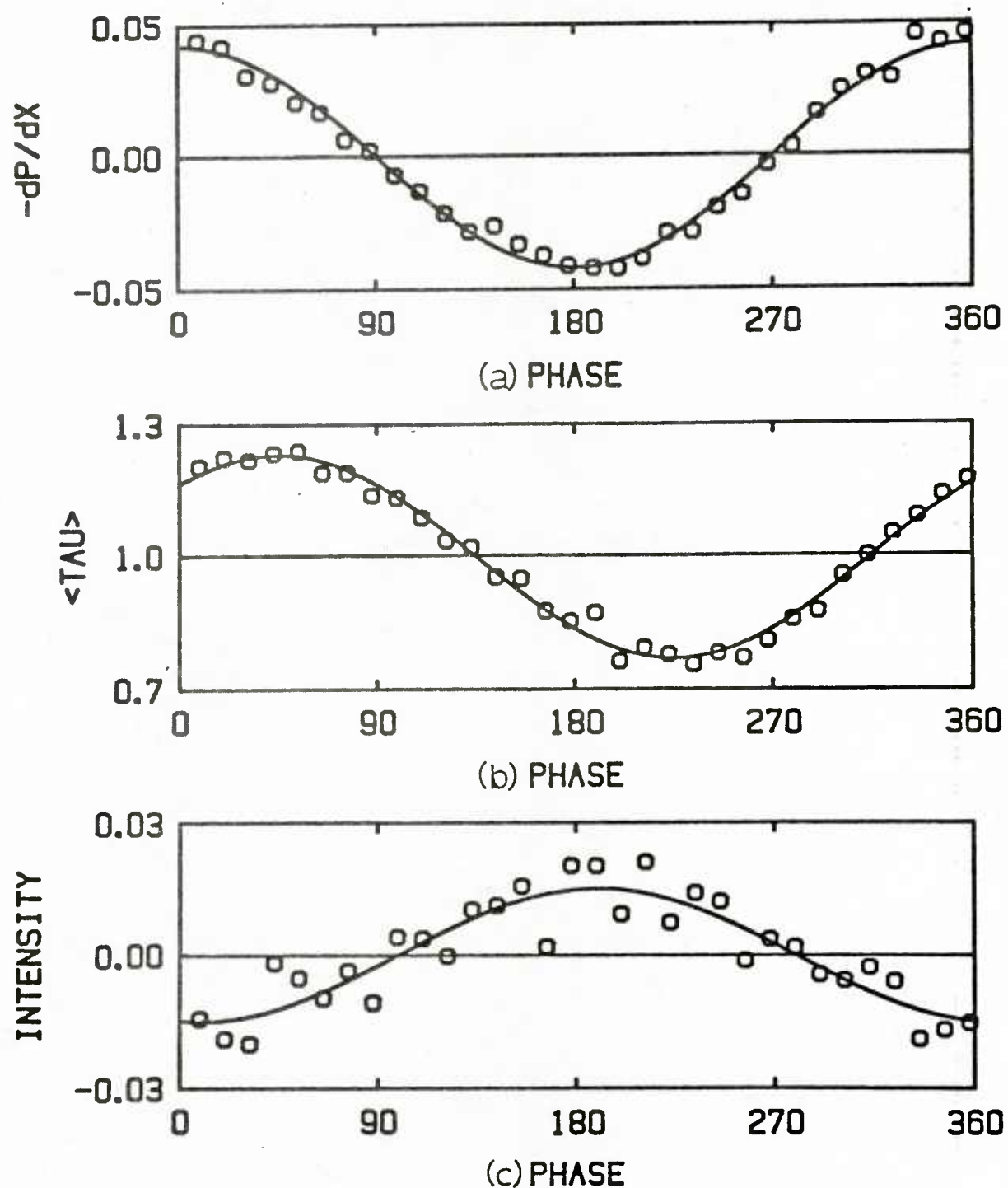


Figure 5.35 Phase averaged values at $Re = 10,700$, $f = 0.50$ Hz,
 $\omega^+ = 0.021$ and $a = 0.102$

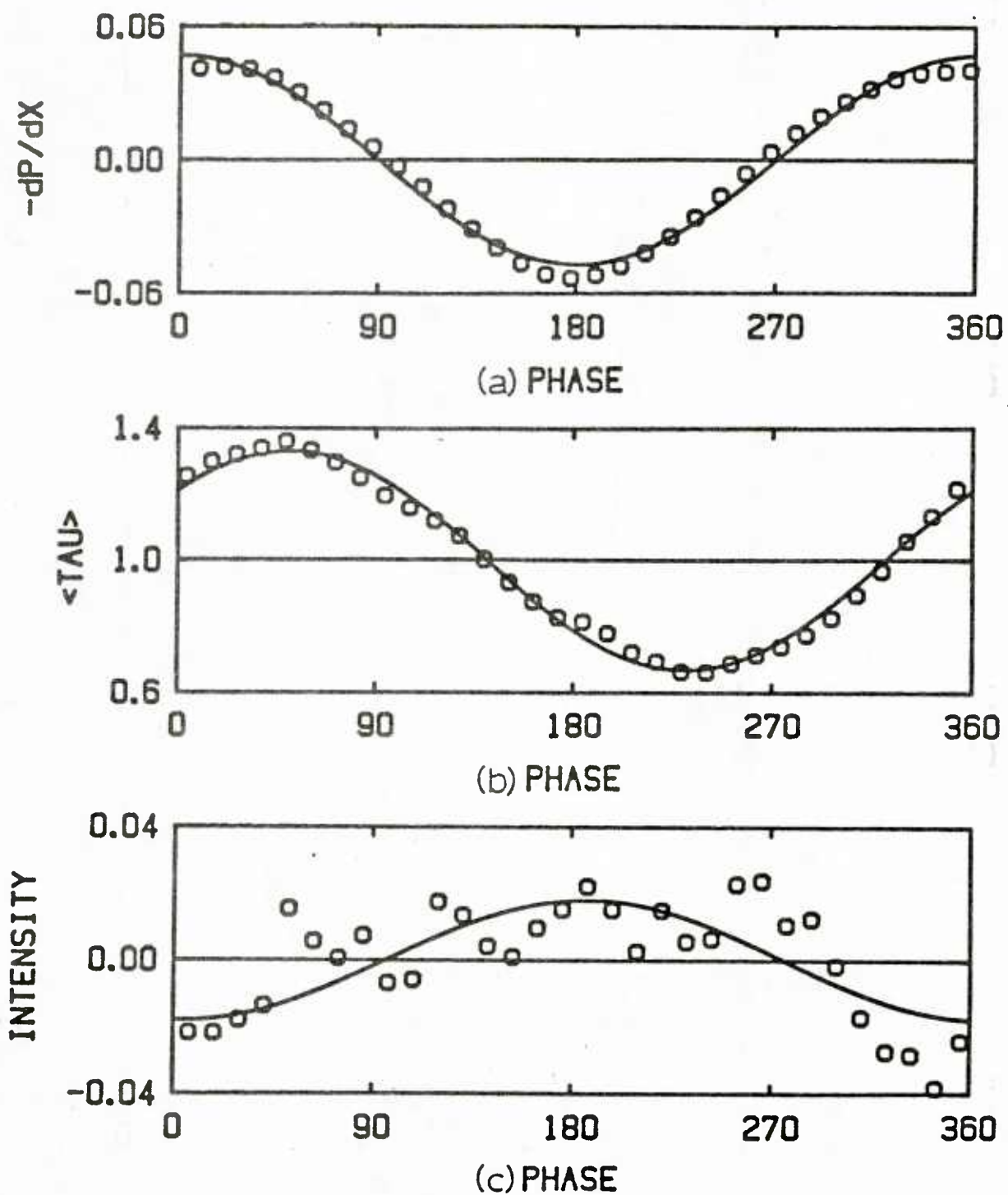


Figure 5.36 Phase averaged values at $Re = 15,300$, $f = 1.00$ Hz,
 $\omega^+ = 0.0225$ and $a = 0.099$

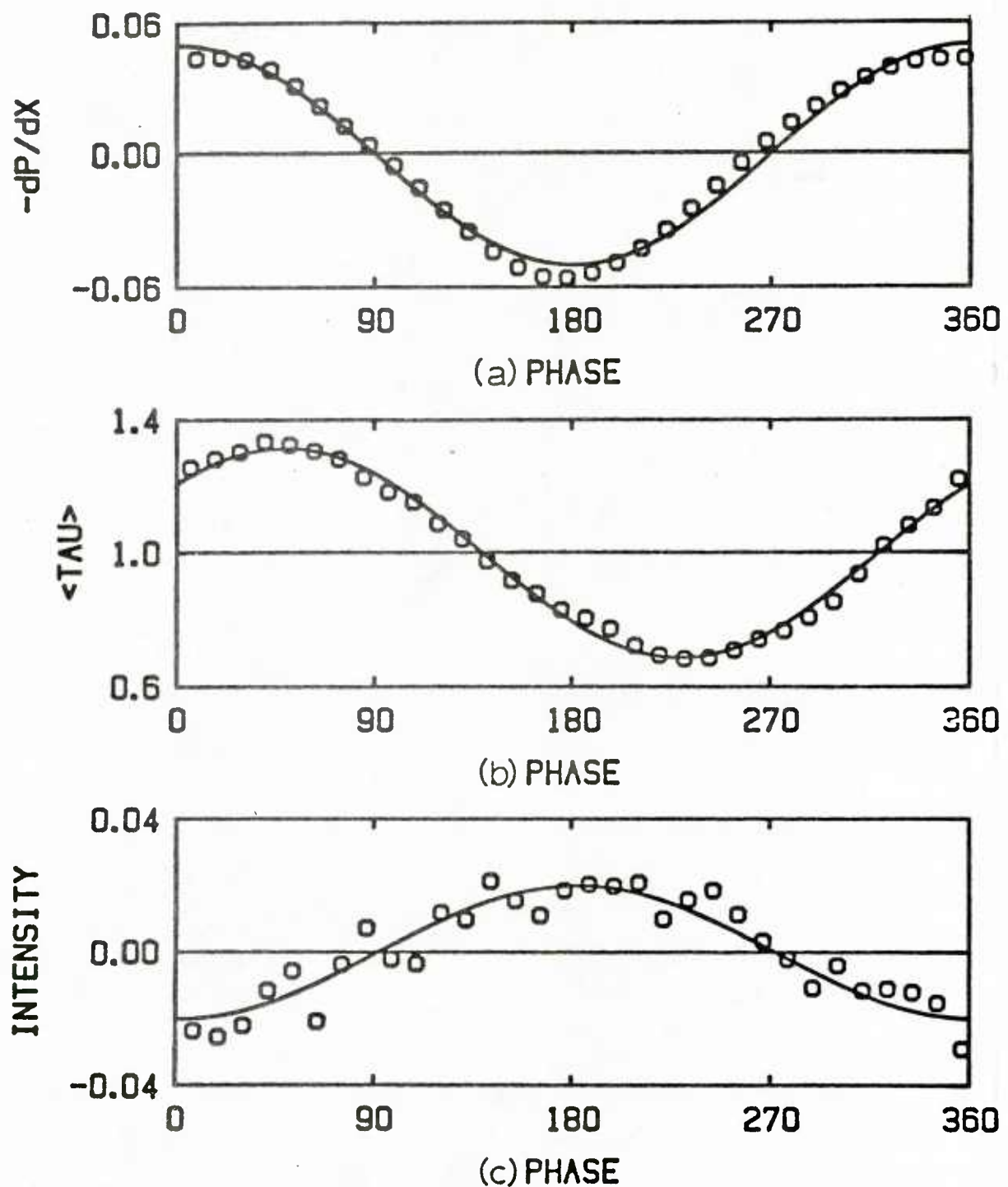


Figure 5.37 Phase averaged values at $Re = 14,600$, $f = 1.00$ Hz,
 $\omega^+ = 0.0244$ and $a = 0.098$

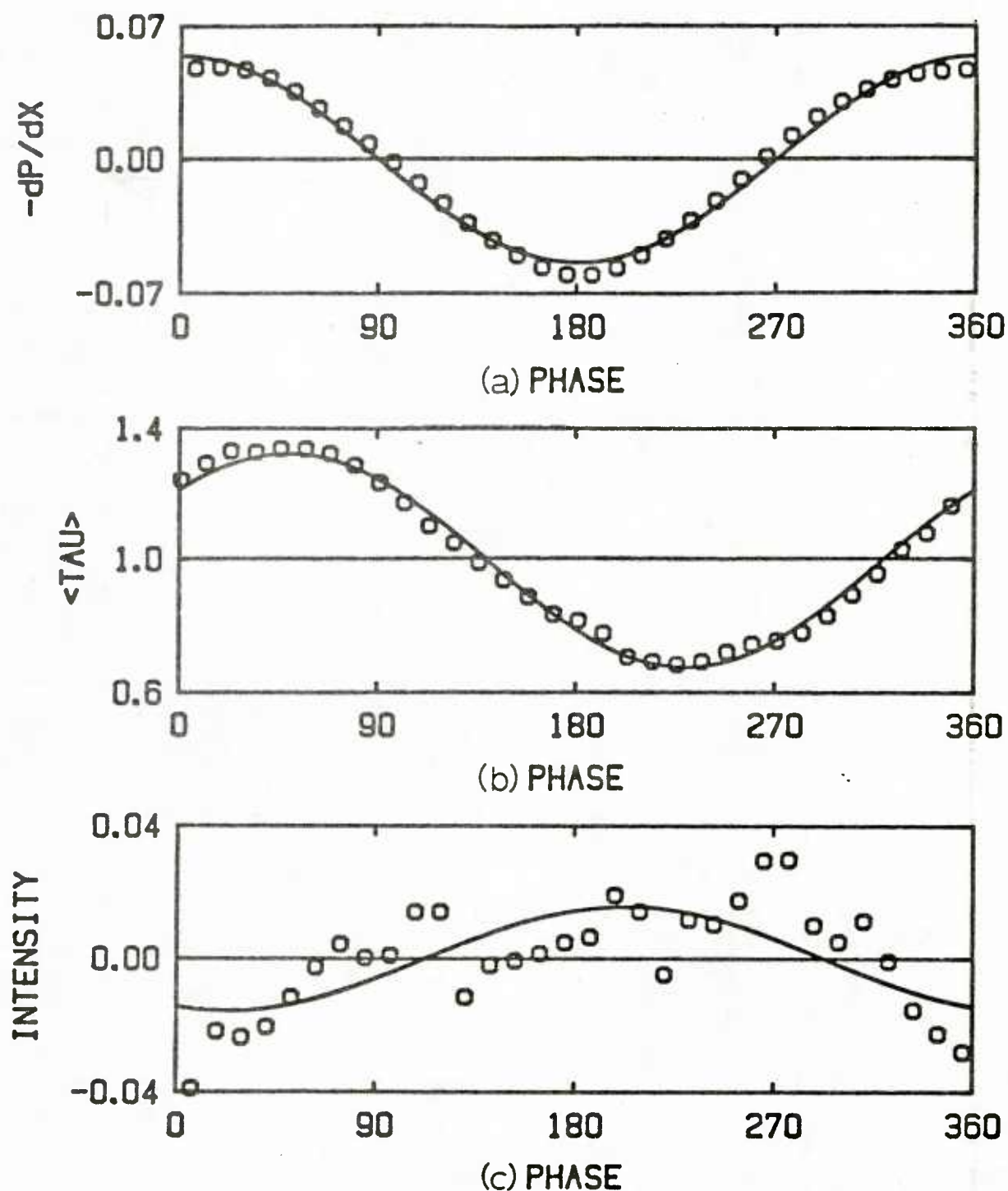


Figure 5.38 Phase averaged values at $Re = 14,200$, $f = 1.00$ Hz,
 $\omega^+ = 0.0258$ and $a = 0.101$

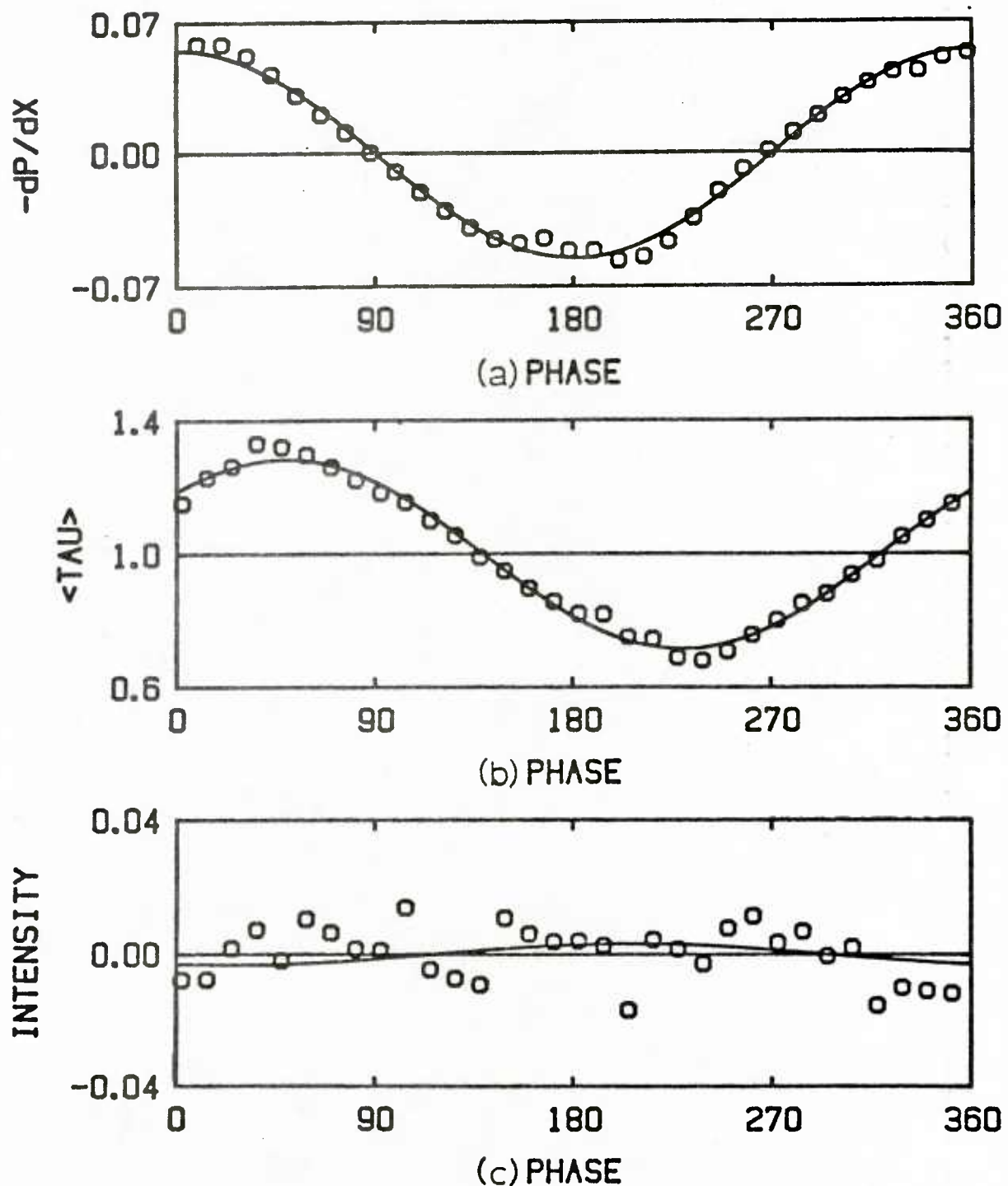


Figure 5.39 Phase averaged values at $Re = 10,300$, $f = 0.60$ Hz,
 $\omega^+ = 0.0270$ and $a = 0.101$

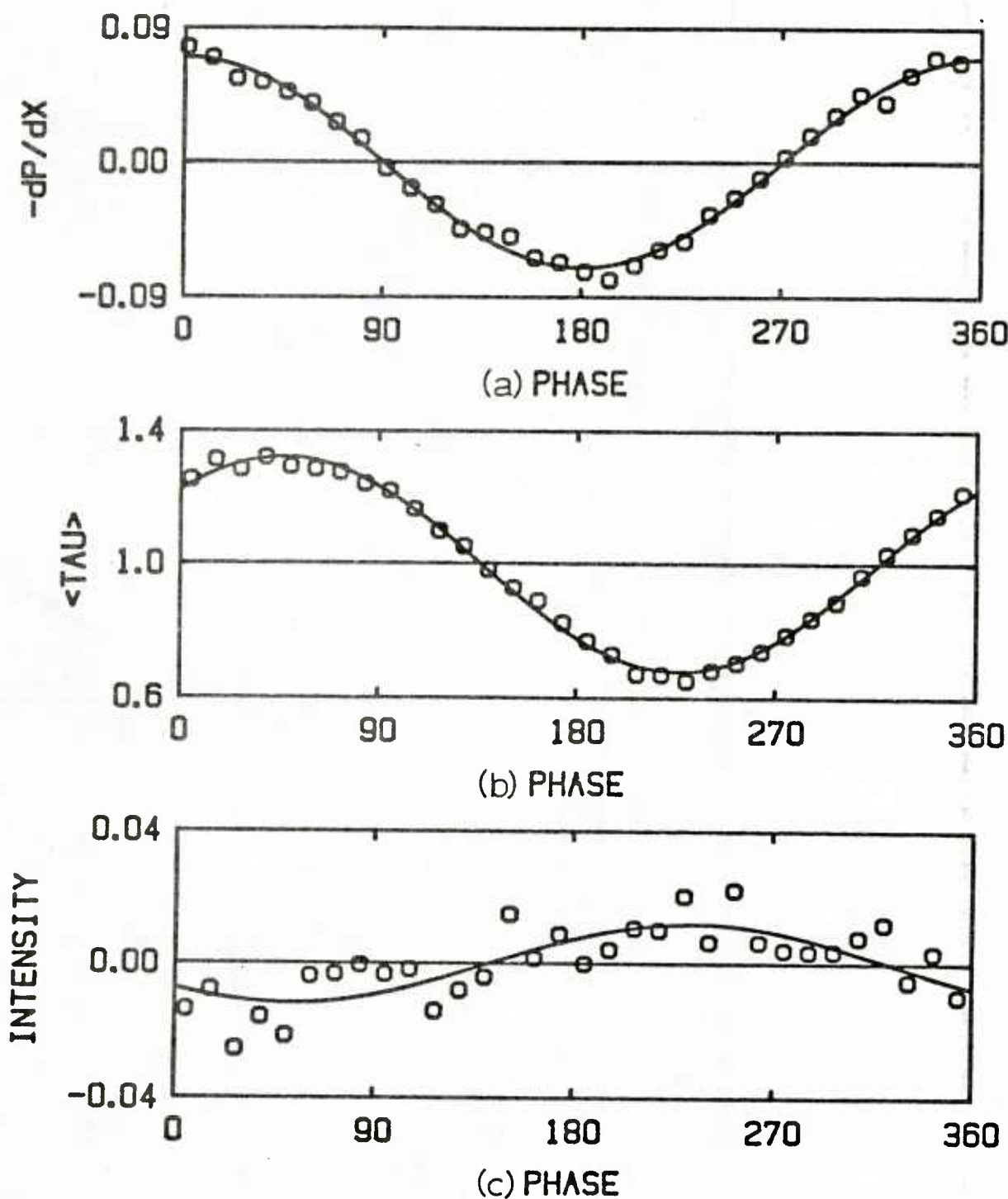


Figure 5.40 Phase averaged values at $Re = 8,750$, $f = 0.60$ Hz,
 $\omega^+ = 0.0360$ and $a = 0.099$

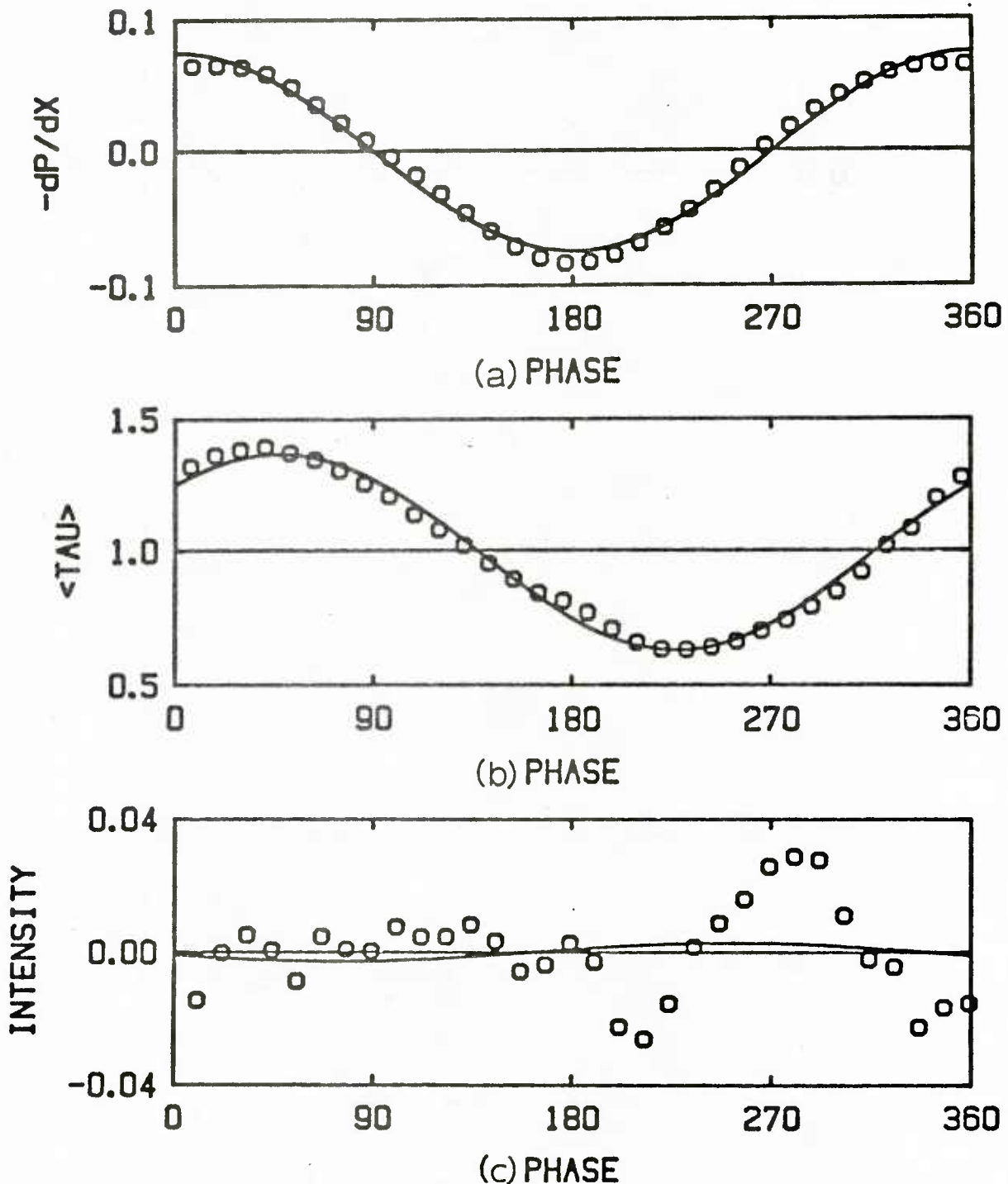


Figure 5.41 Phase averaged values at $Re = 11,400$, $f = 1.00$ Hz,
 $\omega^+ = 0.0375$ and $a = 0.098$

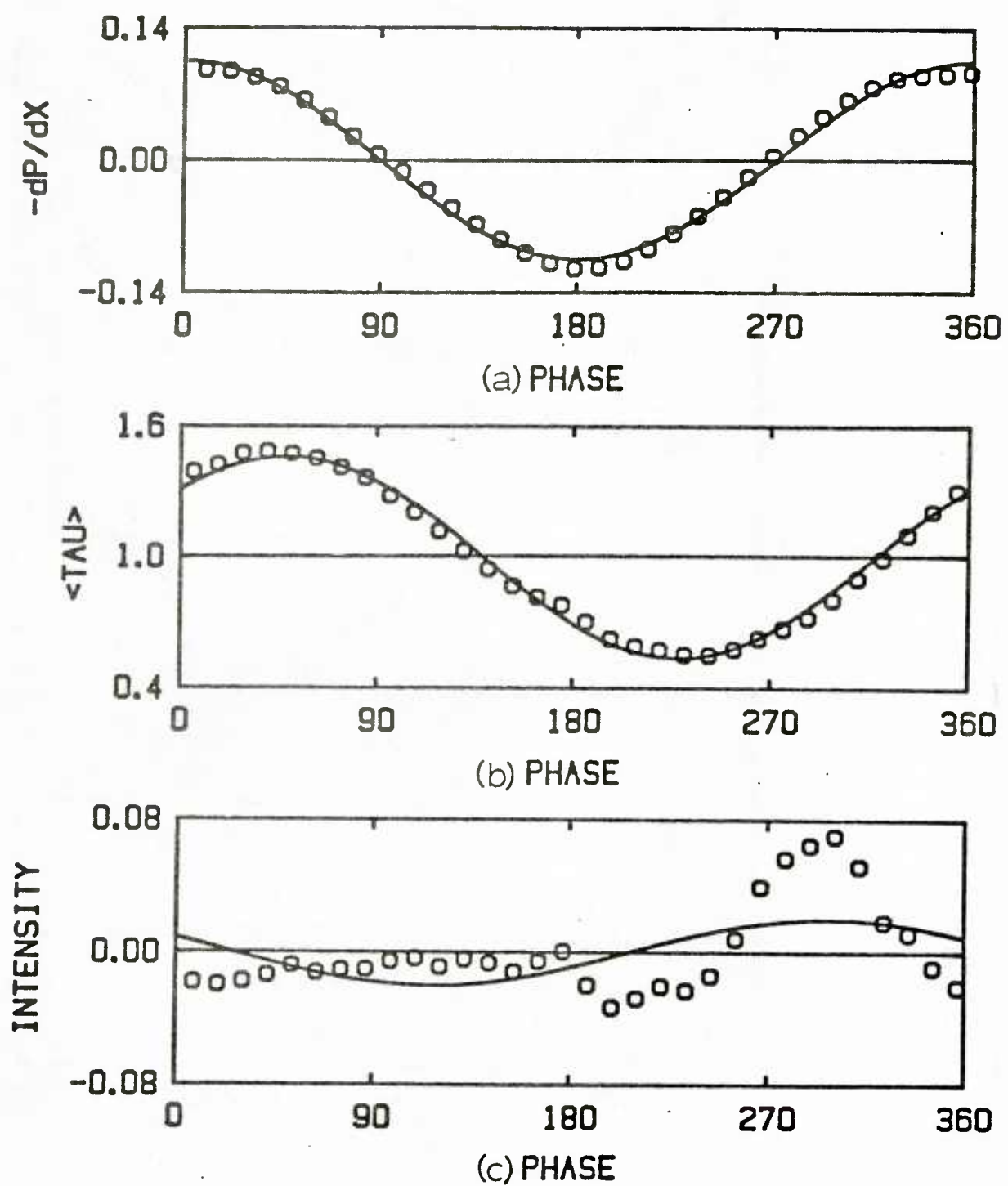


Figure 5.42 Phase averaged values at $Re = 9,200$, $f = 1.00$ Hz,
 $\omega^+ = 0.0550$ and $a = 0.100$

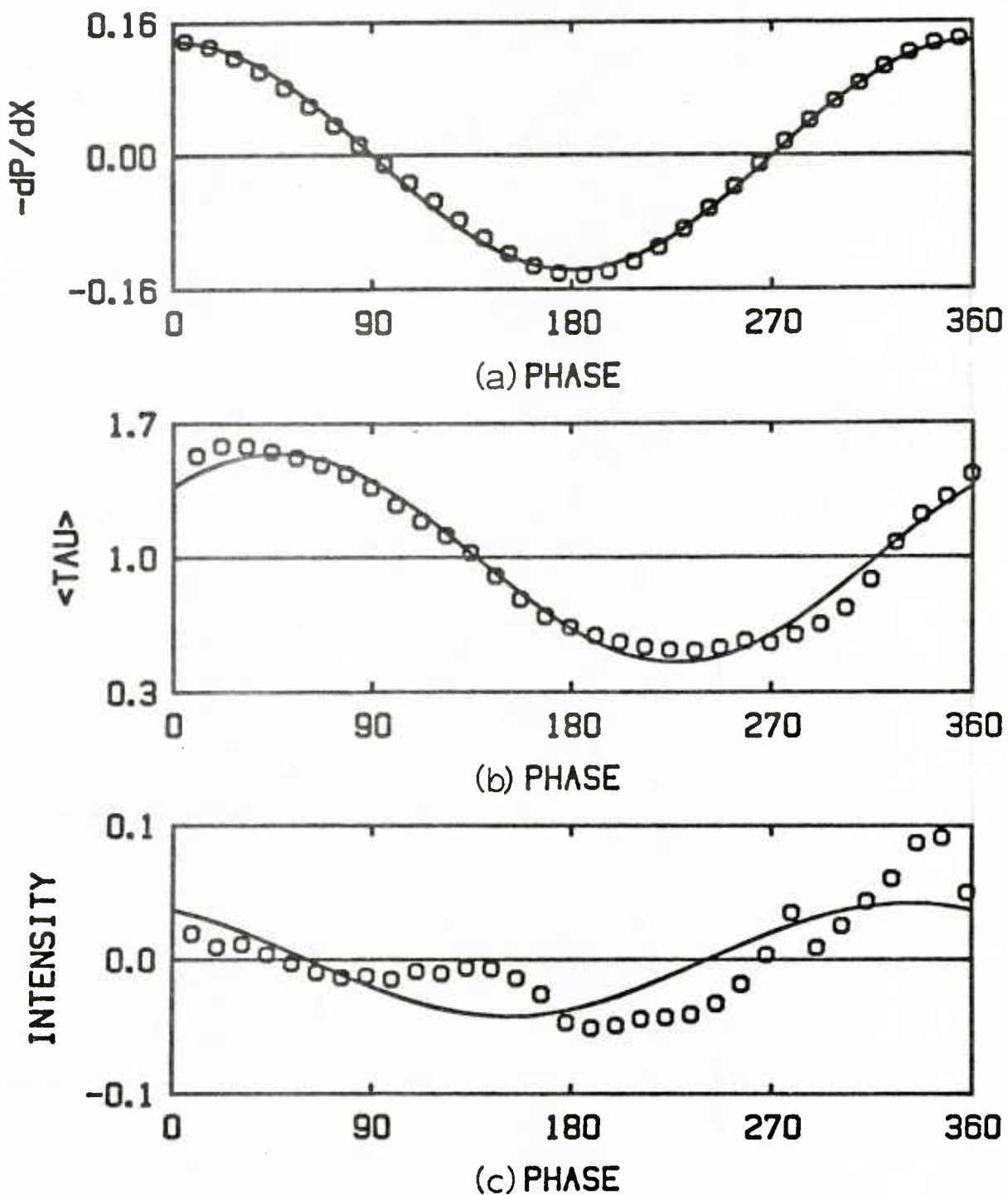


Figure 5.43 Phase averaged values at $Re = 10,300$, $f = 1.50$ Hz,
 $\omega^+ = 0.0675$ and $a = 0.101$

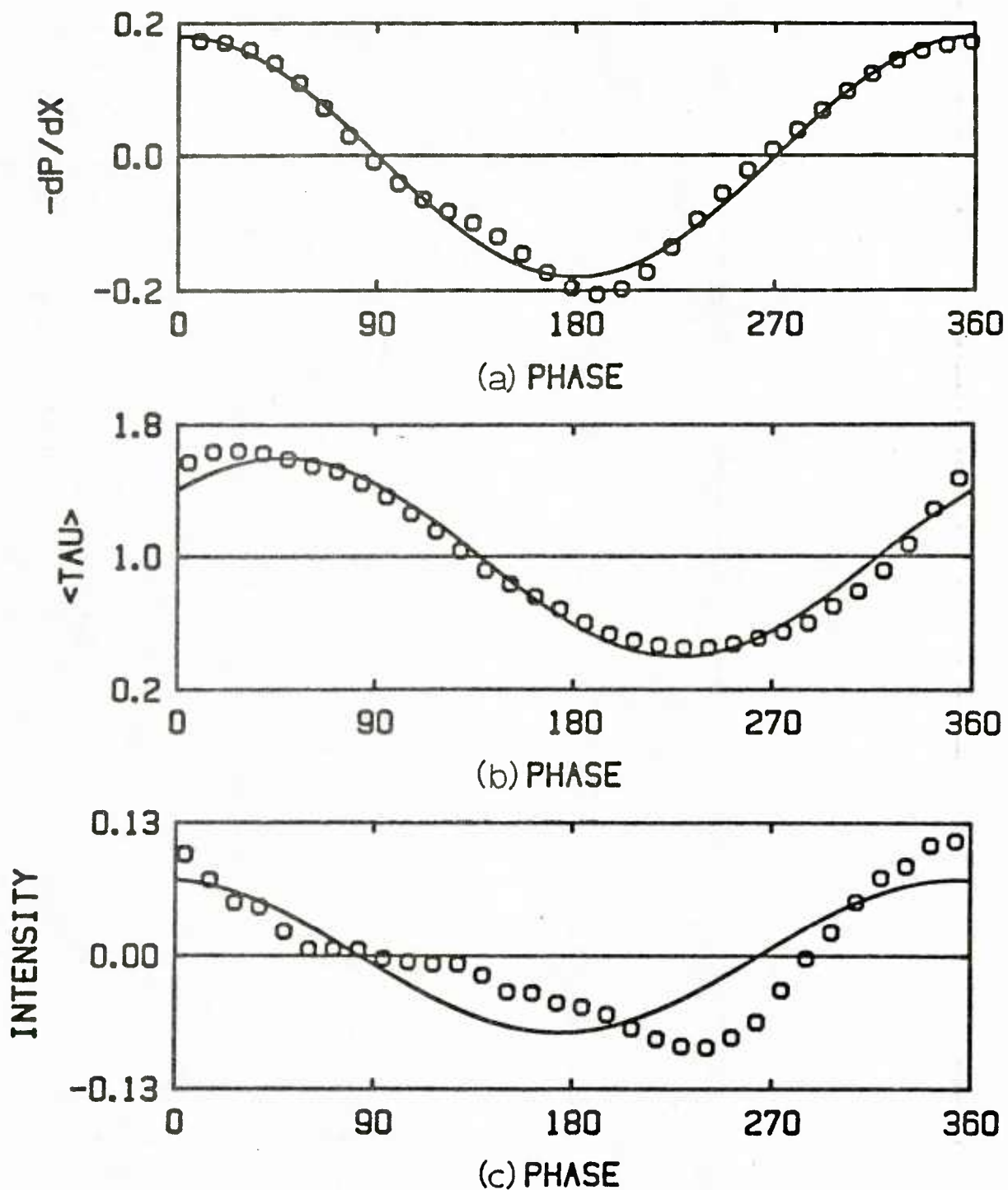


Figure 5.44 Phase averaged values at $Re = 8,650$, $f = 1.50$ Hz,
 $\omega^+ = 0.0915$ and $a = 0.100$

From (5.5), the amplitude of the dimensionless pressure gradient depends on the frequency of pulsation to the first power and the Reynolds number to the $-13/8$ power. The amplitude of the dimensionless pressure gradient is equal to 0.0028 at the low extreme of $\omega^+ = 0.0012$ and equal to 0.180 at the high extreme of $\omega^+ = 0.0915$. Thus, the amplitude of the pressure gradient increases 64 times from the low to the high extremes of the data set.

As can be seen in the figures, the variation of the pressure gradient and the shear stress at the wall is well described by a single harmonic. The solid line in the figures was plotted using the amplitude and phase of the first-harmonic of a three-harmonic fit to the data. The amplitude of the second-harmonic was found to be always less than 10% of that of the first-harmonic. In several of the runs a low amplitude nonlinearity is observed in the phase averaged pressure gradient. This nonlinearity was due to the gears in the pulsating pump having some slack that would cause the pump to "jump" whenever it switched from pushing to pulling or vice versa. This problem is less acute at high Reynolds numbers since the force exerted on the pump by the mean pressure gradient is large enough to prevent the gears from shifting. This problem was low enough in amplitude so as not to affect the results.

Figure 5.22 shows the phase averaged results for $\omega^+ = 0.0012$. This value corresponds to the lowest ω^+ measured in this study. It is seen from Figure 5.22 that the shear stress at the wall lags the favorable pressure gradient by about 90 degrees. The empirical eddy viscosity calculations indicate that plug flow still exists in the center of the pipe. Thus, the variation of the centerline velocity lags behind the imposed pressure gradient by 90 degrees, but is in phase with the wall shear stress. This result implies that the amplitude of the wall shear stress can be described by the pseudo-steady approximation derived in Chapter 3. Relation (3.77)

evaluated for a $Re = 44,900$ gives $|\tau_w^+|/|q_c^+| = 0.088$. This value is in very good agreement with the measured value of 0.084.

The variation of the turbulence is seen in Figure 5.22 to be in phase with the wall shear stress. If the imposed pulsation is low enough in frequency, the variation of the turbulence in the viscous wall region can be described by the scaling arguments and concepts developed for constant imposed pressure gradients. Also, at low frequencies the variation of the shear stress at the wall will be of the same order of magnitude and, roughly, in phase with the shear stress variation at the outer edge of the viscous wall region. Therefore, for this type of flow, (3.25) is approximately equal to the following:

$$\langle q_0^+ \rangle \approx c_1 (\langle \tau_w^+ \rangle)^{\frac{1}{2}}, \quad (5.6)$$

where c_1 is a constant. Assuming that τ_w^+ varies as q_0^+ , (5.6) predicts that the phase of τ_w^+ will be roughly in phase with the variation of the wall shear stress. It is seen from Figure 5.22 that this is the case. This result implies that the imposed pressure gradient is varying slow enough to enable the turbulence to respond to the imposed shear stress. Therefore, the flow at low w^+ is said to be in "equilibrium" with the imposed pressure gradient.

At higher dimensionless frequencies, the turbulence will no longer be able to follow the imposed pressure gradient and the amplitude of the variation of the turbulence will decrease. The phase averaged results for $w^+ = 0.0270$ are shown in Figure 5.39. Even though the amplitude of the imposed pressure gradient is twenty times the one in Figure 5.22, the amplitude of the variation of the turbulence is an order of magnitude less. A dramatic change is also observed in the phase relative to the pressure gradient. The wall shear stress is observed to lag the favorable pressure gradient by 45 degrees. This change in phase lag from 90 to 45 degrees

occurs over a very narrow range of ω^+ values. It is believed that this sharp change in phase is associated with a relaxation phenomena, whereby the turbulence does not respond immediately to the imposed pressure gradient. This same type of phenomena has also been observed in flow over a wavy surface [Abrams and Hanratty (1985)].

At high ω^+ , the variation of the wall shear stress should behave as in laminar pipe flow. This is because all of the change in the pulsating velocity occur very close to the wall where turbulence is negligible. From (3.73), the wall shear stress should lag the pressure gradient by 45 degrees. This is exactly what is observed for the wall shear stress data taken at $\omega^+ = 0.0550$ and shown in Figure 5.42. Since the pulsating component of the velocity is expected to have no effect on the turbulence (which agreement with the quasi-laminar solution implies) the variation of the turbulent quantities should be zero. Instead, a highly nonlinear large amplitude variation is observed in the turbulence measurements. This nonlinearity contrasts with the linear response observed at lower frequencies. Also, the variation appears to be highly deterministic in nature; there is very little variation over the first half of the pulsation cycle and a large variation over the second half. The variation is so highly nonlinear that the second harmonic contains over 50% more the energy of the first. This same behavior was noted by Mao and Hanratty (1986) in their high ω^+ data taken in an eight inch pipe. At present no explanation exists for this behavior at high ω^+ .

The amplitude of the variation of the wall shear stress is plotted in Figure 5.45 as a function of ω^+ along with the data of Mao and Hanratty (1986) and Ramaprian and Tu (1983). The amplitude is normalized with the amplitude of the centerline velocity as suggested by the quasi-laminar solution. The data at low ω^+ have a normalized amplitude of about 0.085.

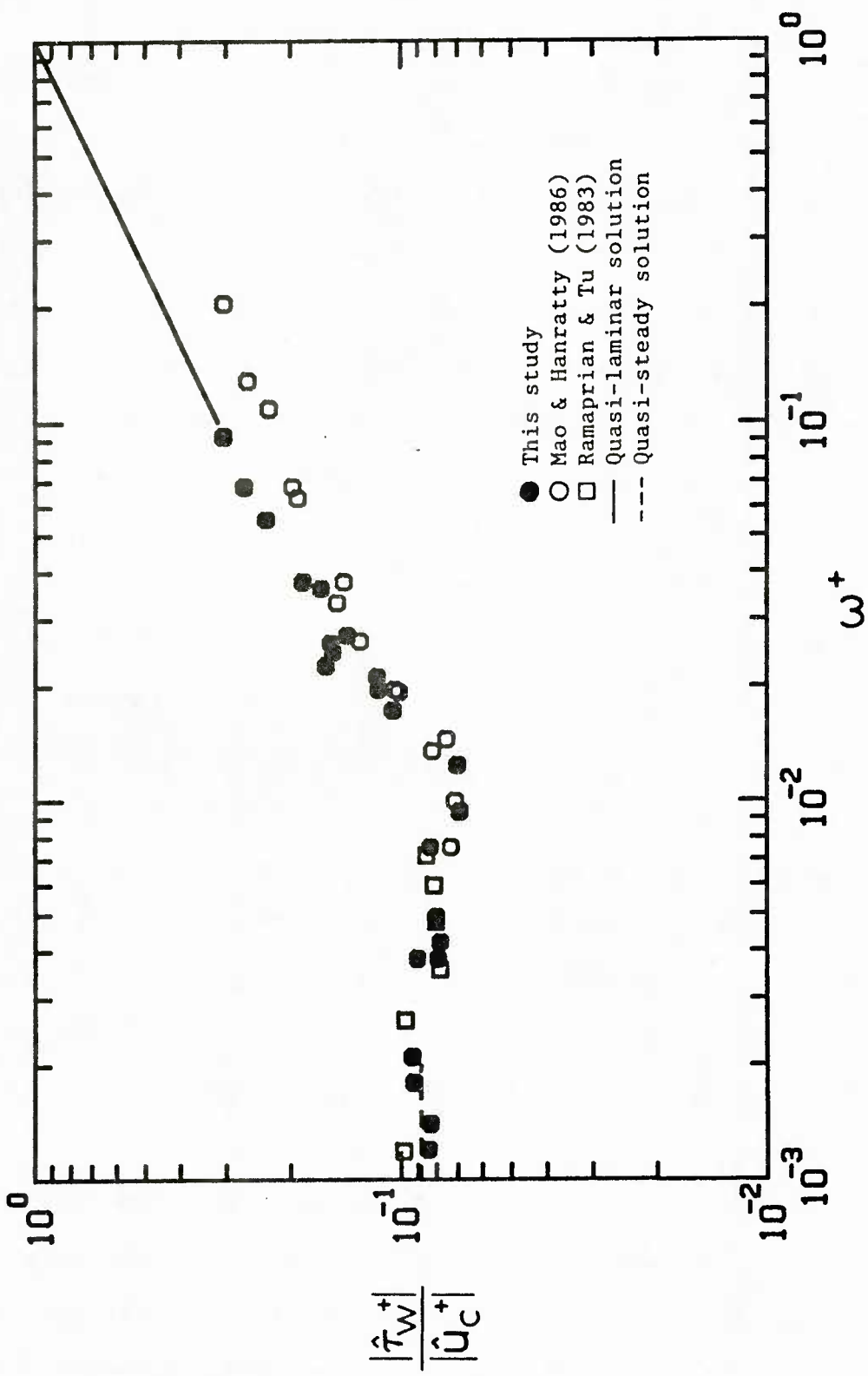


Figure 5.45 Amplitude of the wall shear stress.

The data go through a minimum at about $\omega^+ = 0.01$ and, then, increase as ω^+ is increased. The solid line in Figure 5.45 was generated from the quasi-laminar solution, (3.74). It is observed that the data at high ω^+ agree well with the quasi-laminar solution. However, the data at high ω^+ of Mao and Hanratty show a lower amplitude than the quasi-laminar solution would suggest. The reason for this disagreement is not known. The dashed line in Figure 5.45 was generated from the empirical quasi-steady relation, (3.77), using a Reynolds number of 45,000. Since the dependence of this relation on Reynolds number is not very great, it is not important which Reynolds number was chosen. Even though this relationship should only be valid for ω^+ values much lower than those studied here, good agreement with the data is observed.

The variation of the phase of the wall shear stress with ω^+ is shown in Figure 5.46 along with the data of Mao and Hanratty (1986) and Ramaprian and Tu (1983). Very good agreement with their data is observed. At low ω^+ values the phase lag is about -85 degrees and at high ω^+ values the phase lag is equal to -45 in agreement with the quasi-laminar solution. Mao and Hanratty attribute the dramatic increase in the phase of the wall shear stress at about $\omega^+ = 0.01$ to a relaxation effect whereby the turbulence goes from a state of equilibrium with the imposed pressure gradient to one where the turbulence is no longer able to respond to the rapidly changing pressure gradient. The agreement between the two sets of data in this region is remarkable considering that their data were taken in an eight inch pipe and the data in this study were taken in a two inch pipe. This agreement is strong support for using ω^+ as the parameter to describe the variation of the wall shear stress data.

The variation of the amplitude of the intensities with ω^+ is plotted in Figure 5.47. The data of Mao (1984) is also included in the figure. At

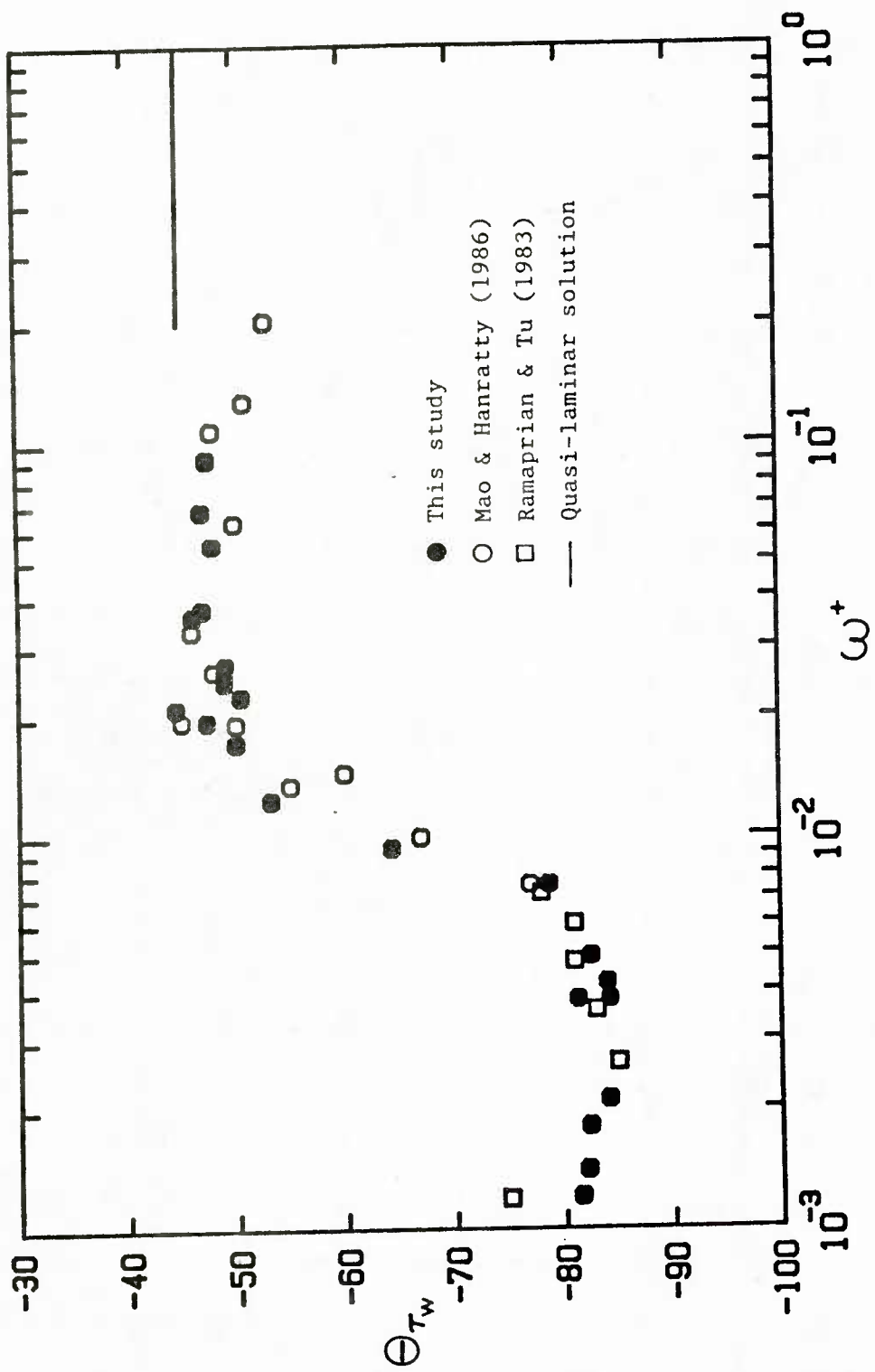


Figure 5.46 Phase lag (relative to the pressure gradient) of the wall shear stress.

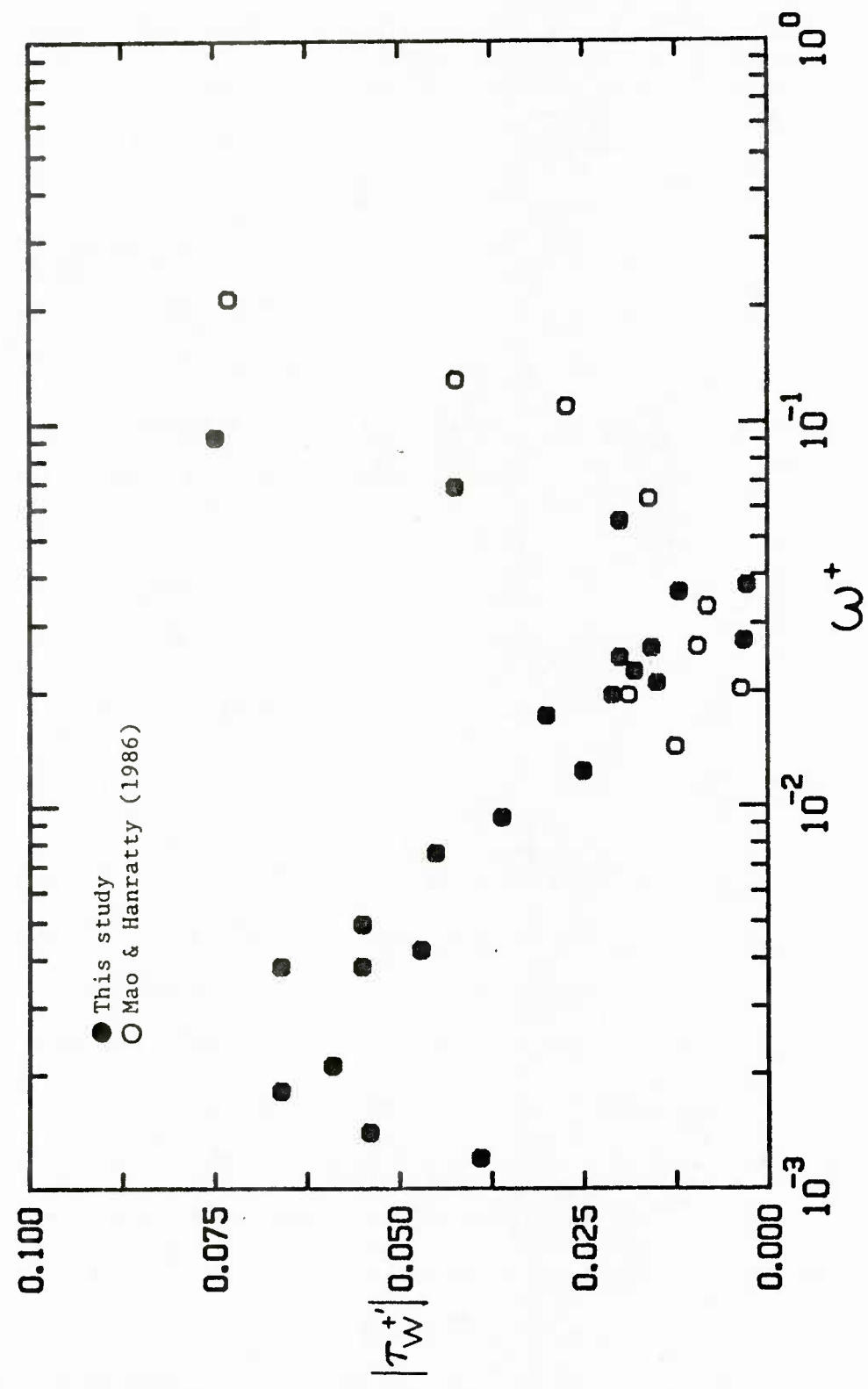


Figure 5.47 Amplitude of the wall shear stress intensity.

low ω^+ values the amplitude increases as ω^+ increases. This behavior is what would be expected if the turbulence was in equilibrium with the time varying pressure gradient. The variation is relatively large considering that the amplitude of the imposed pressure gradient is only about 0.004. This is about one-sixth the pressure gradient found in constant pressure gradient flows to cause relaminarization. The amplitude is observed to go through a peak at about $\omega^+ = 0.003$ and to decrease to zero at $\omega^+ = 0.03$. This attenuation is what is expected if the imposed pressure gradient is varying so fast that the turbulence no longer can respond instantaneously. In the quasi-laminar region, where the turbulence cannot respond at all and is "frozen", the amplitude of the variation should be zero. This is observed in the data for ω^+ values around 0.03. However, at higher ω^+ values the amplitude increases dramatically. The data of Mao (1984) shows the same trend. This agreement between the two sets of data taken in two different flow loops indicates that this nonlinear variation cannot be attributed to some peculiarity of the apparatus such as a resonance phenomena.

The variation of the phase of the intensity with ω^+ is shown in Figure 5.48. At low ω^+ values the phase of the intensity lags the imposed pressure gradient by 90 degrees. As explained earlier, this is consistent with the turbulence being in "equilibrium" with the imposed pressure gradient. The phase lag increases as ω^+ increases till at the high ω^+ extreme of 0.0915 the phase lag is equal to -354 degrees. Thus, the turbulence is in phase with an unfavorable pressure gradient. This result lends support to the belief that at high ω^+ the turbulence does not respond immediately to the imposed pressure gradient.

Due to difficulty in reading the symbols in their figures, the data of Binder et. al. (1985) are not included in Figures 5.45 through 5.48.

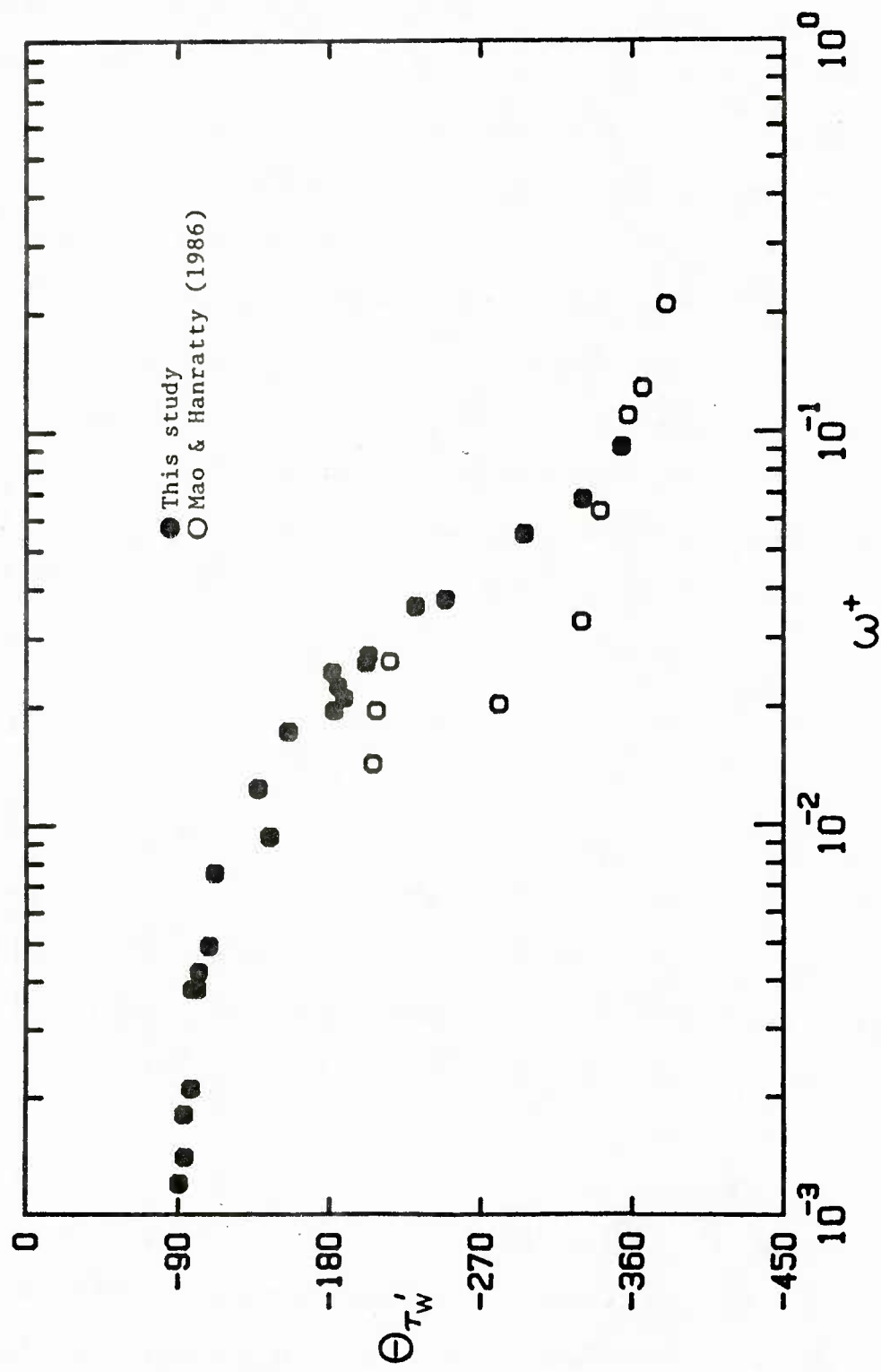


Figure 5.48 Phase lag (relative to the pressure gradient) of the wall shear stress intensity.

However, it is observed that their data, which extends up to $w^+ \approx 0.02$, is in qualitative agreement with the data obtained in this study.

It is desired to obtain quantitative information about the variation of λ_0^+ from measurements of the phase averaged R_{11z}^+ . If the $\lambda_0^+ = 100$ eddy was the only eddy present in the flow close to the wall, the R_{11z}^+ curve would go through a zero crossing at $z^+ = 25$, a minimum of -1 at $z^+ = 50$ and a maximum of 1 at $z^+ = 100$. However, the presence of a wide spectrum of wavenumbers with various phases changes the correlation coefficient curve such that the zero crossing occurs at about $z^+ = 37$ and the magnitudes of the minimum and maximum are much smaller than 1. A typical R_{11z}^+ curve is shown in Figure 5.17. Experimental measurements indicate that the Taylor microscale is related to λ_0^+ by (3.31). At small separation distances, the Taylor microscale can be determined from the following [Hinze (1975)]:

$$R^+ \approx 1 - \frac{z^{+2}}{\lambda_T^{+2}}, \quad (5.7)$$

where λ_T^+ is the Taylor microscale. Thus, (5.7) and (3.31) can be used to estimate λ_0^+ from measurements of the correlation coefficient curve.

The correct correlation coefficient curve to determine λ_0^+ is the transverse correlation coefficient of the transverse velocity gradient at the wall, R_{33z}^+ , curve. However, measurements of R_{33z}^+ at small separation distances are very difficult to make since relatively large V-shaped wall probes must be used. An alternate method of measurement is suggested by the model first proposed by Sirkar and Hanratty (1970) for flow in the viscous wall region. Their idealized flow is shown in Figure 2.1. Lee, Eckelman, and Hanratty (1974) verified the existence of this secondary flow pattern by simultaneously measuring s_x and s_z at a number of locations at the wall. In particular, they found that the s_z sinusoidal variation in

the transverse direction is accompanied by a spatial variation of s_x that is $\pi/4$ out of phase. This is shown in Figures 2.1b and 2.1c.

If this idealized structure is correct, the correlation coefficient curves of the streamwise and transverse velocity fluctuations at the wall should be the same. Finnicum and Hanratty (1985) have shown this to be the case. Therefore, the transverse Taylor microscale can be determined from measurements of the streamwise Taylor microscale. These measurements are easier to perform since small circular electrodes, such as the ones used in this study, can be fabricated at small enough distances so as to accurately determine λ_T^+ .

In order to obtain as wide a range of ω^+ values as possible the Reynolds number of the flow was varied from 8,650 to 44,900. Unfortunately, the separation distance in wall variables between electrodes was too large at the higher Reynolds numbers to use (5.7). At the lower Reynolds numbers, the measured R_{11z}^+ curve is too short to use the maximum or minimum of the curve to determine λ_0^+ . Therefore, since it could be determined accurately for all the runs, it was decided to use the location of the zero crossing to determine λ_0^+ .

The following relationship was used to fit the correlation coefficient curve,

$$R_{11z}^+ = \exp\left[-\left(\frac{\bar{\lambda}_0^+}{\bar{C}_1^+} \frac{z^+}{\lambda_0^+}\right)^2\right] \cos\left(\frac{\pi}{2} \frac{\bar{\lambda}_0^+}{\bar{z}_{\text{zero}}^+} \frac{z^+}{\lambda_0^+}\right), \quad (5.8)$$

where $\bar{\lambda}_0^+ = 100$, \bar{z}_{zero}^+ is the location of the zero crossing, and \bar{C}_1^+ is a constant for each run. At small distances, (5.8) reduces to (5.7) and \bar{C}_1^+ is related to the time averaged Taylor microscale by

$$\bar{C}_1^+ = \frac{1}{\left(\frac{1}{(\bar{\lambda}_T^+)^2} - \frac{\pi^2}{8(\bar{z}_{zero}^+)^2} \right)^{\frac{1}{2}}} . \quad (5.9)$$

Both constants, \bar{C}_1^+ and \bar{z}_{zero}^+ , are determined by fitting (5.9) to the time averaged R_{11z}^+ data run. The R_{11z}^+ data are then fit at each phase to determine the phase averaged λ_0^+ . A nonlinear least squares regression routine is used to determine the best match to the data. The phase averaged λ_0^+ are fit with a three-harmonic cosine function to determine the amplitude and phase of the first harmonic.

The time averaged R_{11z}^+ data for all the runs are shown in Figure 5.49. An averaged Taylor microscale equal to 18.3 was determined by fitting all the data points with values greater than 0.9 to (5.7). Fitting (5.8) to data points with values greater than zero gave values of 18.6 and 35.1 for $\bar{\lambda}_T^+$ and \bar{z}_{zero}^+ , respectively. Curves using these values are plotted in Figure 5.49. As expected, (5.8) reduces to (5.7) at low separation distances. The power of two in the exponential term was necessary to obtain the correct curvature at low z^+ values. However, this dependence forces (5.8) to dampen rapidly near the zero crossing point and a good fit to the data at z^+ values greater than \bar{z}_{zero}^+ is not possible. Powers of 1 and 1.5 did a better job of fitting the data in this region; however, since it was desired to resolve the Taylor microscale, a power of two is necessary in (5.8).

The streak spacing is used in (5.8) instead of the Taylor microscale to describe the variation of the correlation coefficient curve. Relation (3.31) enables this substitution to be made. Therefore, a check on its validity is appropriate. Using $\bar{\lambda}_0^+ = 100$ and (3.31), $\bar{\lambda}_T^+ = 15.9$. This value is in good agreement with the experimental value of 18.3. Finnicum

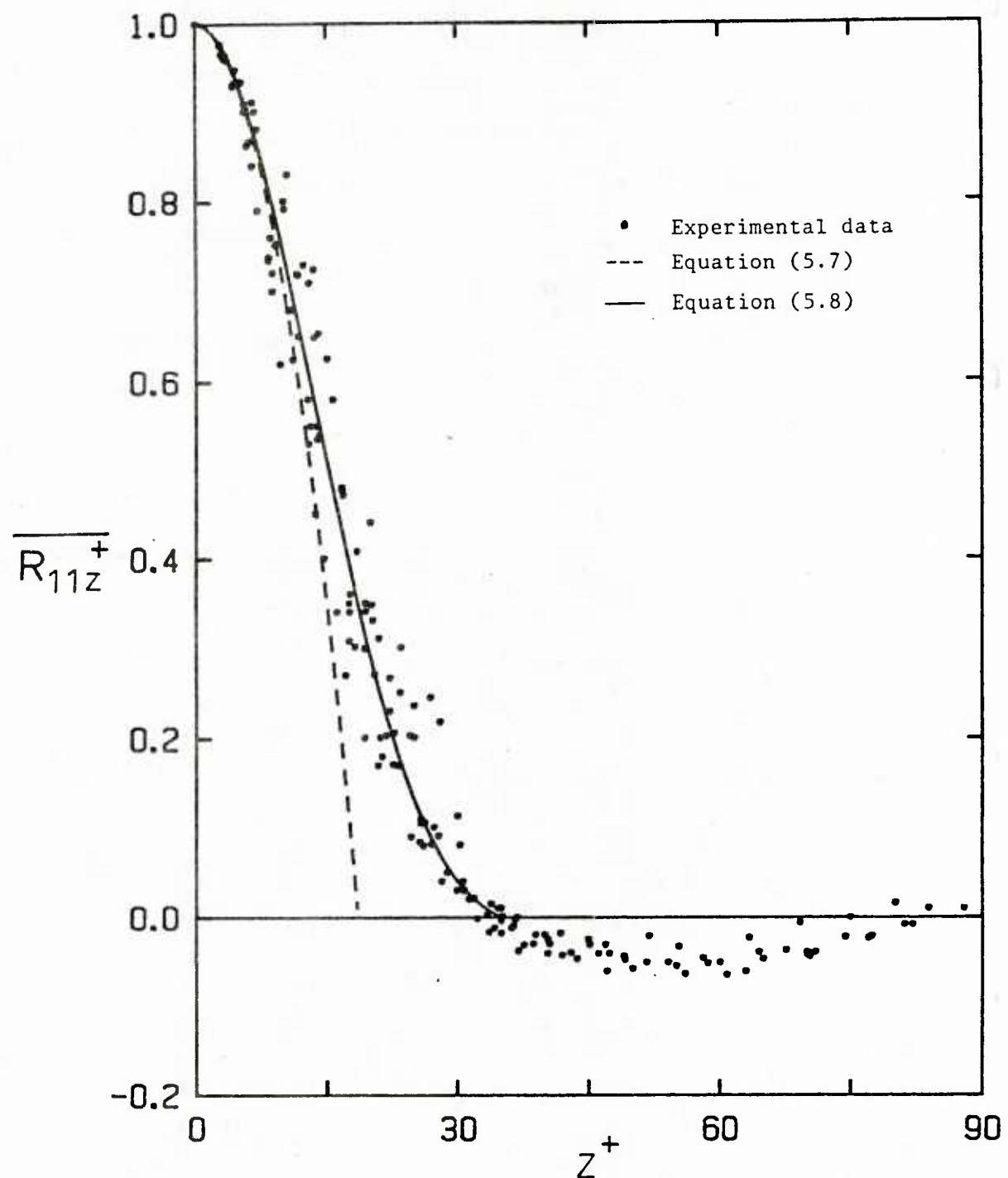


Figure 5.49 Determination of the time averaged Taylor microscale

and Hanratty (1985) showed that $\bar{\lambda}_T^+$ is equal to 17 ± 1.4 in normal pipe flow. (Note: They report $\bar{\lambda}_T^+$ to be equal to 12 ± 1 . However, their definition of $\bar{\lambda}_T^+$ differs from the one in this thesis by $(2)^{1/2}$.) It is noted that both the experimental value and the value estimated from (3.31) are in good agreement with their reported values for $\bar{\lambda}_T^+$.

The method for determining the phase averaged λ_0^+ is illustrated in Figure 5.50 for the $\omega^+ = 0.0012$ run. The circles represent the time averaged R_{11z}^+ data. Also shown are the R_{11z}^+ data points corresponding to the maximum and minimum λ_0^+ of the 32 values obtained from the phase averaged R_{11z}^+ . These data are represented by the squares and triangles, respectively. For this run, $\bar{C}_1^+ = 24.1$, $\bar{\lambda}_T^+ = 19.1$, and $\bar{z}_{\text{zero}}^+ = 35$. The dashed line is generated from (5.9) using $\lambda_0^+ = 110.7$ and the dotted line is generated using $\lambda_0^+ = 90.3$. These values were determined from a nonlinear least square fit to the experimental data. Qualitatively, it is observed that the minimum in the curves agrees with these results. However, as seen in Figure 5.50, small errors in the R_{11z}^+ values can cause large errors in the estimation of λ_0^+ because of the flatness of the curve in the area of the minimum.

The phase average λ_0^+ values determined using (5.9) are shown in Figures 5.51 through 5.67. The phase average favorable pressure gradient, wall shear stress, and intensity of the turbulent fluctuations of the wall shear stress are also included as references. The variation of λ_0^+ with ω^+ is seen to be very similar to that of τ_w^+ . For low ω^+ values, the variation is linear, while, at high ω^+ values the variation is highly nonlinear. At low ω^+ values, the variation of λ_0^+ and τ_w^+ are 180 degrees out of phase with each other. As ω^+ increases, the difference in phase increases, till, at $\omega^+ = 0.0915$, it is roughly 280 degrees out of phase. Particularly interesting are the results shown in Figures 64 and Figure 65.

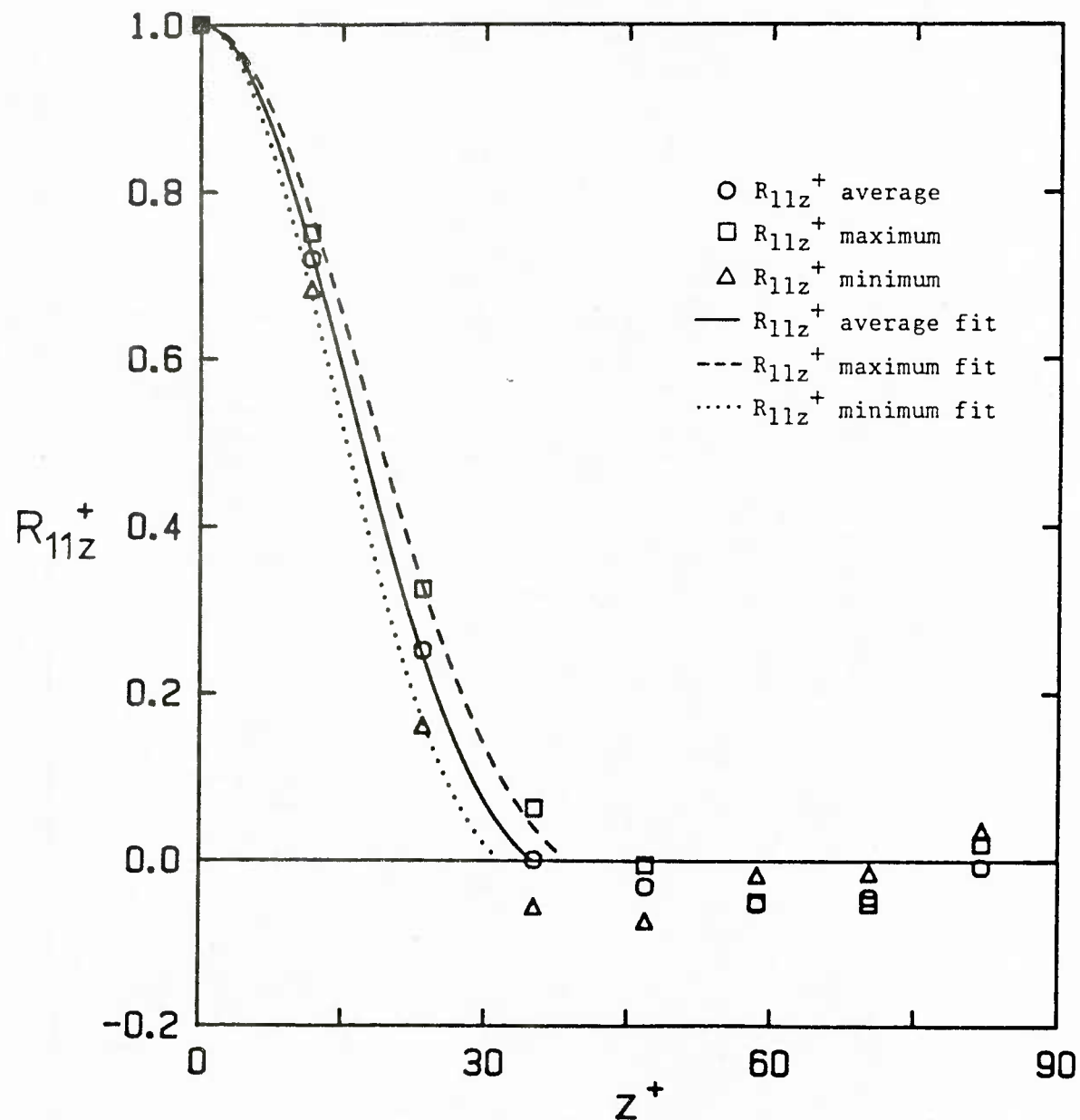


Figure 5.50 Determination of the variation of the streak spacing.

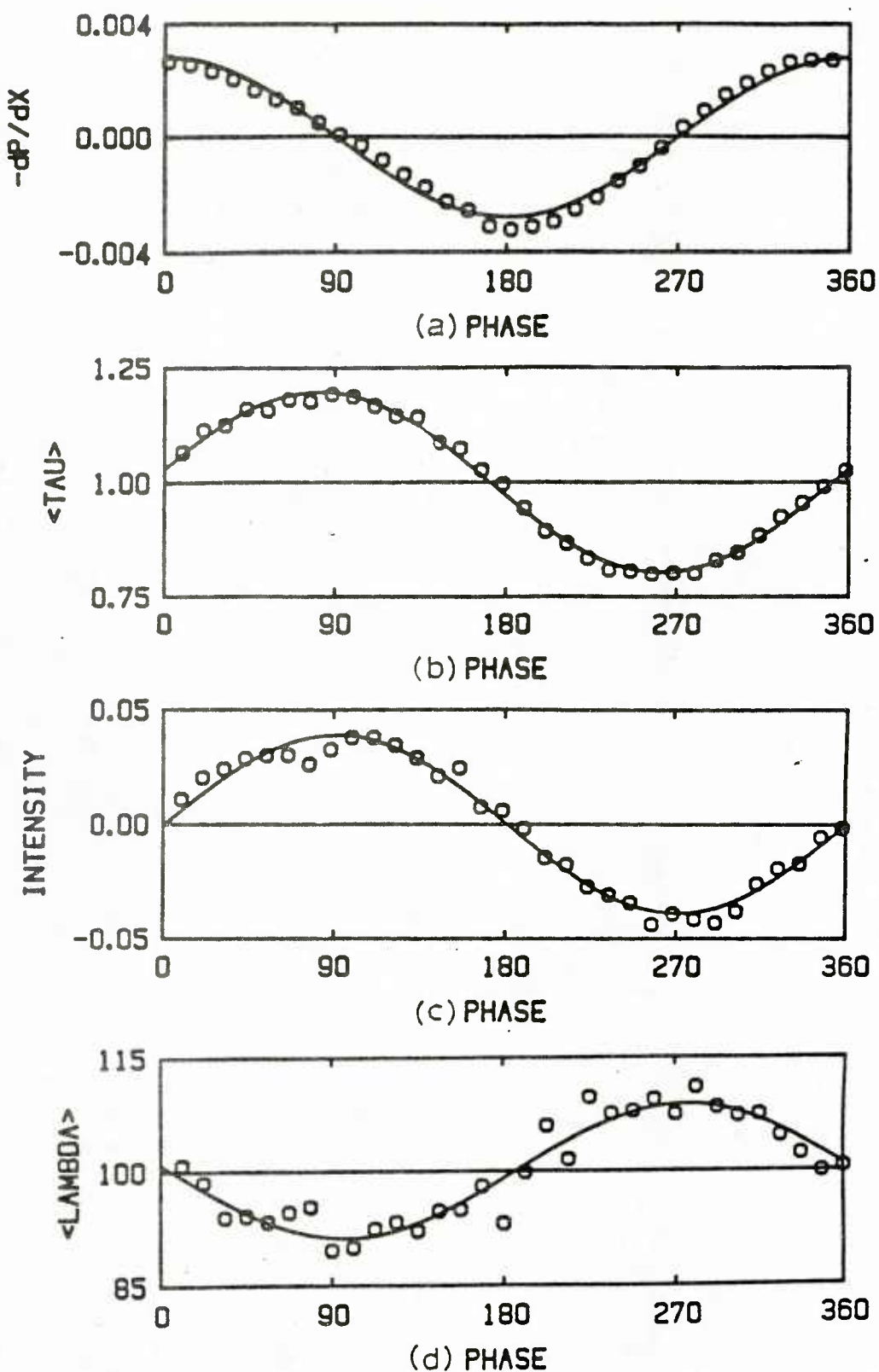


Figure 5.51 Phase averaged streak spacing at $Re = 44,900$,
 $f = 0.35$ Hz, $\omega^+ = 0.0012$ and $a = 0.1$

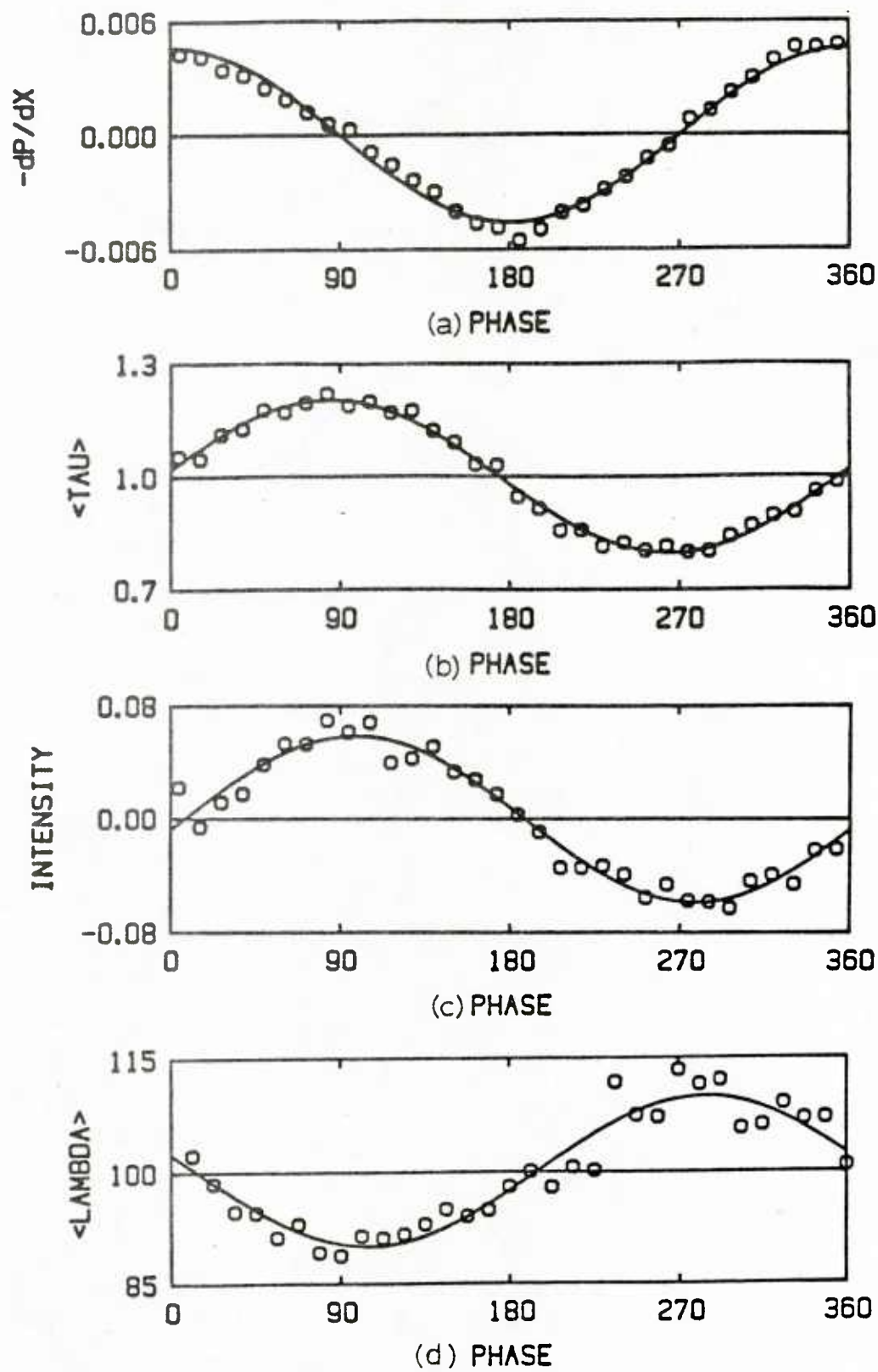


Figure 5.52 Phase averaged streak spacing at $Re = 23,700$, $f = 0.20$ Hz, $\omega^+ = 0.0021$ and $a = 0.1$

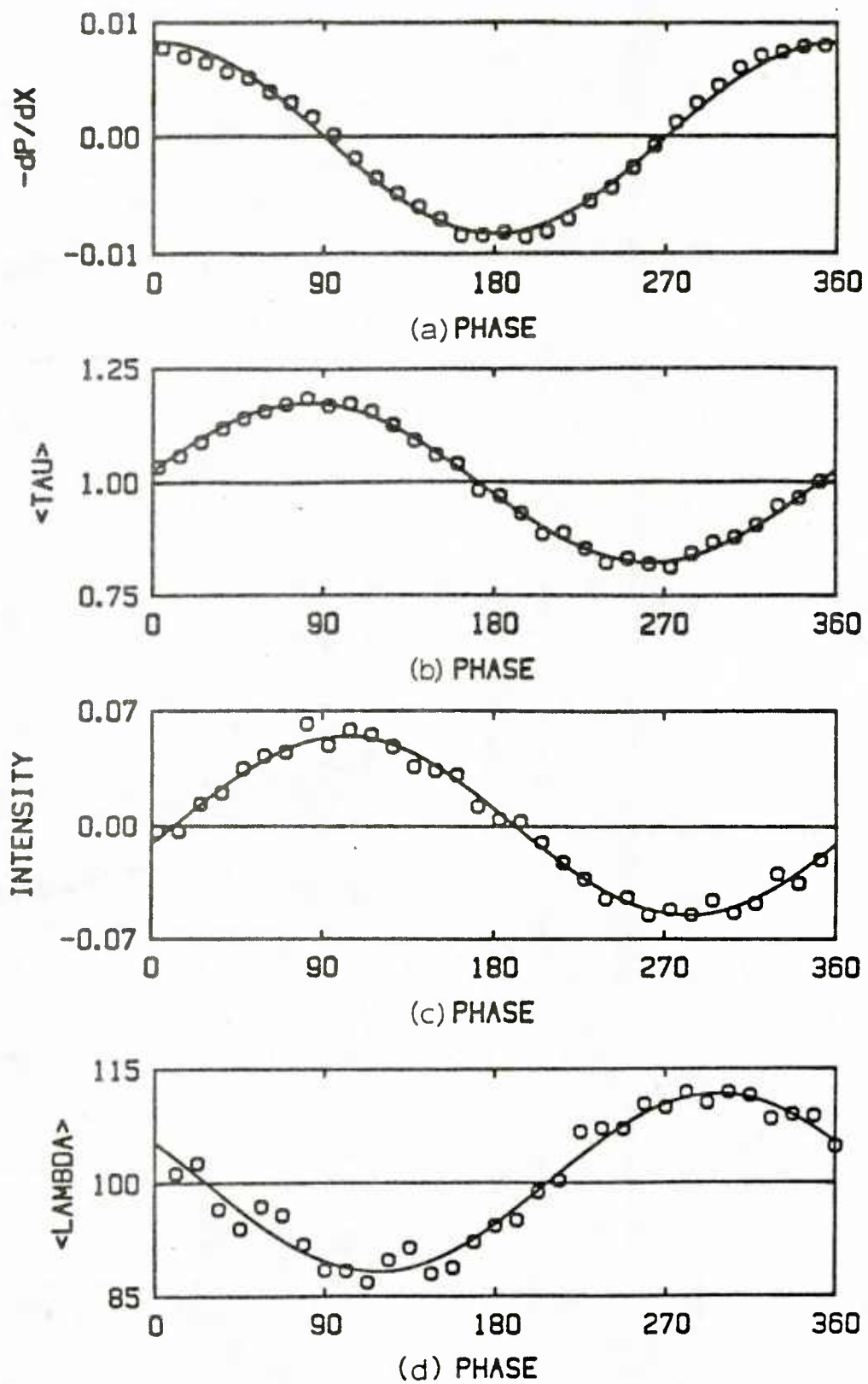


Figure 5.53 Phase averaged streak spacing at $Re = 25,200$, $f = 0.40$ Hz, $\omega^+ = 0.00375$ and $a = 0.1$

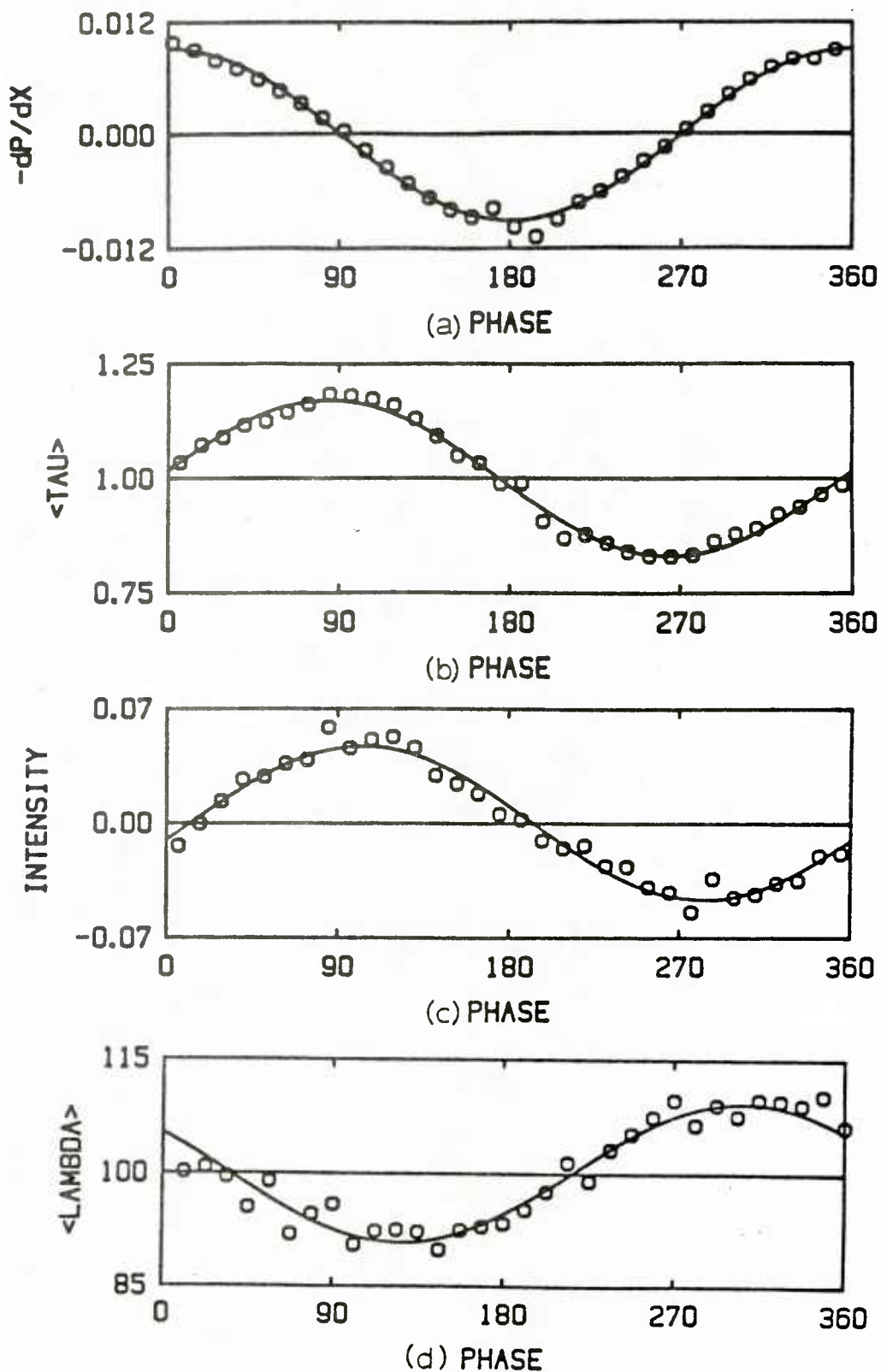


Figure 5.54 Phase averaged streak spacing at $Re = 20,100$, $f = 0.30$ Hz, $\omega^+ = 0.0042$ and $a = 0.101$

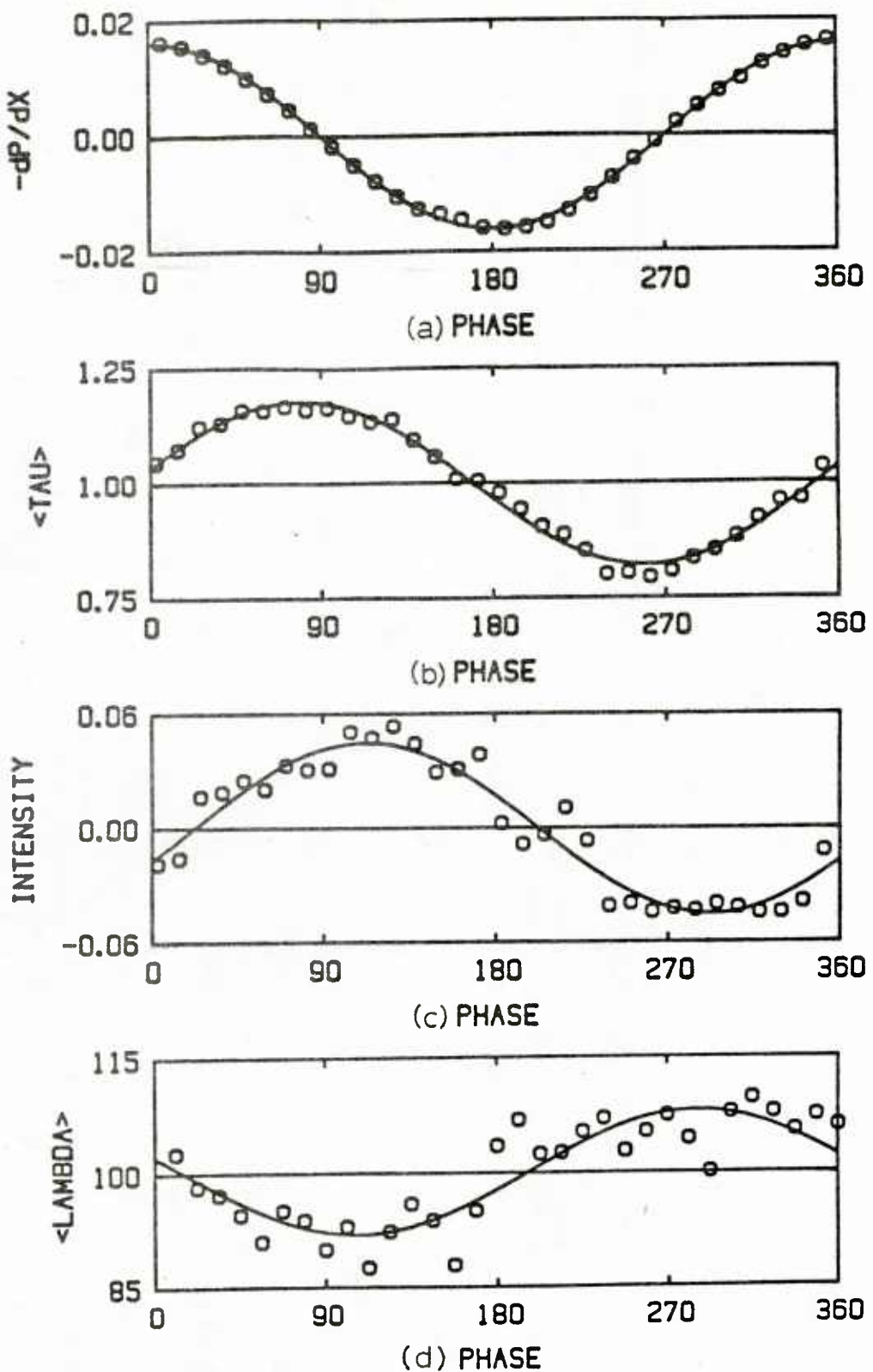


Figure 5.55 Phase averaged streak spacing at $Re = 21,400$,
 $f = 0.60$ Hz, $\omega^+ = 0.0075$ and $a = 0.099$

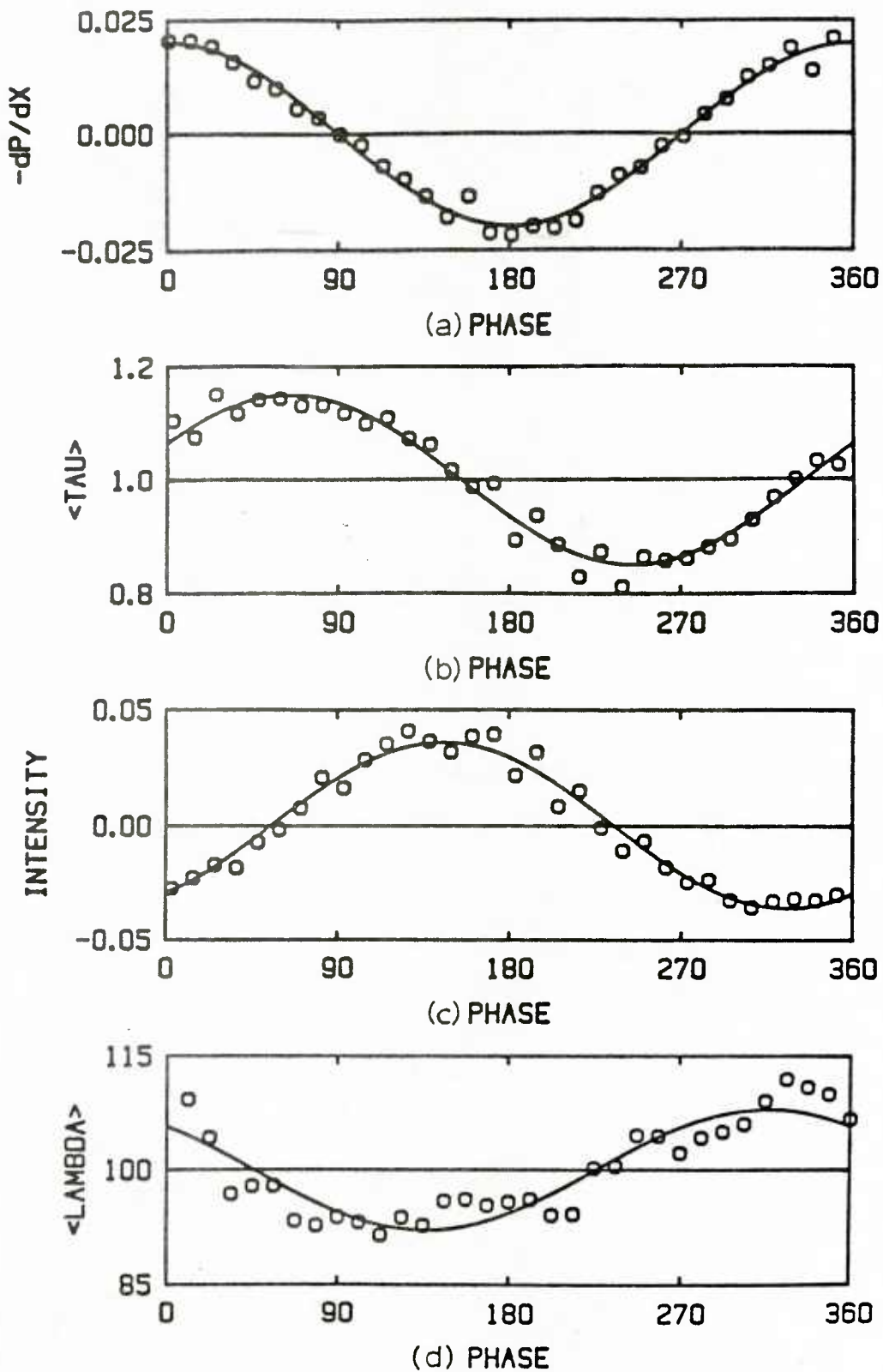


Figure 5.56 Phase averaged streak spacing at $Re = 17,100$,
 $f = 0.50$ Hz, $\omega^+ = 0.0093$ and $a = 0.102$

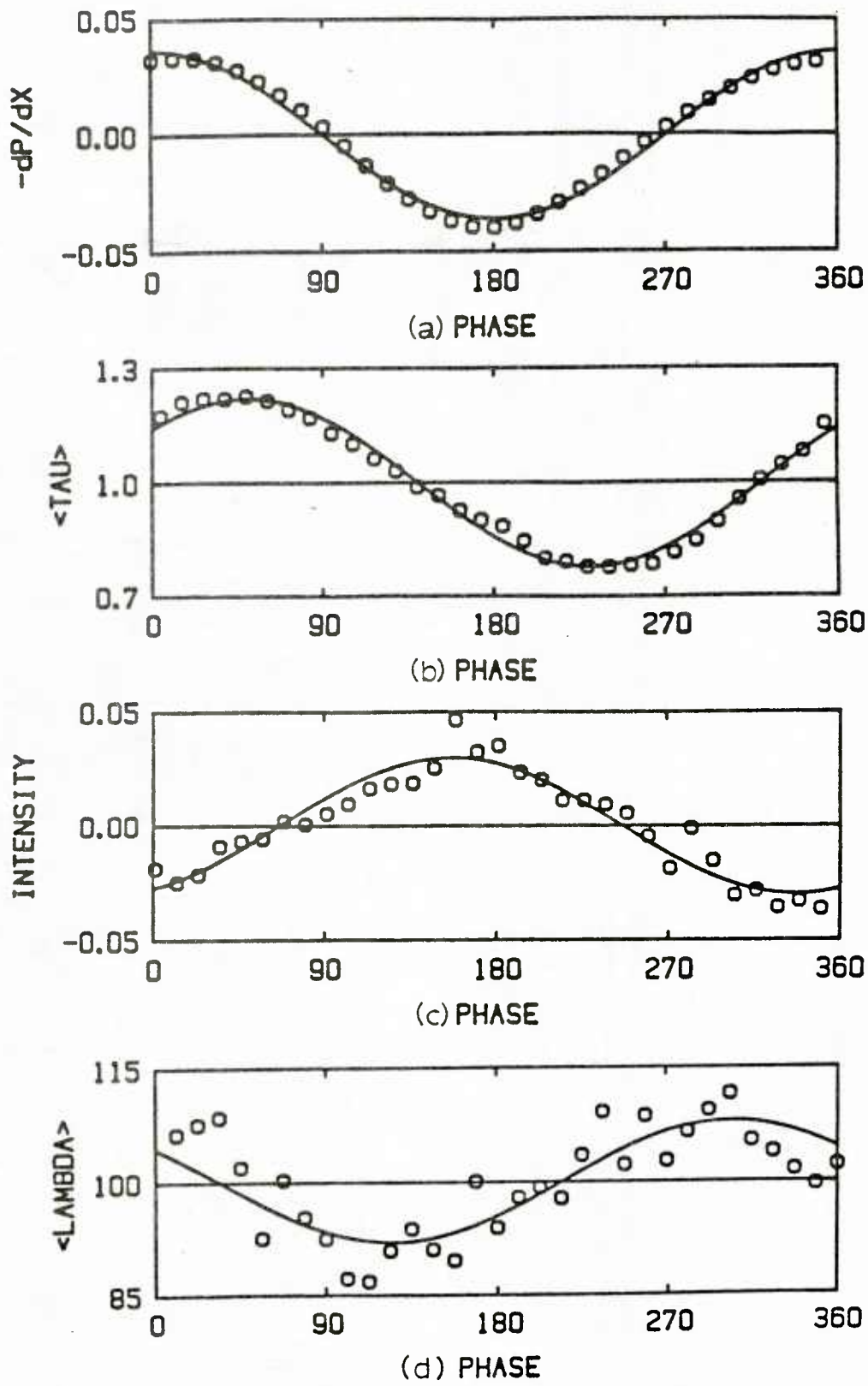


Figure 5.57 Phase averaged streak spacing at $Re = 17,900$,
 $f = 1.00 \text{ Hz}$, $\omega^+ = 0.0172$ and $a = 0.098$

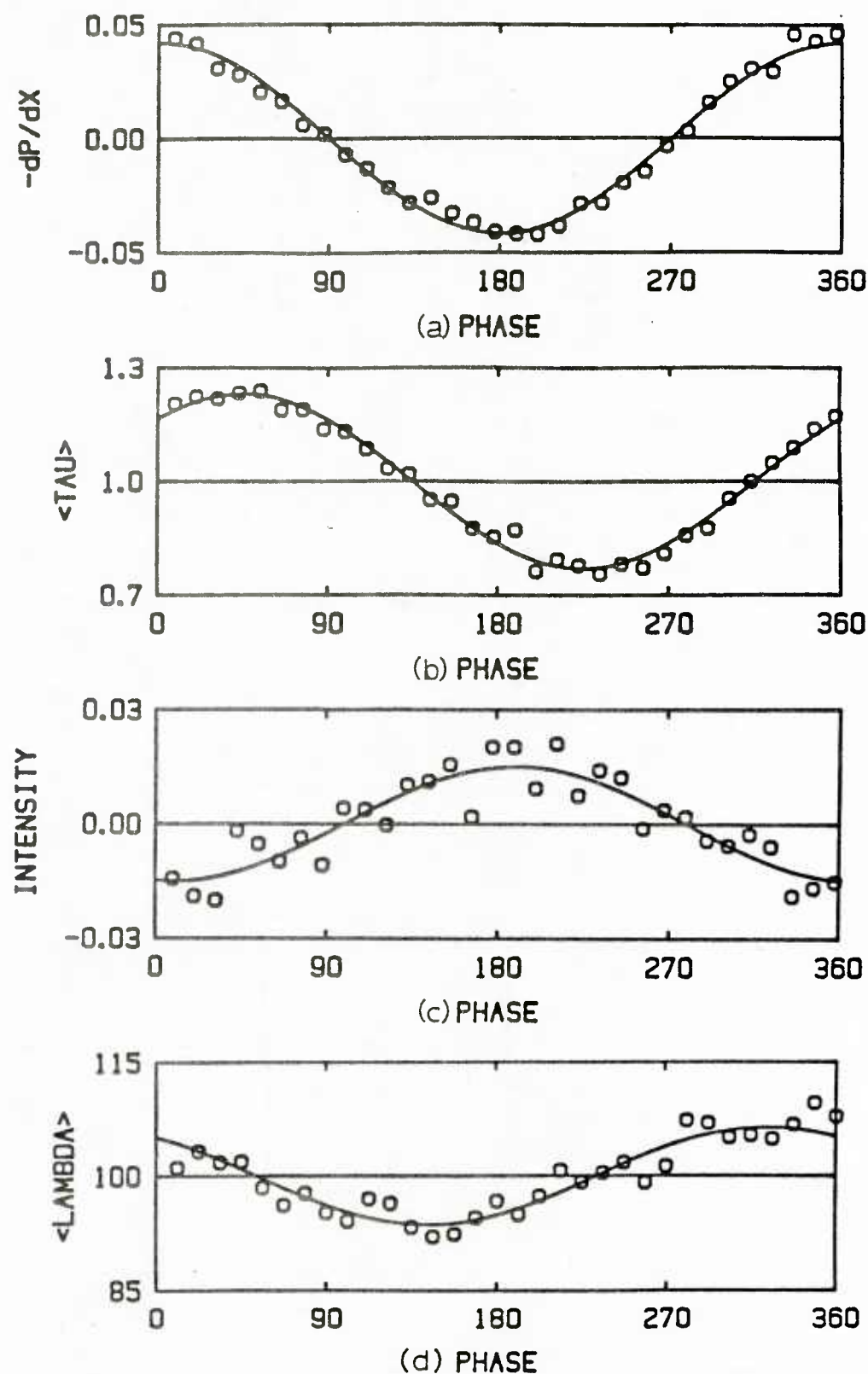


Figure 5.58 Phase averaged streak spacing at $Re = 10,700$,
 $f = 0.50$ Hz, $\omega^+ = 0.021$ and $a = 0.102$

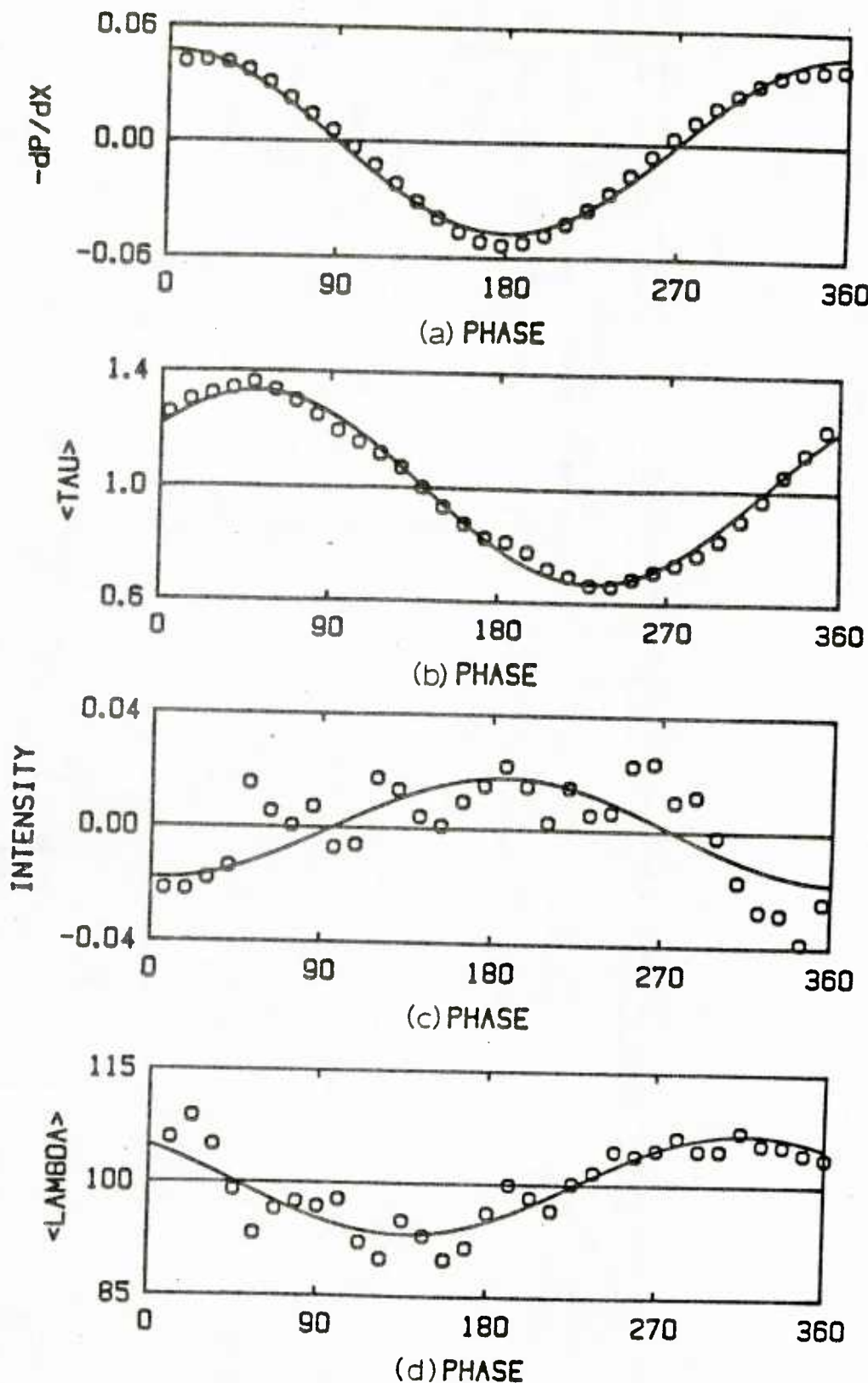


Figure 5.59 Phase averaged streak spacing at $Re = 15,300$,
 $f = 1.00 \text{ Hz}$, $\omega^+ = 0.0225$ and $a = 0.099$

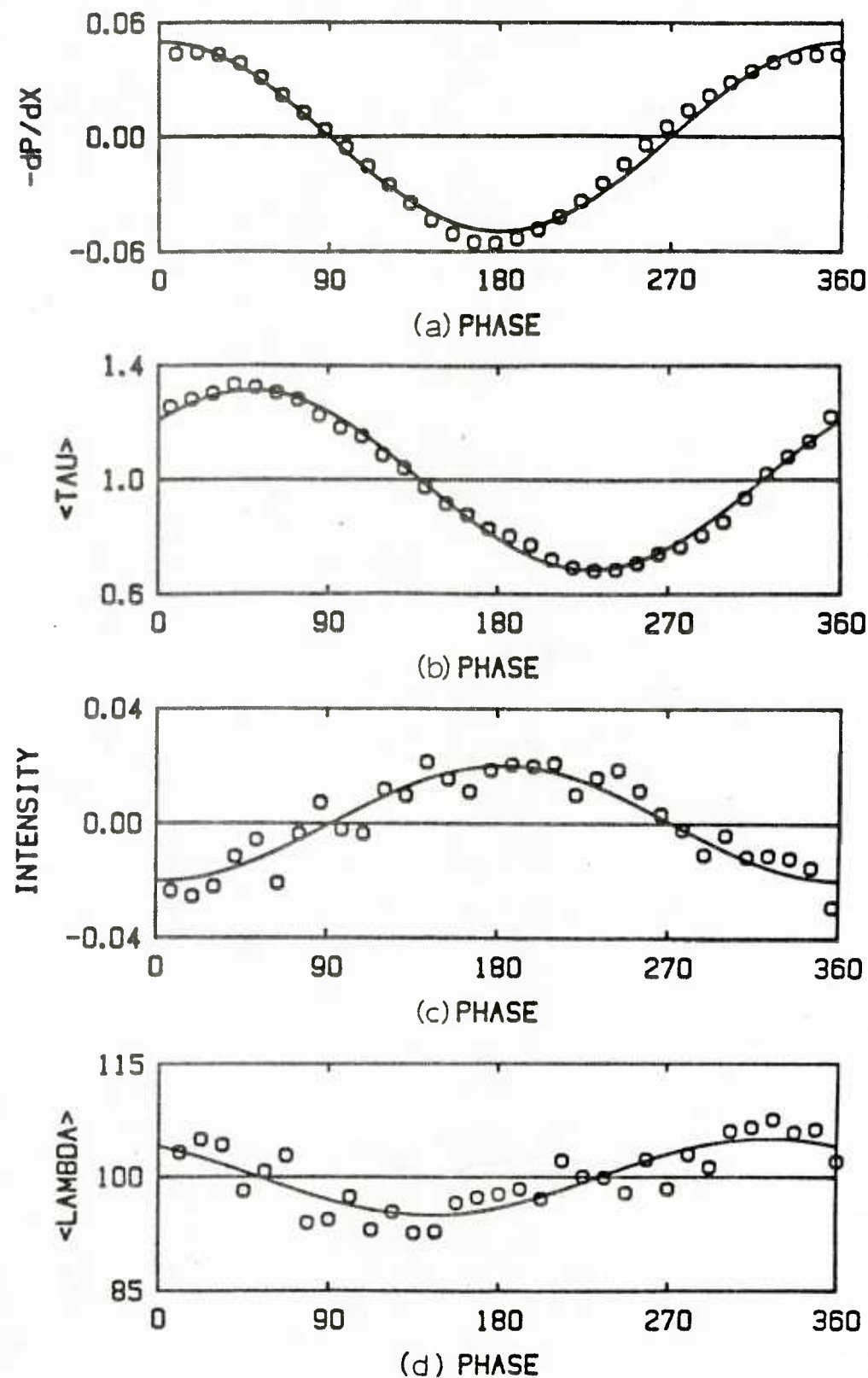


Figure 5.60 Phase averaged streak spacing at $Re = 14,600$,
 $f = 1.00 \text{ Hz}$, $\omega^+ = 0.0244$ and $a = 0.098$

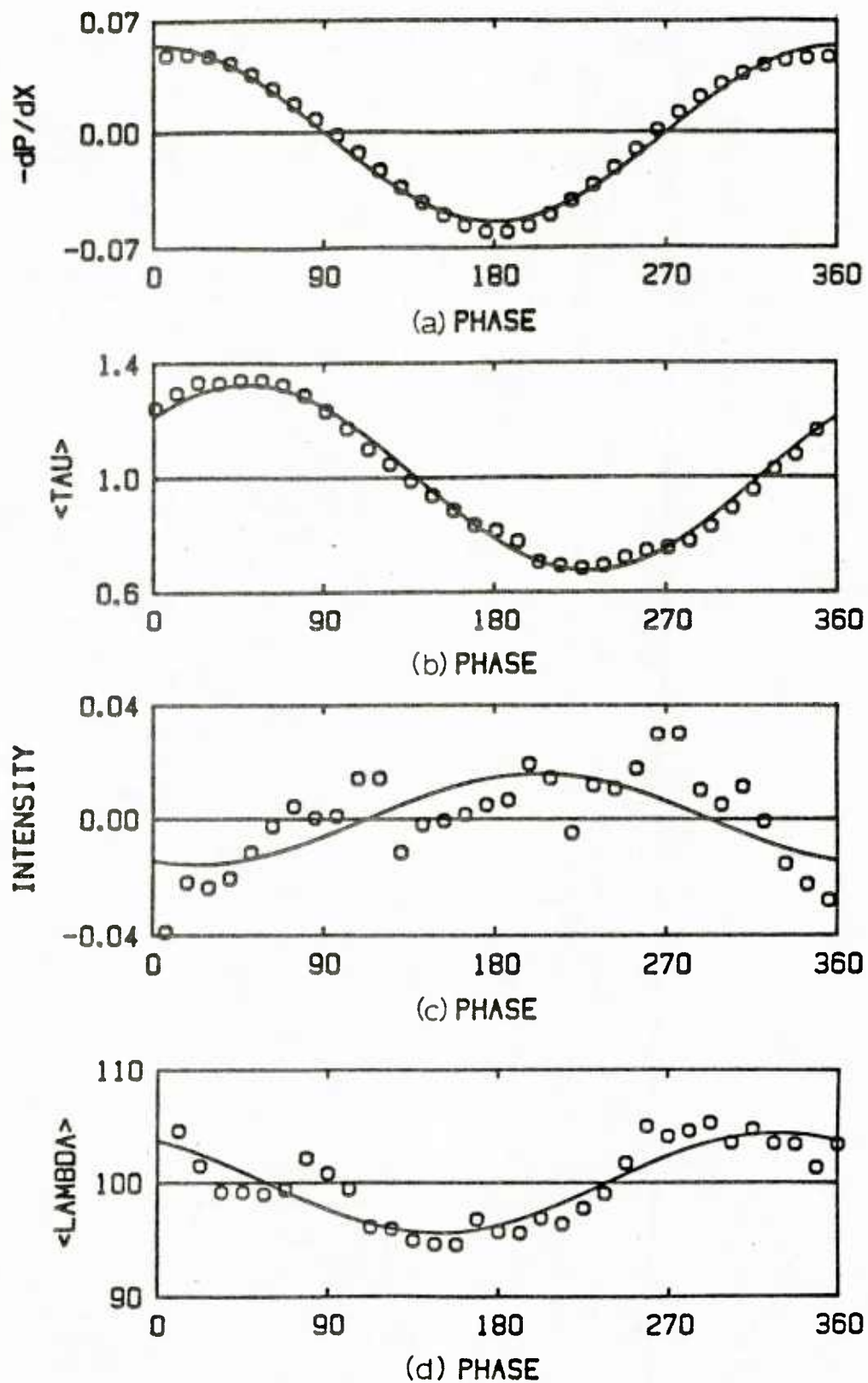


Figure 5.61 Phase averaged streak spacing at $Re = 14,200$,
 $f = 1.00$ Hz, $\omega^+ = 0.0258$ and $\alpha = 0.101$

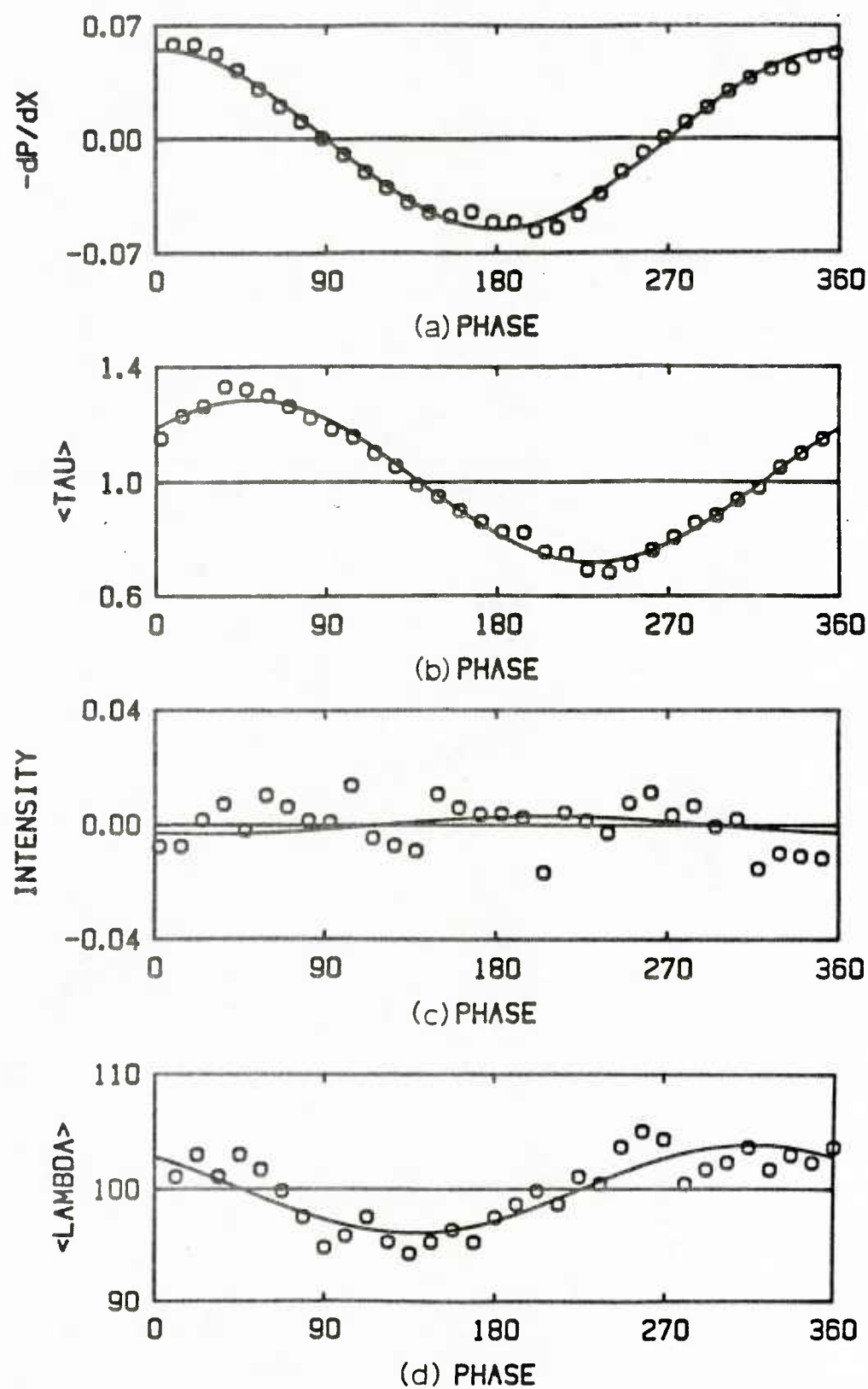


Figure 5.62 Phase averaged streak spacing at $Re = 10,300$,
 $f = 0.60 \text{ Hz}$, $\omega^+ = 0.0270$ and $a = 0.101$

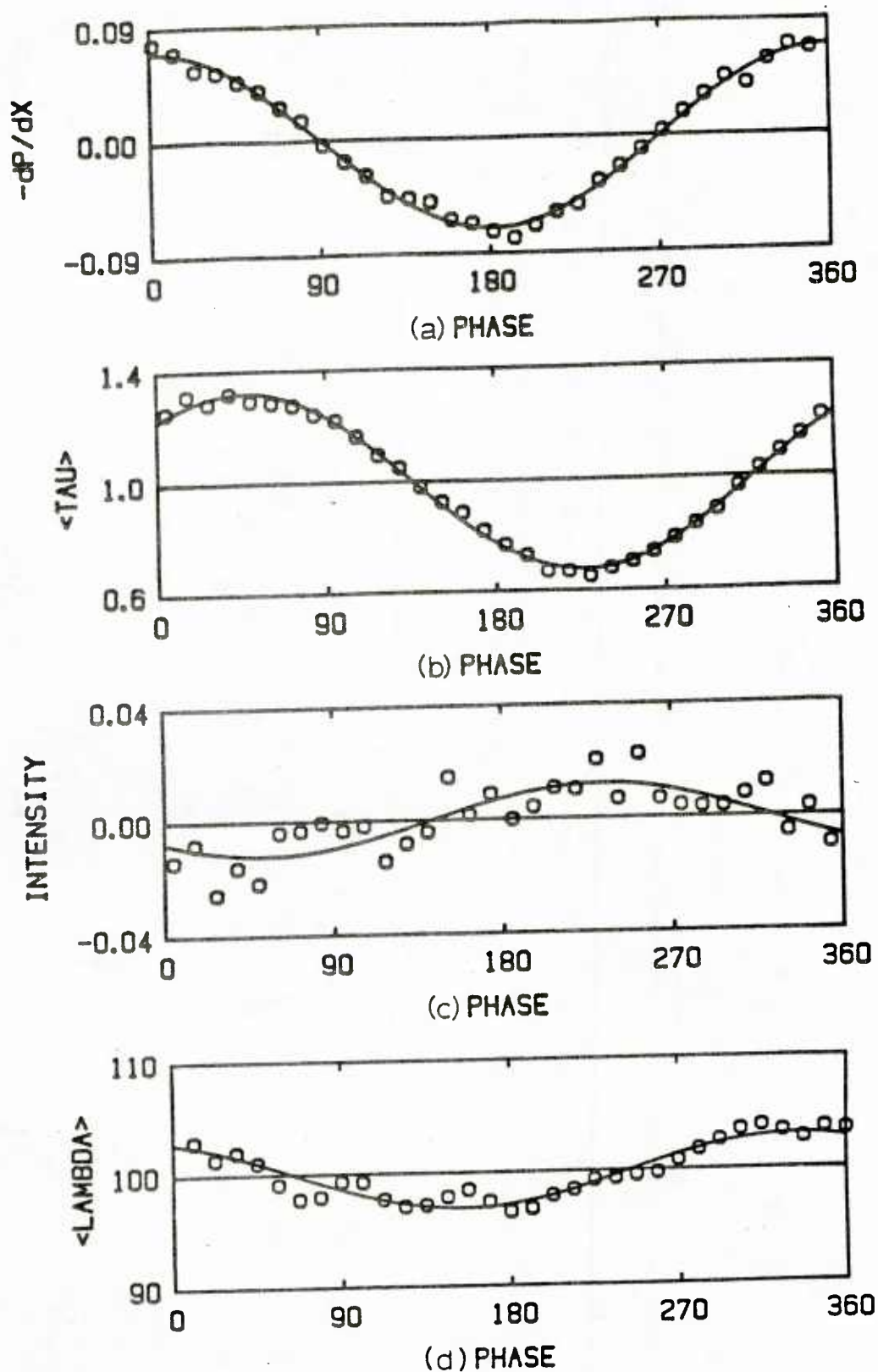


Figure 5.63 Phase averaged streak spacing at $Re = 8,750$,
 $f = 0.60 \text{ Hz}$, $\omega^+ = 0.0360$ and $a = 0.099$

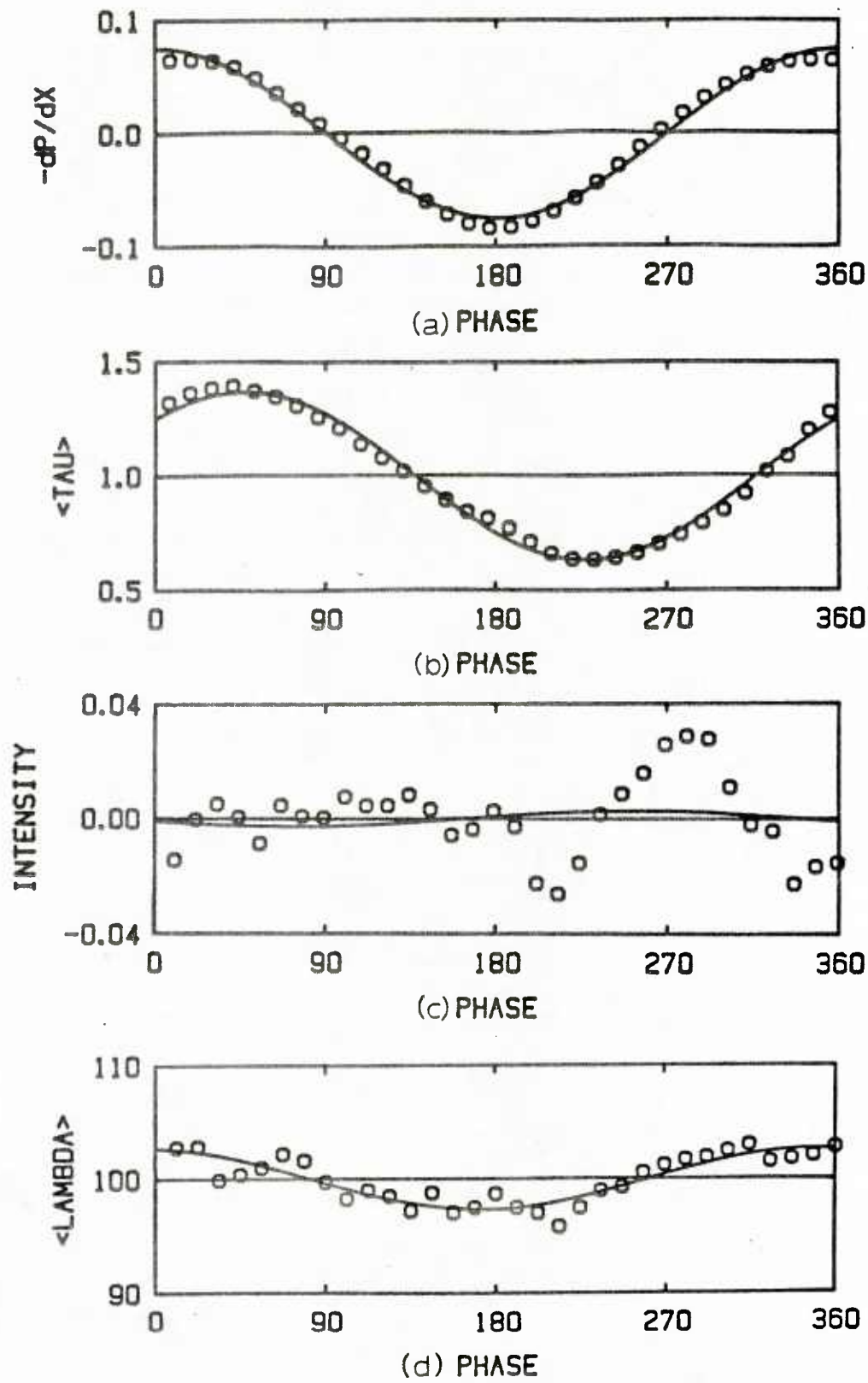


Figure 5.64 Phase averaged streak spacing at $Re = 11,400$,
 $f = 1.00 \text{ Hz}$, $\omega^+ = 0.0375$ and $a = 0.098$

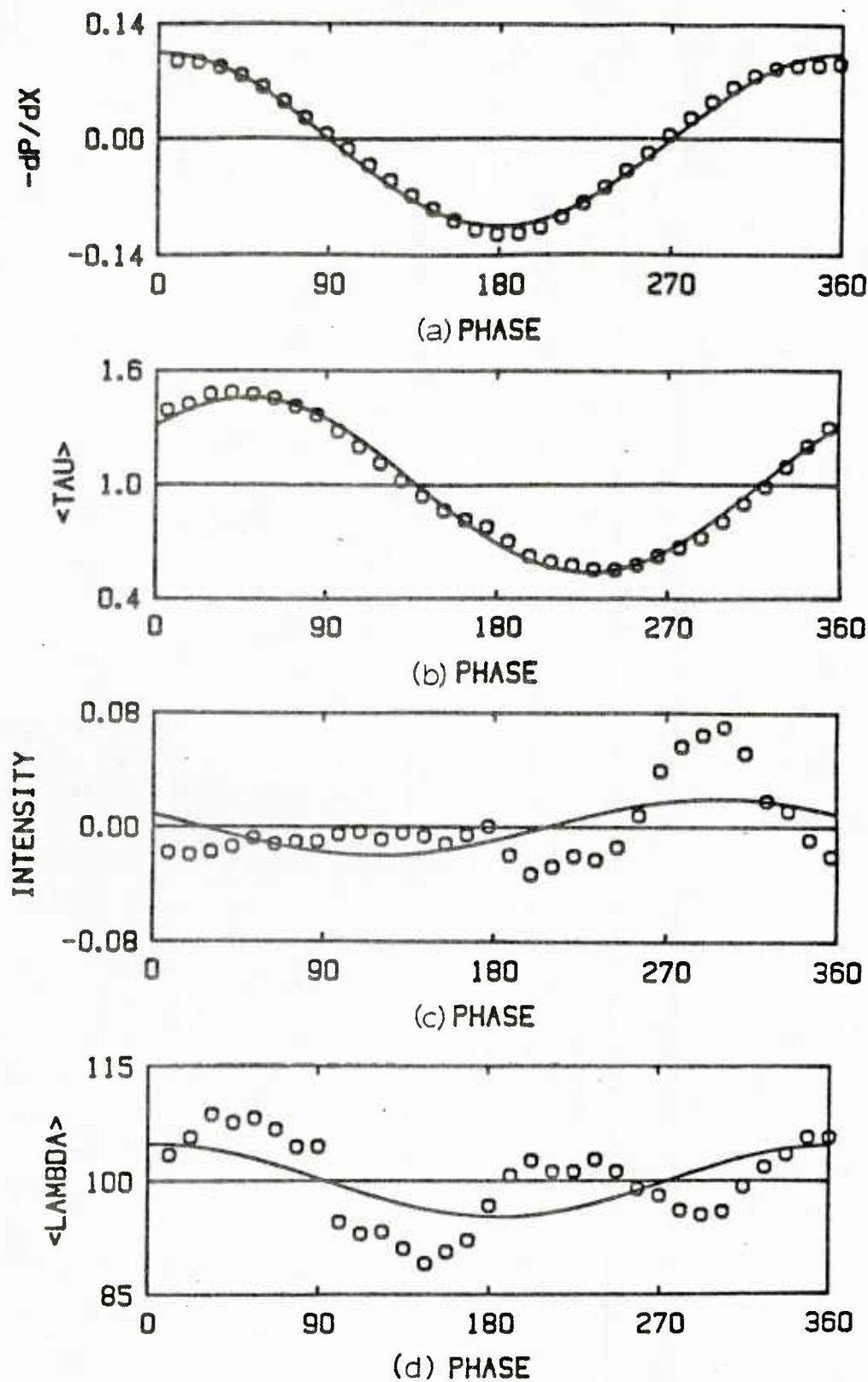


Figure 5.65 Phase averaged streak spacing at $Re = 9,200$,
 $f = 1.00$ Hz, $\omega^+ = 0.0550$ and $a = 0.100$

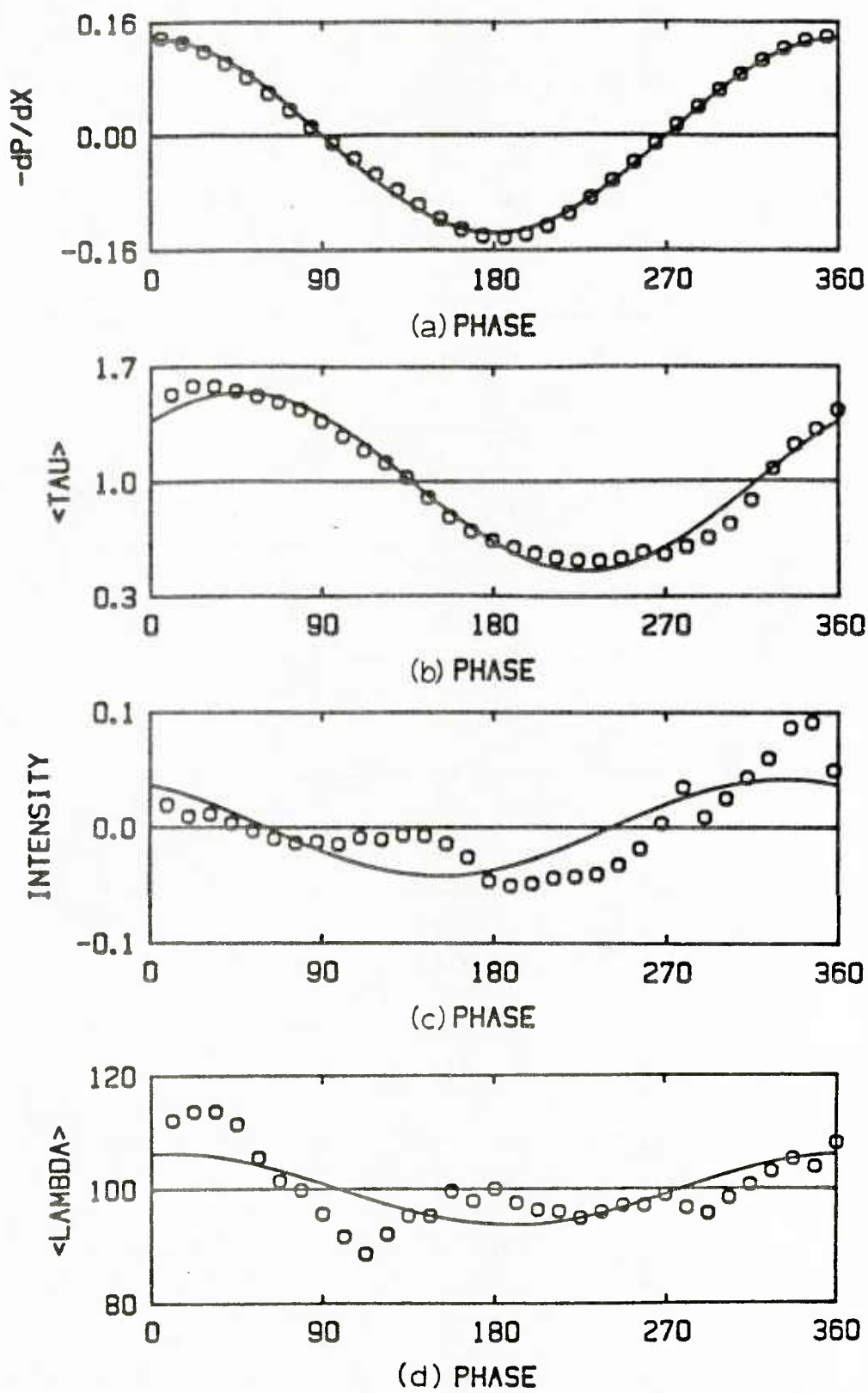


Figure 5.66 Phase averaged streak spacing at $Re = 10,300$,
 $f = 1.50$ Hz, $\omega^+ = 0.0675$ and $a = 0.101$

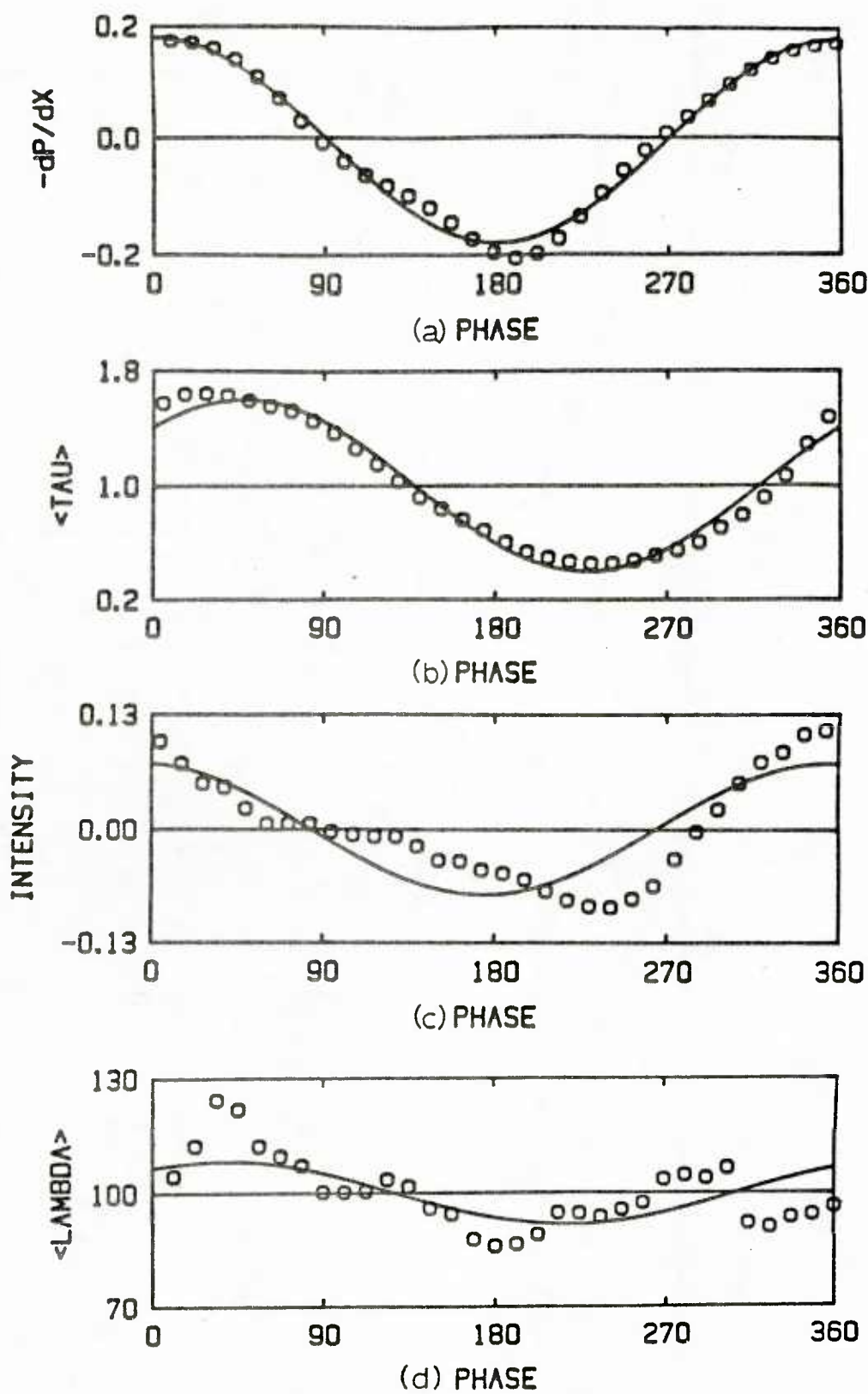


Figure 5.67 Phase averaged streak spacing at $Re = 8,650$,
 $f = 1.50 \text{ Hz}$, $\omega^+ = 0.0915$ and $a = 0.100$

At $\omega^+ = 0.0375$, the highly nonlinear behavior is observed only in the τ_w^{+1} measurements. At $\omega^+ = 0.055$, the nonlinear behavior is observed in both quantities. Thus, it appears that the nonlinear behavior in λ_0^+ starts at slightly higher ω^+ values than for τ_w^{+1} . The reason for this is not known.

The "equilibrium" arguments used to describe the variation of τ_w^{+1} with the imposed pressure gradient can also be used to explain the measured λ_0^+ variation. If the imposed pulsation is low enough in frequency, the variation of the shear stress at the wall will be of the same order of magnitude and, roughly, in phase with the shear stress variation at the outer edge of the viscous wall region. Therefore, for this type of flow (3.33) is approximately equal to the following:

$$\langle \lambda_0^+ \rangle \approx \frac{100}{(\langle \tau_w^+ \rangle)^{\frac{1}{2}}}. \quad (5.10)$$

Relation (5.10) predicts that the phase of λ_0^+ will be roughly 180 degrees out of phase with the variation of the wall shear stress. It is seen from Figure 5.51 that this is the case. Relation (5.10) can also be used to estimate the variation of λ_0^+ from the variation of the wall shear stress. The results of doing this with the wall shear stress data at $\omega^+ = 0.0012$ are compared to the experimentally measured λ_0^+ values in Figure 5.68. The calculated values slightly lead the measured values, but otherwise excellent agreement is observed. Therefore, it is concluded that the variation of λ_0^+ at low frequency can be described by the scaling arguments and concepts developed in Section 3.I.C for constant pressure gradients.

The variation of the streak spacing with ω^+ is plotted in Figure 5.69. At low ω^+ values, the amplitude of the variation is about 10% with a peak occurring at $\omega^+ = 0.03$. This is the same ω^+ value that the peak occurs in the amplitude variation of τ_w^{+1} . Figure 5.70 shows the variation of the

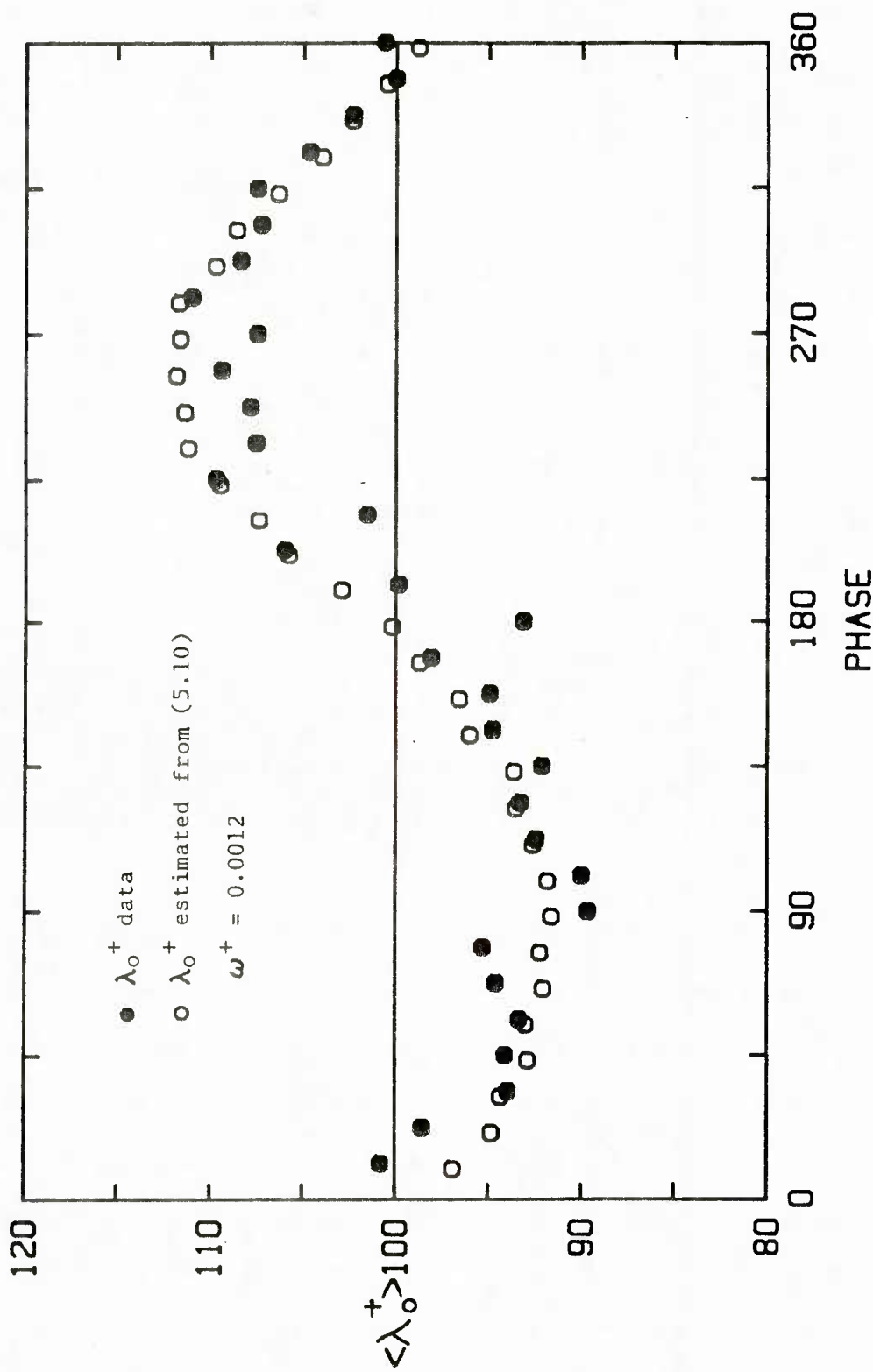


Figure 5.68 Estimation of the phase averaged streak spacing using the constant pressure gradient scaling arguments

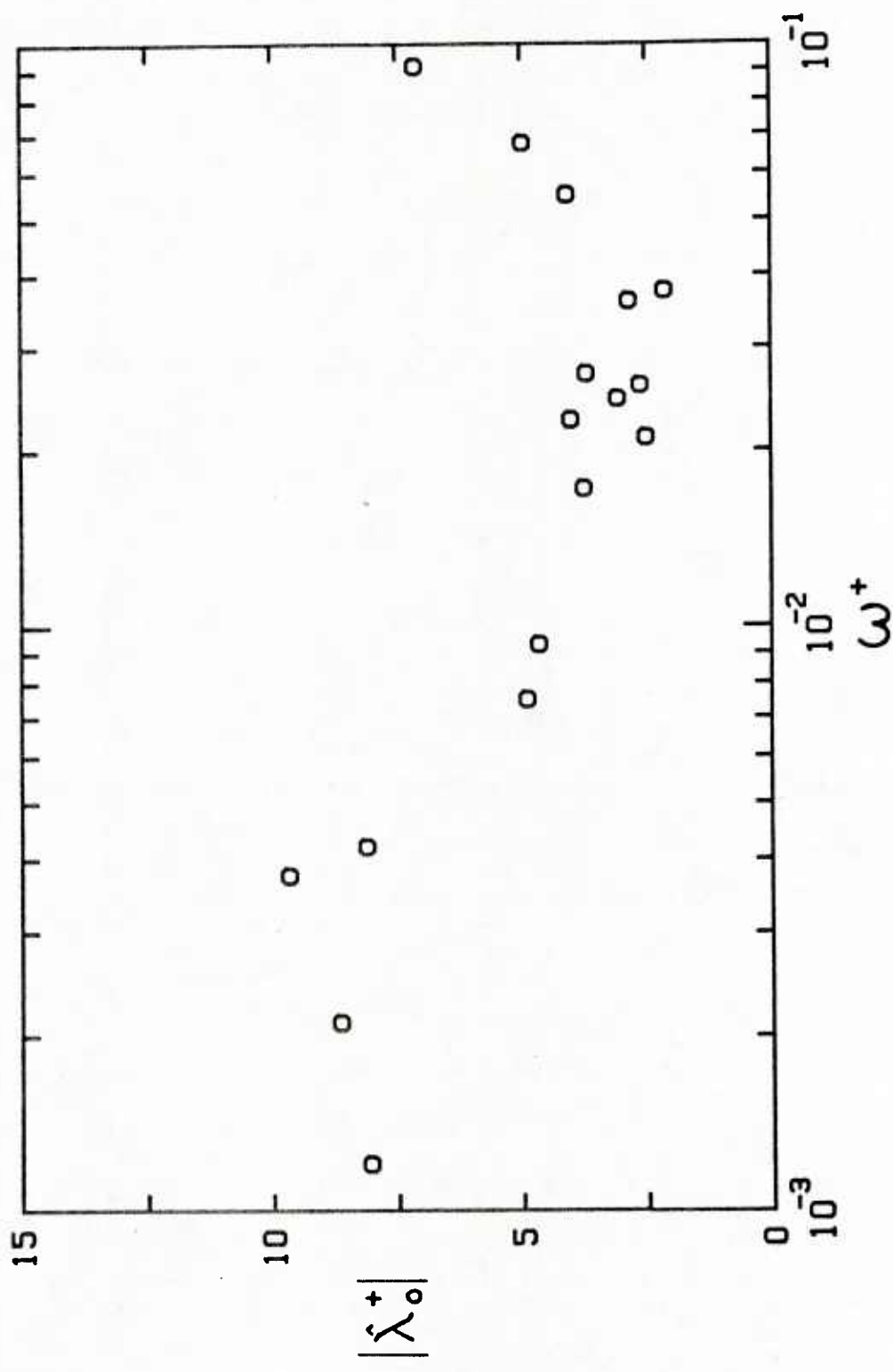


Figure 5.69 Amplitude of the variation of the streak spacing.

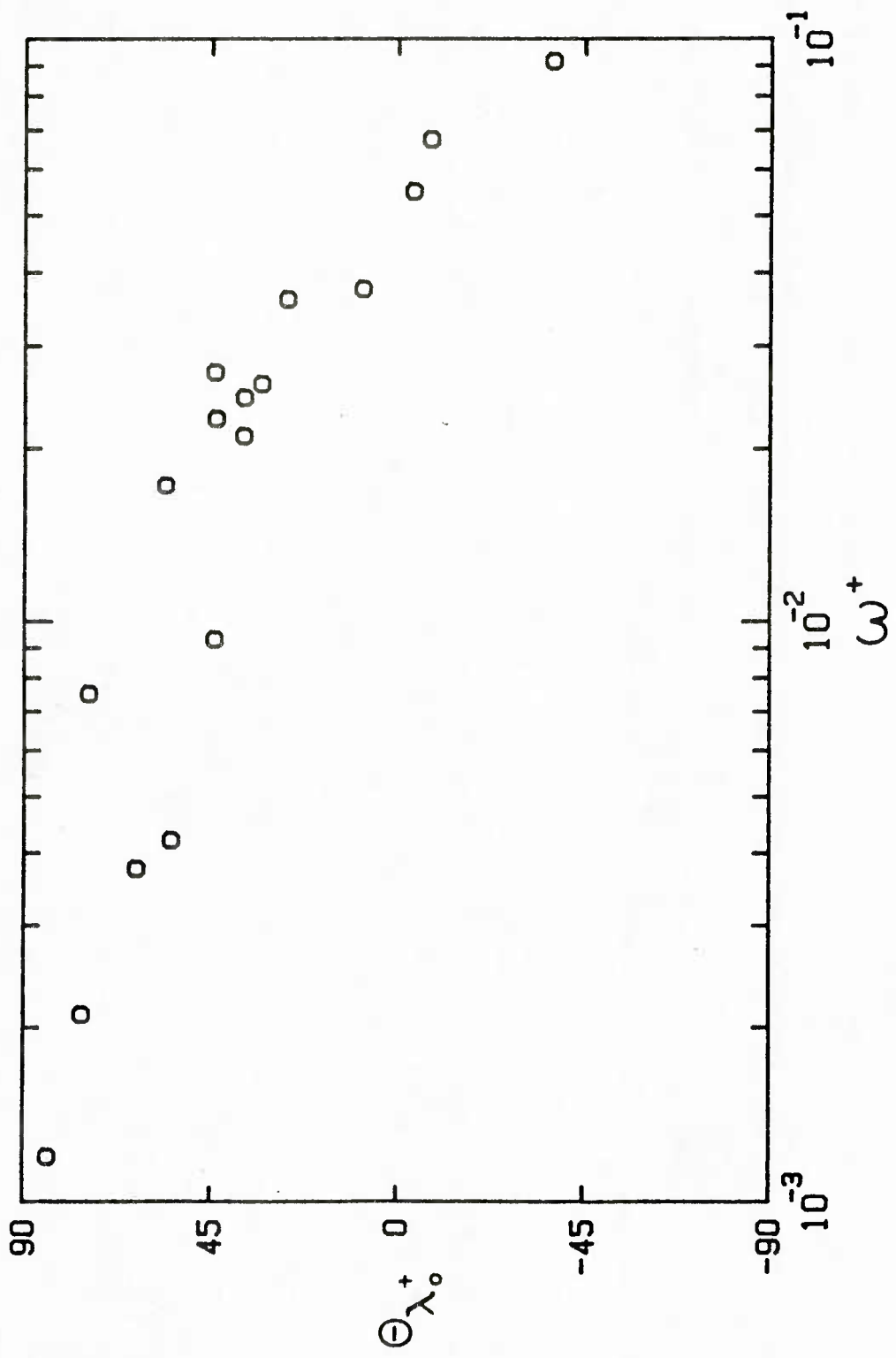


Figure 5.70 Phase (relative to the pressure gradient) of the streak spacing.

phase of the streak spacing with ω^+ . At low ω^+ values the phase of the streak spacing leads the imposed favorable pressure gradient by 85 degrees. The phase lead becomes a phase lag as ω^+ increases till at the high ω^+ extreme of 0.0915 the phase lag is equal to -40 degrees. Since the variation of the streak spacing is very similar to the variation of the intensity at the wall, the comments made earlier about τ_w^+ also apply to the variation of the streak spacing.

B. Empirical Model Results

The experimental wall shear stress data are compared to results obtained from the empirical eddy viscosity models discussed in Chapter 3. Calculations at Reynolds numbers of 20,000 and 50,000 were done in order to estimate the ω^+ value at which the wall shear stress, when normalized with the amplitude of the centerline variation, is no longer independent of Reynolds number.

The amplitude results are compared to the experimental data in Figure 5.71. The top plot shows the results for the Model C calculation and the bottom plot shows the results for Model D. The quasi-steady model (Model C) agrees with the data at high and low ω^+ values, but it does not predict the minimum at $\omega^+ = 0.01$. However, the relaxation model (Model D) using $k_1 = -25$ and $k_r = 3500$ predicts the data very well. These values for the constants are the same as those found by Mao and Hanratty (1986) to describe their data. The results are seen to start to depend upon Reynolds number at ω^+ values less than about 0.005.

Figure 5.72 shows the calculation results for the phases of the wall shear stress variation. The quasi-steady model is unable to predict the sharp rise in phase angle at $\omega^+ = 0.02$. Model D accurately describes this rise, but also exhibits a small under and over shooting of the data at low

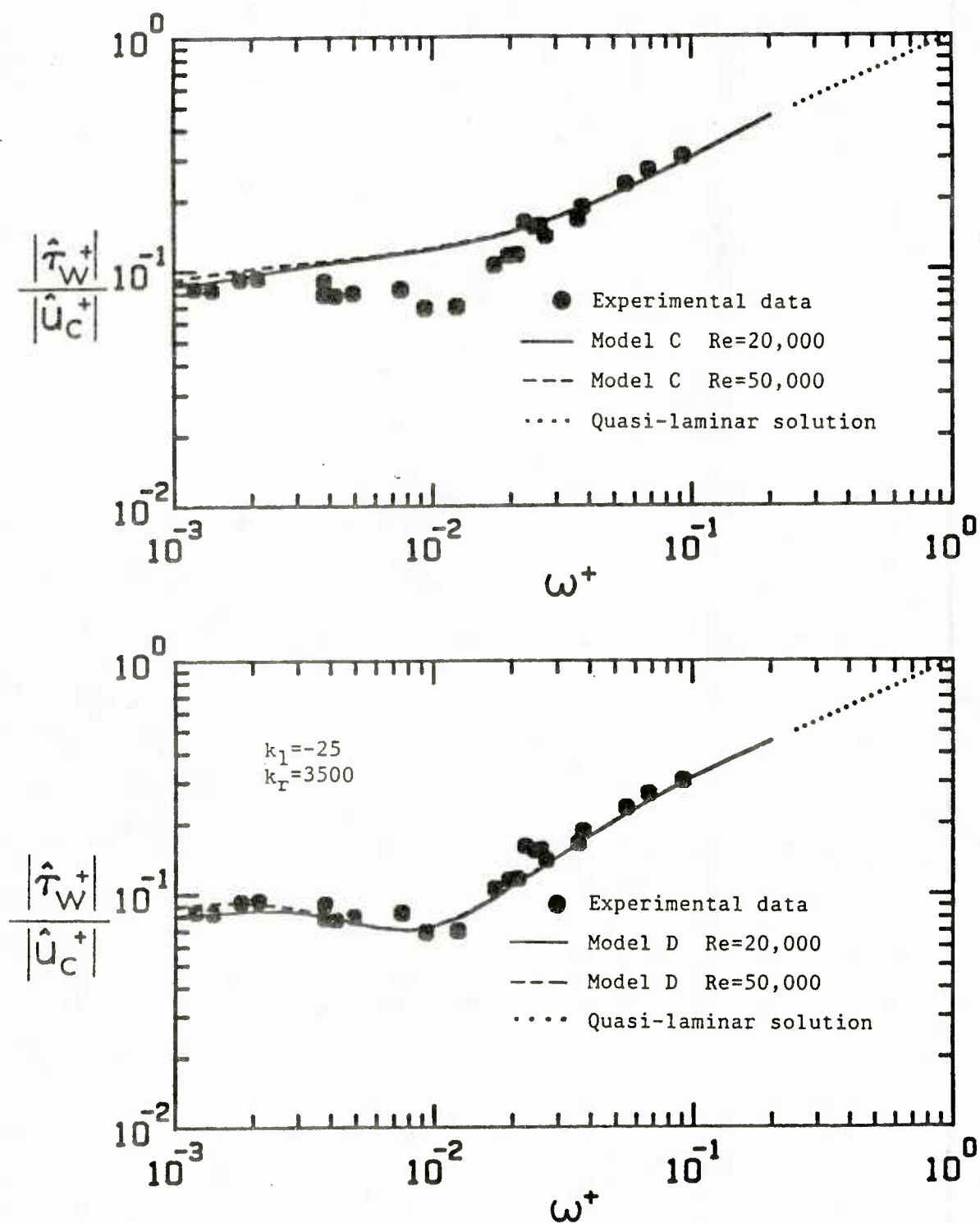


Figure 5.71 Comparison of the phase averaged wall shear stress data with Model C and Model D (amplitude results).

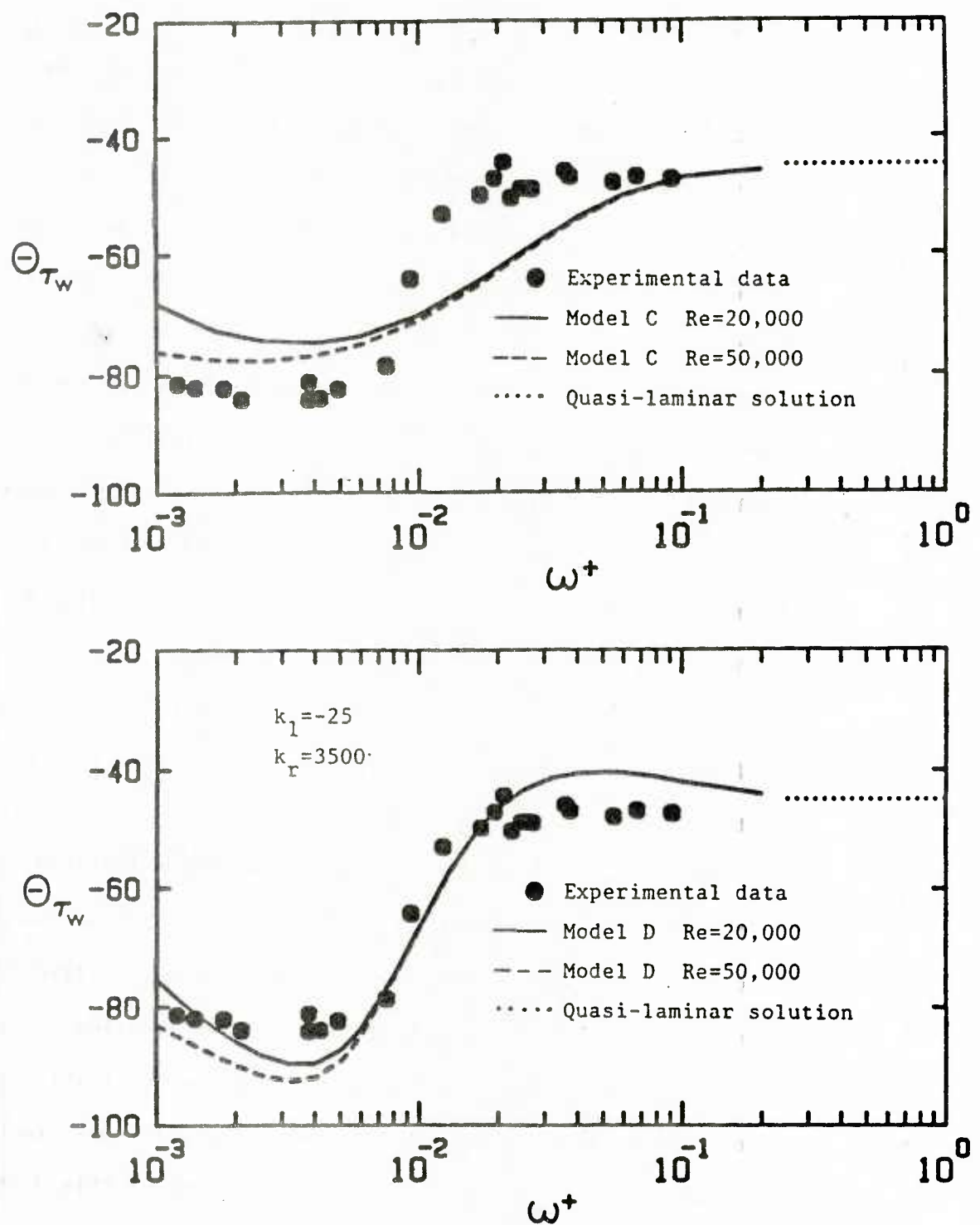


Figure 5.72 Comparison of the phase averaged wall shear stress data with Model C and Model D (phase results).

and high ω^+ values, respectively. Model D introduces an effective pressure gradient that is lower in amplitude and lags in phase relative to the imposed pressure gradient. Figure 5.73 shows the amplitude and phase of the effective pressure gradient for $k_r = 3500$. The amplitude is observed to decrease rapidly as ω^+ increases. It is seen that in the region of the experimental data, the amplitude is less than 10% of the imposed pressure gradient. The phase lag increases dramatically as ω^+ increases, till, at $\omega > 0.001$, it is roughly -90 degrees. Thus, it appears that a model such as Model D, which introduces a lag between the imposed pressure gradient and the change of scale in the viscous wall region, is needed to adequately describe the relaxation phenomena observed in pulsating pipe flow. The phase results are observed to begin to depend upon the Reynolds number at ω^+ values less than 0.01. This value is slightly higher than the one observed in the amplitude results.

The results of the constant pressure gradient part of this thesis indicate that the important hydrodynamic quantity for an equilibrium flow is the shear stress at the outer edge of the viscous wall region and not the imposed pressure gradient. Therefore, the calculated $\langle \tau_0^+ \rangle$ can be used to estimate the variation of λ_0^+ . The shear stress at the edge of the viscous wall region was determined from the empirically calculated shear stress profiles in the following manner: The location of y_0^+ in the flow was determined by the distance away from the wall at which the ratio of the viscous shear stress to the total shear stress is equal to 0.025. This is the same criterion as (3.26). The shear stress at this distance is equal to τ_0^+ and, λ_0^+ is determined from (3.34). The results for Models C and D at a $Re = 50,000$ are compared to the experimental data in Figure 5.74. Excellent agreement with the data are observed for $\omega^+ \leq 0.005$. This implies that "equilibrium" exists up to $\omega^+ = 0.005$. From Figure 5.74, it

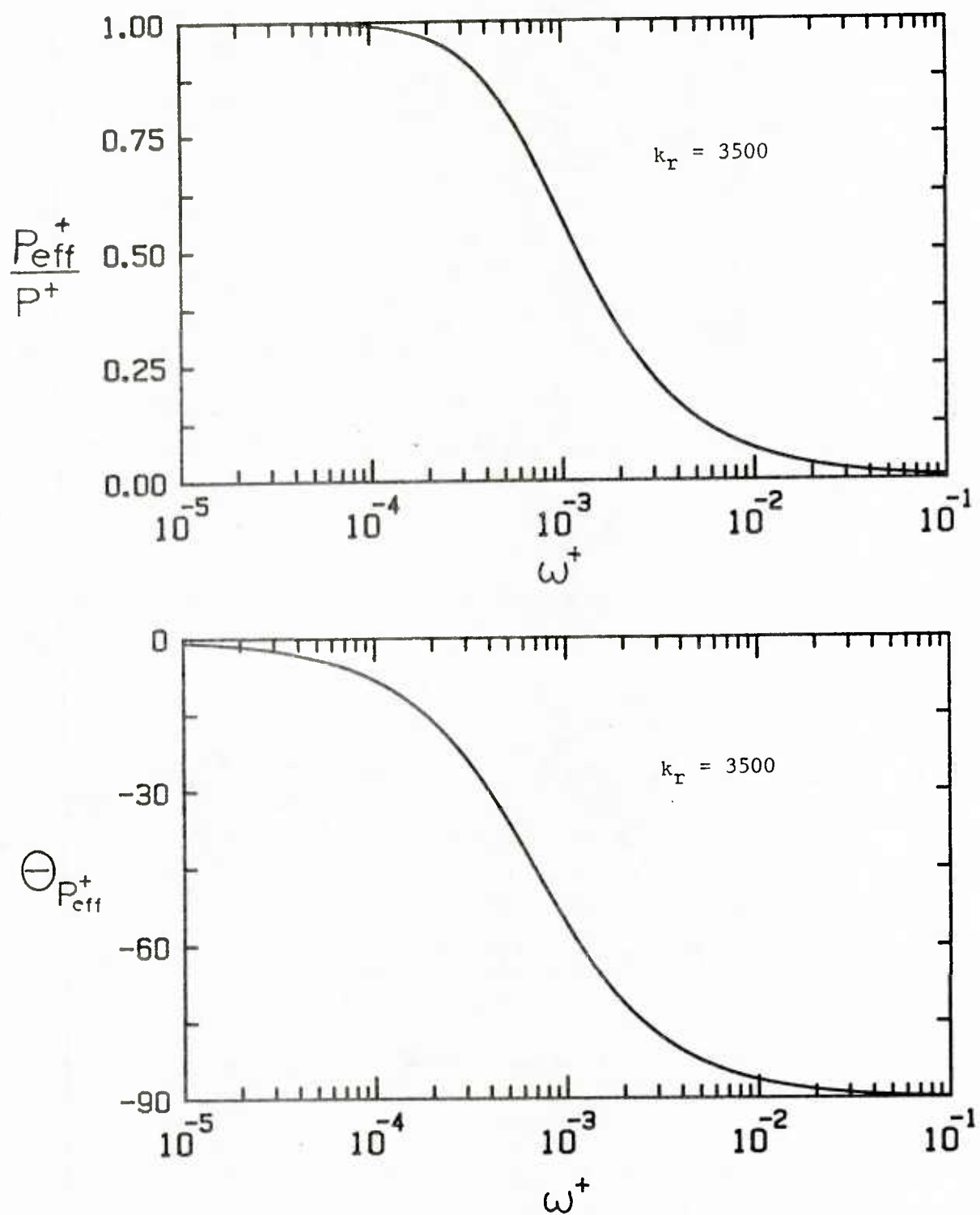


Figure 5.73 Normalized amplitude and phase lag (relative to the imposed pressure gradient) of the effective pressure gradient

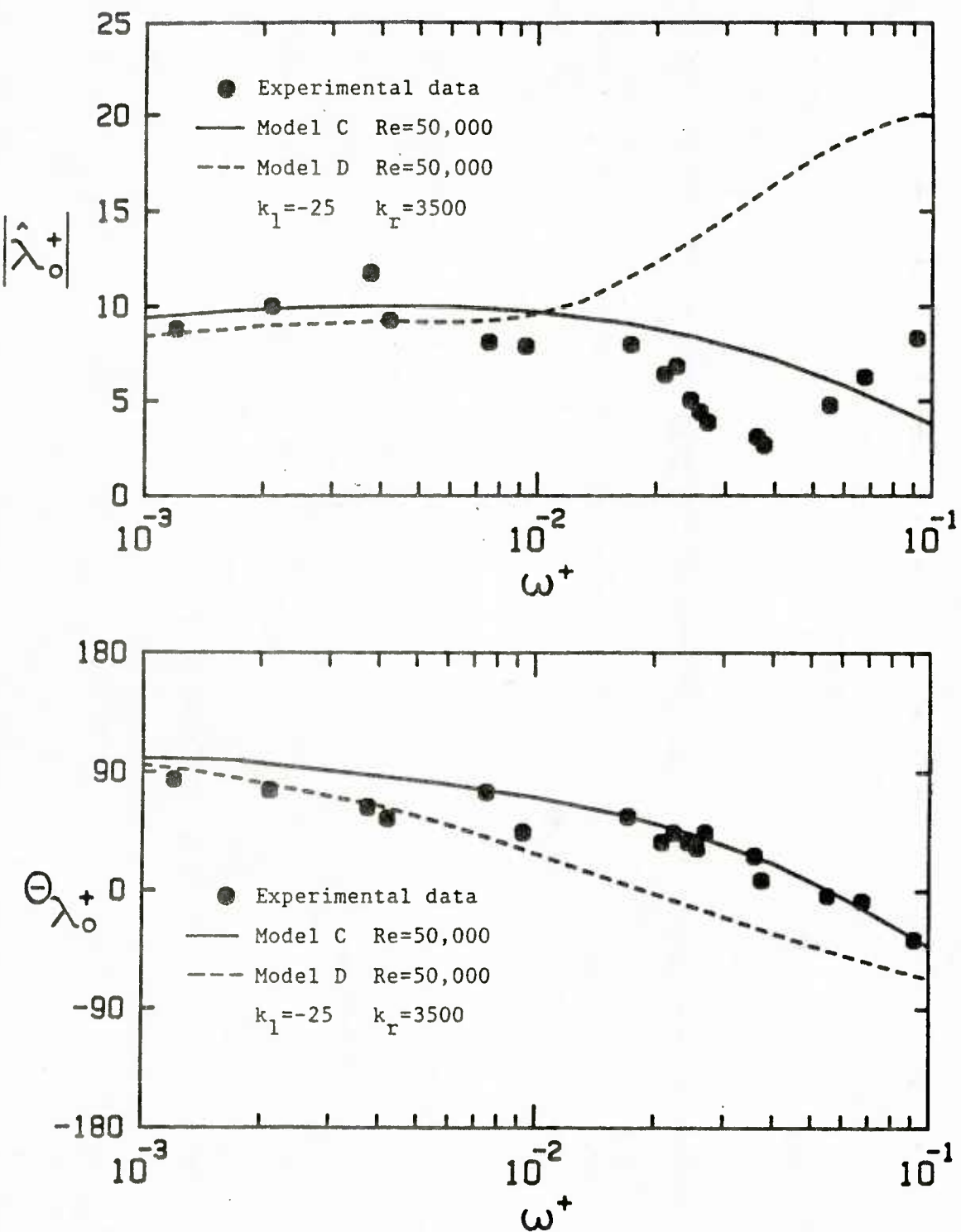


Figure 5.74 Comparison of the streak spacing experimental data with the results of Model C and Model D.

appears that Model C reproduces the data better than Model D at high ω^+ . However, this is misleading since the scaling arguments used to generate the λ_0^+ values are only valid for the situation where there is equilibrium between the turbulence and the imposed pressure gradient.

The amplitude of the pressure gradient that is needed to generate a 10% variation in the centerline velocity is determined from the plug flow relation, (3.70). However, at low ω^+ values the pulsating velocity gradient changes all the way to the center of the pipe and (3.70) is no longer valid. At this point, an iterative method is used in the calculations to determine the necessary pressure gradient to obtain a 10% centerline variation. Figure 5.75 illustrates the ω^+ value at which the plug flow assumption breaks down. Any deviation greater than 0.1 in the amplitude plot indicates that a plug flow no longer exists in the center of the pipe. Also, any deviation from a phase of -90 degrees has the same meaning. It is seen from Figure 5.75 that both quantities begin to deviate from the plug flow relation at about 0.005. The wall shear stress results shown in Figures 5.72 and 5.73 also become dependent on Reynolds number at about this value. Binder et. al. (1985) suggests a Reynolds number dependence when the Stokes layer thickness, δ_s^+ , is greater than 20. This value corresponds to $\omega^+ = 0.005$. Good agreement is observed for the two estimates. Thus, the pulsating wall shear stress is shown to depend upon Reynolds number when the plug flow condition at the center of the pipe disappears.

A Reynolds number effect is observed in the deviation from plug flow in Figure 5.75. Lower Reynolds numbers give higher magnitudes of deviation. The deviation for $Re = 20,000$ at $\omega^+ = 0.001$ is about 10%, while for $Re = 50,000$ the deviation is less than 5%. This result has implications for the experimental data since a plug flow was assumed to exist in the center of

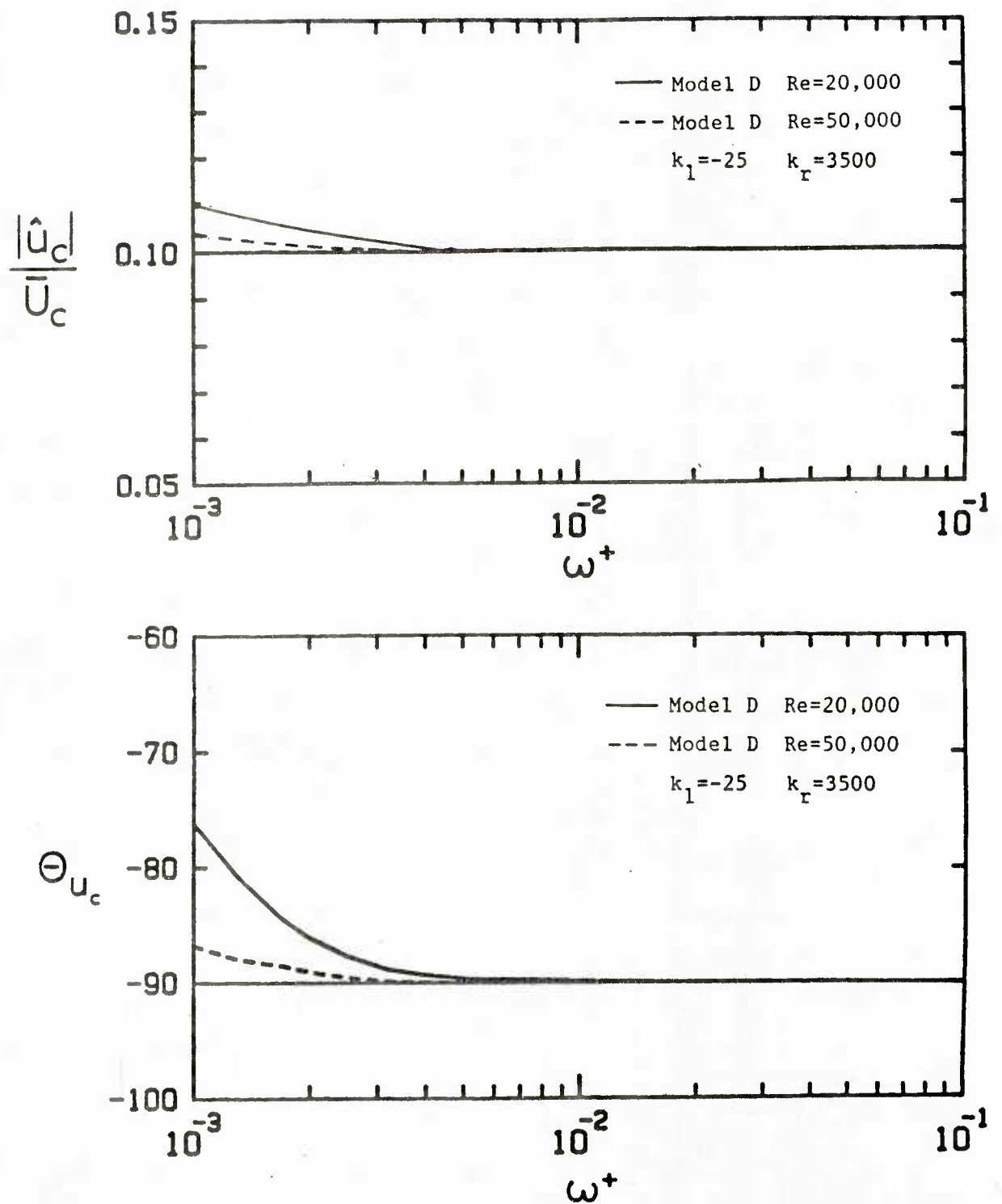


Figure 5.75 Breakdown of the assumption of plug flow in the center of the pipe.

the pipe. At $\omega^+ < 0.005$, this assumption has been shown to be incorrect. However, since most of the data points at ω^+ values less than 0.005 were taken at Reynolds numbers between 30,000 and 45,000, the error in using the plug flow assumption is believed to be less than 5%.

CHAPTER 6. DISCUSSION

In this chapter the results of the constant and pulsating pressure gradient investigations are discussed.

I. Constant Pressure Gradient Turbulent Flows

This section is composed of two parts. The first section deals with the phenomena of relaminarization and the second describes some uses for the scaling arguments presented in Chapter 3.

A. Relaminarization

Arguments are presented that show the minimum in the P_{eo}^+ curve, which occurs at $P_{eo}^+ = -0.00962$, corresponds to the point of imminent relaminarization of a turbulent boundary layer. It is suggested that the logarithmic region disappears at this P_{eo}^+ value. The results of the computer simulation using $P_{eo}^+ = -0.00962$ are found to give good agreement with the literature. The calculated results indicate that the net production of turbulent kinetic energy in the viscous wall region scaled with wall parameters stays roughly constant up to the point of relaminarization. Using some of the scaling arguments presented in Chapter 3, the net production of turbulent kinetic energy in the viscous wall region is shown to decrease after the logarithmic region disappears. This decrease leads to the eventual relaminarization of the flow.

1. Criterion for Relaminarization

In this section, the maximum eddy Reynolds number criterion of Bradshaw (1969) is shown to be consistent with the scaling arguments, presented in Chapter 3, that indicate relaminarization occurs at the minimum P_{eo}^+ . The disappearance of the logarithmic region is adopted as the criterion for the start of relaminarization.

There is considerable disagreement in the literature on the precise criteria or parameter for determining the point of relaminarization in accelerated turbulent flows. Table 6.1 lists some parameters relevant to this study and their estimated values found in the literature.

Table 6.1
Some Proposed Criteria for Relaminarization

<u>Parameter</u>	<u>Range of Values</u>	<u>Researchers</u>
$K = \frac{\nu}{U_{\infty}^2} \frac{dU_{\infty}}{dx}$	$2.5 \times 10^{-6} \geq K \geq 3.5 \times 10^{-6}$	Launder (1963, 1964) Kline et. al. (1967) Moretti & Kays (1965) Launder & Stinchcombe (1967) Back & Seban (1967) Loyd et. al. (1970) Jones & Launder (1972)
$P^+ = \frac{\nu}{\rho u^*^3} \frac{dP}{dx}$	$-0.02 \geq P^+ \geq -0.025$	Patel (1965) Launder & Stinchcombe (1967) Badri Narayanan & Ramjee (1969) Loyd et. al. (1970) Jones & Launder (1972)
$\Delta \tau^+ = \frac{\nu}{\rho u^*^3} \frac{d\tau}{dy}$	$\Delta \tau^+ = -0.009$	Patel & Head (1968)

Several researchers [Preston (1958), Patel (1965), Bradshaw (1969) and, Okamoto and Misu (1977)] also suggest that relaminarization occurs when the logarithmic region disappears. The logarithmic region serves as a buffer between the energy producing region (viscous wall region) and the energy dissipating region (core). It is assumed that relaminarization occurs when these two regions overlap and the turbulent flow becomes directly dependent on viscosity. Bradshaw (1969) suggests that appreciable overlap of these two regions will occur below some critical value of the "eddy Reynolds number", $(\tau/\rho)^{3/2} L/\nu$, where L is equal to the dissipation length parameter defined as $(\tau/\rho)^{3/2}/\epsilon$. In the logarithmic region, where production is equal to dissipation, $L = \kappa y$. This eddy Reynolds number may

be thought of as the ratio of the energy-containing to energy-dissipating length scales. Bradshaw argues that when this ratio is less than unity everywhere in the flow, the two different regions overlap (the logarithmic region no longer exists) and relaminarization will occur.

In a zero pressure gradient flow the maximum eddy Reynolds number occurs at the outer edge of the logarithmic region where $y \approx 0.2 \delta$. Relaminarization of this type of flow occurs when the boundary layer Reynolds number decreases below a certain value and the outer edge of the viscous wall region is located at $y \approx 0.2 \delta$. For flows with large favorable pressure gradients $\tau(y)$ decreases with y so the maximum value of the eddy Reynolds number occurs somewhere within the logarithmic region. According to Bradshaw's criterion, the maximum will be at the edge of the viscous wall region when relaminarization occurs. Comparing the definition of the edge of the viscous wall region, (3.27), and the definition of the eddy Reynolds number, the critical maximum eddy Reynolds number is found to be equal to κy_0^0 . Thus, Bradshaw's the criterion for relaminarization, which is assumed to be universal for all flows, is the following:

$$\left| \frac{(\tau/\rho)^{\frac{1}{2}} \kappa y}{\nu} \right|_{\max} = \kappa y_0^0 . \quad (6.1)$$

For cases for which the maximum occurs within the logarithmic region (large favorable pressure gradients), the derivative of the eddy Reynolds number with respect to y is equal to zero at the maximum. Therefore, in wall units

$$(\tau^+) + \frac{d\tau^+}{dy^+} \frac{y^+}{2} = 0 . \quad (6.2)$$

By substituting in (3.14) for τ^+ , the following criterion is obtained for

y^+ to be at the maximum:

$$y_{\max}^+ = \frac{-1}{P_e^+ + \frac{1}{2} \frac{d\tau^+}{dy^+}} . \quad (6.3)$$

Since relaminarization occurs when $y_{\max}^+ = y_0^+$, $P_e = P_{eo}^+$, and $\tau^+ = \tau_0^+$.

Equation (3.50) can be used in (6.3) to get the following condition for relaminarization:

$$\left[\frac{d\tau^+}{dy^+} \right]_0 = -2 \frac{(y_0^0)^2}{(y_0^+)^3} . \quad (6.4)$$

Figure 6.1 gives $(d\tau^+/dy^+)_0$, y_0^+ values for which relaminarization can occur according to Bradshaw's criterion. However, not all of these are realizable. It can easily shown from (6.3) and (6.4) that the two curves in Figure 6.1 cross at

$$y_0^+ = (3)^{\frac{1}{2}} y_0^0 \quad (6.5)$$

It is seen that (6.5) is satisfied at the minimum in P_{eo}^+ , $P_{eo}^+ = (d\tau^+/dy^+)_0 = -0.00962$, which is in good agreement with the value of -0.009 obtained by Patel and Head in their experiments.

Bradshaw also obtained $(d\tau^+/dy^+)_0 = -0.00962$, by assuming a linear shear stress variation in the viscous wall region. In general such an assumption is not valid physically. It appears that this assumption of Bradshaw is equivalent to assuming $(d\tau^+/dy^+)_0 = P_{eo}^+$ at the edge of the viscous wall region. From the above considerations, this can be satisfied if P_{eo}^+ is a minimum.

Relation (3.15) evaluated at y_0^+ gives the following definition for P_{eo}^+ :

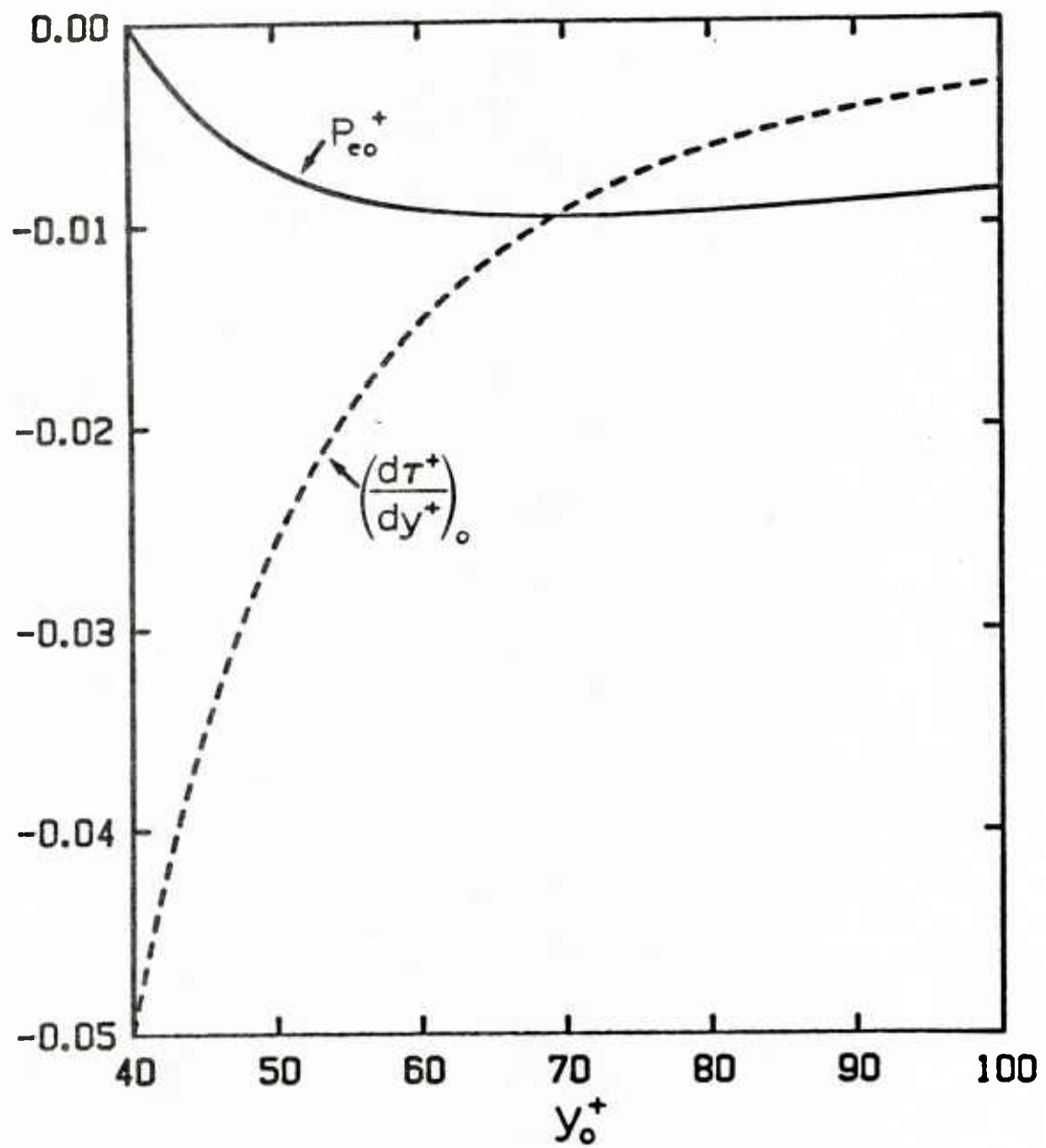


Figure 6.1 Variation of P_{eo}^+ and $(d\tau^+/dy^+)_o$ with the edge of the viscous wall region

$$Peo^+ = P^+ \left[1 - \frac{C_f}{2} \frac{1}{y_0^+} \int_0^{y_0^+} \bar{U}^{+2} dy^+ \right]. \quad (6.6)$$

As discussed in Section 3.E.3 and shown in Figure 3.3, $C_f/2$ is a constant for moderate and large favorable pressure gradients. Therefore, only if the mean velocity profile increases faster than P^+ decreases will a minimum occur. This result agrees with the study of Patel and Head (1968) that showed that a rapid increase in the mean velocity profile is a sign of imminent relaminarization of the flow. Thus, on a physical basis it appears that the minimum in the Peo^+ curve corresponds closely to the beginning of relaminarization.

Bradshaw's maximum eddy Reynolds number criterion for relaminarization is, thus, consistent with the scaling arguments developed in this study that indicates relaminarization to occur at the minimum of the Peo^+ curve.

2. Calculation using $Peo^+ = -0.00962$

A calculation was performed using the scaling parameters corresponding to incipient relaminarization, $Peo^+ = -0.00962$. The average statistics of this run are discussed in Chapter 5. Using the mean velocity profile from the run, P^+ was determined to be equal to -0.0225. This value is in the middle of the range of P^+ values found experimentally to cause relaminarization (see Table 6.1). Since $C_f/2 = 0.0025$, $K = 2.8 \times 10^{-6}$. Good agreement with the literature is also observed for this parameter. Since all three criteria listed in Table 6.1 are satisfied by the calculation at $Peo^+ = -0.00962$, it is concluded that this run is indeed representative of a flow about to relaminarize.

Therefore, a closer look at the calculations of the kinetic energy of the fluctuating velocities, shown in Chapter 5, in order to understand

relaminarization is warranted. Figure 6.2 shows the production and dissipation of turbulent kinetic energy normalized with wall variables in the nonaccelerated flow and in the incipient relaminarization flow. The presence of a large favorable pressure gradient dramatically reduces the magnitudes of these terms in the viscous wall region. However, the two terms are reduced equally and the net production of turbulent kinetic energy in the viscous wall region remains the same. This is shown in Figure 6.2 by the solid line that represents the integral of the difference between the two terms as a function of y^+ . This result indicates that the dominate structures in the viscous wall region change in size and intensity in order to maintain a net production of turbulent kinetic energy. This is consistent with the numerical results of Lyons (1985) which show that in the nonaccelerated flow the dominant wall eddy size ($\lambda_0^+ = 100$) is the one for which the net production of turbulence in the viscous wall region is just enough to supply the energy dissipated in the core region of a pipe or channel. Eddy sizes less than 100 gave a net dissipation of turbulent kinetic energy in the viscous wall region and sizes larger than 100 produced too much turbulent kinetic energy. In flows with favorable pressure gradients, the change in shear in a direction perpendicular to the wall causes the production of turbulent kinetic energy to decrease for a fixed eddy size. Therefore, in order to maintain a net production of turbulent kinetic energy in the viscous wall region, the wall eddies (scaled with the wall shear stress and the kinetic viscosity) must increase in size, which decreases the amount of dissipation in the viscous wall region. Thus, it appears that, as long as a logarithmic region exists, the wall eddies will respond to the imposed favorable pressure gradient in a manner that maintains the turbulence.

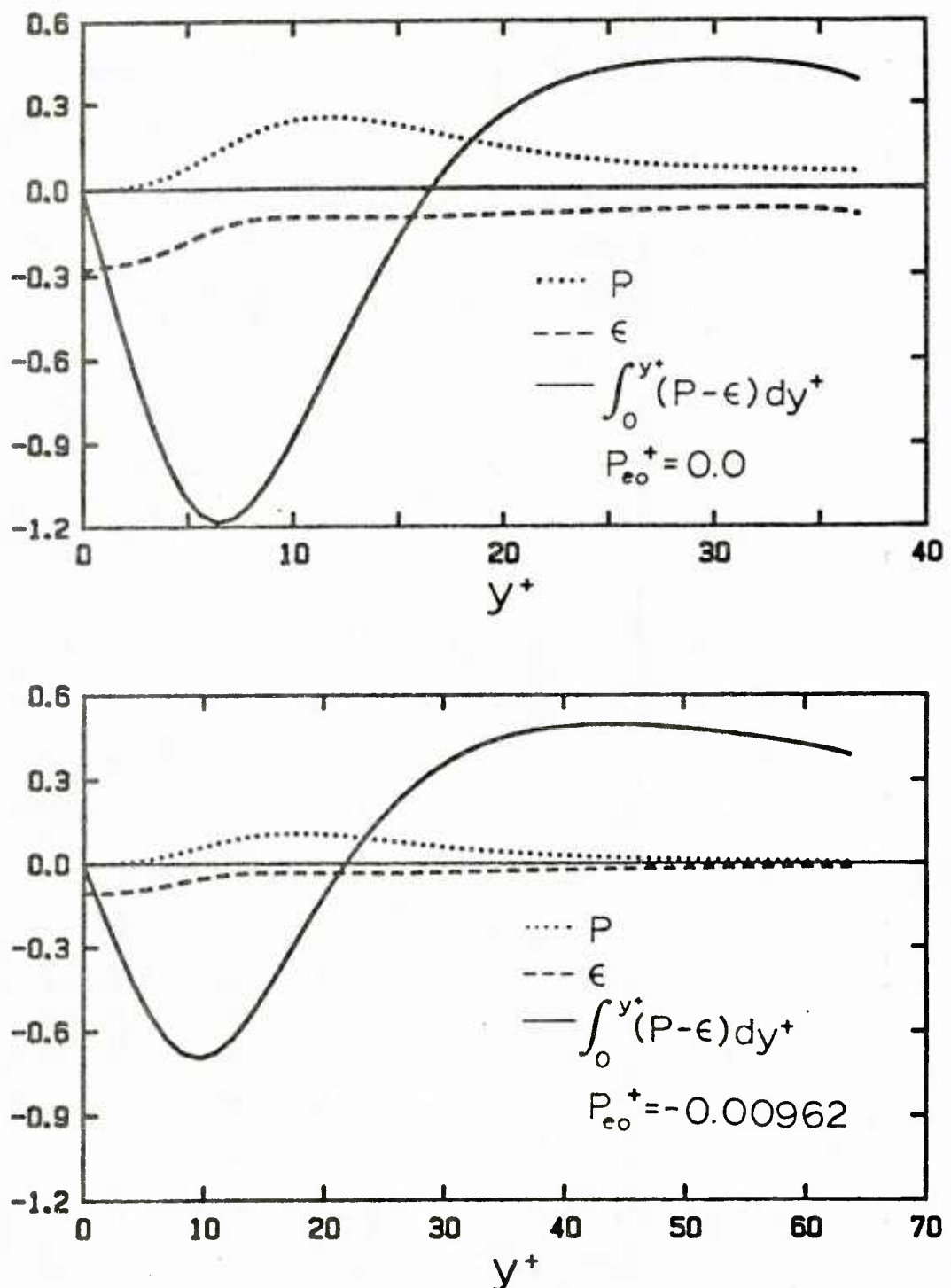


Figure 6.2 Effect of pressure gradient on the dissipation and production of turbulent kinetic energy.

3. Scaling Arguments after the Logarithmic Region Disappears

The scaling arguments presented in Chapter 3, that are used to derive (3.24) and (3.27), are no longer valid once the flow begins to relaminarize and the logarithmic region has disappeared. Unfortunately, new scaling arguments could not be derived to replace them. However, some qualitative information about why relaminarization will occur once the logarithmic region has disappeared can be obtained from the scaling arguments.

The rate of dissipation relation, (3.21), is valid for any flow where there exists only one characteristic length. Thus, (3.21) is a valid relation for the dissipation even if production and dissipation do not balance [Tennekes and Lumley (1981)]. The isotropic rate of dissipation relation, (3.29), should also be valid in a flow in the initial state of relaminarization. Thus, by equating the two relations and assuming q_0 scales as τ_0/ρ , the following is obtained:

$$\left(\frac{\lambda_0(\tau_0/\rho)^{1/2}}{\nu} \right) = C_1 \left(\frac{\ell_0(\tau_0/\rho)^{1/2}}{\nu} \right)^{1/2}. \quad (6.7)$$

where C_1 is a constant. In a flow with a logarithmic region, $\ell_0 = \kappa y$ and (6.7) becomes equal to (3.32). However, after the logarithmic region has disappeared the mixing length at the edge of the viscous wall region becomes equal $c_2\delta$, where δ is the boundary layer thickness. This is the mixing length relation valid for the core region of a nonaccelerated flow. Thus, after relaminarization, λ_0^0 (λ_0 normalized with the local shear stress) becomes independent of the location of the edge of the viscous wall region. As discussed earlier, Lyons (1985) has shown that smaller eddy sizes generate more dissipation in the viscous wall region than larger sizes. Therefore, if λ_0^0 no longer increases as $(y_0^0)^{1/2}$, the relative amount of dissipation will be higher. This situation generates a net

dissipation of turbulent kinetic energy in the viscous wall region and the flow reverts back to a laminar state.

B. Uses for the Scaling Arguments

The location of y_0^+ for different levels of acceleration is a very difficult quantity to determine experimentally. Qualitatively the peak in the U intensity profile is observed to move farther from the wall and the extent at which the mean velocity profile follows the viscous sublayer equation, $\bar{U}^+ = y^+$, increases with acceleration. Relation (3.28) suggests a more quantitative method of determining y_0^+ from either experimentally measured shear stress profiles or from shear stress profiles generated from mean velocity profiles and (3.13). The location of y_0^+ for a given acceleration would be the intersection between a curve generated from (3.28) and the shear stress profile. This is illustrated in Figure 6.3 using the experimentally determined shear stress profiles of several researchers. It is seen that the location of the intersection of the curves increases with acceleration.

The mean velocity profile data of Loyd et. al. (1970) corresponding to $K = 2.55 \times 10^{-6}$ was still changing at the end of their test section. This indicated to the authors that the flow was relaminarizing. The last two measuring station profiles are shown in Figure 6.3. As expected for a flow in the process of relaminarization, the location of y_0^+ increases from 64 to 70. The last value of 70 is just greater than the value of 69.28 suggested by (3.40) as the maximum value of y_0^+ possible in an accelerated flow without undergoing relaminarization. This agreement is strong support for the validity of the scaling arguments presented in Chapter 3.

The τ_0^+ values determined by the intersection of the shear stress profiles with (3.28) can be used with (3.34) and (3.39) to estimate λ^+ and

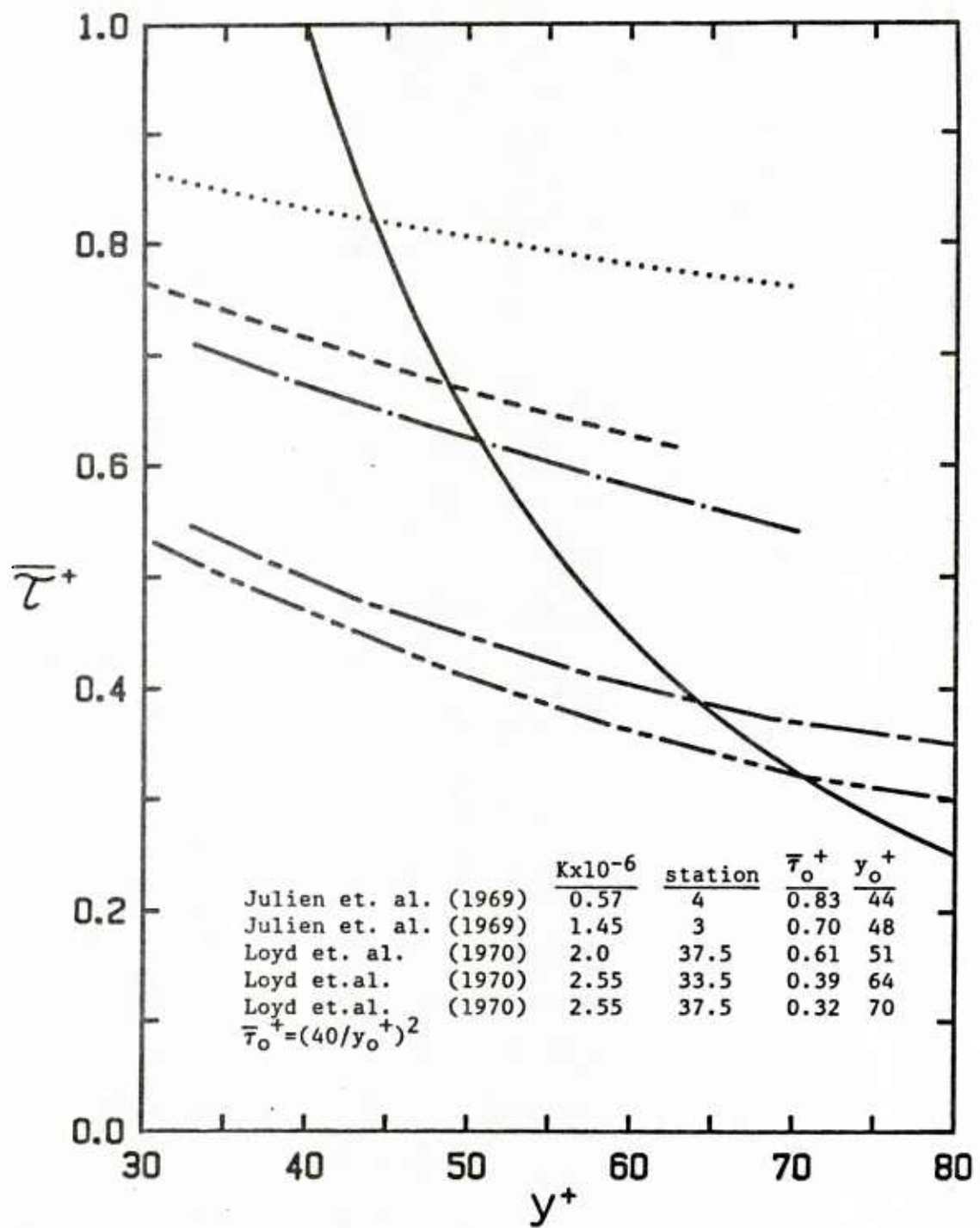


Figure 6.3 Locating the edge of the viscous wall region.

T_B^+ for a given acceleration. The results of the method applied to the data of Julien et. al. (1969) and Loyd et. al. (1970) are plotted in Figures 6.4 and 6.5. The λ^+ and T_B^+ data of Kline et. al. (1967) using dye injection and hydrogen bubble techniques are shown for comparison. Also presented are the values obtained from the computer calculations. Considering the difficulties involved in taking the data the agreement is very good. Thus, the scaling arguments presented in Chapter 3 are shown to provide a working framework for estimating λ^+ and T_B^+ from either a mean velocity or shear stress profile.

II. Pulsating Pressure Gradient Turbulent Flows

This thesis reports on measurements of the variation of the wall shear stress, the turbulent fluctuations of the wall shear stress, and the transverse correlation coefficients of the streamwise velocity gradient at the wall that are caused by the imposition of a sinusoidal pulsation on the flow of a turbulent fluid through a pipe. The correlation coefficient measurements provide information about the variation of the streak spacing with the imposed pressure gradient. Results are presented for dimensionless frequencies, ω^+ , ranging from 0.0012 to 0.0915. By using a small amplitude of imposed pulsation a linear response is obtained whereby the wall shear stress variation can be described by a single harmonic with the same frequency as the imposed oscillation and with an amplitude which varies linearly with the amplitude of the imposed oscillation.

It is found that the measurements are correlated with the parameter ω^+ for values greater than 0.005. This result is consistent with the measurements of Mao and Hanratty (1986), but contrasts with the characterization of turbulent pulsating pipe flow by $\omega D/\bar{U}_B$, as suggested by Jararaman et. al. (1982), and by $\omega D/u^*$, by Ramaprian and Tu (1983). The dimensionless

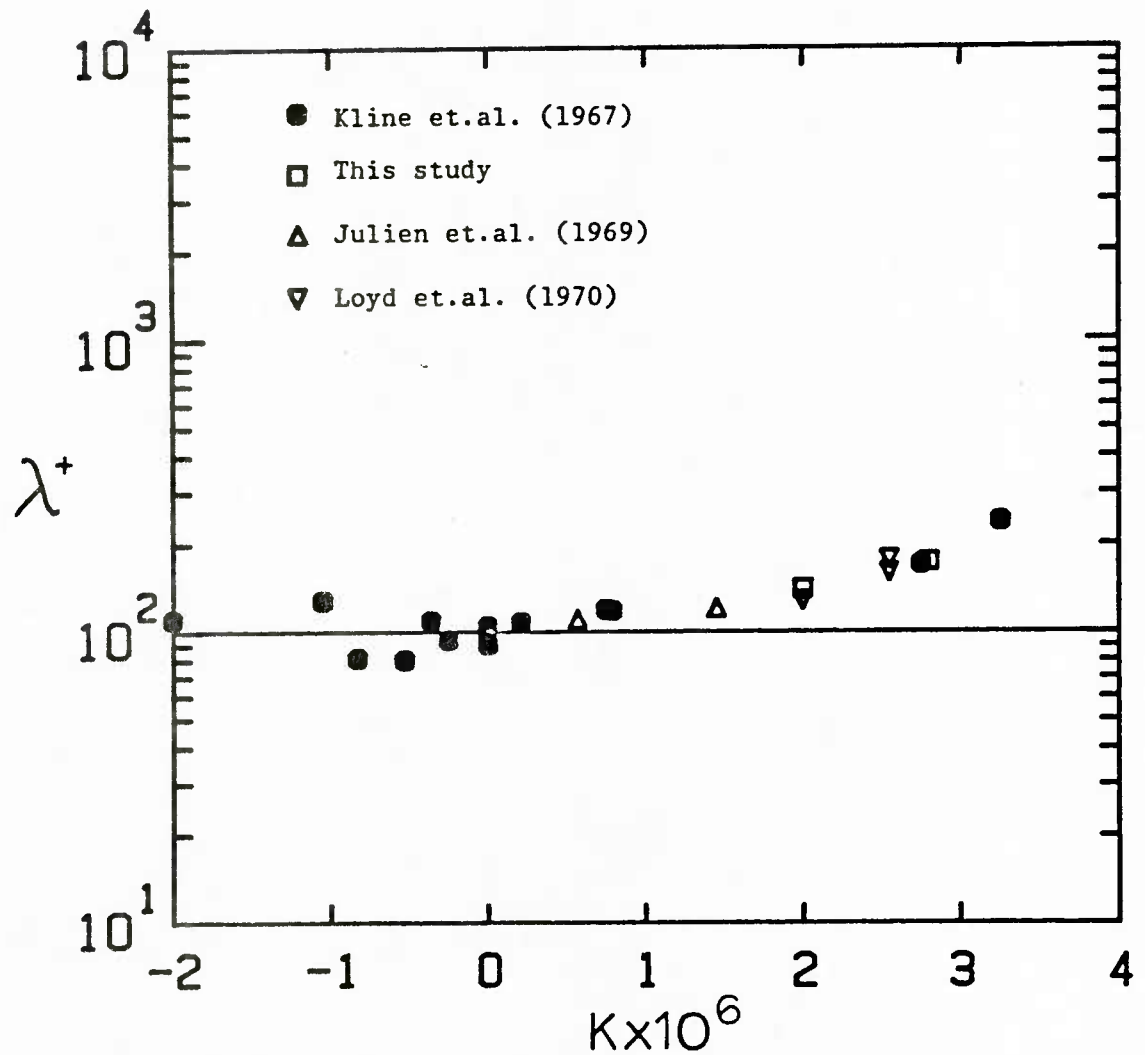


Figure 6.4 Streak spacing obtained using the scaling arguments and the mean profiles of several investigators.

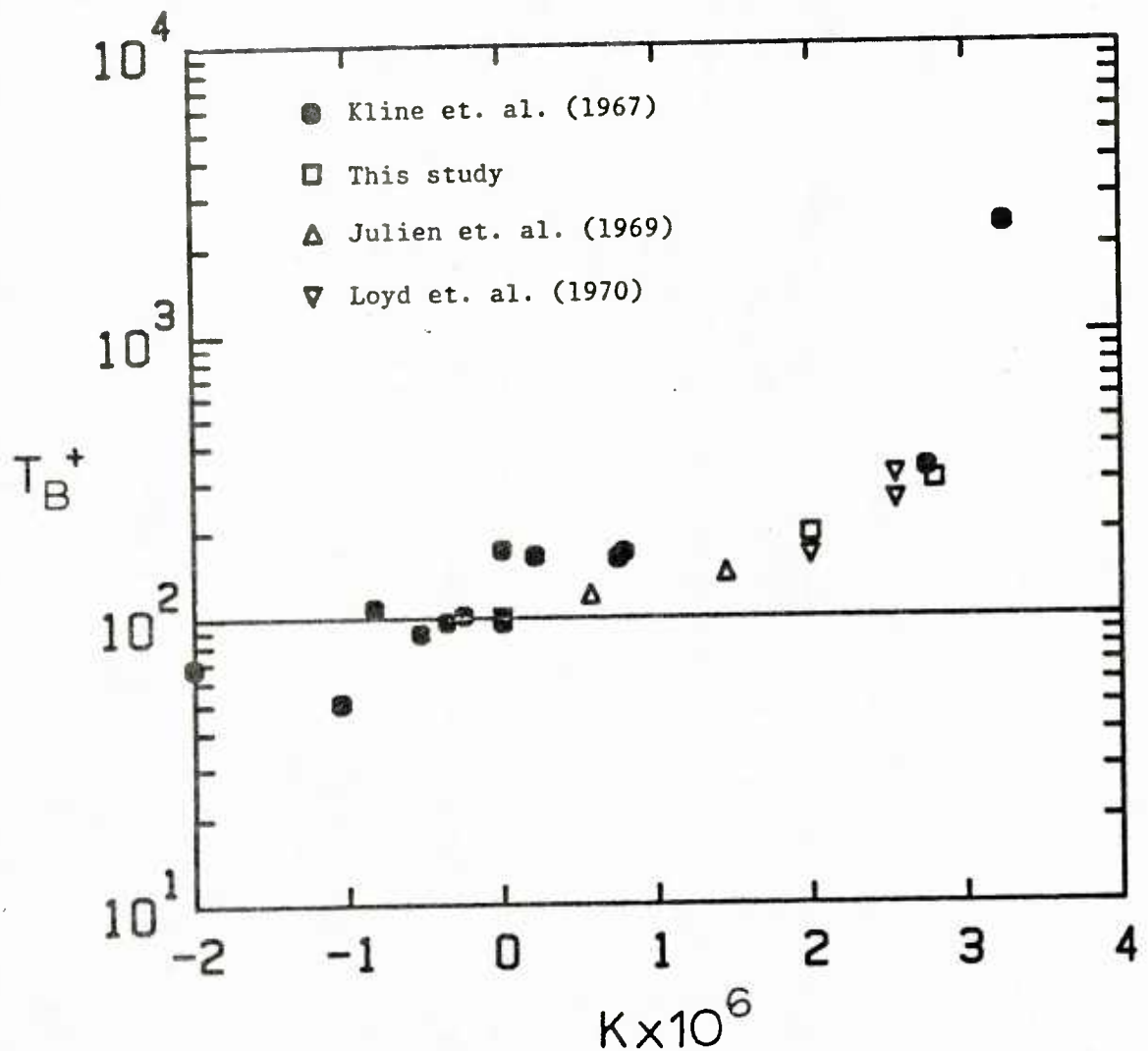


Figure 6.5 Bursting period obtained using the scaling arguments and the mean profiles of several investigators.

frequency is defined as $\omega^+ = 2(\delta_V/\delta_S)^2 = 2(1/\delta_S^+)^2$, where $\delta_V = \nu/u^*$ is the length scale of the viscous sublayer and $\delta_S = (2\nu/\omega)^{1/2}$ is the thickness of the Stokes layer. Binder et. al. (1985) suggests a Reynolds number dependence on the wall shear stress results when δ_S^+ is greater than 20 ($\omega^+ = 0.005$). This value is in agreement with the numerical results that indicate a plug flow condition no longer exists at the center of the pipe for $\omega^+ \leq 0.005$. Thus, it appears that the loss of plug flow in the center of the pipe corresponds to the point where scaling with ω^+ (or δ_S^+) is no longer appropriate.

At high ω^+ values, the experimental wall shear stress results agree with the quasi-laminar solution. Measurements by Ronneberger and Ahrens (1977) also indicate agreement at high frequencies. This conclusion is in disagreement with the measurements of Mao and Hanratty (1986) that had significantly lower amplitudes. The wall shear stress amplitude data of Binder et. al. (1985) were also lower than the quasi-laminar solution at high frequencies. Furthermore, measurements of the velocity field very close to the wall by Jayaraman et. al. (1982) and by Ramaprian and Tu (1983) seem to suggest lower pulsation amplitudes at high frequencies than calculated from the quasi-laminar solution. At present this difference of results cannot be resolved.

The measurements of the transverse correlation coefficients of the streamwise velocity gradient at the wall are believed to be the first of their kind in turbulent pulsating flow. Through (5.7), these measurements are used to estimate the variation of the streak spacing with the imposed pressure gradient. The results for the variation of λ_0^+ can be interpreted so as to indicate which type of interaction between the turbulence and the imposed pressure gradient exists at a specific ω^+ .

At low ω^+ values, the variation of λ_0^+ is roughly 10%. It leads the

favorable pressure gradient by 90 degrees and is 180 degrees out of phase with the wall shear stress and the intensity of the turbulent fluctuations at the wall. This phase behavior suggests that the turbulence in the viscous wall region is in "equilibrium" with the imposed pressure gradient. This implies that the imposed pressure gradient is varying slowly enough to enable the turbulence to respond to the imposed shear stress at the outer edge of the viscous wall region. Thus, the scaling relations developed for constant pressure gradients are found to be applicable for pulsating turbulent flow at low ω^+ values.

At higher dimensionless frequencies, the turbulence is no longer able to follow the imposed pressure gradient and, therefore, the amplitude of the variation of the turbulence quantities decreases. Thus, a region of transition from equilibrium turbulence to that of "frozen" turbulence behavior is observed for ω^+ values between 0.005 and 0.03. The value of 0.03 corresponds to a δ_S^+ value of 8.16. Consequently, the Stokes layer, where all the changes in the pulsating velocity gradient occur, is almost equal to the thickness of the viscous sublayer. Since turbulence has very little effect on the flow in the viscous sublayer, the imposed pulsations in the turbulent velocity field would be expected to have little effect on the turbulent flow field.

In the quasi-laminar limit, the amplitude of the variation of λ_0^+ would be expected to be close to zero. Instead, a highly nonlinear large amplitude variation is observed in both the intensity measurements and the λ_0^+ measurements. The variation is so highly nonlinear that the second harmonic contains over 50% of the energy of the first. The intensity measurements at the wall made by Mao (1984) in an 8 inch flow loop also display this behavior. Thus, this nonlinearity cannot be explained by some type of problem associated with the 2 inch flow loop. It is to be noted

that the bursting frequency of turbulence is at $\omega^+ = 0.063$. The nonlinear variation appears to occur when the dimensionless frequency of the imposed pulsation is equal to or greater than the dominant frequency of the turbulence. This seems consistent with the suggestion by Mizushina et. al. (1973) that significant changes in the turbulence structure occurs when the frequency of the imposed pulsation is the same as the bursting frequency. At present, no explanation can be put forth for this behavior at high ω^+ .

The straightforward application of a turbulence model developed for flow without pulsation, such as Model C, is not capable of describing the experimental wall shear stress results. A model, such as Model D that imposes a lag between the imposed pressure gradient and the change of scale in the viscous wall region, is needed to describe the data. The parameters, $k_1 = -25$ and $k_F = 3500$, chosen to fit the experimental results are very close to those used by Loyd et. al. (1970) to describe boundary layer flows and by Abrams and Hanratty (1985) to describe flow over a wavy surface. This similarity of values implies that the mechanism behind the relaxation phenomenon is the same for all the flows.

CONCLUSIONS AND RECOMMENDATIONS

This thesis reports experimental and numerical results on the effect of an imposed pressure gradient on the viscous wall region. Constant and time varying pressure gradients homogeneous in the streamwise direction are considered. The results are summarized as follows:

- a. The major effect of the imposition of a constant pressure gradient on a turbulent boundary layer is to change the shear of the flow and to be a source of momentum in the viscous wall region. Arguments are presented that show that the turbulence scales with the shear stress at the outer edge of the viscous wall region.
- b. A parameter, P_{eo}^+ , is defined to account for part of the imposed pressure gradient being used to speed up the flow in the viscous wall region. Relaminarization of a turbulent flow is suggested to occur when the effective pressure gradient at the outer edge of the viscous wall region is equal to its minimum value of -0.00962. The maximum eddy Reynolds number criterion of Bradshaw (1969), that suggests relaminarization occurs when the logarithmic region disappears and the length scales of the energy-containing and energy-dissipating eddies overlap, is shown to be consistent with the minimum P_{eo}^+ criterion.
- c. The amplitude and phase of the wall shear stress are found to be correlated by a single parameter ω^+ for values above 0.005. This scaling is shown to breakdown when the variation of the pulsating velocity at the center of the pipe can no longer be described by the inviscid solution of the Navier-Stokes equations.
- d. The variation of λ^+ through a period of pulsation is estimated from measurements of the transverse correlation coefficient of the

streamwise velocity gradient at the wall. These measurements indicate that a substantial variation of λ^+ occurs in the equilibrium region of the flow. The relaxation phenomena observed by Mao and Hanratty (1985) is confirmed in the measurements of λ^+ . However, an unexpected highly nonlinear large variation of λ^+ is observed at ω^+ values higher than the bursting frequency. This behavior at high ω^+ cannot be explained by present theories of turbulence.

Several interesting problems in need of further study emerged from the experimental part of this work:

- a. Further investigation of the enhancement of turbulence at high ω^+ is needed. A direct numerical simulation, a large eddy simulation, and a "2½ D" simulation from wall to wall are possible numerical methods that can be tried in order to obtain a better physical understanding of the variation at high ω^+ . Optical techniques that do not interfere with the flow should also be used to experimentally examine the flow in the viscous wall region at high ω^+ .
- b. Measure the mass transfer coefficient in turbulent pulsating pipe flow in order to determine if the variation of the fluctuations in the mass transfer show the same nonlinearity at high ω^+ as does the turbulent fluctuations at the wall.
- c. The relatively large variation of the turbulence at moderate ω^+ suggests the possibility of obtaining drag reduction using a nonsinusoidal pulsation. One possible pulsation cycle might have a slow variation over most of the cycle followed by a sharp acceleration.
- d. Directly determine, using a hot-wire or optical technique, the ω^+ value at which plug flow in the center of the pipe disappears.

NOMENCLATURE

<u>Symbol</u>		<u>Unit</u>
a	Amplitude of pressure gradient	g/cm-sec ²
A	Amplitude correction factor for frequency response of the probe: van Driest constant	
C	Concentration	mole/cm ³
C _b	Bulk concentration	mole/cm ³
c _f	Skin-friction coefficient	
D	Pipe diameter	cm
f	Frequency	1/sec
F	Faraday's constant	
H	Ratio of two consequent grid sizes; Shape factor	
I	Current flowing in the electrochemical cell	amp
κ	Von Karmen constant 0.41	
k	Time dependent component of mass transfer coefficient	cm/sec
k _I	Imaginary part of k	
k _r	Relaxation constant	
k _R	Real part of k	
K	Mass transfer coefficient; Acceleration parameter	cm/sec
λ	Mixing length	cm
L _e	Effective length of electrode	cm
n _e	Number of electrons transferred in electrochemical reaction	
P	Pressure	g/cm-sec ²
P _e	Effective pressure gradient	
r	Coordinate in radial direction	cm
r ₀	Pipe radius	cm
R	Correlation coefficient	

Re	Reynolds number	
R_2	Momentum-thickness Reynolds number	
q^2	Turbulent kinetic energy	cm^2/sec^2
s	Time dependent component of velocity gradient at the wall	cm/sec^2
s_x	Streamwise velocity gradient fluctuation at the wall	cm/sec^2
S	Velocity gradient at the wall	cm/sec^2
Sc	Schmidt number	
S_x	Streamwise velocity gradient at the wall	cm/sec^2
t	time	
T_b	Bursting period	sec
u	Fluctuating streamwise velocity	cm/sec
u^*	Friction velocity	cm/sec
U	Mean streamwise velocity	cm/sec
U_b	Bulk velocity in pipe	cm/sec
U_∞	Free stream velocity	cm/sec
v	Transverse velocity	cm/sec
w	Spanwise velocity	cm/sec
W	Width of the electrode	cm
x	Coordinate in the flow direction	cm
y	Coordinate normal to the wall	cm
y^+	Dimensionless y . ($y^+ = yu^*/\nu$)	

Greek
Symbol

α	Diffusivity	
δ	Boundary layer thickness	cm
δ^*	Displacement thickness	cm

δ_c	Concentration boundary layer	cm
δ_s, l_s	Stokes layer thickness	cm
δ_v	Viscous sublayer thickness	cm
Δ_τ	Shear stress gradient parameter	
ϵ	Dissipation	
Λ	Pressure gradient parameter	
θ	Phase	degree
λ	Streak spacing	cm
μ	Molecular viscosity	g/cm-sec
ν	Kinematic viscosity	cm ² /sec
ν_t	Turbulent eddy viscosity	cm ² /sec
ρ	Density of fluid	g/cm ³
τ	Shear stress	g/cm-sec ²
$\tau(t)$	Turbulent shear stress	g/cm-sec ²
τ_w	Wall shear stress	g/cm-sec ²
ω	Angular frequency	1/sec
ω^+	Dimensionless ω . ($\omega^+ = \omega\nu/u^{*2}$)	
Ω	Frequency parameter ($\Omega = (\omega/\nu)^{1/2} r_0$)	

Overline and brackets:

\sim	Periodic component
$\bar{-}$	Time average
$\langle \rangle$	Phase average
$ \hat{ } $	Amplitude

Subscripts:

o	Quantity located at the outer edge of the viscous wall region
-----	---------------------------------------------------------------

1 Quantity associated with the inner eddies

2 Quantity associated with the outer eddies

Superscripts:

⁺ Nondimensional with friction velocity
 and kinematic viscosity

⁰ Quantity scaled with the shear stress at the outer
 edge of the viscous wall region and assumed constant
 independent of acceleration

REFERENCES

Abrams, J. and Hanratty, T. J., *J. Fluid Mech.*, 151, 443 (1985).

Antonia, R. A., Danh, H. Q. and Prabhu A., *Phys. Fluids*, 19, 1680 (1976).

Back, L. H. and Seban, R. A., *Proc. Heat Transfer Fluid Mech. Inst.*, 20, 410 (1967).

Badri Narayanan, M. A. and Ramjee, V., *J. Fluid Mech.*, 35, 225 (1969).

Badri Narayanan, M. A. and Narasimha, R., Rep. No. 74 FM-15 Dept. Aero. Eng. Ind. Inst. Sci. Bangalore (1974).

Bakewell, H. P. and Lumley, J. L., *Phys. Fluids*, 10, 1880 (1967).

Binder, G., Tardu, S., Blackwelder, R. F. and Kueny, J. L., *Fifth Symp. On Turb. Shear Flows*, (1985).

Blackwelder, R. F., and Eckelmann, H., *Structure and Mechanisms of Turbulence I*, Lecture Notes in Physics, Vol. 75, p. 190, Springer Verlog (1978).

Blackwelder, R. F. and Haritonidis, J. H., *J. Fluid Mech.*, 132, 87 (1983).

Blackwelder, R. F. and Kaplan, R. E., *J. Fluid Mech.*, 76, 89 (1976).

Blackwelder, R. F. and Kovasznay, L. S. G., *J. Fluid Mech.*, 53, 61 (1972).

Boussinesq, J., *Mém. prés. par div. savant à l'acad. sci. Paris*, 23, 46 (1877).

Bradshaw, P., *J. Fluid Mech.*, 29, 625 (1967).

Bradshaw, P., *J. Fluid Mech.*, 35, 387 (1969).

Carr, L. W., *IUTAM Symp.* (1981).

Cebeci, T. and Smith, A. M. O., Academic Press, New York, New York (1974).

Cess, R. D., *Westinghouse Research Report 8-0529-R24* (1958).

Chapman, D. R. and Kuhn, G. D., *AIAA Paper 81-1024*, Proc. AIAA 5th CFD Conference, Palo Alto, California (1981).

Clark, J. A., *J. Basic Engrg.*, 90, 455 (1968).

Clark, R. A., Ferziger, J. H. and Reynolds, W. C., *J. Fluid Mech.*, 91, 1 (1979).

Coantic, M., *Comptes Rendus*, 20, 849 (1967).

Coles, D. E., *J. Fluid Mech.*, 1, 191 (1956).

Coles, D. E., *Rand. Rep. 403-PR* (1962).

Corino, E. R. and Brodkey, R. S., *J. Fluid Mech.*, 37, 1 (1969).

Corrsin, S., *Symp. On Naval Hydrodyn.*, 373 (1956).

Cousteix, J. and Houdeville, R., *Fifth Symp. on Turb. Shear Flows* (1985).

Deardorff, J. W., *J. Fluid Mech.*, 41, 453 (1970).

Donohue, G. L., Tierderman, W. G. and Reischman, M. M., *J. Fluid Mech.*, 56, 559 (1972).

Eckelman, L. D., Ph.D. Thesis, University of Illinois, Urbana, Illinois (1984).

Eckelmann, H., *J. Fluid Mech.*, 65, 439 (1974).

Elena, M., Fulachier, L. and Dumas, R., AGARD CPP271, 2-1 (1979).

Ferziger, J. H., *AIAA J.*, 15, 1261 (1977).

Finnicum, D. S. and Hanratty, T. J., *Phys. Fluids*, 28, 1654 (1985).

Fortuna, G., Ph.D. Thesis, University of Illinois, Urbana, Illinois (1971).

Fortuna, G. and Hanratty, T. J., *Int. J. Heat Mass Transfer*, 14, 1499 (1971).

Grant, H. L., *J. Fluid Mech.*, 4, 149 (1958).

Gupta, A. K., Laufer, J. and Kaplan, R. E., *J. Fluid Mech.*, 50, 493 (1971).

Gupta, A. K. and Kaplan, R. E., *Phys. Fluids*, 15, 981 (1972).

Hanratty, T. J., Chorn, L. G. and Hatziavramidis, D. T., *Phys. Fluids*, 20, S112 (1977).

Hatziavramidis, D. T. and Hanratty, T. J., *J. Fluid Mech.*, 95, 655 (1979).

Hinze, J. O., *Turbulence*, 2nd Edition, McGraw-Hill (1975).

Hogenes, J. G. A. and Hanratty, T. J., *J. Fluid Mech.*, 124, 363 (1982).

Hussain, A. K. M. F. and Reynolds, W. C., Stanford Univ. Thermosci. Div. Tech. Rep. FM-6 (1970).

Jayaraman, R., Parikh, P. G. and Hanratty, W. C., Stanford Univ. Thermosci. Div. Tech. Rep. TF-18 (1982).

Jones, W. P. and Launder, B. E., *J. Fluid Mech.*, 56, 337 (1972).

Jones, W. P. and Launder, B. E., *Int. J. Heat Mass Transfer*, 16, 1119 (1973).

Julien, H. L., Kays, W. M., and Moffat, R. J., Stanford Univ. Thermosci. Div. Tech. Rep. HMT-4 (1969).

Kebede, W., Launder, B. E., and Younis, B. A., Fifth Symp. on Turb. Shear Flows (1985).

Kim, H. T., Kline, S. J. and Reynolds, W. C., J. Fluid Mech., 50, 133 (1971).

Kim, J. and Moin, P., NASA TM 86657 (1984).

Kline, S. J., Reynolds, W. C., Schraub, F. A. and Runstadler, P. W., J. Fluid Mech., 30, 741 (1967).

Kline, S. J. and Runstadler, P. W., J. Appl. Mech., 2, 166 (1959).

Kutateladze, S. S., Khabakhpasheva, E. M., Orlov, V. V., Pereplitsa, B. V. and Mikhailova, E. S., Proc. Symp. on Turbulent Shear Flows, Penn State Univ. (1977).

Laufer, J., NACA TN-1174 (1954).

Launder, B. E., Rep. No. 71 Gas Turbine Lab., Mass. Int. of Tech., Cambridge (1963).

Launder, B. E., Rep. No. 77 Gas Turbine Lab., Mass. Int. of Tech., Cambridge (1964).

Launder, B. E. and Jones, W. P., J. Fluid Mech., 38, 817 (1969).

Launder, B. E. and Stinchcombe, H. S., Imp. Coll. Note TWF/TN 21 Dept. Mech. Eng. (1967).

Lee, M. K., Eckelman, L. D. and Hanratty, T. J., J. Fluid Mech., 66, 17 (1974).

Lilly, D. K., Proc. of the IBM Sci. Comp. Symp. on Environ. Sci., IBM Form No. 320-1951, 195 (1967).

Loyd, R. J., Moffat, R. J. and Kays, W. M., Stanford Univ. Thermosc. Rep. HMT-13 (1970).

Lyons, S., M. Sc. Thesis, University of Illinois, Urbana, Illinois (1985).

Mao, Z.-X., Ph.D. Thesis, University of Illinois, Urbana, Illinois (1984).

Mao, Z.-X. and Hanratty, T. J., Exp. in Fluids, 3, 129 (1985).

Mao, Z.-X. and Hanratty, T. J., To be published in J. Fluid Mech. (1986).

Meek, R. L., AICHE j., 18, 854 (1972).

Mitchell, J. E. and Hanratty, T. J., J. Fluid Mech., 26, 199 (1966).

Mizushina, T., Maruyama, T. and Shiozaki, Y., J. of Chem. Engrg. of Japan, 8, 210 (1973).

Moin, P. and Kim, J., J. Fluid Mech., 118, 341 (1982).

Moin, P., Reynolds, W. C. and Ferziger, J. H., Rep. No. TF-12, Thermosci. Div., Dept. of Mech. Eng., Stanford Univ. (1978).

Moretti, P. H. and Kays, W. M., Int. J. Heat Transfer, 8, 1187 (1965).

Morrison, W. R. B., Kronauer, R. E., J. Fluid Mech., 39, 117 (1969).

Moser, R. D. and Moin, P., NASA TM 85974 (1984).

Narasimha, R. and Sreenivasan, K. R., J. Fluid Mech., 61, 417 (1973).

Nikolaides, C., Ph.D. Thesis, University of Illinois, Urbana, Illinois (1984).

Nychas, S. G., Hershey, H. C. and Brodkey, R. S., J. Fluid Mech., 61, 513 (1973).

Offen, G. R. and Kline, S. J., J. Fluid Mech., 62, 223 (1974).

Okamoto, T. and Misu, I., Trans. Jpn. Soc. Aerosp. Sci., 20, 1 (1977).

Ota, D. K. and Chapman, D. R., Rep. No. AA CFD 85-2, Aero. and Astro. Dept., Stanford University (1985).

Patankar, S. V. and Spalding, D. B., Morgan-Grampian Press, London (1967).

Patel, V. C., J. Fluid Mech., 23, 185 (1965).

Patel, V. C. and Head, M. R., J. Fluid Mech., 34, 371 (1968).

Praturi, A. K. and Brodkey, R. S., J. Fluid Mech., 89, 251 (1978).

Preston, J. H., J. Fluid Mech., 3, 373 (1958).

Ramaprian, B. R. and Tu, S. W., J. Fluid Mech., 100, 513 (1980).

Ramaprian, B. R. and Tu, S. W., IIHR Report 238, Iowa Institute of Hydraulic Research, The University of Iowa, Iowa City, Iowa (1982).

Ramaprian, B. R. and Tu, S. W., J. Fluid Mech., 137, 59 (1983).

Rao, K. N., Narasimha, R. and Badri Narayanan, M. A., J. Fluid Mech., 48, 339 (1971).

Reddy, V., McLaughlin, J. B. and Nunge, R. J., J. Fluids Eng., 107, 205 (1985).

Reichardt, J., Arch. Ges. Warmetchnik, 6/7, 129 (1951).

Reiss, L. P. and Hanratty, T. J., A.I.Ch.E. J., 9-2, 154 (1963).

Reynolds, W. C., Annual Rev. Fluid Mech., 8, 183 (1976).

Rice, S. O., Selected Papers on Noise and Stochastic Processes, Dover Publ., New York (1954).

Roache, P. J., Computational Fluid Dynamics, Hermosa Publ. (1982).

Rodi, W., Turbulence Models and Their Application in Hydraulics, Int. Assoc. for Hydraulic Research, Delft (1980).

Ronneberger, D. and Ahrens, C. D., J. Fluid Mech., 83, 433 (1977).

Runstadler, P. W., Kline, S. J. and Reynolds, W. C., Rep. No. MD-8, Thermosci. Div., Mech. Eng. Dept., Stanford University (1963).

Sandborn, V. A. and Slogar, R. J., NACA TN-3264 (1955).

Schildnect, M., Miller, J. A. and Meier, G., J. Fluid Mech., 90, 67 (1979).

Schraub, F. A. and Kline, S. J., Rep. No. MD-12, Thermosci. Div., Mech. Eng. Dept., Stanford University (1965).

Schumann, U., J. Comp. Physics, 18, 376 (1975).

Sexl, L., Z. Phys., 61, 349 (1930).

Shemer, L. and Wygnaski, I., Third Symp. On Turb. Shear Flows, (1981).

Sirkar, K. K., Ph.D. Thesis, University of Illinois, Urbana, Illinois (1984).

Sirkar, K. K. and Hanratty, T. J., J. Fluid Mech., 44, 589 (1970).

Smagorinsky, J., Manabe, S. and Holloway, J. L., Mon. weath. Rev., 93, 727 (1965).

Spalart, P. R. and Leonard, A., Fifth Symp. On Turb. Shear Flows, (1985).

Sreenivasan, K. R., Antonia, R. A. and Danh, H. Q., Phys. Fluids, 20, 1800 (1977).

Sreenivasan, K. R., Prabu, A. and Narasimha, R., J. Fluids Mech., 137, 251 (1983).

Tennekes, H. and Lumley, J. L., A First Course in Turbulence, The MIT Press, 7th Printing (1981).

Thorsness, C. B., Morrisroe, P. E. and Hanratty, T. J., Chem. Eng. Science, 33, 579 (1978).

Townsend, A. A., The Structure of Turbulent Shear Flow, Cambridge University Press (1976).

Townsend, A. A., J. Fluid Mech., 11, 97 (1961).

Tritton, D. J., J. Fluid Mech., 28, 439 (1967).

Tu, S. W. and Ramprian, B. R., J. Fluid Mech., 137, 31 (1983).

Uchida, S., ZAMP 7 (1956).

Ueda, H. and Hinze, J. O., J. Fluid Mech., 28, 125 (1975).

Van Driest, E. R., J. Aero. Sci., 23, 1007 (1957).

APPENDIX I. Amplitudes and Phases of the Phase Averaged Data

(a) Wall Shear Stress

ω^+	Re	f (Hz.)	$ \hat{\tau}_w^+ $	θ_τ	$ \hat{\tau}_w^+ / \hat{u}_c^+ $
0.00120	44,900	0.35	0.197	-81.5	0.084
0.00135	42,000	0.35	0.195	-82.1	0.083
0.00180	29,400	0.25	0.204	-82.3	0.092
0.00210	23,700	0.20	0.204	-84.1	0.093
0.00375	31,800	0.60	0.195	-84.2	0.088
0.00375	25,200	0.40	0.175	-81.3	0.079
0.00420	20,100	0.30	0.170	-84.0	0.078
0.00495	23,000	0.45	0.172	-82.5	0.080
0.00750	21,400	0.60	0.179	-78.7	0.083
0.00930	17,100	0.50	0.149	-64.3	0.069
0.0123	14,500	0.50	0.146	-53.2	0.070
0.0172	17,900	1.00	0.220	-50.0	0.105
0.0195	10,600	0.45	0.233	-47.3	0.115
0.0210	10,700	0.50	0.231	-44.5	0.116
0.0225	15,300	1.00	0.332	-50.5	0.160
0.0244	14,600	1.00	0.313	-49.0	0.153
0.0258	14,200	1.00	0.325	-49.0	0.155
0.0270	10,300	0.60	0.283	-49.1	0.140
0.0360	8,750	0.60	0.321	-46.1	0.165
0.0375	11,400	1.00	0.368	-47.0	0.185
0.0550	9,200	1.00	0.461	-48.0	0.233
0.0675	10,300	1.50	0.543	-47.0	0.268
0.0915	8,650	1.50	0.600	-47.5	0.305

(b) Turbulent Fluctuations of the Wall Shear Stress

w^+	Re	f(Hz.)	$\bar{\tau}_w'$	$ \hat{\tau}_w' $	θ_{τ}'
0.00120	44,900	0.35	0.291	0.039	-90.7
0.00135	42,000	0.35	0.310	0.054	-93.9
0.00180	29,400	0.25	0.307	0.066	-93.6
0.00210	23,700	0.20	0.315	0.059	-97.6
0.00375	31,800	0.60	0.309	0.066	-98.4
0.00375	25,200	0.40	0.298	0.055	-101.6
0.00420	20,100	0.30	0.308	0.047	-102.5
0.00495	23,000	0.45	0.305	0.055	-108.6
0.00750	21,400	0.60	0.318	0.045	-112.1
0.00930	17,100	0.50	0.297	0.360	-144.8
0.0123	14,500	0.50	0.307	0.025	-137.9
0.0172	17,900	1.00	0.312	0.030	-156.0
0.0195	10,600	0.45	0.315	0.021	-183.2
0.0210	10,700	0.50	0.306	0.015	-189.0
0.0225	15,300	1.00	0.319	0.018	-185.5
0.0244	14,600	1.00	0.319	0.020	-182.0
0.0258	14,200	1.00	0.315	0.016	-202.2
0.0270	10,300	0.60	0.317	0.003	-203.5
0.0360	8,750	0.60	0.318	0.012	-231.5
0.0375	11,400	1.00	0.312	0.003	-249.2
0.0550	9,200	1.00	0.304	0.020	-296.0
0.0675	10,300	1.50	0.304	0.42	-330.7
0.0915	8,650	1.50	0.314	0.075	-353.8

(c) Streak Spacing

ω^+	Re	f(Hz.)	$ \hat{\lambda}_0^+ $	θ_{λ_0}
0.00120	44,900	0.35	8.05	84.1
0.00210	23,700	0.20	8.65	75.9
0.00375	25,200	0.40	9.67	62.8
0.00420	20,100	0.30	8.12	54.5
0.00750	21,400	0.60	4.90	74.4
0.00930	17,100	0.50	4.66	44.2
0.0172	17,900	1.00	3.75	56.0
0.0210	10,700	0.50	2.50	37.1
0.0225	15,300	1.00	4.01	43.8
0.0244	14,600	1.00	3.07	37.0
0.0258	14,200	1.00	2.61	32.8
0.0270	10,300	0.60	3.70	44.1
0.0360	8,750	0.60	2.84	-26.6
0.0375	11,400	1.00	2.13	-8.30
0.0550	9,200	1.00	4.08	-2.80
0.0675	10,300	1.50	4.96	-8.00
0.0915	8,650	1.50	7.11	-37.4

APPENDIX II. Constant Pressure Gradient Program

```

*****
C***** PROGRAM CONSTANT PRESSURE GRAD.
C
C      THIS PROGRAM CALCULATES THE STREAMLINES PATTERN
C      FOR A FIXED CELL OF THE MODEL FLOW IN THE WALL REGION.
C
C      BOUNDARY CONDITIONS AT Y=Y0:
C      W=W0(Z,T)    V=V0(Z,T)
C
C      INPUT FILES
*****
C      FOR021=PZU(NBEF): CONTAINS PSI,ZETA AND UCOM FROM
C                          PREVIOUS RUN
C      FOR022=UB0(NBEF): CONTAINS THE MEAN STREAMWISE VELOCITY
C                          AT Y0+ OF THE PREVIOUS RUN. QUANTITY
C                          HAS ALREADY BEEN CORRECTED WITH THE
C                          STREAMWISE GRADIENT AT THE WALL.
C      FOR023=UAB(NBEF): CONTAINS THE STREAMWISE MEAN VELOCITY
C                          TO BE USED TO CALCULATE THE MEAN
C                          NORMAL VELOCITY
C      FOR024=PSI(T): CONTAINS PSI AT EVERY TIME STEP
C      FOR025=ZBC(T): CONTAINS ZETA AT THE UPPER AND LOWER
C                          BOUNDARIES AT EVERY TIME STEP
C      FOR026=UCM(T): CONTAINS UCOM AT EVERY TIME STEP
*****
C      OUTPUT FILES
*****
C      FOR031=PZU(NTOT): CONTAINS PZU,ZETA AND UCOM AT THE
C                          END OF THIS RUN
C      FOR032=UB0: CONTAINS THE CORRECTED MEAN STREAMWISE VELOCITY
C                          AT Y0+ FOR THE NEXT RUN AND THE RATIO
C                          OF COUTTE VELOCITY TO STREAMWISE GRADIENT
C                          AT THE WALL.
C      FOR033=UAB: CONTAINS UAB AT THE END OF THE RUN UNCORRECTED.
C      FOR034=ZBC: CONTAINS ZETA AT THE UPPER AND LOWER BOUNDARIES
C                          AT EVERY TIME STEP
C      FOR035=PSI: CONTAINS PSI AT EVERY TIME STEP
C      FOR036=DPL: CONTAINS STATISTICAL QUANTITIES AT END OF RUN
C      FOR037=TS: CONTAINS # OF STEPS AND TOTAL TIME AS THE RUN
C                          IS BEING CALCULATED
C      FOR038=UCM: CONTAINS UCOM AT EVERY TIME STEP
*****
C
DIMENSION PSI(51,101),PSI1(51,101),ZETA(51,101),ZETA1(51,101)
DIMENSION ZETA2(51,101),WTAX(51),UTAX(51),PSIUP(51),DVDZ(51)
DIMENSION WORK(5000),WGR(51),UGR(51),DUDZ(51)
DIMENSION UCOM(51,101),VBEF(51),PEFF(101),ALPHA(101)
DIMENSION BDA(101),BDB(101),BDC(101),VTAX(51),USA(101)
DIMENSION Y(101),Z(51),DWDZ(51),ZETABC(51,2)
DIMENSION UAVE(101),VAVE(101),WAVE(101),UB2(101),UB(101)
DIMENSION YPLUS(101)
DIMENSION UINTYO(101),VINTYO(101),WINTYO(101),AU2(101)

```

```

REAL LAM, INDEXM, NINDEX, NIPTS, KP
INTEGER CYCLE
COMMON/AREA1/R, FOVRE, FOVRE1, BETAP, BETAM, GAMAP, GAMAM
COMMON/AREA2/A, B, C, D, IDIMF
COMMON/AREA3/M, MP1, MM1, MM2, N, NP1, NM1, NM2
COMMON/AREA4/WORK, BDA, BDB
COMMON/AREA5/CHVEL, CHLEN, ACON

COMMON/AREA6/RE, DY, DZ, DT, TDY, TDZ, DY2, DZ2
COMMON/AREA7/NCTOT, SXBAR, SZBAR, SXS, SZSB
COMMON/AREA9/NCB, NINDEX
COMMON/AREA10/Y, Z, KSTAT, DTE
COMMON/AREA13/SZBARA, SZBARB, SZSBA, SZSBB
COMMON/ONE/PS11
COMMON/TWO/ZETA1
COMMON/THREE/ZETA2
COMMON/FOUR/UAVE, VAVE, WAVE, UINTYO, VINTYO, WINTYO
COMMON/FIX1/ALPHA
COMMON/FIX2/PPLUS, VAX
SAVE
READ*, INDEXM, VAX, STAT, RELCON
READ*, ITERM, DTE, E
READ*, RATIO2, E2, FINALE
READ*, UINPO, VINPO, WINPO
READ*, EU1, EV1, EW1
READ*, THETU1, THETU2, THETV1, THETV2, THETW1, THETW2
READ*, PM, WAVEM, YOO
READ*, PPLUS, YOUT, CFD2, APLUS, AU2I
READ*, FTOG, UTOG
READ*, FIELDI, PZIINC
READ*, FIELDO, PZOINC
READ*, UCOMI, UIINC
READ*, UCOMO, UOINC
IF(FTOG.EQ.1)OPEN(21,FILE='PZUI',FI=S,RE=V,FM=U,SIZE=13',
$STATUS='OLD')
IF(UTOG.EQ.1)OPEN(22,FILE='UBOI',STATUS='OLD',FORM='FORMATTED')
IF(UTOG.EQ.1)OPEN(23,FILE='UABI',STATUS='OLD',FORM='FORMATTED')
IF(FIELDI.EQ.1)OPEN(24,FILE=':TEMP:PSII',FI=S,RE=V,FM=U,
$SIZE=13',STATUS='OLD')
IF(FIELDI.EQ.1)OPEN(25,FILE=':TEMP:ZBCI',FI=S,RE=V,FM=U,
$SIZE=13',STATUS='OLD')
IF(FIELDO.EQ.1)OPEN(35,
$FILE=':HOST:SYS$OVERFLOW:[240016.OSC]PSIO.DAT,
$LE=49288,SI=13,SB=8192,FIL=S,RE=V,FM=U,BLOCKS=2',STATUS='NEW')
IF(FIELDO.EQ.1)OPEN(34,FILE=':HOST:DRA3:[240016.APSTOR]ZBCO.DAT,
$LE=8192,SI=13,SB=2048,FIL=S,RE=V,FM=U,BLOCKS=2',STATUS='NEW')
IF(UCOMI.EQ.1)OPEN(26,FILE=':TEMP:UCMI',FI=S,RE=V,FM=U,SIZE=13',
$STATUS='OLD')
IF(UCOMO.EQ.1)OPEN(39,FILE=':HOST:DRA3:[240016.APSTOR]UCMO.DAT,
$LE=49288,SI=13,SB=8192,FIL=S,RE=V,FM=U,BLOCKS=2',STATUS='NEW')
U1=2*SQRT(EU1)
U2=2*SQRT(1-EU1)
V1=2*SQRT(EV1)
V2=2*SQRT(1-EV1)
W1=2*SQRT(EW1)

```

```

W2=2*SQRT(1-EW1)
PRINT*, *****
PRINT*, '          TWO WAVELENGTH RUN'
IF(VAX.EQ.0)PRINT*, ' THIS IS AN ARRAY PROCESSOR RUN'
IF(VAX.EQ.1)PRINT*, ' THIS IS A VAX RUN'
IF(STAT.EQ.1)PRINT*, ' STATISTICS WILL BE GENERATED THIS RUN'
IF(FIELDI.EQ.1)PRINT*, ' PSI,ZETA FIELD IS INPUT AT EACH TIME STEP'
IF(FIELD0.EQ.1)PRINT*, ' PSI,VBC AT EVERY TIME STEP IS OUTPUT'
IF(UCOMI.EQ.1)PRINT*, ' UCOM AT EVERY TIME STEP IS INPUT'
IF(UCOMO.EQ.1)PRINT*, ' UCOM AT EVERY TIME STEP IS OUTPUT'
IF(FTOG.EQ.0)PRINT*, ' INITIAL PSI,ZETA FIELD IS CALCULATED'
IF(FTOG.EQ.1)PRINT*, ' INITIAL PSI,ZETA FIELD IS INPUT'
IF(UTOG.EQ.0)PRINT*, ' INTIAL UBAR PROFILE IS CALCULATED'
IF(UTOG.EQ.1)PRINT*, ' INITAL UBAR PROFILE IS INPUT'
IF(FIELDI.EQ.1)WRITE(6,1430)PZIINC
IF(FIELD0.EQ.1)WRITE(6,1330)PZOINC
IF(UCOMI.EQ.1)WRITE(6,1450)UIINC
IF(UCOMO.EQ.1)WRITE(6,1440)UOINC
PRINT*, *****
WRITE(6,1310)DTE,E
WRITE(6,1320)RATIO2,E2,FINALE
WRITE(6,1400)ITERM,INDEXM
WRITE(6,1340)UINPO,VINPO,WINPO
WRITE(6,1410)EU1,EV1,EW1
WRITE(6,1350)U1,U2,V1,V2,W1,W2
WRITE(6,1360)THETU1,THETU2,THETV1,THETV2,THETW1,THETW2
WRITE(6,1370)PM,WAVEM
WRITE(6,1380)YOO
WRITE(6,1390)PPLUS,APLUS,AU2I
C*****
C*** DEFINITIONS OF IMPORTANT VARIABLES THAT ARE NOT
C*** INPUT VARIABLES
C*****
C   B: DIMENSIONLESS LENGTH OF THE COMPUTATIONAL
C       DOMAIN IN THE SPANWISE DIRECTION
C   D: DIMENSIONLESS LENGTH OF THE COMPUTATIONAL
C       DOMAIN IN THE NORMAL DIRECTION
C   CU1,CU2: CONSTANTS THAT ADJUST THE STREAMWISE
C             INTENSITY AT THE UPPER BOUNDARY
C   CV1,CV2: CONSTANTS THAT ADJUST THE NORMAL
C             INTENSITY AT THE UPPER BOUNDARY
C   CW1,CW2: CONSTANTS THAT ADJUST THE SPANWISE
C             INTENSITY AT THE UPPER BOUNDARY
C   ALU1,ALU2: DIMENSIONLESS WAVELENGTHS OF THE U-FLUCTUATIONS
C   ALV1,ALV2: DIMENSIONLESS WAVELENGTHS OF THE V-FLUCTUATIONS
C   ALW1,ALW2: DIMENSIONLESS WAVELENGTHS OF THE W-FLUCTUATIONS
C   THETU1,THETU2: PHASES OF THE U-FLUCTUATIONS IN DEGREES
C   THETV1,THETV2: PHASES OF THE V-FLUCTUATIONS IN DEGREES
C   THETW1,THETW2: PHASES OF THE W-FLUCTUATIONS IN DEGREES
C*****
C*** READS INPUT PARAMETERS
C*****
C   INDEXM: INTEGER MULTIPLE OF TP2 BY WHICH THE
C             TOTAL TIME STEPS(NINDEX) IS SET.
C   VAX: 0 = ARRAY PROCESOR RUN

```

```

C   1 = VAX RUN
C   ITERM: MAXIMUM NUMBER OF ITERATIONS OF ADI
C           SCHEME AT EACH TIME STEP
C   E: ACCURACY OF CONVERGENCE OF ADI SCHEME
C   DTE: EXPERIMENTAL TIME STEP IN WALL PARAMETERS
C   RELCON: RELAXATION CONSTANT FOR THE ITERATION ON THE
C           ADI-SCHEME
C   PPLUS: CONSTANT PRESSURE GRADIENT IN THE
C           STREAMWISE DIRECTION
C   CFD2: SKIN-FRICTION OF FLOW
C   YOUT: OUTER EDGE OF SUBLAYER REGION IN PLUS UNITS
C   APLUS: VAN DRIEST SUBLAYER THICKNESS CONSTANT
C   U1,U2: AMPLITUDES OF THE STREAMWISE FLUCTUATIONS
C   V1,V2: AMPLITUDES OF THE NORMAL FLUCTUATIONS
C   W1,W2: AMPLITUDES OF THE TRANSVERSE FLUCTUATIONS
C   UINBC,VINBC,WINBC: INTENSITIES AT THE UPPER BOUNDARY
C           IN WALL UNITS.
C   PM: INTEGER MULTIPLIER OF 1ST TIME PERIOD.
C       I.E. TP2=PM*TP1
C   WAVEM: INTEGER MULTIPLIER OF 1ST WAVELENGTH
C       I.E. ALU2=ALU1*WAVEM
C   FTOG: 0=CALCULATES THE INITIAL PSI,ZETA,FIELD
C       1=READS IN THE INITIAL PSI,ZETA,FIELD
C   UTOG: 0=CALCULATE INITIAL UBAR PROFILE
C       1=INPUT UBAR PROFILE
C   PARAMETERS FOR THE MODEL FLOW
C
A=0.0
C=0.0
M=50
N=100
IDIMF=M+1
MP1=M+1
FMP1=FLOAT(MP1)
MM1=M-1
NP1=N+1
NM1=N-1
NM2=N-2
MM2=M-2
PI=4.*ATAN(1.)
TPI=2.*PI
PEFFO=YOO**2/YOUT**3-1/YOUT
TAUOSR=YOO/YOUT
TAUO=TAUOSR**2
LAM=100/TAUOSR
LAM=NINT(LAM)
CHLEN=LAM
TP1=100/TAUO
TP1=NINT(TP1)
TP2=NINT(PM*TP1)
UINBC=UINPO*TAUOSR
VINBC=VINPO*TAUOSR
WINBC=WINPO*TAUOSR
CUVO=--((SQRT(EU1*EV1)*COS((THETU1-THETV1)*PI/180))+  

$(SQRT((1-EU1)*(1-EV1))*COS((THETU2-THETV2)*PI/180)))

```

```

UV0=CUVO*UINBC*VINBC
DUDYO=TAUO-UV0
CHVEL=2.*VINBC
CU1=U1*UINBC/CHVEL
CU2=U2*UINBC/CHVEL
CV1=V1*VINBC/CHVEL
CV2=V2*VINBC/CHVEL
CW1=W1*WINBC/CHVEL
CW2=W2*WINBC/CHVEL
ALU1=LAM/CHLEN
ALV1=LAM/CHLEN
ALW1=LAM/CHLEN
ALU2=ALU1*WAVEM
ALV2=ALV1*WAVEM
ALW2=ALW1*WAVEM
D=YOUT/CHLEN
DY=D/FLOAT(N)
NINDEX=INDEXM*TP2
WRITE(6,1000)NINDEX
WRITE(6,1010)UINBC,VINBC,WINBC
WRITE(6,1020)CU1,CU2,CV1,CV2,CW1,CW2
WRITE(6,1300)TAUO,UV0,DUDYO,CUVO
WRITE(6,1030)CFD2,YOUT,PEFFO
WRITE(6,1040)ALW1*CHLEN,ALW2*CHLEN,TP1,TP2
B=LAM*WAVEM/(2*CHLEN)
DZ=B/FLOAT(M)
TDY=2.*DY
TDZ=2.*DZ
DY2=DY**2
DZ2=DZ**2
R=DZ/DY
RE=CHVEL*CHLEN
ACON=CHVEL/CHLEN
DTV=RE*DZ2/(2.*(1.+R**2))
WRITE(6,1060)CHVEL,CHLEN,RE
C*****
C GENERATES MESH COORDINATES
C*****
DO 100 I=1,MP1
100 Z(I)=FLOAT(I-1)*DZ
DO 110 J=1,NP1
YPLUS(J)=FLOAT(J-1)*YOUT/FLOAT(N)
110 Y(J)=FLOAT(J-1)*DY
NCOUNT=0.
C*****
**** CALCULATE THE TEMPORAL PART OF
**** THE UPPER BOUNDARY CONDITIONS
C*****
VPRIN1=1.
VPRIN2=0.
TSTEP=FLOAT(NCOUNT)*DTE+DTE
TIME1=TPI*TSTEP/TP1
TIME2=TPI*TSTEP/TP2
UVEL1=CU1*COS(TIME1+THETU1*PI/180)
UVEL2=CU2*COS(TIME2+THETU2*PI/180)

```

```

VVEL1=CV1*COS(TIME1+THETV1*PI/180)
VVEL2=CV2*COS(TIME2+THETV2*PI/180)
WVEL1=CW1*COS(TIME1+THETW1*PI/180)
WVEL2=CW2*COS(TIME2+THETW2*PI/180)
C*****
C*** READS STREAM FUNCTION, VORTICITY AND
C*** STREAMWISE VELOCITY FROM TIME STEP N.
C*****
IF(FTOG.EQ.1.OR.UTOG.EQ.1)THEN
READ(21)PSI
READ(21) ZETA
READ(21) UCOM
DO 115 I=1,MP1
DO 115 J=1,NP1
PSI(I,J)=PSI(I,J)*2*LAM*TAUOSR/(CHLEN*CHVEL)
ZETA(I,J)=ZETA(I,J)*CHLEN*TAUOSR/(CHVEL*2*LAM)
115 UCOM(I,J)=UCOM(I,J)/CHVEL
CLOSE(21)
ELSE IF(FTOG.EQ.0)THEN
C*****
C*** CALCULATES INITIAL PSI,ZETA
C*****
DO 120 I=1,MP1
WTAX(I)=WVEL1*SIN(TPI*Z(I)/ALW1)+WVEL2*SIN(TPI*Z(I)/ALW2)
DO 120 J=1,NP1
ZETA(I,J)=0.0
PSI(I,J)=ZETA(I,J)
120 CONTINUE
CALL HWSCRT(A,B,M,1,BDA,BDB,C,D,N,2,BDC,WTAX,O.,PSI,IDLIMF,
$PERTRB,IERROR,WORK)
END IF
C*****
C ZEROES ALL THE COUNTERS
C*****
IFLAG=2
IFL=0
NC=0
NCTOT=0
ITERS=0
NCOUNT=0
NCYCLE=0
CYCLE=0
NCB=0
DTS=0.0
STEP=YOUT/N
TCOUNT=0.0
NSTATP=0.0
NTOT=0
TSOC=0.0
C*****
C*** IF DESIRED CALCULATE NEW U PROFILE
C*****
IF(UTOG.EQ.0)THEN
IF(PPLUS.NE.0)AU20=YOUT*(1-PEFFO/PPLUS)/CFD2
IF(PPLUS.EQ.0)AU20=AU2I

```

```

      CALL VAND(M,N,YOUT,PEFF0,CFD2,PPLUS,AU20,APLUS,
$UB,PEFF,YPLUS,AU2)
      UBNW=UB(NP1)
      DO 160 J=1,NP1
      ALPHA(J)=PPLUS*(1-CFD2*UB(J)**2)
      DO 160 I=1,MP1
      UCOM(I,J)=UB(J)/CHVEL
160   CONTINUE
      RATIO=1
C*****
C**** IF DESIRED READ IN U PROFILE
C*****
      ELSE
      READ(22,1120)UBNEW,RATIO,NCYCLE,DUMMY1,DUMMY2
      DO 170 J=1,NP1
170   READ(23,1080)DUMMY,UB(J)
C*****
C**** BEGIN NEW ITERATION CYCLE
C*****
      70  AU2(1)=0.0
      PZOC=0.0
      UCOMOC=0.0
      AREA=0.0
      DO 180 L=1,NP1
      UB(L)=UB(L)/RATIO
      UB2(L)=UB(L)**2
      IF(L.NE.1.)CALL PARBL(UB2,1,STEP,L,AREA,IRROR)
180   AU2(L)=AREA
      AU20=AU2(NP1)
      PPLUS=PEFF0/(1-(CFD2*AU20/YOUT))
      ALPHA(1)=PPLUS
      PEFF(1)=PPLUS
      DO 190 J=2,NP1
      ALPHA(J)=PPLUS*(1-CFD2*UB(J)**2)
      ZIG=1-(CFD2*UB(J)**2)
      IF(ZIG.LE.0.0)ALPHA(J)=0.0
190   PEFF(J)=PPLUS*(1-(CFD2*AU2(J)/YPLUS(J)))
      END IF
      CYCLE=CYCLE+1
      WRITE(6,1140)CYCLE
      UL=UBNEW/CHVEL
      WRITE(6,1070)PPLUS,AU20,UL
      DO 210 J=1,NP1
      USAV(J)=0.0
      IF(J.EQ.1)PRINT*, ' Y+      ALPHA+    PEFF+    UAB+ '
      WRITE(6,1050)YPLUS(J),ALPHA(J),PEFF(J),UB(J)
      DO 210 I=1,MP1
210   UCOM(I,J)=UCOM(I,J)/RATIO
      DT=DTE*ACON
      BETAM=8.*(.RE-DZ**2./DT)
      BETAP=8.*(.RE+DZ**2./DT)
      GAMAP=8.*(R**2./RE+DZ**2./DT)
      GAMAM=8.*(R**2./RE-DZ**2./DT)
      FOVRE=4./RE
      FOVRE1=R**2*FOVRE

```

```

C*****
C*** NEW TIME STEP
C*****
74  NCOUNT=NCOUNT+1
    NTOT=NTOT+1
    TSOC=TSOC+1
    IF(NINT(TSOC).EQ.50)THEN
        OPEN(37,FILE='HOSTCHAR:DRA3:[240016.APSTOR]TSO.DAT',
$STATUS='NEW', FORM='FORMATTED')
        TNTOT=FLOAT(NTOT)*DTE
        WRITE(37,1150)CYCLE,TNTOT
        CLOSE(37)
        TSOC=0.0
    END IF
    DTS=DTS+DT
C*****
C*** CALCULATION OF V AT THE UPPER
C*** BOUNDARY FOR TIME STEP N.
C*****
DO 230 I=1,MP1
230  VBEF(I)=VPRIN1*COS(TPI*Z(I)/ALV1)+VPRIN2*COS(TPI*Z(I)/ALV2)
C*****
C*** CALCULATION OF U,PSI,W AND DV/DZ
C*** AT THE UPPER BOUNDARY FOR TIME STEP N+1.
C*****
DO 240 I=1,MP1
    WTAX(I)=WVEL1*SIN(TPI*Z(I)/ALW1)+WVEL2*SIN(TPI*Z(I)/ALW2)
    UTAX(I)=UL+UVEL1*COS(TPI*Z(I)/ALU1)+UVEL2*COS(TPI*Z(I)/ALU2)
    PSIUP(I)=-(VVEL1*ALV1*SIN(TPI*Z(I)/ALV1)+VVEL2*ALV2*
$SIN(TPI*Z(I)/ALV2))/TPI
    DVDZ(I)=-TPI*(VVEL1*SIN(TPI*Z(I)/ALV1)/ALV1+VVEL2*
$SIN(TPI*Z(I)/ALV2)/ALV2)
240  CONTINUE
C*****
C   IF DESIRED INPUT PSI AND ZETA FIELDS EVERY TIME STEPS
C*****
IF(FIELDI.EQ.1)THEN
    DO 263 KL=1,PZIINC
263  READ(24)ZETA2
    IF(NINT((FLOAT(NCOUNT)*DTE*100)).EQ.NINT(TP2*100))REWIND(24)
    DO 265 I=1,MP1
    DO 265 J=1,NP1
265  ZETA2(I,J)=ZETA2(I,J)*2*LAM*TAUOSR/(CHVEL*CHLEN)
    IF(NCYCLE.EQ.0)GOTO 260
    DO 283 KL=1,PZIINC
283  READ(25)ZETABC
    DO 285 I=1,MP1
        ZETA1(I,1)=ZETABC(I,1)*TAUOSR*CHLEN/(CHVEL*2*LAM)
        ZETA1(I,NP1)=ZETABC(I,2)*TAUOSR*CHLEN/(CHVEL*2*LAM)
        DO 285 J=2,N
            ZETA1(I,J)=(ZETA2(I+1,J)-2*ZETA2(I,J)+ZETA2(I-1,J))/DZ2
$+(ZETA2(I,J+1)-2*ZETA2(I,J)+ZETA2(I,J-1))/DY2
285  CONTINUE
260  END IF
C*****

```

```

C      GUESS FOR STREAM FUNCTION AND BOUNDARY VORTICITY
C      IN THE FIRST ITERATION OF THE CURRENT TIME STEP.
C      PSI IS PSI FOR TIME STEP N
C      PSI1 IS GUESS FOR TIME STEP N+1
C      ZETA2 IS RESULT FOR TIME STEP N+1
C      ZETA IS ZETA FOR TIME STEP N
C      ZETA1 IS ZETA FOR TIME STEP N+1
C*****
C***** IF(FIELDI.EQ.0)THEN
      DO 250 I=1,MP1
      DO 250 J=1,NP1
250  PSI1(I,J)=PSI(I,J)
      DO 270 J=2,N
      ZETA1(1,J)=ZETA(1,J)
270  ZETA1(MP1,J)=ZETA(MP1,J)
      DO 280 I=2,M
      ZETA2(I,1)=ZETA(I,1)
280  ZETA2(I,NP1)=ZETA(I,NP1)
      ITER=0
C*****
C      NEW ITERATION AT THE CURRENT TIME STEP
C*****
42   ITER=ITER+1
C*****
C      ADI-SOLVER FOR THE V-W VELOCITY FIELD
C*****
      CALL VWSOL(PSI,PSI1,ZETA,ZETA1,ZETA2,IER)
      IF(IER.EQ.129) GO TO 22
C*****
C      POISSON-SOLVER FOR THE STREAM FUNCTION
C*****
      DO 290 I=2,M
      DO 290 J=1,NP1
290  ZETA1(I,J)=ZETA2(I,J)
      DO 320 I=2,M
      ZETA2(I,1)=0.
320  ZETA2(I,NP1)=PSIUP(I)
      DO 510 J=1,NP1
      ZETA2(1,J)=0.
510  ZETA2(MP1,J)=0.
      CALL HWSCRT(A,B,M,1,BDA,BDB,C,D,N,1,BDC,BDD,0.,ZETA2,1D1MF,
     1PERTRB,IERROR,WORK)
      IF(IERROR.GT.0) GO TO 26
      IF(ITER.EQ.1) GO TO 30
      AMAXI=0.
      DO 330 I=1,MP1
      DO 330 J=1,NP1
      DEV=ABS(ZETA2(I,J)-PSI1(I,J))
330  AMAXI=AMAX1(AMAXI,DEV)
      IF(AMAXI.LE.E) GO TO 34
      IF(ITER.EQ.ITERM) GO TO 38
C*****
C      STORES ESTIMATE OF STREAM FUNCTION AND UPDATES
C      BOUNDARY VORTICITY FOR THE NEXT ITERATION
C*****

```

```

30 DO 350 I=1,MP1
      DO 350 J=1,NP1
350 PSI1(I,J)=ZETA2(I,J)
      DO 370 J=2,N
      ZETA1(1,J)=0.
370 ZETA1(MP1,J)=0.
      DO 380 I=2,M
      ZETA2(I,1)=RELCOM*ZETA1(I,1)+(1.-RELCOM)*(8.*PSI1(I,2)-PSI1(I,3))
      $/(2.*DY2)
      ZETA2(I,NP1)=RELCOM*ZETA1(I,NP1)+(1.-RELCOM)*(2.*((PSI1(I,N)-
      $PSI1(I,NP1))/DY2+WTAX(I)/DY)-DVDZ(I))
380 CONTINUE
      GO TO 42
34 ITERS=ITERS+ITER
END IF
C*****
C**** INPUT U FIELD AT EVERY TIME STEP IF DESIRED
C*****
IF(UCOMI.EQ.1)THEN
DO 580 KL=1,UIINC
580 READ(26) UCOM
IF((NINT(FLOAT(NCOUNT)*DTE*100)).EQ.NINT(TP2*100))REWIND(26)
DO 590 I=1,MP1
DO 590 J=1,NP1
590 UCOM(I,J)=UCOM(I,J)/CHVEL
ELSE
C*****
C ADI-SOLVER FOR THE U-VELOCITY FIELD
C*****
CALL USOL(PSI,ZETA2,UCOM,UTAX,IER)
IF(IER.EQ.129) GO TO 46
END IF
C*****
C**** SUM U VELOCITY FIELD FOR AVERAGING
C*****
DO 390 J=1,NP1
DO 390 I=1,M
USAV(J)=USAV(J)+UCOM(I,J)
390 CONTINUE
C*****
C UPDATES THE VORTICITY FOR THE NEXT TIME STEP
C*****
DO 410 I=2,M
DO 410 J=2,N
410 ZETA(I,J)=ZETA1(I,J)
DO 430 J=1,NP1
ZETA(1,J)=0.
430 ZETA(MP1,J)=0.
DO 440 I=2,M
ZETA(I,1)=(8.*ZETA2(I,2)-ZETA2(I,3))/(2.*DY2)
440 ZETA(I,NP1)=2.*((ZETA2(I,N)-ZETA2(I,NP1))/DY2+WTAX(I)/DY)-DVDZ(I)
C*****
C UPDATES THE STREAM FUNCTION FOR THE
C NEXT TIME STEP
C*****

```

```

      DO 450 I=1,MP1
      DO 450 J=1,NP1
450  PSI(I,J)=ZETA2(I,J)
      DO 470 I=1,MP1
      UGR(I)=(4.*UCOM(I,2)-UCOM(I,3))/TDY
      WGR(I)=ZETA2(I,1)
470  CONTINUE
C*****
C*** OUTPUT PSI,ZBC IF DESIRED
C*****
C     NOTE: ZETA1 IS A DUMMY VARIABLE HERE
C           AS IT IS NO LONGER NEEDED
      PZOC=PZOC+1
      IF(NCYCLE.EQ.1.AND.PZOC.EQ.PZOINC.AND.FIELD0.EQ.1)THEN
      DO 385 I=1,MP1
      ZETABC(I,1)=ZETA(I,1)*CHVEL*2*LAM/(CHLEN*TAUOSR)
      ZETABC(I,2)=ZETA(I,NP1)*CHVEL*2*LAM/(CHLEN*TAUOSR)
      DO 385 J=1,NP1
385  ZETA1(I,J)=PSI(I,J)*CHVEL*CHLEN/(2*LAM*TAUOSR)
      WRITE(35)ZETA1
      WRITE(34)ZETABC
      END IF
      IF(PZOC.EQ.PZOINC)PZOC=0.0
C*****
C*** OUTPUT UCOM IF DESIRED
C*****
C     NOTE: ZETA1 IS USED AS A DUMMY VARIABLE
      UCOMOC=UCOMOC+1
      IF(NCYCLE.NE.1.OR.UCOMOC.NE.UOINC.OR.UCOMO.NE.1)GOTO 387
      DO 389 I=1,MP1
      DO 389 J=1,NP1
389  ZETA1(I,J)=UCOM(I,J)*CHVEL
      WRITE(39)ZETA1
387  IF(UCOMOC.EQ.UOINC)UCOMOC=0.0
C*****
C*** CALCULATES PRESSURE FIELD AND STATISTICS
C*** IF DESIRED ON THE LAST CYCLE
C*****
      IF(NCYCLE.EQ.1.AND.STAT.EQ.1)THEN
C*****
C     CALCULATION OF V AND DW/DZ AT
C     THE UPPER BOUNDARY FOR TIME STEP N+1.
C*****
      DO 480 I=1,MP1
      VTAX(I)=VVEL1*COS(TPI*Z(I)/ALV1)+VVEL2*COS(TPI*Z(I)/ALV2)
      DWDZ(I)=TPI*(WVEL1*COS(TPI*Z(I)/ALW1)/ALW1+WVEL2*
$COS(TPI*Z(I)/ALW2)/ALW2)
480  CONTINUE
      CALL PRESD(PSI,ZETA,VTAX,WTAX,DVDZ,DWDZ,
$VBEF,IERROR,DEVMAX)
      IF(IERROR.GT.0) GO TO 58
C*****
C     CALCULATION OF DU/DZ AT
C     THE UPPER BOUNDARY FOR TIME STEP N+1.
C*****

```

```

DO 490 I=1,MP1
DUDZ(I)=TPI*(UVEL1*SIN(TPI*Z(I)/ALU1)/ALU1+UVEL2*
$SIN(TPI*Z(I)/ALU2)/ALU2)
490 CONTINUE
IF(NCYCLE.EQ.1.AND.NINT(FLOAT(NCOUNT)*DTE*100).EQ.NINT(TP2*100))
$NSTATP=1
NC=NC+1
CALL STATIS(PSI,ZETA,UCOM,DUDZ,VTAX,DVDZ,W TAX,DWDZ,
$UGR,WGR,NC,NSTATP,IFLAG)
END IF
IF(NINT((FLOAT(NCOUNT)*DTE*100)).NE.NINT(TP2*100))GOTO 66
C*****
C**** AT THE END OF EACH CYCLE CALCULATE NEW U INPUTS
C**** AND OUTPUT RESULTS
C*****
DO 500 J=1,NP1
UB(J)=USA V(J)*CHVEL/(FLOAT(M)*NINT(TP2/DTE))
500 CONTINUE
UCOUTT=YPLUS(2)+PEFF(2)*YPLUS(2)**2/2.
WRITE(6,1090)YPLUS(2),UB(2)
WRITE(6,1100)YPLUS(2),UCOUTT
RATIO=UB(2)/UCOUTT
WRITE(6,1110)YPLUS(2),RATIO
UBNEW=UB(NP1)/RATIO
ULO=UL*CHVEL
WRITE(6,1130)ULO,UB(NP1),UBNEW,RATIO
OPEN(33,FILE=':HOSTCHAR:DRA3:[240016.APSTOR]UABO.DAT',
$STATUS='NEW',FORM='FORMATTED')
DO 560 J=1,NP1
WRITE(33,1080)YPLUS(J),UB(J)
UB2(J)=(UB(J)/RATIO)**2
560 CONTINUE
CLOSE(33)
OPEN(32,FILE=':HOSTCHAR:DRA3:[240016.APSTOR]UBOO.DAT',
$STATUS='NEW',FORM='FORMATTED')
CALL PARBL(UB2,1,STEP,NP1,AOUT,IERROR)
PPLUSO=PEFFO/(1-(CFD2*AOUT/YOUT))
KP=CFD2**1.5*PPLUSO*1.E06
WRITE(6,1420)CYCLE,PPLUSO,KP
WRITE(32,1120)UBNEW,RATIO,NCYCLE,PPLUSO,KP
CLOSE(32)
OPEN(31,FILE=':HOST:DRA3:[240016.APSTOR]PZUO.DAT',
$LE=50000,SI=13,SB=8192,FIL=S,RE=V,FM=U,BLOCKS=2',STATUS='NEW')
DO 520 I=1,MP1
DO 520 J=1,NP1
520 ZETA1(I,J)=PSI(I,J)*CHVEL*CHLEN/(2*LAM*TAUOSR)
WRITE(31) ZETA1
DO 530 I=1,MP1
DO 530 J=1,NP1
530 ZETA1(I,J)=ZETA(I,J)*CHVEL*2*LAM/(CHLEN*TAUOSR)
WRITE(31) ZETA1
DO 540 I=1,MP1
DO 540 J=1,NP1
540 ZETA1(I,J)=UCOM(I,J)*CHVEL
WRITE(31) ZETA1

```

```

CLOSE(31)
IF(NINT((FLOAT(NCOUNT)*DTE*100)).EQ.NINT(TP2*100))NCOUNT=0
IF(CYCLE.EQ.NINT(INDEXM))GOTO 62
IF(NCYCLE.EQ.1)GOTO 62
IF(ABS(1-RATIO).LE.0.001)NCYCLE=1
IF(NCYCLE.EQ.1)E=FINALE
IF(ABS(1-RATIO).LE.RATIO2.AND.NCYCLE.NE.1)E=E2
66 CONTINUE
C***** CALCULATE THE TEMPORAL PART OF
C***** THE UPPER BOUNDARY CONDITIONS
C*****
VPRIN1=VVEL1
VPRIN2=VVEL2
TSTEP=FLOAT(NCOUNT)*DTE+DTE
TIME1=TPI*TSTEP/TP1
TIME2=TPI*TSTEP/TP2
UVEL1=CU1*COS(TIME1+THETU1*PI/180)
UVEL2=CU2*COS(TIME2+THETU2*PI/180)
VVEL1=CV1*COS(TIME1+THETV1*PI/180)
VVEL2=CV2*COS(TIME2+THETV2*PI/180)
WVEL1=CW1*COS(TIME1+THETW1*PI/180)
WVEL2=CW2*COS(TIME2+THETW2*PI/180)
IF(NCOUNT.EQ.0)GOTO 70
GO TO 74
C*****
C      END OF THIS RUN
C*****
62 DT=DT/ACON
DTS=DTS/ACON
NIPTS=FLOAT(ITER)/FLOAT(NTOT)
WRITE(6,1160)NTOT,ITER,NIPTS,DT,DTS
IF(NSTATP.NE.1)GOTO 78
WRITE(6,1170) NC,NCTOT,SXBAR,SZBARA,SXSB,
$SZSBA,UINTYO(NP1),VINTYO(NP1),WINTYO(NP1)
WRITE(6,1180)
WRITE(6,1200) (UAVE(L),L=1,NP1)
WRITE(6,1190)
WRITE(6,1200) (VAVE(L),L=1,NP1)
WRITE(6,1210)
WRITE(6,1200) (WAVE(L),L=1,NP1)
WRITE(6,1220)
WRITE(6,1200) (UINTYO(L),L=1,NP1)
WRITE(6,1230)
WRITE(6,1200) (VINTYO(L),L=1,NP1)
WRITE(6,1240)
WRITE(6,1200) (WINTYO(L),L=1,NP1)
GO TO 78
C*****
C***** ERROR MESSAGES
C*****
38 WRITE(6,1250) NCOUNT
ITER=ITER+ITER
IFL=1
GO TO 62

```

```

26  WRITE(6,1260) NCOUNT,ITER,IERROR
    ITERS=ITERS+ITER
    IFL=1
    GO TO 62
22  WRITE(6,1270) NCOUNT,ITER,IER
    ITERS=ITERS+ITER
    IFL=1
    GO TO 62
46  WRITE(6,1280) NCOUNT,IER
    IFL=1
    GO TO 62
58  WRITE(6,1290) NCOUNT,IERROR
    IFL=1
    GO TO 62
78  STOP
1000 FORMAT(1X,'MAXIMUM AMOUNT OF TIME= ',F8.2)
1010 FORMAT(1X,'UINBC= ',F6.4,3X,'VINBC= ',F6.4,3X,'WINBC= ',F6.4)
1020 FORMAT(1X,'CU1= ',F6.4,' CU2= ',F6.4,/,,
      $1X,'CV1= ',F6.4,' CV2= ',F6.4,/,,
      $1X,'CW1= ',F6.4,' CW2= ',F6.4)
1030 FORMAT(1X,'DRAG-COEFFICIENT/2= ',F6.5,/,,
      $1X,'FOR THIS RUN, Y0+= ',F6.3,/,,
      $1X,'EFFECTIVE PRESSURE GRADIENT AT Y0+= ',F7.5)
1040 FORMAT(1X,'LAM1= ',F7.3,' LAM2= ',F7.3,/,,
      $1X,'TP1= ',F7.3,' TP2= ',F8.3)
1050 FORMAT(1X,F5.2,3X,F7.5,3X,F7.5,3X,F6.3)
1060 FORMAT(1X,'CHVEL= ',F5.3,' CHLEN= ',F4.0,' RE= ',F5.1)
1070 FORMAT(1X,'PWALL= ',F6.4,2X,'AU20= ',F6.0,2X,'UL=',F5.2)
1080 FORMAT(1X,F8.3,3X,F8.4)
1090 FORMAT(1X,'AVERAGE VELOCITY AT Y+= ',F7.4,' IS ',F7.4)
1100 FORMAT(1X,'COUETTE VELOCITY AT Y+= ',F7.4,' IS ',F7.4)
1110 FORMAT(1X,'RATIO AVERAGE TO COUTTE AT Y+= ',F7.4,' IS ',F7.4)
1120 FORMAT(1X,F8.4,2X,F7.4,2X,I2,2X,F8.5,2X,F7.3)
1130 FORMAT(1X,'INPUT UBAR=',F7.4,1X,'OUTPUT UBAR=',F7.4,1X,
      $'UBAR NEW=',F7.4,1X,'RATIO= ',F7.4)
1140 FORMAT(1X,//,' BEGINNING OF CYCLE # ',I2)
1150 FORMAT(1X,' CYCLE= ',I2,3X,' TOTAL TIME STEPS= ',F6.0)
1160 FORMAT(/,1X,'TOTAL NUMBER OF STEPS= ',I5,/,,
      $1X,'TOTAL NUMBER OF ITERATIONS= ',I6,/,,
      $1X,'AVERAGE # OF ITERATIONS PER TIME STEP= ',F5.2,/,,
      $1X,'TIME STEP= ',F7.4,/,,
      $1X,'TOTAL TIME ELAPSED= ',F8.2)
1170 FORMAT(1X,'NUMBER OF POINTS FOR STAT.CALC. IN THIS RUN= ',I5,
      $/,1X,'TOTAL NUMBER OF POINTS FOR STAT.CALC.= ',I5,/,1X,
      $'STREAMWISE VELOCITY GRADIENT AT THE WALL= ',F6.4,/,,
      $1X,'SPANWISE VELOCITY GRADIENT AT THE WALL= ',F6.4,/,1X,
      $'STREAMWISE WALL INTENSITY= ',F6.4,/,1X,
      $'SPANWISE WALL INTENSITY= ',F6.4,/,1X,
      $'STREAMWISE INTENSITY AT Y0= ',F6.4,/,1X,
      $'NORMAL INTENSITY AT Y0= ',F6.4,/,1X,
      $'SPANWISE INTENSITY AT Y0= ',F6.4,/)
1180 FORMAT(5X,'AVERAGE VELOCITY DISTRIBUTIONS',/,5X,
      $'STREAMWISE VELOCITY')
1190 FORMAT(/,.5X,'NORMAL VELOCITY')
1200 FORMAT(1X,7E12.5)

```

```

1210 FORMAT(/,5X,'SPANWISE VELOCITY')
1220 FORMAT(/,5X,'VELOCITY R.M.S. VALUES IN WALL PARAMETERS',
$/,5X,'STREAMWISE R.M.S. VALUES')
1230 FORMAT(/,5X,'NORMAL R.M.S. VALUES')
1240 FORMAT(/,5X,'SPANWISE R.M.S. VALUES')
1250 FORMAT(2X,'ADI SCHEME DID NOT CONVERGE AT NCOUNT= ',I5,///)
1260 FORMAT(5X,'ERROR DETECTED WHEN CALLING HWSCRT FOR THE SOLUTION',
$' OF THE PSI FIELD',//,5X,'NCOUNT=',I3,2X,'ITER=',I2,2X,'IERROR=',
$I5,///)
1270 FORMAT(5X,'ERROR DETECTED WHEN CALLING LEQT1B FOR THE V-W FIELD',
$' ADI-SOLVER',//,5X,'NCOUNT=',I3,2X,'ITER=',I2,2X,'IER=',I5,///)
1280 FORMAT(5X,'ERROR DETECTED WHEN CALLING LEQT1B FOR THE U-FIELD',
$' ADI-SOLVER',//,5X,'NCOUNT= ',I3,2X,'IER= ',I5,///)
1290 FORMAT(5X,'ERROR DETECTED WHEN CALLING HWSCRT FOR THE SOLUTION',
$' OF THE PIESH FIELD',//,5X,'NCOUNT= ',I3,2X,'IERROR= ',I5,///)
1300 FORMAT(1X,'SHEAR STRESS AT YO+= ',F5.3,/,
$1X,'REYNOLDS STRESS AT YO+= ',F5.3,/,
$1X,'DUDY AT YO+= ',F5.3,/,
$1X,'UV CORRELATION COEFFICIENT AT YO+= ',F5.3)
1310 FORMAT(1X,'TIME STEP IN + UNITS= ',F4.1,/
$,1X,'ADI ERROR LIMIT= ',E12.1)
1320 FORMAT(1X,'RATIO AT WHICH INTERMEDIATE E IS USED= ',F5.3,/
$,1X,'INTERMEDIATE ADI ERROR LIMIT= ',E12.1,/
$,1X,'FINAL CYCLES ADI ERROR LIMIT= ',E12.1)
1330 FORMAT(1X,'PSI OUTPUT STEP INCREMENT= ',F4.1)
1340 FORMAT(1X,'UINPO= ',F6.4,' VINPO= ',F6.5,' WINPO= ',F6.4)
1350 FORMAT(1X,'U1= ',F6.4,' U2= ',F6.4,/,
$1X,'V1= ',F6.4,' V2= ',F6.4,/,
$1X,'W1= ',F6.4,' W2= ',F6.4)
1360 FORMAT(1X,'THETU1= ',F4.0,' THETU2= ',F4.0,/
$,1X,'THETV1= ',F4.0,' THETV2= ',F4.0,/
$,1X,'THETW1= ',F4.0,' THETW2= ',F4.0)
1370 FORMAT(1X,'SECOND PERIOD MULTIPLE OF THE FIRST= ',F2.0,/
$,1X,'SECOND WAVELENGTH MULTIPLE OF THE FIRST= ',F2.0)
1380 FORMAT(1X,'EDGE OF VISCOUS SUBLAYER FOR P+=0 = ',F3.0)
1390 FORMAT(1X,'INPUT P+= ',F7.5,' INPUT APLUS= ',F7.4,
$' INPUT AU20= ',F6.0)
1400 FORMAT(1X,'MAX. # OF ITERATIONS PER TIME STEP= ',I3,/
$,1X,'MAX. # OF CYCLES= ',F8.2)
1410 FORMAT(1X,'EU1= ',F4.2,' EV1= ',F4.2,' EW1= ',F4.2)
1420 FORMAT(1X,'END OF CYCLE #',I2,' PWALL= ',F8.5,' K= ',F7.3)
1430 FORMAT(1X,' PSI INPUT STEP INCREMENT= ',F4.1)
1440 FORMAT(1X,' UCOM OUTPUT STEP INCREMENT= ',F4.1)
1450 FORMAT(1X,' UCOM INPUT STEP INCREMENT= ',F4.1)
END

```

SUBROUTINE PRESD(PSI,ZETA,VTAX,WTAX,DVDZ,DWDZ,
\$VBEF,IERROR,DEVMAX)

C**** THIS VERSION SETUP FOR 101,51

C

C THIS SUBROUTINE CALCULATES THE PRESSURE FIELD
C FOR ONE CELL OF THE MODEL FLOW

C

DIMENSION PSI(101,51),ZETA(101,51),VTAX(101),WTAX(101),Y(51)

```

DIMENSION PIESH(101,51),BDA(51),BDB(51),BDC(101)
DIMENSION BDD(101),VBEF(101)
DIMENSION WORK(5000),RHS(101,51),DVDZ(101),DWDZ(101),Z(101)
COMMON/AREA2/A,B,C,D,IDIMF
COMMON/AREA3/M,MP1,MM1,MM2,N,NP1,NM1,NM2
COMMON/AREA4/WORK,BDA,BDB
COMMON/AREA6/RE,DY,DZ,DT,TDY,TDZ,DY2,DZ2
COMMON/AREA10/Y,Z,KSTAT,DTE
COMMON/ONE/PIESH
COMMON/TWO/RHS
SAVE
TWDELZ=2./DZ
TWDELY=2./DY
DO 10 I=2,M
    BDC(I)=(-1./RE)*(ZETA(I+1,1)-ZETA(I-1,1))/TDZ
10 CONTINUE
    BDC(1)=(-1./RE)*(-3.*ZETA(1,1)+4.*ZETA(2,1)-ZETA(3,1))/TDZ
    BDC(MP1)=(-1./RE)*(ZETA(MM1,1)-4.*ZETA(M,1)+3.*ZETA(MP1,1))/TDZ
    DO 20 J=1,NP1
        BDA(J)=0.
        BDB(J)=0.
20 CONTINUE
    DO 30 I=2,M
        BDD(I)=(-1./RE)*(ZETA(I+1,NP1)-ZETA(I-1,NP1))/TDZ-(VTAX(I)-
$VBEF(I))/DTE--(-VTAX(I)*DWDZ(I)+WTAX(I)*DVDZ(I))
30 CONTINUE
    BDD(1)=(-1./RE)*(-3.*ZETA(1,NP1)+4.*ZETA(2,NP1)-ZETA(3,NP1))/TDZ-
$(VTAX(1)-VBEF(1))/DTE--(-VTAX(1)*DWDZ(1)+WTAX(1)*DVDZ(1))
    BDD(MP1)=(-1./RE)*(ZETA(MM1,NP1)-4.*ZETA(M,NP1)+3.*ZETA(MP1,NP1))/
$TDZ-(VTAX(MP1)-VBEF(MP1))/DTE--(-VTAX(MP1)*DWDZ(MP1)+WTAX(MP1)*
$DVDZ(MP1))
    DO 40 I=2,M
    DO 50 J=2,N
        PIESH(I,J)=2.*((PSI(I,J+1)-2.*PSI(I,J)+PSI(I,J-1))*(
$(PSI(I+1,J)-2.*PSI(I,J)+PSI(I-1,J))/(DY2*DZ2)-((PSI(I+1,
$J+1)-PSI(I+1,J-1)-PSI(I-1,J+1)+PSI(I-1,J-1))/(TDY*TDZ))**2)
50 CONTINUE
40 CONTINUE
    DO 60 I=1,MP1
        PIESH(I,1)=0.
60 CONTINUE
    DO 70 J=2,N
        PIESH(1,J)=-2.*((-3.*((PSI(1,J+1)-PSI(1,J-1))+4.*((PSI(2,J+1)-
$PSI(2,J-1))-((PSI(3,J+1)-PSI(3,J-1))))/(TDY*TDZ))**2
        PIESH(MP1,J)=-2.*(((PSI(MM1,J+1)-PSI(MM1,J-1))-4.*((PSI(M,
$J+1)-PSI(M,J-1))+3.*((PSI(MP1,J+1)-PSI(MP1,J-1))))/
$(TDY*TDZ))**2 .
70 CONTINUE
    DO 80 I=1,MP1
        PIESH(I,NP1)=-2.*((DWDZ(I)**2+DVDZ(I)*(ZETA(I,NP1)+DVDZ(I))))
80 CONTINUE
    DO 310 I=1,MP1
    DO 320 J=1,NP1
        RHS(I,J)=PIESH(I,J)
320 CONTINUE

```

```

310  CONTINUE
      DO 311 J=1,NP1
      RHS(1,J)=PIESH(1,J)+BDA(J)*TWDELZ
      RHS(MP1,J)=PIESH(MP1,J)-BDB(J)*TWDELZ
311  CONTINUE
      DO 312 I=1,MP1
      RHS(I,1)=PIESH(I,1)+BDC(I)*TWDELY
      RHS(I,NP1)=PIESH(I,NP1)-BDD(I)*TWDELY
312  CONTINUE
      CALL HWSCRT(A,B,M,3,BDA,BDB,C,D,N,3,BDC,BDD,O.,PIESH,IDLIMF,
$PERTRB,IERROR,WORK)
      RHSAVE=0.
      DO 90 I=1,MP1
      DO 100 J=1,NP1
      RHSAVE=RHSAVE+ABS(RHS(I,J))
100  CONTINUE
90   CONTINUE
      RHSAVE=RHSAVE/FLOAT(MP1*NP1)
      DEVMAX=ABS(PERTRB)*100./RHSAVE
      PCON=(PIESH(13,1)+PIESH(14,1))/2.
      DO 313 I=1,MP1
      DO 314 J=1,NP1
      . .
      PIESH(I,J)=PIESH(I,J)-PCON
314  CONTINUE
313  CONTINUE
      RETURN
      END

```

```

SUBROUTINE VWSOL(PSI,PSI1,ZETA,ZETA1,ZETA2,IER)
C**** THIS VERSION SETUP FOR 51,101
C
C   THIS SUBROUTINE CALCULATES THE VORTICITY
C   FIELD USING A CONSERVATIVE
C   FINITE DIFFERENCE SCHEME AND * LEQT1B *
C   FOR THE INVERSION OF THE RESULTING
C   TRIDIAGONAL MATRICES
C   BOUNDARY CONDITION AT Y=Y0 ZETA=ZETAO(Z,T)
C
      DIMENSION PSI(51,101),PSI1(51,101),ZETA(51,101)
      DIMENSION ZETA1(51,101),ZETA2(51,101),P(99,3),Q(99),XL(198)
      COMMON/AREA1/R,FOVRE,FOVRE1,BETAP,BETAM,GAMAP,GAMAM
      COMMON/AREA3/M,MP1,MM1,MM2,N,NP1,NM1,NM2
      COMMON/SCRA/P,Q,XL
      SAVE
      ND=MM1
      IF(NM1.GT.MM1)ND=NM1
      DO 40 J=2,N
      DO 30 K=1,MM1
      PSM1DJ=(PSI(K,J+1)-PSI(K,J-1)+PSI1(K,J+1)-PSI1(K,J-1))*0.5
      PSP1DJ=(PSI(K+2,J+1)-PSI(K+2,J-1)+PSI1(K+2,J+1)-
$PSI1(K+2,J-1))*0.5
      PSM1DI=(PSI(K+2,J-1)-PSI(K,J-1)+PSI1(K+2,J-1)-PSI1(K,J-1))*0.5
      PSP1DI=(PSI(K+2,J+1)-PSI(K,J+1)+PSI1(K+2,J+1)-PSI1(K,J+1))*0.5
      P(K,1)=R*PSM1DJ+FOVRE

```

```

P(K,3)=-R*PSP1DJ+FOVRE
P(K,2)=-BETAP
Q(K)=(R*PSM1DI-FOVRE1)*ZETA(K+1,J-1)+GAMAM*ZETA(K+1,J)-
$(R*PSP1DI+FOVRE1)*ZETA(K+1,J+1)
30 CONTINUE
Q(1)=Q(1)-P(1,1)*ZETA1(1,J)
Q(MM1)=Q(MM1)-P(MM1,3)*ZETA1(MP1,J)
P(1,1)=0.
P(MM1,3)=0.
CALL LEQT1B(P,MM1,1,1,ND,Q,1,ND,0,XL,IER)
IF(IER.EQ.129) GO TO 136
DO 50 I=2,M
IA=I-1
ZETA1(I,J)=Q(IA)
50 CONTINUE
40 CONTINUE
DO 60 I=2,M
DO 70 K=1,NM1
PSM1DI=(PSI(I+1,K)-PSI(I-1,K)+PSI1(I+1,K)-PSI1(I-1,K))*0.5
PSP1DI=(PSI(I+1,K+2)-PSI(I-1,K+2)+PSI1(I+1,K+2)-
$PSI1(I-1,K+2))*0.5
PSM1DJ=(PSI(I-1,K+2)-PSI(I-1,K)+PSI1(I-1,K+2)-PSI1(I-1,K))*0.5
PSP1DJ=(PSI(I+1,K+2)-PSI(I+1,K)+PSI1(I+1,K+2)-PSI1(I+1,K))*0.5
P(K,1)=-R*PSM1DI+FOVRE1
P(K,3)=R*PSP1DI+FOVRE1
P(K,2)=-GAMAP
Q(K)=-(R*PSM1DJ+FOVRE)*ZETA1(I-1,K+1)+BETAM*ZETA1(I,K+1)-
$(R*PSP1DJ-FOVRE)*ZETA1(I+1,K+1)
70 CONTINUE
Q(1)=Q(1)-P(1,1)*ZETA2(I,1)
Q(NM1)=Q(NM1)-P(NM1,3)*ZETA2(I,NP1)
P(1,1)=0.
P(NM1,3)=0.
CALL LEQT1B(P,NM1,1,1,ND,Q,1,ND,0,XL,IER)
IF(IER.EQ.129) GO TO 136
DO 80 J=2,N
JA=J-1
ZETA2(I,J)=Q(JA)
80 CONTINUE
60 CONTINUE
136 RETURN
END

```

```

SUBROUTINE USOL(PSI,ZETA2,UCOM,UTAX,IER)
C**** THIS VERSION SETUP FOR 51,101
C
C THIS SUBROUTINE CALCULATES THE STREAMWISE
C VELOCITY FIELD USING A CONSERVATIVE
C FINITE DIFFERENCE SCHEME AND * LEQT1B *
C FOR THE INVERSION OF THE RESULTING
C TRIDIAGONAL MATRICES
C BOUNDARY CONDITION AT Y=Y0 IS U=U0
C
DIMENSION PSI(51,101),ZETA2(51,101),UCOM(51,101),UHAL(51,101)

```

```

DIMENSION P(99, 3), Q(99), XL(198), UTA(51), ALPHA(101)
COMMON/AREA1/R, FOVRE, FOVRE1, BETAP, BETAM, GAMAP, GAMAM
COMMON/AREA3/M, MP1, MM1, MM2, N, NP1, NM1, NM2
COMMON/AREA5/CHVEL, CHLEN, ACON
COMMON/AREA6/RE, DY, DZ, DT, TDY, TDZ, DY2, DZ2
COMMON/SCRA/P, Q, XL
COMMON/ONE/UHAL
COMMON/FIX1/ALPHA
SAVE
ND=MM1
IF(NM1.GT.MM1)ND=NM1
DO 151 J=2,N
DO 162 K=1,MM1
PSM1DJ=(PSI(K,J+1)-PSI(K,J-1)+ZETA2(K,J+1)-
$ZETA2(K,J-1))*0.5
PSP1DJ=(PSI(K+2,J+1)-PSI(K+2,J-1)+ZETA2(K+2,J+1)-
$ZETA2(K+2,J-1))*0.5
C-----
PSM1DI=(PSI(K+2,J-1)-PSI(K,J-1))
PSP1DI=(PSI(K+2,J+1)-PSI(K,J+1))
C-----
P(K,1)=R*PSM1DJ+FOVRE
P(K,3)=-R*PSP1DJ+FOVRE
P(K,2)=-BETAP
Q(K)=(R*PSM1DI-FOVRE1)*UCOM(K+1,J-1)+GAMAM*UCOM(K+1,J)-
$(R*PSP1DI+FOVRE1)*UCOM(K+1,J+1)+ALPHA(J)*4*DZ**2*CHLEN/
$CHVEL**2
162 CONTINUE
P(1,2)=P(1,2)+4.*P(1,1)/3.
P(1,3)=P(1,3)-P(1,1)/3.
P(MM1,1)=P(MM1,1)-P(MM1,3)/3.
P(MM1,2)=P(MM1,2)+4.*P(MM1,3)/3.
P(1,1)=0.
P(MM1,3)=0.
CALL LEQT1B(P,MM1,1,1,ND,Q,1,ND,0,XL,IER)
IF(IER.EQ.129) GO TO 136
DO 163 I=2,M
IA=I-1
UHAL(I,J)=Q(IA)
163 CONTINUE
151 CONTINUE
DO 194 J=2,N
UHAL(1,J)=(4.*UHAL(2,J)-UHAL(3,J))/3.
UHAL(MP1,J)=(4.*UHAL(M,J)-UHAL(MM1,J))/3.
194 CONTINUE
DO 164 I=2,M
DO 165 K=1,NM1
C-----
PSM1DI=(ZETA2(I+1,K)-ZETA2(I-1,K))
PSP1DI=(ZETA2(I+1,K+2)-ZETA2(I-1,K+2))
C-----
PSM1DJ=(PSI(I-1,K+2)-PSI(I-1,K)+ZETA2(I-1,K+2)-
$ZETA2(I-1,K))*0.5
PSP1DJ=(PSI(I+1,K+2)-PSI(I+1,K)+ZETA2(I+1,K+2)-
$ZETA2(I+1,K))*0.5

```

```

P(K,1)=-R*PSM1DI+FOVRE1
P(K,3)=R*PSP1DI+FOVRE1
P(K,2)=-GAMAP
Q(K)=-(R*PSM1DJ+FOVRE)*UHAL(I-1,K+1)+BETAM*UHAL(I,K+1) +
$(R*PSP1DJ-FOVRE)*UHAL(I+1,K+1)+ALPHA(K+1)*4*DZ**2*CHLEN/CHVEL**2
165  CONTINUE
      Q(1)=Q(1)-P(1,1)*UCOM(I,1)
      Q(NM1)=Q(NM1)-P(NM1,3)*UTAX(I)
      P(1,1)=0.
      P(NM1,3)=0.
      CALL LEQT1B(P,NM1,1,1,ND,Q,1,ND,0,XL,IER)
      IF(IER.EQ.129) GO TO 136
      DO 166 J=2,N
         JA=J-1
         UCOM(I,J)=Q(JA)
166  CONTINUE
164  CONTINUE
      DO 718 I=2,M
         UCOM(I,NP1)=UTAX(I)
718  CONTINUE
      DO 719 J=1,NP1
         UCOM(1,J)=(4.*UCOM(2,J)-UCOM(3,J))/3.
         UCOM(MP1,J)=(4.*UCOM(M,J)-UCOM(MM1,J))/3.
719  CONTINUE
136  RETURN
      END

```

```

SUBROUTINE VAND(M,N,YOUT,PEFF0,CFD2,PPLUS,AU2OF
&,APLUS,UB,PEFFM,Y1,AU21)
DIMENSION UB(101),PEFFM(101),U(201),AU2(201),U2(201),SS(201)
DIMENSION PEFF(201),Y(201),FX(201),Y1(101),AU21(101)
REAL KA
SS1=1
MP1=M+1
NP1=N+1
N2P1=2*N+1
KA=0.44
DYPLUS=YOUT/FLOAT(2*N)
AU2OB=AU2OF+15
APLUS1=APLUS
DO 2001 J=1,N2P1
Y(J)=DYPLUS*(J-1)
2001 SS(J)=SS1
DO 1005 KK=1,100
DO 1000 K=1,100
DO 500 J=1,N2P1
D=1-EXP(-Y(J)*SQRT(SS(J))/APLUS)
FX(J)=2*SS(J)/(1+SQRT(1+4*SS(J)*(KA*Y(J)*D)**2))
500  CONTINUE
DO 2002 J=1,N2P1
IF(J.EQ.1)AREA1=0.0
IF(J.EQ.1)AREA2=0.0
IF(J.NE.1)CALL PARBL(FX,1,DYPLUS,J,AREA1,IRROR)
U(J)=AREA1

```

```

U2(J)=U(J)**2
IF(J.NE.1)CALL PARBL(U2,1,DYPLUS,J,AREA2,IRROR)
IF(J.EQ.1)AU2(1)=0.0
IF(J.NE.1)AU2(J)=AREA2
IF(J.EQ.1)PEFF(J)=PPLUS
IF(J.NE.1)PEFF(J)=PPLUS*(1-CFD2*AREA2/Y(J))
SS(J)=1+PEFF(J)*Y(J)
IF(J.EQ.N2P1)AU20=AREA2
2002 CONTINUE
IF(ABS(AU20-AU20B).LE.10.) GOTO 2005
1000 AU20B=AU20
2005 IF(ABS(AU20-AU20F).LE.0.1)GOTO 2010
1005 APLUS=APLUS*AU20F/AU20
2010 CONTINUE
PRINT*, 'NEW APLUS=' ,APLUS
DO 800 J=1,NP1
NBA=(J-1)*2+1
AU21(J)=AU2(NBA)
Y1(J)=Y(NBA)
PEFFM(J)=PEFF(NBA)
UB(J)=U(NBA)
800 CONTINUE
RETURN
END

```

```

SUBROUTINE STATIS(PSI,ZETA,UCOM,DUDZ,VTAX,DVDZ,WTAX,DWDZ,
$UGR,WGR,NC,NSTATP,IFLAG)
DIMENSION PSI(101,51),UCOM(101,51),W(101,51),V(101,51)
DIMENSION SU(101),SU2(101),SU3(101),SU4(101),SV(101),SV2(101)
DIMENSION SV4(101),SW(101),SW2(101),SW3(101),SW4(101),SUV(101)
DIMENSION SVW(101),SUV2(101),SU2W(101),ZETA(101,51)
DIMENSION SZET(101),SUW2(101)
DIMENSION SV3(101),SUW(101),WGR(51),UGR(51),SP2(101)
DIMENSION SP(101),SU2V(101),SVW2(101),SUVW(101),SV2W(101),SUP(101)
DIMENSION SVP(101),SWP(101),SPVY(101),SPWZ(101),SPUY(101)
DIMENSION SPVZ(101),SPWY(101),SUY2(101),SUZ2(101),SVY2(101)
DIMENSION SVZ2(101),SPUZ(101),SZET2(101)
DIMENSION SWY2(101),SWZ2(101),SUYVY(101),SUZVZ(101),SUYWY(101)
DIMENSION SUZWZ(101),SVYWY(101),SVZWZ(101),PIESH(101,51)
DIMENSION DUDZ(51),VTAX(51),DVDZ(51),WTAX(51),DWDZ(51)
COMMON/ONE/PIESH
COMMON/TWO/W
COMMON/THREE/V
COMMON/FIVE/SU,SU2,SU3,SU4,SV,SV2,SV3,SV4,SW,SW2,SW3,SW4,SUV,SUW,
$SVW,SSX,SSX2,SSZ,SSZ2,SUV2,SP,SU2V,SVW2,SUVW,SV2W,SUP,SVP,SWP,
$SPVY,SPWZ,SPUY,SPUZ,SPVZ,SPWY,SUY2,SUZ2,SVY2,SVZ2,SWY2,SWZ2,
$SUYVY,SUZVZ,SUYWY,SUZWZ,SVYWY,SVZWZ,SP2,SU2W,SUW2,SZET,SZET2,
$SSZA,SSZB,SSZ2A,SSZ2B
COMMON/AREA3/M,MP1,MM1,MM2,N,NP1,NM1,NM2
COMMON/AREA6/RE,DY,DZ,DT,TDY,TDZ,DY2,DZ2
COMMON/AREA7/NCTOT,SXBAR,SZBAR,SXSB,SZSB
COMMON/AREA9/NCB,NINDEX
SAVE
NCTOT=NCB+NC

```

```

TDZY=TDZ*TDY
TDZ2=TDZ**2
TDY2=TDY**2

C
C   CALCULATION OF V AND W VELOCITY FIELDS
C
      DO 40 I=2,M
      DO 50 J=2,N
      W(I,J)=(PSI(I,J+1)-PSI(I,J-1))/TDY
      V(I,J)=-(PSI(I+1,J)-PSI(I-1,J))/TDZ
  50 CONTINUE
  40 CONTINUE
      DO 60 I=1,MP1
      W(I,1)=0.
      V(I,1)=0.
      W(I,NP1)=WTAX(I)
      V(I,NP1)=VTAX(I)
  60 CONTINUE
      DO 70 J=2,N
      W(1,J)=0.
      W(MP1,J)=0.
      V(1,J)=-(PSI(2,J)-PSI(1,J))/DZ
      V(MP1,J)=-(PSI(MP1,J)-PSI(M,J))/DZ
  70 CONTINUE

C
C   IF NC=1 AND NCB=0, STATISTICAL STORAGE ARRAYS
C           ARE ZEROED
C   IF NC>1 STATISTICAL CALCULATIONS BEGIN
C
      IF(NC.GT.1) GO TO 888
      SSX=0.
      SSX2=0.
      SSZ=0.
      SSZA=0.
      SSZB=0.
      SSZ2=0.
      SSZ2A=0.
      SSZ2B=0.
      DO 810 J=1,NP1
      SU(J)=0.
      SU2(J)=0.
      SU3(J)=0.
      SU4(J)=0.
      SV(J)=0.
      SV2(J)=0.
      SV3(J)=0.
      SV4(J)=0.
      SW(J)=0.
      SW2(J)=0.
      SW3(J)=0.
      SW4(J)=0.
      SUV(J)=0.
      SUW(J)=0.
      SVW(J)=0.
      SP(J)=0.

```

```

SP2(J)=0.
SUV2(J)=0.
SU2V(J)=0.
SVW2(J)=0.
SV2W(J)=0.
SUW2(J)=0.
SU2W(J)=0.
SUVW(J)=0.
SUP(J)=0.
SVP(J)=0.
SWP(J)=0.
SPVY(J)=0.
SPWZ(J)=0.
SPUY(J)=0.
SPUZ(J)=0.
SPVZ(J)=0.
SPWY(J)=0.
SUY2(J)=0.
SUZ2(J)=0.
SVY2(J)=0.
SVZ2(J)=0.
SWY2(J)=0.
SWZ2(J)=0.
SUYVY(J)=0.
SUZVZ(J)=0.
SUYWY(J)=0.
SUZWZ(J)=0.
SVYWY(J)=0.
SVZWZ(J)=0.
SZET(J)=0.
SZET2(J)=0.

```

810 CONTINUE

C UPDATES STATISTICAL STORAGE ARRAYS

C

888 CONTINUE

```

DO 160 I=1,M
SSX=SSX+UGR(I)
SSX2=SSX2+UGR(I)**2
SSZ=SSZ+WGR(I)
SSZA=SSZA+(4.*W(I,2)-W(I,3))/TDY
SSZB=SSZB+(18.*W(I,2)-9.*W(I,3)+2.*W(I,4))/(3.*TDY)
SSZ2=SSZ2+WGR(I)**2
SSZ2A=SSZ2A+((4.*W(I,2)-W(I,3))/TDY)**2
SSZ2B=SSZ2B+((18.*W(I,2)-9.*W(I,3)+2.*W(I,4))/(3.*TDY))**2

```

160 CONTINUE

DO 140 J=1,NP1

DO 140 I=1,M

```

SU(J)=SU(J)+UCOM(I,J)
SU2(J)=SU2(J)+UCOM(I,J)**2
SU3(J)=SU3(J)+UCOM(I,J)**3
SU4(J)=SU4(J)+UCOM(I,J)**4
SV(J)=SV(J)+V(I,J)
SV2(J)=SV2(J)+V(I,J)**2
SV3(J)=SV3(J)+V(I,J)**3
SV4(J)=SV4(J)+V(I,J)**4

```

```

SW(J)=SW(J)+W(I,J)
SW2(J)=SW2(J)+W(I,J)**2
SW3(J)=SW3(J)+W(I,J)**3
SW4(J)=SW4(J)+W(I,J)**4
SUV(J)=SUV(J)+UCOM(I,J)*V(I,J)
SUW(J)=SUW(J)+UCOM(I,J)*W(I,J)
SVW(J)=SVW(J)+V(I,J)*W(I,J)
SP(J)=SP(J)+PIESH(I,J)
SP2(J)=SP2(J)+PIESH(I,J)**2
SUV2(J)=SUV2(J)+UCOM(I,J)*V(I,J)**2
SU2V(J)=SU2V(J)+UCOM(I,J)**2*V(I,J)
SVW2(J)=SVW2(J)+V(I,J)*W(I,J)**2
SV2W(J)=SV2W(J)+V(I,J)**2*W(I,J)
SUW2(J)=SUW2(J)+UCOM(I,J)*W(I,J)**2
SU2W(J)=SU2W(J)+UCOM(I,J)**2*W(I,J)
SUVW(J)=SUVW(J)+UCOM(I,J)*V(I,J)*W(I,J)
SUP(J)=SUP(J)+UCOM(I,J)*PIESH(I,J)
SVP(J)=SVP(J)+V(I,J)*PIESH(I,J)
SWP(J)=SWP(J)+W(I,J)*PIESH(I,J)
SZET(J)=SZET(J)+ZETA(I,J)
SZET2(J)=SZET2(J)+ZETA(I,J)**2
140 CONTINUE
DO 774 J=2,N
DO 774 I=2,M
SPWZ(J)=SPWZ(J)+PIESH(I,J)*(W(I+1,J)-W(I-1,J))/TDZ
SPUZ(J)=SPUZ(J)+PIESH(I,J)*(UCOM(I+1,J)-UCOM(I-1,J))/TDZ
SPVZ(J)=SPVZ(J)+PIESH(I,J)*(V(I+1,J)-V(I-1,J))/TDZ
SUZ2(J)=SUZ2(J)+((UCOM(I+1,J)-UCOM(I-1,J))/TDZ)**2
SVZ2(J)=SVZ2(J)+((V(I+1,J)-V(I-1,J))/TDZ)**2
SWZ2(J)=SWZ2(J)+((W(I+1,J)-W(I-1,J))/TDZ)**2
SUZVZ(J)=SUZVZ(J)+(UCOM(I+1,J)-UCOM(I-1,J))*(V(I+1,J)-V(I-1,J))/TDZ2
SUZWZ(J)=SUZWZ(J)+(UCOM(I+1,J)-UCOM(I-1,J))*(W(I+1,J)-W(I-1,J))/TDZ2
SVZWZ(J)=SVZWZ(J)+(V(I+1,J)-V(I-1,J))*(W(I+1,J)-W(I-1,J))/TDZ2
774 CONTINUE
DO 776 I=1,M
SPWZ(NP1)=SPWZ(NP1)+PIESH(I,NP1)*DWDZ(I)
SPUZ(NP1)=SPUZ(NP1)+PIESH(I,NP1)*DUDZ(I)
SPVZ(NP1)=SPVZ(NP1)+PIESH(I,NP1)*DVDZ(I)
SUZ2(NP1)=SUZ2(NP1)+DUDZ(I)**2
SVZ2(NP1)=SVZ2(NP1)+DVDZ(I)**2
SWZ2(NP1)=SWZ2(NP1)+DWDZ(I)**2
SUZVZ(NP1)=SUZVZ(NP1)+DUDZ(I)*DVDZ(I)
SUZWZ(NP1)=SUZWZ(NP1)+DUDZ(I)*DWDZ(I)
SVZWZ(NP1)=SVZWZ(NP1)+DVDZ(I)*DWDZ(I)
776 CONTINUE
DO 994 J=2,N
SPWZ(J)=SPWZ(J)-PIESH(MP1,J)*(V(MP1,J+1)-V(MP1,J-1))/TDY
SWZ2(J)=SWZ2(J)+((V(MP1,J+1)-V(MP1,J-1))/TDY)**2
994 CONTINUE
DO 775 J=2,N
SPWZ(J)=SPWZ(J)-PIESH(1,J)*(V(1,J+1)-V(1,J-1))/TDY
SWZ2(J)=SWZ2(J)+((V(1,J+1)-V(1,J-1))/TDY)**2
775 CONTINUE

```

```

DO 884 J=2,N
DO 884 I=1,M
SPVY(J)=SPVY(J)+PIESH(I,J)*(V(I,J+1)-V(I,J-1))/TDY
SPUY(J)=SPUY(J)+PIESH(I,J)*(UCOM(I,J+1)-UCOM(I,J-1))/TDY
SPWY(J)=SPWY(J)+PIESH(I,J)*(W(I,J+1)-W(I,J-1))/TDY
SUY2(J)=SUY2(J)+((UCOM(I,J+1)-UCOM(I,J-1))/TDY)**2
SVY2(J)=SVY2(J)+((V(I,J+1)-V(I,J-1))/TDY)**2
SWY2(J)=SWY2(J)+((W(I,J+1)-W(I,J-1))/TDY)**2
SUYVY(J)=SUYVY(J)+(UCOM(I,J+1)-UCOM(I,J-1))*(V(I,J+1)-V(I,J-1))/TDY2
SUYWY(J)=SUYWY(J)+(UCOM(I,J+1)-UCOM(I,J-1))*(W(I,J+1)-W(I,J-1))/TDY2
884 CONTINUE
DO 995 I=1,M
SPVY(NP1)=SPVY(NP1)-PIESH(I,NP1)*DWDZ(I)
SPUY(1)=SPUY(1)+PIESH(I,1)*UGR(I)
SPUY(NP1)=SPUY(NP1)+PIESH(I,NP1)*(3.*UCOM(I,NP1)-4.*UCOM(I,N)+$UCOM(I,NM1))/TDY
SPWY(1)=SPWY(1)+PIESH(I,1)*WGR(I)
SPWY(NP1)=SPWY(NP1)+PIESH(I,NP1)*(ZETA(I,NP1)+DVDZ(I))
SUY2(1)=SUY2(1)+UGR(I)**2
SUY2(NP1)=SUY2(NP1)+((3.*UCOM(I,NP1)-4.*UCOM(I,N)+UCOM(I,NM1))/TDY)**2
SVY2(NP1)=SVY2(NP1)+DWDZ(I)**2
SWY2(1)=SWY2(1)+WGR(I)**2
SWY2(NP1)=SWY2(NP1)+(ZETA(I,NP1)+DVDZ(I))**2
SUYVY(NP1)=SUYVY(NP1)-(3.*UCOM(I,NP1)-4.*UCOM(I,N)+UCOM(I,NM1))*$DWDZ(I)/TDY
SUYWY(1)=SUYWY(1)+UGR(I)*WGR(I)
SUYWY(NP1)=SUYWY(NP1)+(3.*UCOM(I,NP1)-4.*UCOM(I,N)+UCOM(I,NM1))*$(ZETA(I,NP1)+DVDZ(I))/TDY
SVWY(NP1)=SVWY(NP1)-DWDZ(I)*(ZETA(I,NP1)+DVDZ(I))
995 CONTINUE
IF(NSTATP.NE.1) GOTO 777
CALL STCALC
777 RETURN
END

```

SUBROUTINE STCALC

```

C*****
C*** SUBROUTINE TO CALCULATE ALL THE STATISTICAL QUANTITIES
C*** IN THE KINETIC ENERGY AND MEAN KINETIC ENERGY EQUATIONS
C*****
C      NOTE: THIS VERSION IS SETUP FOR 51,101 GRID POINTS
C      NOTE: THE COMMON STATEMENT ONE USES SPACE FROM OTHER
C      SUBROUTINES AND THUS HAS TO BE DIMENSIONED CORRECTLY
C      DUM VARIABLE IS USED FOR THIS PURPOSE. IF DIMENSIONED
C      INCORRECTLY SOME MACHINES WILL GENERATE NON-FATAL
C      ERROR MESSAGES.
DIMENSION UDUV(101)
C*****
DIMENSION SU(101),SU2(101),SU3(101),SU4(101),SV(101),SV2(101)
DIMENSION SV4(101),SW(101),SW2(101),SW3(101),SW4(101),SUV(101)

```

```

DIMENSION SVW(101),SUV2(101),SU2W(101),SUW2(101),SZET(101)
DIMENSION SV3(101),SUW(101),SP2(101),PSB(101),PINTW(101)
DIMENSION SP(101),SU2V(101),SVW2(101),SUVW(101),SV2W(101),SUP(101)
DIMENSION SVP(101),SWP(101),SPVY(101),SPWZ(101),SPUY(101)
DIMENSION SZET2(101),SPUZ(101),SVZ2(101)
DIMENSION SPVZ(101),SPWY(101),SUY2(101),SUZ2(101),SVY2(101)
DIMENSION SWY2(101),SWZ2(101),SUYVY(101),SUZVZ(101),SUYWY(101)
DIMENSION SUZWZ(101),SVYWY(101),SVZWZ(101),ZINTW(101)
DIMENSION VBAR(101),WBAR(101),USB(101),VSB(101),WSB(101),UCB(101)
DIMENSION WCB(101),UFB(101),VFB(101),WFB(101),UVB(101),UWB(101)
DIMENSION UINTL(101),VINTL(101),WINTL(101),UINTW(101),VINTW(101)
DIMENSION USQ(100),VSQ(100),WSQ(100),UFL(100),VFL(100),WFL(100)
DIMENSION UWCOR(100),VWCOR(100),UVWALL(101),UWWALL(101)
DIMENSION UBAR(101),VCB(101),DUBY(101),DVBY(101),DWBY(101)
DIMENSION VWB(101),WINTW(101),UVCOR(100),VWWALL(101)
DIMENSION PBAR(101),U2VB(101),VW2B(101),UVWB(101),V2WB(101)
DIMENSION ZSB(101),UPB(101)
DIMENSION VPB(101),WPB(101),PVYB(101),PWZB(101),PUYB(101)
DIMENSION PVZB(101),PWYB(101),UY2B(101),UZ2B(101),VY2B(101)
DIMENSION WY2B(101),WZ2B(101),UYVYB(101),UZVZB(101),UYWYB(101)
DIMENSION UZWZB(101),VYWYB(101),VZWZB(101),UV2B(101),ADU2(101)
DIMENSION PRU2(101),VZ2B(101),PUZB(101)
DIMENSION TDU2(101),GDU2(101),DISU2(101),ADV2(101),PRV2(101)
DIMENSION PDV2(101),GDV2(101),DISV2(101),ADW2(101),PRW2(101)
DIMENSION GDW2(101),DISW2(101),ADUV(101),PRUV(101),TDUV(101)
DIMENSION PDUV(101),TDW2(101),TDV2(101)
DIMENSION GDUV(101),DISUV(101),ADUW(101),PRUW(101),TDUW(101)
DIMENSION DISUW(101),ADVW(101),PRVW(101),TDVW(101),PDVW(101)
DIMENSION GDVW(101),DISVW(101),UVU(101),DUDU(101),UDU(101)
DIMENSION PMU2(101),PRW(101),TRS(101),TVS(101),DISM(101)
DIMENSION GDUW(101),PVZWY(101)
COMMON/AREA3/M,MP1,MM1,MM2,N,NP1,NM1,NM2
COMMON/AREA5/CHVEL,CHLEN,ACON
COMMON/AREA6/RE,DY,DZ,DT,TDY,TDZ,DY2,DZ2
COMMON/AREA7/NCTOT,SXBAR,SZBAR,SXSB,SZSB
COMMON/AREA13/SZBARA,SZBARB,SZSBA,SZSBB
COMMON/ONE/ADU2,PRU2,TDU2,GDU2,DISU2,ADV2,PRV2,TDV2,PDV2,
$GDV2,DISV2,ADW2,PRW2,TDW2,GDW2,DISW2,ADUV,PRUV,TDUV,PDUV,
$GDUV,DISUV,ADUW,PRUW,TDUW,GDUW,VINTL,WINTL,UVWALL,
$UPB,VPB,WPB,PWZB,PUZB,PVZB,UZ2B,VZ2B,WZ2B,UZVZB,UZWZB,
$VZWZB,PUYB,PVYB,PWYB,UY2B,VY2B,WY2B,UYVYB,UYWYB,VYWYB,UV2B,UINTL,
$DISUW,ADVW,PRVW,TDVW,PDVW,PVZWY,USB,VSB,WSB,UCB,PMU2,PRW,TRS,
$VCB,WCB,UFB,VFB,WFB,UVB,UWB,VWB,DUBY,DVBY,DWBY,PBAR,U2VB,VW2B,
$V2WB,UVWB,TVS,DISM,UVUV,GDVW,DISVW,UVU,DUDU,UDU,DUM(12,51)
COMMON/FOUR/UBAR,VBAR,WBAR,UINTW,VINTW,WINTW
COMMON/FIVE/SU,SU2,SU3,SU4,SV,SV2,SV3,SV4,SW,SW2,SW3,SW4,SUV,SUW,
$SVW,SSX,SSX2,SSZ,SSZ2,SUV2,SP,SU2V,SVW2,SUVW,SV2W,SUP,SVP,SWP,
$SPVY,SPWZ,SPUY,SPUZ,SPVZ,SPWY,SUY2,SUZ2,SVY2,SVZ2,SWY2,
$SWZ2,SUYVY,SUZVZ,SUYWY,SUZWZ,SVYWY,SVZWZ,SP2,SU2W,SUW2,SZET,SZET2,
$SSZA,SSZB,SSZ2A,SSZ2B
COMMON/FIX2/PPLUS,VAX
SAVE
IN=M*NCTOT
FIN=FLOAT(IN)

```

```

C      CALCULATES THE NECESSARY STATISTICAL
C      QUANTITIES
C
      DO 166 J=1, NP1
      PBAR(J)=SP(J)/FIN
      UBAR(J)=SU(J)/FIN
      VBAR(J)=SV(J)/FIN
      WBAR(J)=SW(J)/FIN
      PSB(J)=SP2(J)/FIN-(SP(J)/FIN)**2
      ZSB(J)=SZET2(J)/FIN-(SZET(J)/FIN)**2
      USB(J)=SU2(J)/FIN-(SU(J)/FIN)**2
      VSB(J)=SV2(J)/FIN-(SV(J)/FIN)**2
      WSB(J)=SW2(J)/FIN-(SW(J)/FIN)**2
      UCB(J)=SU3(J)/FIN-(SU(J)/FIN)**3-3.*((SU(J)/FIN)*((SU2(J)/FIN)-
      $(SU(J)/FIN)**2)
      VCB(J)=SV3(J)/FIN-(SV(J)/FIN)**3-3.*((SV(J)/FIN)*((SV2(J)/FIN)-
      $(SV(J)/FIN)**2)
      WCB(J)=SW3(J)/FIN-(SW(J)/FIN)**3-3.*((SW(J)/FIN)*((SW2(J)/FIN)-
      $(SW(J)/FIN)**2)
      UFB(J)=SU4(J)/FIN+(SU(J)/FIN)**4-4.*((SU(J)/FIN)*((SU3(J)/FIN)+
      $(SU(J)/FIN)**3)+6.*((SU2(J)/FIN)*(SU(J)/FIN)**2
      VFB(J)=SV4(J)/FIN+(SV(J)/FIN)**4-4.*((SV(J)/FIN)*((SV3(J)/FIN)+
      $(SV(J)/FIN)**3)+6.*((SV2(J)/FIN)*(SV(J)/FIN)**2
      WFB(J)=SW4(J)/FIN+(SW(J)/FIN)**4-4.*((SW(J)/FIN)*((SW3(J)/FIN)+
      $(SW(J)/FIN)**3)+6.*((SW2(J)/FIN)*(SW(J)/FIN)**2
      UVB(J)=SUV(J)/FIN-(SU(J)/FIN)*(SV(J)/FIN)
      UWB(J)=SUW(J)/FIN-(SU(J)/FIN)*(SW(J)/FIN)
      VWB(J)=SVW(J)/FIN-(SV(J)/FIN)*(SW(J)/FIN)
      UVU(J)=UVB(J)*UBAR(J)
166   CONTINUE
      DO 167 J=2, N
      DUBY(J)=(UBAR(J+1)-UBAR(J-1))/TDY
      DVBY(J)=(VBAR(J+1)-VBAR(J-1))/TDY
      DWBY(J)=(WBAR(J+1)-WBAR(J-1))/TDY
      DUDU(J)=DUBY(J)**2
      UDU(J)=UBAR(J)*DUBY(J)
167   CONTINUE
      DUBY(1)=(4.*UBAR(2)-UBAR(3))/TDY
      DVBY(1)=0.
      DWBY(1)=SZET(1)/FIN
      DUBY(NP1)=(3.*UBAR(NP1)-4.*UBAR(N)+UBAR(NM1))/TDY
      DVBY(NP1)=0.
      DWBY(NP1)=SZET(NP1)/FIN
      UDU(1)=UBAR(1)*DUBY(1)
      DUDU(1)=DUBY(1)**2
      UDU(NP1)=UBAR(NP1)*DUBY(NP1)
      DUDU(NP1)=DUBY(NP1)**2
      DO 168 J=1, NP1
      U2VB(J)=SU2V(J)/FIN-VBAR(J)*USB(J)-UBAR(J)*(UVB(J)+SUV(J)/FIN)
      VW2B(J)=SVW2(J)/FIN-VBAR(J)*WSB(J)-WBAR(J)*(VWB(J)+SVW(J)/FIN)
      UVWB(J)=SUVW(J)/FIN-UBAR(J)*SVW(J)/FIN-VBAR(J)*SUW(J)/FIN-WBAR(J)
      $*SUV(J)/FIN+2.*UBAR(J)*VBAR(J)*WBAR(J)
      V2WB(J)=SV2W(J)/FIN-WBAR(J)*VSB(J)-VBAR(J)*(VWB(J)+SVW(J)/FIN)
      UPB(J)=SUP(J)/FIN-UBAR(J)*PBAR(J)
      VPB(J)=SVP(J)/FIN-VBAR(J)*PBAR(J)

```

```

WPB(J)=SWP(J)/FIN-WBAR(J)*PBAR(J)
PWZB(J)=SPWZ(J)/FIN
PUZB(J)=SPUZ(J)/FIN
PVZB(J)=SPVZ(J)/FIN
UZ2B(J)=SUZ2(J)/FIN
VZ2B(J)=SVZ2(J)/FIN
WZ2B(J)=SWZ2(J)/FIN
UZVZB(J)=SUZVZ(J)/FIN
UZWZB(J)=SUZWZ(J)/FIN
VZWZB(J)=SVZWZ(J)/FIN
PVYB(J)=SPVY(J)/FIN-PBAR(J)*DVBY(J)
PUYB(J)=SPUY(J)/FIN-PBAR(J)*DUBY(J)
PWYB(J)=SPWY(J)/FIN-PBAR(J)*DWBY(J)
UY2B(J)=SUY2(J)/FIN-DUBY(J)**2
VY2B(J)=SVY2(J)/FIN-DVBY(J)**2
WY2B(J)=SWY2(J)/FIN-DWBY(J)**2
UYVYB(J)=SUYVY(J)/FIN-DUBY(J)*DVBY(J)
UYWYB(J)=SUYWY(J)/FIN-DUBY(J)*DWBY(J)
VYWYB(J)=SVYWY(J)/FIN-DVBY(J)*DWBY(J)
UV2B(J)=SUV2(J)/FIN-UBAR(J)*VSB(J)-VBAR(J)*(UVB(J)+SUV(J)/FIN)

168 CONTINUE
SXBAR=SSX/FIN
SZBAR=SSZ/FIN
SZBARA=SSZA/FIN
SZBARB=SSZB/FIN
SXS B=SSX2/FIN-SXBAR**2
S ZSB=SSZ2/FIN-SZBAR**2
S ZSBA=SSZ2A/FIN-SZBARA**2
S ZSBB=SSZ2B/FIN-SZBARB**2
SXBAR=SXBAR*ACON
SXS B=SQRT(SXSB)*ACON
SZBAR=SZBAR*ACON
SZBARA=SZBARA*ACON
SZBARB=SZBARB*ACON
S ZSB=SQRT(SZSB)*ACON
S ZSBA=SQRT(SZSBA)*ACON
S ZSBB=SQRT(SZSBB)*ACON

C
C CALCULATES THE TERMS FOR THE BALANCES OF THE
C REYNOLDS STRESS TENSOR COMPONENTS EXPRESSED IN
C WALL PARAMETERS.
C
BCON=CHVEL**3/CHLEN
DO 514 J=2,N
ADU2(J)=BCON*0.5*VBAR(J)*(USB(J+1)-USB(J-1))/TDY
PRU2(J)=-BCON*UVB(J)*DUBY(J)
TDU2(J)=-BCON*0.5*(U2VB(J+1)-U2VB(J-1))/TDY
GDU2(J)=BCON*0.5*(1./RE)*(USB(J+1)-2.*USB(J)+USB(J-1))/DY2
DISU2(J)=-BCON*(1./RE)*(UY2B(J)+UZ2B(J))
ADV2(J)=BCON*0.5*VBAR(J)*(VSB(J+1)-VSB(J-1))/TDY
PRV2(J)=-BCON*VSB(J)*DVBY(J)
TDV2(J)=-BCON*0.5*(VCB(J+1)-VCB(J-1))/TDY
PDV2(J)=-BCON*(VPB(J+1)-VPB(J-1))/TDY
GDV2(J)=BCON*0.5*(1./RE)*(VSB(J+1)-2.*VSB(J)+VSB(J-1))/DY2
DISV2(J)=-BCON*(1./RE)*(VY2B(J)+VZ2B(J))

```

```

ADW2(J)=BCON*0.5*VBAR(J)*(WSB(J+1)-WSB(J-1))/TDY
PRW2(J)=-BCON*VWB(J)*DWBY(J)
TDW2(J)=-BCON*0.5*(VW2B(J+1)-VW2B(J-1))/TDY
GDW2(J)=BCON*0.5*(1./RE)*(WSB(J+1)-2.*WSB(J)+WSB(J-1))/DY2
DISW2(J)=-BCON*(1./RE)*(WY2B(J)+WZ2B(J))
ADUV(J)=BCON*VBAR(J)*(UVB(J+1)-UVB(J-1))/TDY
PRUV(J)=-BCON*(VSB(J)*DUBY(J)+UVB(J)*DVBY(J))
TDUV(J)=-BCON*(UV2B(J+1)-UV2B(J-1))/TDY
PDUV(J)=-BCON*(UPB(J+1)-UPB(J-1))/TDY
GDUV(J)=BCON*(1./RE)*(UVB(J+1)-2.*UVB(J)+UVB(J-1))/DY2
DISUV(J)=-BCON*(2./RE)*(UYVYB(J)+UZVZB(J))
ADUW(J)=BCON*VBAR(J)*(UWB(J+1)-UWB(J-1))/TDY
PRUW(J)=-BCON*(VWB(J)*DUBY(J)+UVB(J)*DWBY(J))
TDUW(J)=-BCON*(UVWB(J+1)-UVWB(J-1))/TDY
GDUW(J)=BCON*(1./RE)*(UWB(J+1)-2.*UWB(J)+UWB(J-1))/DY2
DISUW(J)=-BCON*(2./RE)*(UYWYB(J)+UZWZB(J))
ADVW(J)=BCON*VBAR(J)*(VWB(J+1)-VWB(J-1))/TDY
PRVW(J)=-BCON*(VWB(J)*DVBY(J)+VSB(J)*DWBY(J))
TDVW(J)=-BCON*(V2WB(J+1)-V2WB(J-1))/TDY
PDVW(J)=-BCON*(WPB(J+1)-WPB(J-1))/TDY
PVZWY(J)=BCON*(PVZB(J)+PWYB(J))
GDVW(J)=BCON*(1./RE)*(VWB(J+1)-2.*VWB(J)+VWB(J-1))/DY2
DISVW(J)=-BCON*(2./RE)*(VYWYB(J)+VZWZB(J))
PMU2(J)=BCON*UVB(J)*DUBY(J)
PRW(J)=-UBAR(J)*PPLUS*CHVEL
TRS(J)=-BCON*(UVU(J+1)-UVU(J-1))/TDY
TVS(J)=BCON*(1/RE)*(UDU(J+1)-UDU(J-1))/TDY
DISM(J)=-BCON*(1/RE)*DUDU(J)
UDUV(J)=-BCON*UBAR(J)*(UVB(J+1)-UVB(J-1))/TDY
514 CONTINUE
ADU2(1)=BCON*0.5*VBAR(1)*(4.*USB(2)-USB(3))/TDY
PRU2(1)=-BCON*UVB(1)*DUBY(1)
TDU2(1)=-BCON*0.5*(4.*U2VB(2)-U2VB(3))/TDY
GDU2(1)=BCON*0.5*(1./RE)*(2.*USB(1)-5.*USB(2)+4.*USB(3)-USB(4))/
$DY2
DISU2(1)=-BCON*(1./RE)*(UY2B(1)+UZ2B(1))
PMU2(1)=BCON*UVB(1)*DUBY(1)
PRW(1)=-UBAR(1)*PPLUS*CHVEL
TRS(1)=-BCON*(4*UVU(2)-UVU(3))/TDY
TVS(1)=BCON*(1/RE)*(4*UDU(2)-UDU(3))/TDY
DISM(1)=-BCON*(1/RE)*DUDU(1)
UDUV(1)=-BCON*UBAR(1)*(4*UDUV(2)-UDUV(3))/TDY
ADU2(NP1)=BCON*0.5*VBAR(NP1)*(3.*USB(NP1)-4.*USB(N)+USB(NM1))/TDY
PRU2(NP1)=-BCON*UVB(NP1)*DUBY(NP1)
TDU2(NP1)=-BCON*0.5*(3.*U2VB(NP1)-4.*U2VB(N)+U2VB(NM1))/TDY
GDU2(NP1)=BCON*0.5*(1./RE)*(2.*USB(NP1)-5.*USB(N)+4.*USB(NM1)-
$USB(NM2))/DY2
DISU2(NP1)=-BCON*(1./RE)*(UY2B(NP1)+UZ2B(NP1))
PMU2(NP1)=BCON*UVB(NP1)*DUBY(NP1)
PRW(NP1)=-UBAR(NP1)*PPLUS*CHVEL
TRS(NP1)=-BCON*(3*UVU(NP1)-4*UVU(N)+UVU(NM1))/TDY
TVS(NP1)=BCON*(1/RE)*(3*UDU(NP1)-4*UDU(N)+UDU(NM1))/TDY
DISM(NP1)=-BCON*(1/RE)*DUDU(NP1)
UDUV(NP1)=-BCON*UBAR(NP1)*(3*UDUV(NP1)-4*UDUV(N)+UDUV(NM1))/TDY
ADV2(1)=BCON*0.5*VBAR(1)*(4.*VSB(2)-VSB(3))/TDY

```

```

PRV2(1)=-BCON*VSB(1)*DVBY(1)
TDV2(1)=-BCON*0.5*(4.*VCB(2)-VCB(3))/TDY
PDV2(1)=-BCON*(4.*VPB(2)-VPB(3))/TDY
GDV2(1)=BCON*0.5*(1./RE)*(2.*VSB(1)-5.*VSB(2)+4.*VSB(3)-VSB(4))/
$DY2
DISV2(1)=-BCON*(1./RE)*(VY2B(1)+VZ2B(1))
ADV2(NP1)=BCON*0.5*VBAR(NP1)*(3.*VSB(NP1)-4.*VSB(N)+VSB(NM1))/TDY
PRV2(NP1)=-BCON*VSB(NP1)*DVBY(NP1)
TDV2(NP1)=-BCON*0.5*(3.*VCB(NP1)-4.*VCB(N)+VCB(NM1))/TDY
PDV2(NP1)=-BCON*(3.*VPB(NP1)-4.*VPB(N)+VPB(NM1))/TDY
GDV2(NP1)=BCON*0.5*(1./RE)*(2.*VSB(NP1)-5.*VSB(N)+4.*VSB(NM1)-
$VSB(NM2))/DY2
DISV2(NP1)=-BCON*(1./RE)*(VY2B(NP1)+VZ2B(NP1))
ADW2(1)=BCON*0.5*VBAR(1)*(4.*WSB(2)-WSB(3))/TDY
PRW2(1)=-BCON*VWB(1)*DWBY(1)
TDW2(1)=-BCON*0.5*(4.*VW2B(2)-VW2B(3))/TDY
GDW2(1)=BCON*0.5*(1./RE)*(2.*WSB(1)-5.*WSB(2)+4.*WSB(3)-WSB(4))/
$DY2
DISW2(1)=-BCON*(1./RE)*(WY2B(1)+WZ2B(1))
ADW2(NP1)=BCON*0.5*VBAR(NP1)*(3.*WSB(NP1)-4.*WSB(N)+WSB(NM1))/TDY
PRW2(NP1)=-BCON*VWB(NP1)*DWBY(NP1)
TDW2(NP1)=-BCON*0.5*(3.*VW2B(NP1)-4.*VW2B(N)+VW2B(NM1))/TDY
GDW2(NP1)=BCON*0.5*(1./RE)*(2.*WSB(NP1)-5.*WSB(N)+4.*WSB(NM1)-
$WSB(NM2))/DY2
DISW2(NP1)=-BCON*(1./RE)*(WY2B(NP1)+WZ2B(NP1))
ADUV(1)=BCON*VBAR(1)*(4.*UVB(2)-UVB(3))/TDY
PRUV(1)=-BCON*(VSB(1)*DUBY(1)+UVB(1)*DVBY(1))
TDUV(1)=-BCON*(4.*UV2B(2)-UV2B(3))/TDY
PDUV(1)=-BCON*(4.*UPB(2)-UPB(3))/TDY
GDUV(1)=BCON*(1./RE)*(2.*UVB(1)-5.*UVB(2)+4.*UVB(3)-UVB(4))/DY2
DISUV(1)=-BCON*(2./RE)*(UYVYB(1)+UZVZB(1))
ADUV(NP1)=BCON*VBAR(NP1)*(3.*UVB(NP1)-4.*UVB(N)+UVB(NM1))/TDY
PRUV(NP1)=-BCON*(VSB(NP1)*DUBY(NP1)+UVB(NP1)*DVBY(NP1))
TDUV(NP1)=-BCON*(3.*UV2B(NP1)-4.*UV2B(N)+UV2B(NM1))/TDY
PDUV(NP1)=-BCON*(3.*UPB(NP1)-4.*UPB(N)+UPB(NM1))/TDY
GDUV(NP1)=BCON*(1./RE)*(2.*UVB(NP1)-5.*UVB(N)+4.*UVB(NM1)-UVB(NM2))
$)/DY2
DISUV(NP1)=-BCON*(2./RE)*(UYVYB(NP1)+UZVZB(NP1))
ADUW(1)=BCON*VBAR(1)*(4.*UWB(2)-UWB(3))/TDY
PRUW(1)=-BCON*(VWB(1)*DUBY(1)+UVB(1)*DWBY(1))
TDUW(1)=-BCON*(4.*UVWB(2)-UVWB(3))/TDY
GDUW(1)=BCON*(1./RE)*(2.*UWB(1)-5.*UWB(2)+4.*UWB(3)-UWB(4))/DY2
DISUW(1)=-BCON*(2./RE)*(UYWYB(1)+UZWZB(1))
ADUW(NP1)=BCON*VBAR(NP1)*(3.*UWB(NP1)-4.*UWB(N)+UWB(NM1))/TDY
PRUW(NP1)=-BCON*(VWB(NP1)*DUBY(NP1)+UVB(NP1)*DWBY(NP1))
TDUW(NP1)=-BCON*(3.*UVWB(NP1)-4.*UVWB(N)+UVWB(NM1))/TDY
GDUW(NP1)=BCON*(1./RE)*(2.*UWB(NP1)-5.*UWB(N)+4.*UWB(NM1)-UWB(NM2))
$)/DY2
DISUW(NP1)=-BCON*(2./RE)*(UYWYB(NP1)+UZWZB(NP1))
ADVW(1)=BCON*VBAR(1)*(4.*VWB(2)-VWB(3))/TDY
PRVW(1)=-BCON*(VWB(1)*DVBY(1)+VSB(1)*DWBY(1))
TDVW(1)=-BCON*(4.*V2WB(2)-V2WB(3))/TDY
PDVW(1)=-BCON*(4.*WPB(2)-WPB(3))/TDY
PVZFY(1)=BCON*(PVZB(1)+PWYB(1))
GDVW(1)=BCON*(1./RE)*(2.*VWB(1)-5.*VWB(2)+4.*VWB(3)-VWB(4))/TDY

```

```

DISVW(1)=-BCON*(2./RE)*(VYWYB(1)+VZWZB(1))
ADVW(NP1)=BCON*VBAR(NP1)*(3.*VWB(NP1)-4.*VWB(N)+VWB(NM1))/TDY
PRVW(NP1)=-BCON*(VWB(NP1)*DVBY(NP1)+VSB(NP1)*DWBY(NP1))
TDVW(NP1)=-BCON*(3.*V2WB(NP1)-4.*V2WB(N)+V2WB(NM1))/TDY
PDVW(NP1)=-BCON*(3.*WPB(NP1)-4.*WPB(N)+WPB(NM1))/TDY
PVZWY(NP1)=BCON*(PVZB(NP1)+PWYB(NP1))
GDVW(NP1)=BCON*(1./RE)*(2.*VWB(NP1)-5.*VWB(N)+4.*VWB(NM1)-VWB(NM2)
$)/DY2
DISVW(NP1)=-BCON*(2./RE)*(VYWYB(NP1)+VZWZB(NP1))

C
C      CALCULATES STATISTICAL QUANTITIES LOCALLY
C      AND IN WALL PARAMETERS
C
ZINTW(1)=SQRT(ZSB(1))*ACON
PINTW(1)=SQRT(PSB(1))*CHVEL**2
UINTL(1)=SXSB/SXBAR
VINTL(1)=0.
WINTL(1)=SZSB/SXBAR
UINTW(1)=0.
VINTW(1)=0.
WINTW(1)=0.
UVWALL(1)=0.
UWWALL(1)=0.
VWWALL(1)=0.
UBAR(1)=0.
VBAR(1)=0.
WBAR(1)=0.
PUZB(1)=BCON*PUZB(1)
PWZB(1)=BCON*PWZB(1)
PUYB(1)=BCON*PUYB(1)
PVYB(1)=BCON*PVYB(1)
DO 225 J=2,NP1
ZINTW(J)=SQRT(ZSB(J))*ACON
PINTW(J)=SQRT(PSB(J))*CHVEL**2
UINTL(J)=SQRT(USB(J))/UBAR(J)
VINTL(J)=SQRT(VSB(J))/UBAR(J)
WINTL(J)=SQRT(WSB(J))/UBAR(J)
UINTW(J)=SQRT(USB(J))*CHVEL
VINTW(J)=SQRT(VSB(J))*CHVEL
WINTW(J)=SQRT(WSB(J))*CHVEL
USQ(J-1)=UCB(J)/USB(J)**1.5
VSQ(J-1)=VCB(J)/VSB(J)**1.5
WSQ(J-1)=WCB(J)/WSB(J)**1.5
UFL(J-1)=UFB(J)/USB(J)**2
VFL(J-1)=VFB(J)/VSB(J)**2
WFL(J-1)=WFB(J)/WSB(J)**2
UVCOR(J-1)=UVB(J)/SQRT(USB(J)*VSB(J))
UWCOR(J-1)=UWB(J)/SQRT(USB(J)*WSB(J))
VWCOR(J-1)=VWB(J)/SQRT(VSB(J)*WSB(J))
UVWALL(J)=UVB(J)*CHVEL**2
UWWALL(J)=UWB(J)*CHVEL**2
VWWALL(J)=VWB(J)*CHVEL**2
UBAR(J)=UBAR(J)*CHVEL
VBAR(J)=VBAR(J)*CHVEL
WBAR(J)=WBAR(J)*CHVEL

```

```
PUZB(J)=BCON*PUZB(J)
PWZB(J)=BCON*PWZB(J)
PUYB(J)=BCON*PUYB(J)
PVYB(J)=BCON*PVYB(J)

225 CONTINUE

C
C     PRINTS DATPL FILE
C
IF(VAX.EQ.0)OPEN(36,FILE='DPLO',FI=S,RE=V,FM=U',
$STATUS='NEW')
IF(VAX.EQ.1)OPEN(36,FILE='DPLO',STATUS='NEW')
WRITE(36) UINTL
WRITE(36) VINTL
WRITE(36) WINTL
WRITE(36) UINTW
WRITE(36) VINTW
WRITE(36) WINTW
WRITE(36) UVWALL
WRITE(36) UWWALL
WRITE(36) VWWALL
WRITE(36) UBAR
WRITE(36) VBAR
WRITE(36) WBAR
WRITE(36) USQ
WRITE(36) VSQ
WRITE(36) WSQ
WRITE(36) UFL
WRITE(36) VFL
WRITE(36) WFL
WRITE(36) UVCOR
WRITE(36) UWCOR
WRITE(36) VWCOR
WRITE(36) ADU2
WRITE(36) PRU2
WRITE(36) TDU2
WRITE(36) GDU2
WRITE(36) DISU2
WRITE(36) ADV2
WRITE(36) PRV2
WRITE(36) TDV2
WRITE(36) PDV2
WRITE(36) GDV2
WRITE(36) DISV2
WRITE(36) ADW2
WRITE(36) PRW2
WRITE(36) TDW2
WRITE(36) GDW2
WRITE(36) DISW2
WRITE(36) PRW
WRITE(36) PMU2
WRITE(36) TRS
WRITE(36) TVS
WRITE(36) DISM
WRITE(36) UDUV
WRITE(36) ADUV
```

```
WRITE(36) PRUV
WRITE(36) TDUV
WRITE(36) PDUV
WRITE(36) GDUV
WRITE(36) DISUV
WRITE(36) ADUW
WRITE(36) PRUW
WRITE(36) TDUW
WRITE(36) GDUW
WRITE(36) DISUW
WRITE(36) ADVW
WRITE(36) PRVW
WRITE(36) TDVW
WRITE(36) PDVW
WRITE(36) PVZWY
WRITE(36) GDVW
WRITE(36) DISVW
WRITE(36) PUYB
WRITE(36) PVYB
WRITE(36) PUZB
WRITE(36) PWZB
WRITE(36) PINTW
WRITE(36) ZINTW
RETURN
END
```

APPENDIX III. Pulsating Pressure Gradient Program

```

PROGRAM MAIN
IMPLICIT DOUBLE PRECISION (A-H,O-Z)
IMPLICIT INTEGER*4 (I-N)
DIMENSION YP(0:500),UPN(0:500),BY(0:500)
DIMENSION UPN1(0:500),CP(0:500),UP0(0:500),TAUPN1(0:500)
DIMENSION TURBKV(0:500),DY(0:500),TAUL(1:71)
DIMENSION UA(0:500),UT(1:71,0:300),TAUT(1:71,0:300),Z(71)
DIMENSION PPT(0:100000),AP(0:100000),TEMP(1:501),YPP1(1:501)
DIMENSION UMAG(0:300),UANG(0:300),TAUMAG(0:300),TAUANG(0:300)
DIMENSION B1(0:500),B2(0:500),B3(0:500)
REAL*8 H,KAPPA,KV,K1,KR,MAG
COMMON/ALL/RP,NT,NT1,WP,TP,DTP,H,NJ,NJ1,DYP1,PI
COMMON/ PARA/KAPPA,APA,YOO,K1,KR
COMMON/ ONE/A1,A2,A3,B1,B2,B3,D4,D5,E1,E2,E3
C
C
C-----  

C          INPUT
C      V = 0 PROGRAM TO BE RUN ON THE VAX
C          1 PROGRAM TO BE RUN ON THE AP
C
C      DTP:
C
C-----  

C      READ*,V
C      IF(V.EQ.1)OPEN(11,FILE=
C      $':HOSTCHAR:DRA3:[240016.EMP.STORE]OSC.DAT'
C      $,STATUS='NEW',FORM='FORMATTED')
C      WRITE(11,1200)V
C      WRITE(6,1200)V
C      READ*,DTP,DYP1,DYPL,INCY
C      WRITE(11,1035)DTP,DYP1,DYPL,INCY
C      WRITE(6,1035)DTP,DYP1,DYPL,INCY
C      READ*,TAUW,WP,AV,YOO,K1,KR
C      WRITE(11,1020)TAUW,WP,AV,YOO,K1,KR
C      WRITE(6,1020)TAUW,WP,AV,YOO,K1,KR
C
C      AV = 0.1
C      K1 = -25
C      KR = 3500
C      YOO = 40.
C      PI = 4.*DATAN(1.D0)
C      KAPPA = 0.41D0
C      APA = 26.D0
C      KV = 0.00886D0
C      ROE = 1.0D0
C      W = WP*TAUW/(ROE*KV)
C      R = 2.54D0
C      F = W / 2.*PI
C      USTAR = DSQRT(TAUW/ROE)

```

```

RP = R*USTAR/KV
PPA = 2./RP
STOKE = DSQRT(2.*KV/W)
STOKEP = USTAR * STOKE / KV
VISLEN = KV/USTAR

C-----
C DETERMINE NT AND NJ SUCH THAT NT/INCT IS AN INTEGER
C AND NJ/INCY IS AN INTEGER
C-----
INCT = 70
H = 1 + (DYP1/RP)*(DYPL/DYP1-1)
NJ = DLOG(DYPL/DYP1)/DLOG(H)
NJJ = IDNINT(DFLOAT(NJ/INCY))
NJ = NJJ * INCY
DYP1 = RP * (H-1) / (H**NJ-1)
DYPL = DYP1 * H**NJ
NJ1 = NJ + 1
DO 50 J=0,NJ
YP(J) = DYP1 * ((H**J)-1.) / (H-1.)
50 CONTINUE
TP = 2.*PI/WP
NT = TP / DTP
ND = IDNINT(DFLOAT(NT/INCT))
NT = ND * INCY
DTP = TP / DFLOAT(NT)
NT1 = NT + 1
DT = DTP * (ROE*KV) / TAUW

C-----
WRITE(11,1000)TAUW,USTAR,PPA,RP,STOKEP,VISLEN
WRITE(6,1000)TAUW,USTAR,PPA,RP,STOKEP,VISLEN
WRITE(11,1040)DTP,DYP1,DYPL,NT,NJ,H
WRITE(6,1040)DTP,DYP1,DYPL,NT,NJ,H
WRITE(11,1045)INCT,NJ/INCY
WRITE(6,1045)INCT,NJ/INCY

C
C
C
C-----INITIALIZATION-----
C**** SET UP COMMON ONE ****
A1 = -H / (DYP1*(H+1.))
A2 = (H-1) / (DYP1*H)
A3 = 1. / (DYP1 * H * (H+1))
DO 45 J=1,NJ-1
B1(J) = (RP-YP(J-1)) / ((RP-YP(J)) * H**((J-1)))
B2(J) = (RP-YP(J)) / ((RP-YP(J)) * H**((J-1)))
B3(J) = (RP-YP(J+1)) / ((RP-YP(J)) * H**((J-1)))
45 CONTINUE
D1 = YP(NJ) - YP(NJ-1)
D2 = YP(NJ-1) - YP(NJ-2)
D3 = YP(NJ) - YP(NJ-2)
D4 = D3**2/(D2*(D1+D3))
D5 = D1**2/(D2*(D1+D3))
E1 = YP(2)*YP(3)/(YP(1)*(YP(1)-YP(2))*(YP(1)-YP(3)))
E2 = YP(1)*YP(3)/(YP(2)*(YP(2)-YP(1))*(YP(2)-YP(3)))
E3 = YP(1)*YP(2)/(YP(3)*(YP(3)-YP(1))*(YP(3)-YP(2)))

```

```

C*****
C
      CALL INIT(YP,AV,AMPP,UPO,BY,YPP1,TEMP,TURBKV,CP,C1,C2)
      DO 80 N=0,NT
      PPF = AMPP * DCOS(2.*PI*DTP*DFLOAT(N)/TP)
      PPT(N) = PPA + PPF
      AP(N) = APA * (1.+K1*(-1*PPF))
 80 CONTINUE
      IF(KR.NE.0.DO .AND. K1.NE.0.DO)CALL PEFF(PPA,PPT,AP)
      FINAL = 0.DO
      NCOUNT = 0
      DO 100 J=0,NJ
      UPN(J) = UPO(J)
      TAUPN1(J) = 2.
 100 CONTINUE
C-----BEGINNING OF OUTER LOOP-----
      LOOP = 0.0
      DO 200 LO=1,15
      LOOP = LOOP + 1
      IF(FINAL.EQ.1.DO)GOTO 265
      DO 260 J=0,NJ
      UA(J) = 0.0
 260 CONTINUE
 265 CONTINUE
C-----BEGINNING OF INNER LOOP-----
      DO 300 LI=1,NT
      CALL USOLVE(YP,PPT(LI-1),TURBKV,UPN,CP,UPN1)
      CALL LOGTAU(YP,BY,AP(LI),C1,C2,CP,TAULOG,NK)
      CALL TAU(NK,TAULOG,AP(LI),YP,BY,TURBKV,CP,TAUPN1)
      IF(FINAL.NE.1.DO)GOTO 280
      NCOUNT = NCOUNT + 1
      IF(ND.NE.NCOUNT)GOTO 280
      TAUL(LI/ND+1) = TAULOG
      NCOUNT = 0
      DO 270 J=0,NJ,INCY
      UT(LI/ND+1,J/INCY) = UPN1(J)
      TAUT(LI/ND+1,J/INCY) = TAUPN1(J)
 270 CONTINUE
 280 CONTINUE
      DO 305 J=0,NJ
      IF(FINAL.EQ.1.DO)UA(J) = UA(J) + UPN1(J)
      UPN(J) = UPN1(J)
 305 CONTINUE
 300 CONTINUE
C-----END OF INNER LOOP-----
      DELTA = 0.ODO
      DO 400 J=0,NJ
      IF(FINAL.EQ.1.DO)UA(J) = UA(J) / DFLOAT(NT)
      DIFF = DABS(UPN1(J) - UPO(J))
      IF(DIFF.GT.DELTA)DELTA = DIFF
      UPO(J) = UPN1(J)
 400 CONTINUE
      WRITE(11,1240)LOOP,DELTA
      WRITE(6,1240)LOOP,DELTA
      IF(V.EQ.1)OPEN(99,FILE=

```

```

$' :HOSTCHAR:DRA3:[240016.EMP.STORE]LOOP.DAT'
$,STATUS='NEW',FORM='FORMATTED')
WRITE(99,1210)LOOP,DELTA,UPO(2),UPO(3),UPO(NJ-1),UPO(NJ)
CLOSE(99)
IF(FINAL.EQ.1.DO)GOTO 600
IF(DELTA.LE.0.03)FINAL =1.DO
200 CONTINUE
WRITE(11,1220)
WRITE(6,1220)
STOP
600 CONTINUE
WRITE(11,1230)LO-1
WRITE(6,1230)LO-1
C-----END OF OUTER LOOP-----
C
      IF(V.EQ.1)OPEN(51,FILE=' :HOSTCHAR:DRA3:[240016.EMP.STORE]LOG.DAT'
$,STATUS='NEW',FORM='FORMATTED')
      TAUL(1) = TAUL(INCT+1)
      DO 290 N=1,INCT+1
      WRITE(51,1250)N*360./DFLOAT(INCT+1),TAUL(N)
      Z(N) = TAUL(N)
290 CONTINUE
CLOSE(51)
CALL EFIT(9999.,INCT+1,TEMP,Z,AMAG,ANGD)
WRITE(11,1030)AMAG,ANGD
WRITE(6,1030)AMAG,ANGD
DO 650 J=0,NJ/INCY
UT(1,J) = UT(INCT+1,J)
TAUT(1,J) = TAUT(INCT+1,J)
650 CONTINUE
DO 700 J=1,NJ1
TEMP(J) = (2./RP) * UA(J-1) * (1.-YPP1(J)/RP)
700 CONTINUE
CALL INTEG(YPP1,TEMP,NJ1,1,1,0,UBULK,IRROR)
UCP = UA(NJ)
WRITE(11,1055)UCP,UBULK,UBULK/UCP
WRITE(6,1055)UCP,UBULK,UBULK/UCP
RE = 2.*RP*UBULK
WRITE(11,1050)TAUW,RE
WRITE(6,1050)TAUW,RE
C-----
C      DETERMINES THE NORMALIZED WALL SHEAR STRESS, THE
C      PHASE OF THE WALL SHEAR STRESS, THE PHASE OF UC,
C      AND THE AMPLITUDE OF THE CENTER VELOCITY VARIATION
C-----
      DO 705 I=1,INCT+1
      Z(I) = UT(I,NJ/INCY)
705 CONTINUE
CALL EFIT(9999.,INCT+1,TEMP,Z,AMAG,ANGD)
UMAG(NJ/INCY) = AMAG
UANG(NJ/INCY) = ANGD
DO 710 I=1,INCT+1
Z(I) = TAUT(I,0)
710 CONTINUE
CALL EFIT(9999.,INCT+1,TEMP,Z,AMAG,ANGD)

```

```

TAUMAG(0) = AMAG
TAUANG(0) = ANGD
CAMP = UMAG(NJ/INCY) / UCP
TAUAMP = TAUMAG(0) / UMAG(NJ/INCY)
WRITE(11,1090)W,WP
WRITE(6,1090)W,WP
WRITE(11,1100)CAMP,UANG(NJ/INCY),TAUAMP
$,TAUANG(0),TAUANG(0)-UANG(NJ/INCY)
WRITE(6,1100)CAMP,UANG(NJ/INCY),TAUAMP,TAUANG(0)
$,TAUANG(0)-UANG(NJ/INCY)
CLOSE(11)

C-----
C      OUPUT OF U VELOCITY INFORMATION
C-----

      IF(V.EQ.1)OPEN(31,FILE=':HOSTCHAR:DRA3:[240016.EMP.STORE]UA.DAT',
$STATUS='NEW',FORM='FORMATTED')
      DO 720 J=0,NJ
      WRITE(31,1060)YP(J)/RP,UA(J)
720 CONTINUE
      CLOSE(31)
      DO 730 J=1,NJ/INCY
      DO 740 I=1,INCT+1
      Z(I) = UT(I,J)
740 CONTINUE
      CALL EFIT(YP(J*INCY),INCT+1,TEMP,Z,AMAG,ANGD)
      UMAG(J) = AMAG
      UANG(J) = ANGD
730 CONTINUE
      IF(V.EQ.1)OPEN(32,FILE=':HOSTCHAR:DRA3:[240016.EMP.STORE]UMAG.DAT',
$STATUS='NEW',FORM='FORMATTED')
      IF(V.EQ.1)OPEN(33,FILE=':HOSTCHAR:DRA3:[240016.EMP.STORE]UANG.DAT',
$STATUS='NEW',FORM='FORMATTED')
      UMAG(0) = 0.D0
      UANG(0) = UANG(1)-YP(INCY)*(UANG(2)-UANG(1))/(YP(2*INCY)-YP(INCY))
      DO 750 J=0,NJ/INCY
      WRITE(32,1070)YP(J*INCY)/RP,UMAG(J)/UMAG(NJ/INCY)
      WRITE(33,1080)YP(J*INCY)/RP,UANG(J)
750 CONTINUE
      CLOSE(32)
      CLOSE(33)

C-----
C      OUTPUT OF SHEAR STRESS INFORMATION
C-----

      DO 830 J=0,NJ/INCY-1
      DO 840 I=1,INCT+1
      Z(I) = TAUT(I,J)
840 CONTINUE
      CALL EFIT(YP(J*INCY),INCT+1,TEMP,Z,AMAG,ANGD)
      TAUMAG(J) = AMAG
      TAUANG(J) = ANGD
830 CONTINUE
      IF(V.EQ.1)OPEN(41,FILE=
$':HOSTCHAR:DRA3:[240016.EMP.STORE]TMAG.DAT'
$STATUS='NEW',FORM='FORMATTED')
      IF(V.EQ.1)OPEN(42,FILE=

```

```

$' :HOSTCHAR:DRA3:[240016.EMP.STORE]TANG.DAT'
$, STATUS= 'NEW', FORM= 'FORMATTED')
TAUMAG(NJ/INCY) = 0.0D0
DO 850 J=0,NJ/INCY
WRITE(41,1070)YP(J*INCY)/RP,TAUMAG(J)
IF(J .NE. NJ/INCY)WRITE(42,1080)YP(J*INCY)/RP,TAUANG(J)
850 CONTINUE
CLOSE(41)
CLOSE(42)
1000 FORMAT(' WALL SHEAR STRESS =',F8.4,/, ' FRICTION VELOCITY =',F8.4,/,
'$' TIME-AVERAGE PRESSURE GRADIENT=',F10.5,/.
'$' R+=',F8.3,/
'$' STOKE+',F5.1,/, ' VIS. LENGTH =',F5.4)
1020 FORMAT(' ENTER TAUW,WP',/,1X,2(3X,F8.4))
1030 FORMAT(' MAG. OF SHEAR STRESS AT Y0+',F6.4,/
$, ' PHASE OF SHEAR STRESS AT Y0+',F6.1)
1035 FORMAT(' ENTER INITIAL DTP,DYP1,DYPL AND INCY',/,1X,
$3(3X,F6.3),2X,I3)
1040 FORMAT(1X,'DTP=',F5.3,' DYP1=',F5.3,' DYPL=',F5.2,/,
'$' NT=',I6,' NJ=',I4,' H=',F6.4)
1045 FORMAT(1X,'TIME PLOTTING INC.=',I3,' Y PLOTTING INC.=',I3)
1050 FORMAT(1X,'TAUW=',F7.3,' FINAL RE=',F6.0)
1055 FORMAT(1X,'TIME-AVERAGE CENTERLINE VELOCITY=',F5.2,/,
'$' TIME-AVERAGE BULK VELOCITY=',F5.2,/
'$' RATIO OF UB/UC=',F5.3)
1060 FORMAT(1X,F8.3,2X,F6.3)
1070 FORMAT(1X,F8.3,2X,F8.5)
1080 FORMAT(1X,F8.3,2X,F6.1)
1090 FORMAT(' FREQUENCY=',F8.4,/
'$' DIMENSIONLESS FREQUENCY=',F7.4)
1100 FORMAT(' AMP. OF THE CENTER OSC. VELOCITY=',F6.3,/, 
'$' PHASE OF THE CENTER OSC. VELOCITY=',F6.1,/, 
'$' AMP. OF THE NORM. OSC. WALL SHEAR STRESS=',F6.3,/, 
'$' PHASE OF THE OSC. WALL SHEAR STRESS=',F6.1,/, 
'$' PHASE OF THE OSC. WALL SHEAR STRESS RELATIVE TO UC=',F6.1)
1200 FORMAT(' ENTER 0=VAX,1=AP',1X,F3.1)
1210 FORMAT(' OUTER LOOP=',I2,' DELTA=',F10.5,/, 
'$' UPO(2)=',F8.4,' UPO(3)=',F8.4,/, 
'$' UPO(NJ-1)=',F8.4,' UPO(NJ)=',F8.4)
1220 FORMAT(' OUTER LOOP DID NOT CONVERGE')
1230 FORMAT(' OUTER LOOP CONVERGED AT ITERATION #',I2)
1240 FORMAT(' LOOP=',I3,' DELTA=',F6.4)
STOP
1250 FORMAT(1X,F5.1,1X,F7.4)
END

```

```

SUBROUTINE INIT(YP,AV,AMPP,UPO,BY,YPP1,TEMP,TURBKV,
$CP,C1,C2)
IMPLICIT DOUBLE PRECISION (A-H,O-Z)
DIMENSION YP(0:NJ),BY(0:NJ),UPO(0:NJ),CP(0:NJ)
DIMENSION TEMP(1:NJ1),YPP1(1:NJ1),TURBKV(0:NJ)
COMMON/ALL/RP,NT,NT1,WP,TP,DTP,H,NJ,NJ1,DYP1,PI
COMMON/ PARA/KAPPA,APA,YOO,K1,KR
REAL*8 KAPPA,K1,KR

```

```

C
C
TAULOG = 1. - YOO/RP
DO 100 J=0,NJ
YPP1(J+1) = YP(J)
Z = YP(J)/RP
BY(J) = ((KAPPA*YP(J)*2./3.)*(1.-Z/2.) * (3.-4.*Z+2.*Z**2))**2
TAU = 1.-Z
IF(TAU .LT. TAULOG)TAU = TAULOG
E = (1.-DEXP(-YP(J) * DSQRT(TAULOG) / APA))**2
TURBKV(J) = 0.5 * (-1. + DSQRT(1.+TAU*BY(J)*E))
TEMP(J+1) = (1.-Z)/(1.+TURBKV(J))
100 CONTINUE
Z = YOO/RP
B = ((1.-Z/2.) * (3.-4.*Z+2.*Z**2))**2
TAU00 = 1.-Z
A = (4./9.) * TAU00 * (KAPPA*YOO)**2
D = -YOO * DSQRT(TAU00)/APA
E = (1.-DEXP(D))**2
C1 = 0.5 * (-1. + DSQRT(1.+A*B*E))
C2 = C1 - 1.

C
C**** NOTE: TO USE INTEG QUANTITIES MUST GO FROM 1:NJ1
C
UPO(0) = 0.0
UPO(1) = DYP1 * (TEMP(2)+TEMP(1))/2.
DO 200 J=3,NJ1
CALL INTEG(YPP1,TEMP,J,1,1,0,UPP1,IRROR)
IF(IRROR.EQ.2)WRITE(11,1200)
IF(IRROR.EQ.2)WRITE(6,1200)
1200 FORMAT(' ERROR 2 IS GENERATED')
UPO(J-1) = UPP1
200 CONTINUE
DO 250 J=1,NJ1
TEMP(J) = (2./RP) * UPO(J-1) * (1.-YP(J-1)/RP)
250 CONTINUE
CALL INTEG(YPP1,TEMP,NJ1,1,1,0,UBP,IRROR)
UCP = UPO(NJ)
RE = 2.*RP*UBP
AMPP = WP*AV*UCP
WRITE(6,1000)RE,UBP,UCP,AMPP
WRITE(11,1000)RE,UBP,UCP,AMPP
1000 FORMAT(' INITIAL RE=',F7.0,/, ' INITIAL UB+=',F6.2,/,,
$' INITIAL UC+=',F6.2,/, ' INITIAL A+=',F10.6)
WRITE(6,1010)C1,C2
WRITE(11,1010)C1,C2
1010 FORMAT(1X,'LOG CONSTANTS FOR THIS RUN (C1,C2) =',2(1X,F5.2))
C
C
A1 = -H / (DYP1*(H+1.))
A2 = (H-1) / (DYP1*H)
A3 = 1. / (DYP1 * H * (H+1))
D1 = YP(2) - YP(1)
D2 = YP(1) - YP(0)
D3 = YP(2) - YP(0)

```

```

CP(0) = UP0(1)*D3/(D1*D2) - UP0(2)*D2/(D1*D3)
DO 300 J=1,NJ-1
  CP(J) = (A1*UP0(J-1) + A2*UP0(J) + A3*UP0(J+1))
  $/ H**(J-1)
300 CONTINUE
  CP(NJ) = 0.0D0
  RETURN
  END

```

```

SUBROUTINE PEFF(PPA,PPT,AP)
IMPLICIT DOUBLE PRECISION (A-H,O-Z)
DIMENSION PPT(0:NT),AP(0:NT)
COMMON/ALL/RP,NT,NT1,WP,TP,DTP,H,NJ,NJ1,DYP1,PI
COMMON/PARA/KAPPA,APA,YOO,K1,KR
REAL*8 KAPPA,K1,KR
C-----
C      PPE = EFFECTIVE PRESSURE GRADIENT
C      PPA = TIME-AVERAGED PRESSURE GRADIENT
C      PPT = PHASE-AVERAGED PRESSURE GRADIENT
C-----
C**** NOTE1: AP IS A DUMMY VARIABLE IN THE ITERATION LOOP. IT IS
C****      EQUAL TO THE EFFECTIVE PRESSURE GRADIENT AT N+1
C**** NOTE2: PRESSURE GRADIENTS INPUT ARE -(dP/dX). THEREFORE, THE
C****      'EFFECTIVE PRESSURE GRADIENT' IS MULTIPLIED BY -1
C****      IN THE EQUATION FOR AP
  S1 = DTP/(KR/15.)
  S2 = 1. - S1
  PPEN = PPT(0) - PPA
  DO 200 KK=1,500
    PPEOLD = PPEN
    DO 300 N=0,NT-1
      AP(N+1) = S2 * PPEN + S1 * (PPT(N)-PPA)
      PPEN = AP(N+1)
300 CONTINUE
  AP(0) = AP(NT)
  IF(PPEOLD.EQ.PPEN)GOTO 350
200 CONTINUE
  WRITE(11,1000)
  WRITE(6,1000)
1000 FORMAT(' PRESSURE ITERATION DID NOT CONVERGE')
  STOP
350 CONTINUE
  WRITE(11,1010)KK
  WRITE(6,1010)KK
1010 FORMAT(' PRESSURE ITERATION CONVERGED AT ITERATION #',I3)
  DO 400 N=0,NT
    AP(N) = APA * (1. + K1*(-1.*AP(N)))
400 CONTINUE
  RETURN
  END

```

```

SUBROUTINE USOLVE(YP,PPN,TURBV,UPN,CP,UPN1)
IMPLICIT DOUBLE PRECISION (A-H,O-Z)

```

```

DIMENSION YP(0:NJ), UPN(0:NJ)
DIMENSION CP(0:NJ), UPN1(0:NJ), TURBKV(0:NJ)
DIMENSION B1(0:500), B2(0:500), B3(0:500)
COMMON/ALL/RP, NT, NT1, WP, TP, DTP, H, NJ, NJ1, DYP1, PI
COMMON/ONE/A1, A2, A3, B1, B2, B3, D4, D5, E1, E2, E3

C
C
UPN1(0) = 0.0D0
G = DTP*PPN
DO 100 J=1,NJ-1
B11 = B1(J) * (1.+TURBKV(J-1)) * CP(J-1)
B22 = B2(J) * (1.+TURBKV(J)) * CP(J)
B33 = B3(J) * (1.+TURBKV(J+1)) * CP(J+1)
PART = DTP * (A1*B11 + A2*B22 + A3*B33)
UPN1(J) = UPN(J) + G + PART
100 CONTINUE
UPN1(NJ) = D4*UPN1(NJ-1) - D5*UPN1(NJ-2)

C
C
CP(0) = UPN1(1)*E1 + UPN1(2)*E2 + UPN1(3)*E3
DO 200 J=1,NJ-1
CP(J) = (A1*UPN1(J-1) + A2*UPN1(J) + A3*UPN1(J+1))
$/ H***(J-1)
200 CONTINUE
CP(NJ) = 0.0D0
RETURN
END

```

```

SUBROUTINE LOGTAU(YP,BY,AP,C1,C2,CP,TAULOG,NK)
IMPLICIT DOUBLE PRECISION (A-H,O-Z)
DIMENSION YP(0:NJ),CP(0:NJ),BY(0:NJ)
COMMON/ALL/RP,NT,NT1,WP,TP,DTP,H,NJ,NJ1,DYP1,PI
DO 100 J=0,NJ-1
TAUE1 = C1 * CP(J)
E = (1. - DEXP(-YP(J) * DSQRT(TAUE1) / AP))**2
TKV1 = 0.5 * (-1. + DSQRT(1. + BY(J)*TAUE1*E))
IF(TKV1 .GE. C2)NC = J-1
IF(TKV1 .GE. C2)GOTO 200
100 CONTINUE
200 CONTINUE
TAUE2 = C1 * CP(NC)
E = (1. - DEXP(-YP(NC) * DSQRT(TAUE2) / AP))**2
TKV2 = 0.5 * (-1. + DSQRT(1. + BY(NC)*TAUE2*E))
TAULOG = TAUE2 - (TAUE2-TAUE1) * (TKV2-C2)/(TKV2-TKV1)
NK = NC + 1
RETURN
END

```

```

SUBROUTINE TAU(NK,TAULOG,AP,YP,BY,TURBKV,CP,TAUPN1)
IMPLICIT DOUBLE PRECISION (A-H,O-Z)
DIMENSION YP(0:NJ),CP(0:NJ),BY(0:NJ)
DIMENSION TAUPN1(0:NJ),TURBKV(0:NJ)
COMMON/ALL/RP,NT,NT1,WP,TP,DTP,H,NJ,NJ1,DYP1,PI

```

```

COMMON/ PARA/KAPPA, APA, YOO, K1, KR
REAL*8 H, KAPPA, K1, KR
C-----
C INPUT: CP(N+1), TURBKV(N), DY, BY, TAULE
C OUTPUT: TURBKV(N+1), TAUPN1(N+1)
C-----
C MODELS WHERE THE EDDY VISCOSITY IS A FUNCTION
C IN SOME FORM OF THE LOCAL SHEAR STRESS
C-----
DO 100 J=1,NJ
TAUO = TAUPN1(J)
DO 200 K=1,100
TAUD = TAUPN1(J)
IF(J .GE. NK)TAUD = TAULOG
E = (1-DEXP(-YP(J) * DSQRT(TAUD) / AP))**2
TAUPN1(J) = CP(J)/2. * (1. + DSQRT(1.+TAUD*BY(J)*E))
IF(J .GE. NK)GOTO 250
IF(DABS(TAUPN1(J)-TAUO) .LE. 0.0001)GOTO 250
TAUO = TAUPN1(J)
200 CONTINUE
250 CONTINUE
TAUD = TAUPN1(J)
IF(J .GE. NK)TAUD = TAULOG
TURBKV(J) = -.5 + .5*DSQRT(1. + TAUD*BY(J)*E)
100 CONTINUE
TURBKV(0) = 0.0
TAUPN1(0) = CP(0)
RETURN
END

```

```

SUBROUTINE EFIT(YDIS,NP,X,Z,MAG,PHASE)
IMPLICIT DOUBLE PRECISION (A-H,O-Z)
DIMENSION A(6,6),B(6,1)
DIMENSION AMAG(3),ANGD(3),ANG(3),RAT(3)
DIMENSION Z(1:NP),X(1:NP)
REAL*8 MAG
NPPP1 = NP
NHARMO = 3
NHR = 3
N=NHARMO*2
MAX=(NPPP1/2)
PI = 4. * DATAN(1.D0)
X(1)=0.D0
DO 200 I=1,NPPP1-1
X(I+1)=I*(1./(DFLOAT(NPPP1-1)))*2*PI
200 CONTINUE
DO 88 J=1,NP-1
ZAVG = ZAVG + Z(J)
88 CONTINUE
ZAVG = ZAVG / DFLOAT(NP-1)
DO 89 J=1,NP
Z(J) = Z(J) - ZAVG
89 CONTINUE
DO 1 I=1,N

```

```

      DO 2 J=1,N
2     A(I,J)=0.D0
1     CONTINUE
C
      DO 3 K=1,N
3     B(K,1)=0.D0
      DO 5 M=1,NPPP1
         II=0
         DO 6 JJ=1,N,2
            II=II+1
            B(JJ,1)=B(JJ,1)+Z(M)*DSIN(X(M)*II)
            B(JJ+1,1)=B(JJ+1,1)+Z(M)*DCOS(X(M)*II)
            MM=0
            DO 7 KK=1,N,2
               MM=MM+1
               A(JJ,KK)=A(JJ,KK)+DSIN(X(M)*II)*DSIN(X(M)*MM)
               A(JJ,KK+1)=A(JJ,KK+1)+DSIN(X(M)*II)*DCOS(X(M)*MM)
               A(JJ+1,KK)=A(JJ+1,KK)+DCOS(X(M)*II)*DSIN(X(M)*MM)
               A(JJ+1,KK+1)=A(JJ+1,KK+1)+DCOS(X(M)*II)*DCOS(X(M)*MM)
7     CONTINUE
6     CONTINUE
5     CONTINUE
      CALL MATRIX(A,B,N,1)
C
      IF=0
      DO 8 IE=1,N,2
         IF=IF+1
         AMAG(IF)=DSQRT(B(IE,1)**2+B(IE+1,1)**2)
         BB=-B(IE,1)
         BBB=B(IE+1,1)
         ANG(IF)=DATAN2(BB,BBB)
         ANGD(IF)=ANG(IF)*360./(2.*PI)
         RAT(IF)=AMAG(IF)/AMAG(1)
8     CONTINUE
      IF(YDIS .EQ. 9999) GOTO 555
555  CONTINUE
      MAG = AMAG(1)
      PHASE = ANGD(1)
      RETURN
      END
      SUBROUTINE MATRIX(A,B,N,M)
      IMPLICIT DOUBLE PRECISION(A-H,O-Z)
      DIMENSION AUG(10,11),B(N),A(N,N)
C      MAX. ORDER EQUAL TO 10
C      N = ORDER OF SQUARE MATRIX
C      M = # OF RIGHT HAND SOLUTIONS
      EPS = 0.00000000001
      NPLUSM = N + M
      DO 2 I=1,N
      DO 3 J=1,N
         AUG(I,J) = A(I,J)
3     CONTINUE
      AUG(I,NPLUSM) = B(I)
2     CONTINUE
C

```

```
C BEGIN ELIMINATION PROCESS
C
C CALCULATE THE DETERMINANT
    DETER = 1.D0
    DO 9 K=1,N
        DETER = DETER * AUG(K,K)
C CHECK FOR PIVOT ELEMENT TOO SMALL
    IF(DABS(AUG(K,K)).GT.EPS) GOTO 5
    WRITE(6,1000)
1000 FORMAT(1X,' MATRIX MAY BE SINGULAR')
    RETURN
5   KP1 = K + 1
    DO 6 J=KP1,NPLUSM
6   AUG(K,J) = AUG(K,J) / AUG(K,K)
    AUG(K,K) = 1.
C ELIMINATE K(TH) COLUMN ELEMENTS EXCEPT FOR PIVOT
    DO 9 I=1,N
        IF(I.EQ.K .OR. AUG(I,K).EQ.0.) GOTO 9
        DO 8 J=KP1,NPLUSM
8   AUG(I,J) = AUG(I,J) - AUG(I,K)*AUG(K,J)
        AUG(I,K) = 0.D0
9   CONTINUE
    DO 10 I=1,N
        B(I) = AUG(I,NPLUSM)
10  CONTINUE
    RETURN
END
```

Distribution List

Editor
Applied Mechanics Review
Southwest Research Institute
8500 Culebra Road
San Antonio, TX 78206

Army Research Office
P. O. Box 12211
Research Triangle Park, NC 27709

Defense Research and Development Attaché
Australian Embassy
1601 Massachusetts Avenue, NW
Washington, DC 20036

Mr. Dennis Bushnell
NASA Langley Research Center
Langley Station
Hampton, VA 23365

Dr. Gary Chapman
Ames Research Center
Mail Stop 227-4
Moffett Field, CA 94035

Librarian Station 5-2
Coast Guard Headquarters
NASSIF Building
400 Seventh Street, SW
Washington, DC 20591

Professor Stanley Corrsin
The Johns Hopkins University
Department of Mechanics and
Materials Sciences
Baltimore, MD 21218

Technical Library
Naval Surface Weapons Center
Dahlgren Laboratory
Dahlgren, VA 22418

Library
David W. Taylor Naval Ship Research
and Development Center
Code 522.1
Bethesda, MD 20084

Mr. Justin H. McCarthy, Jr.
David W. Taylor Naval Ship Research
and Development Center
Code 1552
Bethesda, MD 20084

Dr. William B. Morgan
David W. Taylor Naval Ship Research
and Development Center
Code 1540
Bethesda, MD 20084

Defense Technical Information Center
Cameron Station
Alexandria, VA 22314 12 copies

Engineering Documents Center
University of Illinois
208 Engineering Hall
1308 West Green Street
Urbana, IL 61801 2 copies

Engineering Societies Library
345 East 47th Street
New York, NY 10017

Professor Robert E. Falco
Michigan State University
Department of Mechanical Engineering
East Lansing, MI 48824

Professor H. F. Fasel
Aerospace and Mech. Engr. Dept.
University of Arizona
Tucson, AZ 85721

Professor Thomas J. Hanratty
University of Illinois at Urbana-Champaign
Department of Chemical Engineering
205 Roger Adams Laboratory
1209 West California Street
Urbana, IL 61801

Mr. R. J. Hansen
Naval Research Laboratory
Code 8441
Washington, DC 20375

Professor J. H. Haritonides
Department of Aero & Astro.
Massachusetts Institute
of Technology
Cambridge, MA 02139

Dr. A. K. M. Fazle Hussain
University of Houston
Department of Mechanical Engineering
Houston, TX 77004

Professor R. E. Kaplan
Department of Aero Engineering
University of Southern California
University Park
Los Angeles, CA 90007

Dr. Phillip S. Klebanoff
National Bureau of Standards
Mechanics Section
Washington, DC 20234

Professor Louis Landweber
The University of Iowa
Institute of Hydraulic Research
Iowa City, IA 52242

Professor L. Gary Leal
California Institute of Technology
Division of Chemistry and
Chemical Engineering
Pasadena, CA 91125

Library of Congress
Science and Technology Division
Washington, DC 20540

Professor H. W. Liepmann
California Institute of Technology
Graduate Aeronautical Laboratories
Pasadena, CA 91125

Lorenz G. Straub Library
University of Minnesota
St. Anthony Falls Hydraulic Laboratory
Minneapolis, MN 55414

Professor John L. Lumley
Cornell University
Sibley School of Mechanical
and Aerospace Engineering
Ithaca, NY 14853

Donald McEligot
Gould Defense Systems Inc.
1 Corporative Park
Middletown, RI 02840

Dr. D. K. McLaughlin
Dynamics Technology Inc.
21311 Hawthorne Blvd., Suite 200
Torrance, CA 90503

Dr. Jim McMichael
Air Force Office of Scientific
Research/NA
Building 410
Bolling AFB
Washington, DC 20332

Dr. Arthur B. Metzner
University of Delaware
Department of Chemical Engineering
Newark, DE 19711

Professor Richard W. Miksad
The University of Texas at Austin
Department of Civil Engineering
Austin, TX 78712

NASA Scientific and Technical
Information Facility
P. O. Box 8757
Baltimore/Washington International
Airport
Maryland 21240

Professor Paul M. Naghdhi
University of California
Department of Mechanical Engineering
Berkeley, CA 94720

Technical Library
Naval Costal System Laboratory
Panama City, FL 32401

Technical Library
Naval Missile Center
Point Mugu, CA 93041

Technical Library
Naval Ocean Systems Center
San Diego, CA 92151

Library
Naval Postgraduate School
Monterey, CA 93940

Library
Naval Sea Systems Command A
Code 09GS
Washington, DC 20362

Mr. Thomas E. Peirce
Naval Sea Systems Command B
Code 63R21
Washington, DC 20362

Librarian
Naval Surface Weapons Center
White Oak Laboratory
Silver Spring, MD 20910

Technical Library
Naval Underwater Systems Center
Newport, RI 02840

Library
Naval Weapons Center
China Lake, CA 93555

Office of Naval Research
Code 1132F
800 N. Quincy Street
Arlington, VA 22217 3 copies

Director
Office of Naval Research
Eastern/Central Regional Office
Building 114, Section D
666 Summer Street
Boston, MA 02210

Director
Office of Naval Research
Western Regional Office
1030 E. Green Street
Pasadena, CA 91101

Professor T. Francis Ogilvie
The University of Michigan
Department of Naval Architecture
and Marine Engineering
Ann Arbor, MI 48109

Professor S. I. Pai
University of Maryland
Institute of Fluid Dynamics
and Applied Mathematics
College Park, MD 20742

Professor Eli Reshotko
Case Western Reserve University
Department of Mechanical and
Aerospace Engineering
Cleveland, OH 44106

Professor A. Roshko
California Institute of Technology
Graduate Aeronautical Laboratories
Pasadena, CA 91125

The Society of Naval Architects and
Marine Engineers
One World Trade Center, Suite 1369
New York, NY 10048

Professor W. G. Tiederman
School of Mechanical Engineering
Purdue University
West Lafayette, IN 47907

Professor P. S. Virk
Massachusetts Institute of Technology
Department of Chemical Engineering
Cambridge, MA 02139

Professor John V. Wehausen
University of California
Department of Naval Architecture
Berkeley, CA 94720

Professor W. W. Willmarth
The University of Michigan
Department of Aerospace Engineering
Ann Arbor, MI 48109

Professor Theodore Y. Wu
California Institute of Technology
Engineering Science Department
Pasadena, CA 91125

Professor C. -S. Yih
The University of Michigan
Department of Engineering Mechanics
Ann Arbor, MI 48109

U22773A